SYNTHESIS AND PROPERTIES OF GIANT PORPHYRIN NANORINGS

A thesis submitted to the board of the Faculty of Physical Sciences in partial fulfillment of the requirements for the degree of

Doctor of Philosophy of the University of Oxford

By

Dmitry (Dmytro) Kondratiuk

The Chemistry Research Laboratory and Merton College, Oxford

Trinity Term 2013

SYNTHESIS AND PROPERTIES OF GIANT PORPHYRIN NANORINGS

D.Phil Thesis, Trinity Term 2013

Dmitry (Dmytro) Kondratiuk, Merton College, University of Oxford

Abstract

Fully conjugated porphyrin nanorings combine an end-free π-system with well defined size and shape. They provide models for testing our understanding of light harvesting in natural photosynthetic systems, and may lead to the creation of new functional materials. This thesis describes the template-directed synthesis of novel 10, 16, 18, 20, 24, 30, 40 and 50-porphyrin nanorings using small templates, as well as the investigation of their structure, electronic properties and supramolecular chemistry in solution and on surfaces. This work illustrates the scope of Vernier templating as a tool for the synthesis of monodisperse molecules of unprecedented sizes.

Chapter 1 introduces key properties of porphyrins and π-conjugated linear and cyclic porphyrin oligomers and describes the principle methods of preparing non-conjugated and conjugated cyclic polymers. It also covers recent advances in the synthesis of fully-conjugated porphyrin nanorings, in particular Vernier templating.

Chapter 2 discusses the formation of higher order porphyrin nanorings (18- and 24-porphyrin nanorings) in the classical synthesis of 6-porphyrin nanoring and the Vernier-templated synthesis of 12-porphyrin nanoring.

Chapter 3 describes the Vernier-templated synthesis of 24-porphyrin nanoring and its characterization.

Chapter 4 shows that the flexibility of 24-porphyrin nanoring can be locked by the formation of a "sandwich" complex in the presence of a bidentate ligand or by solvent-induced formation of aggregates.

Chapter 5 demonstrates the use of templates to control the cyclooligomerization of linear porphyrin oligomers. Vernier-templated synthetic routes to 10-, 30- and 40-porphyrin nanorings are investigated.

Chapter 6 reports the electronic properties of porphyrin nanorings as probed by electrochemistry (for 6-porphyrin nanoring) or fluorescence anisotropy measurements (for 24-porphyrin nanoring). Crystal structures of 6- and 12-porphyrin nanoring-template complexes are presented.

Chapter 7 contains experimental procedures and characterization data of known and novel compounds synthesized in the course of this thesis.

Abbreviations

AFM	Atomic force microscopy	m	multiplet (in NMR)
aq	Aqueous	Me	Methyl
Ar	Aryl	MM	Molecular mechanics
ATP	Adenosine triphosphate	MW	Molecular weight
B band	Soret band, porphyrin S_0-S_2 absorption band	NBS	*N*-Bromosuccinimide
		NIR	Near-infrared
BChl	Bacteriochlorophyll	NMR	Nuclear magnetic resonance
Bipy	4,4'-bipyridine	Ph	Phenyl
CNT	Carbon nanotube	PL	Photoluminescence
c-PPA	Cyclic *para*-phenylacetylene	PLE	Photoluminescence excitation
c-PP	Cyclic *para*-phenylene	PDF	Pair distribution function
d	Doublet (in NMR)	Q band	Porphyrin S_0-S_1 absorption band
Da	Dalton		
DABCO	1,4-Diazabicyclo[2.2.2]-octane	RC	Reaction centre
		r.t.	Room temperature
dba	Dibenzylideneacetone	SAXS	Small angle X-ray scattering
DDQ	2,3-Dichloro-5,6-dicyano-*para*-benzoquinone	SEC	Size exclusion chromatography
DFT	Density functional theory	STM	Scanning tunneling microscopy
DNA	Desoxyribonucleic acid		
Et	Ethyl	t	Triplet (in NMR)
FRET	Förster resonance energy transfer	*t*	tertiary carbon
		TBAF	Tetra-*n*-butylammonium fluoride
GPC	Gel permeation chromatography		
		TD	Time dependent
HOMO	Highest occupied molecular orbital	TFA	Trifluoroacetic acid
		THF	Tetrahydrofuran
HOPG	Highly oriented pyrolitic graphite	THS	Trihexylsilyl
		TIPS	Tri*iso*propysilyl
IR	Infrared	TLC	Thin layer chromatography
LH	Light harvesting system	TOF	Time of flight
LUMO	Lowest unoccupied molecular orbital	UHV	Ultrahigh vacuum
		UV	Ultra-violet
MALDI	Matrix-assisted laser desorption ionization	Vis	Visible

Acknowledgements

First of all, I must thank my supervisor, Prof. Harry Anderson, for continuous support over my time in the group and keeping the standards of research very high. I really do hope I managed to learn a bit of it too.

This work involves contributions from numerous very bright people who I was very lucky to work with. Thanks to Dr. Tim Claridge and Dr. Barbara Odell (Oxford Chemistry) for help, discussion and recording some NMR spectra, Dr. Luis Perdigão, Simon Svatek, and Prof. Peter Beton (Nottingham Physics) for STM imaging, Dr. Chaw Keong Yong, Wei-Hsin Chen and Dr. Laura Herz (Oxford Physics) for the PL anisotropy measurements, EPSRC mass spectrometry service (Swansea) and Gareth Smith (Manchester Chemistry) for mass spectrometry, Dr. Mark Malfois (Diamond Light Source) for help with SAXS experiments. A particular big thanks and big hug go to Dr. Amber L. Thompson (Oxford Chemistry) for unbelievable crystallography work, great jokes and optimism under any circumstances.

Oxford will remain deep in my heart due to incredible people I have met here. These include my former and present colleagues and friends outside of chemistry. I would like to particularly thank Dr. Johannes Sprafke for being a good friend, introducing me to porphyrin chemistry and Opera. Thanks to Dr. Hazel Collins and James Wilkinson (and Alice!) for making me love people of this country very much. Thanks to Karolina Korzycka and Dr. Nicola Davis for nice conversations on everything; to Ishmael Lopez (and Macarena), Kanokkorn Sirithip, Nuntaporn Kamonsutthipaijit for warm-heartedness and unlimited kindness; to Dr. Christiane Knappke for caring, attention and hugs. Crazy professor - Dr. Mitsuhiko Morisue – thanks for being a constant source of so much laughter! Thanks to Dr. Sophie Rousseaux for proofreading parts of my thesis and pushing me to make important decisions about future. Phoom Chairatana, William Peveler and Levon Movsisyan, thank you guys for being great people to supervise and work with. Big thank you to Adam Kendrick for teaching me so many things while I was supervising your Part II! Thanks to Sebastien, Louisa, Giuseppe, Sally, Jan, John, Georg, Stephen, Kayli, Kuoren, Guzman, Qianfu, Patrik, Julien, Melanie, Wojciech, Rene and many others for making the lab a great place to be! Thanks to members of the Queen just for writing all those great songs!

I am greatly indebted to my great family (my dad, my mum, my sister) and friends for keeping my sanity and giving support whenever I needed. I would like to dedicate this work to them.Thanks to my friend and almost a brother Joseph Tymkovski. I think I have no proper words to express my gratitude I have you, man, in my life! Thanks to Igor Boczarow and Akiko Soiji for being there with me, understanding and unconditional acceptance. I really do hope our friendship lasts beyond our times at Oxford. Igor, big thank you for proofreading parts of this thesis too!

Finally, as a tradition, best of luck to Peng Peng, Sophie and Nun and all the future bearers of the burden!

Table of Contents

In my beginning is my end…In my end is my beginning.

T. S. Eliot, “Four Quartets”

Chapter 1

Introduction

This chapter outlines the importance of porphyrins and porphyrinoids as building blocks in natural and man-made functional systems. The effects of introducing porphyrins and their derivatives on the electronic, structural and self-assembly properties of such systems are discussed. A short review on the synthesis and properties of cyclic polymers (both conjugated and non-conjugated) is presented, as well as a summary of the contribution of Anderson’s group to this field. The synthesis of the starting compounds required for my work is also covered.

1.1 Porphyrins – Nature's Macrocycles of Life

Porphyrins are a family of macrocyclic compounds comprised of four pyrrole units connected through their α positions by methine bridges of which porphin **1** is the simplest member (Figure 1.1a). It is common to refer to porphyrins as "aromatic" due to the presence in their structure of the [18]-annulene pathway and the favourable comparison of their ^{1}H NMR with analogous macrocycles such as 1,6-imino[10]annulene **2** and and *syn*-1,6:8,13-diimino[14]annulene **3**.[1] The commonplace numbering systems for porphyrins is presented in Figure 1.1a for porphin **1**, however it is typical to refer to the positions 2, 3, 7, 8, 12, 13, 17, 18 as β-pyrrole centres and to the positions 5, 10, 15, 20 as *meso* centres. The structural diversity of the porphyrins is attained through modification at β and *meso* centres. Porphyrins and their derivatives are amphoteric. Basicity of porphyrins led to the frequently used term "free-base" porphyrin and enables protonation by acids generating double protonated species. The acidity of porphyrins combined with their rigid geometry and favourable location of four electron donating nitrogens in the corresponding dianion render them excellent chelating ligands which form metallocomplexes (metalloporphyrins) with numerous metals (Figure 1.1b). Interestingly, formation of the free double anion has not been observed, in contrast to the mono-anion.[2]

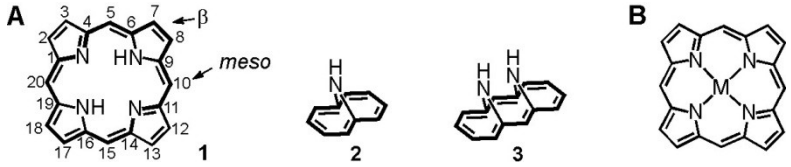

Figure 1.1. (a) Structure of the free-base porphin **1** (with the assignement of the positions), its homologues **2** and **3** and (b) metalloporphyrins.

Porphyrin derivatives are the most common natural pigments and they serve various functions. The heme structure features an iron porphyrin moiety and is a common prosthetic group of hem-containing proteins: hemoglobin and myoglobin participate in transporting oxygen in blood; cytochromes are electron mediators responsible for the formation of ATP in cells. Cofactor F430 is a nickel porphyrinoid which is a part of the enzyme methyl coenzyme M-reductase catalyzing formation of methane in bacteria. Vitamin B12 contains a cobalt porphyrinoid part and participates in the transfer of hydrogen and methyl groups in biochemical transformations; its hydroxo form is also an important antidote for poisoning with cyanides. Abnormal metabolism of porphyrin- and porphyrinoid-containing compounds in the human body may lead to severe diseases such as anemia and porphyria. Of these, the most notable case is certainly that of the King of Great Britain Georg III, whose mental disorder, which led to the regency crisis in Britain, is believed to have been a consequence of porphyria. Finally, chlorophylls, which are magnesium-containing porphyrin derivatives, are key pigments of the photosynthesis. In Nature it occurs in the so-called photosystems of which the photosystems of purple bacteria are among the best studied.[3-5]

The photosystems of the purple bacteria provide an excellent example of how Nature elegantly

uses tools of supramolecular chemistry for precisely positioning pigment moieties to achieve the most efficient sun energy harvesting and transfer and subsequently charge-separation in the reaction centre (Figure 1.2). The photosystem is embedded within the cell membrane of the photosynthetic bacteria and typically consists of two types of the light-harvesting (LH) pigment-protein complexes called LH1 and LH2 (Figure 1.2a), and the reaction centre (RC) contained within LH2. Each of the LHs is comprised of rings of molecules of bacteriochlorophylls a (BChl *a*), which is a magnesium-containing porphyrinoid. Depending on the absorption wavelength, there are several types of BChls *a* (B800, B850, B875 and B880; the number stands for the absorption maximum) that can be found in LHs. The different absorption maxima arise from different interactions with the amino acid residues of the protein scaffold. LH1 consists of 30-32 molecules of B875 whereas LH2 contains 9 residues of B800 and 18 residues of B850 perpendicular to each other (Figure 1.2a); in both LHs, the BChls *a* are held strictly in place by a protein scaffold and its interactions (through nitrogens of the amino acid residues) with the Mg-centres, so that there are only a few shortest pigment-pigment distances which determine the degree of electronic coupling and the rate of Förster resonance energy transfer (FRET) between different BChls within and between LHs (Figure 1.2b,c). In the LH2 structure there are two different sets of nearest neighbour pigment-pigment distances within the complex, one short, 9 Å (centre-to-centre distance), for the B850-B850 contacts, and one longer, 18 Å, for the B800-B800 and B800-B850 distances; in the LH1 the B875-B875 distances are essentially the same as B850-B850 of LH2; the longest distances are estimated between nearest B850-B875 of LH2 and LH1 (30 Å) and between B875-B880 of LH1 and RC (45 Å).[3] The short B850-B850 and B875-B875 distances within LH2 and LH1 respectively lead to the strong exciton coupling between all of the chromophores within LHs. The overall very precise arrangement of the energetically matching chromphores leads to the rapid, efficient, and directional downhill energy flow from LHC II to LHC I and finally to the reaction centre in less than 100 ps with overall quantum efficiency >90%.[6] The funneled energy drives the charge separation in the reaction centre and is then accummulated in the form of ATP. Such a high quantum efficiency is believed to be in particular due to the ability of the strongly coupled BChls moieties within LH1 and LH2 to support highly delocalized excited states.[7-9] Due to this, the LH2, for example, exhibits ultrafast delocalization of excitations across all of its 18 B850 moieties within less than 100 fs as probed by absorption[10] and emission[8] spectroscopy. Such a quick delocalization in the LH2 invited the term “quantum coherence” when describing its exciton transfer behaviour. In this context, the coherence means that the molecules in these cyclic arrays directly affect each other instantaneously with no time delay and the phase of the excited state is preserved as it delocalizes over the set of chromophores. It has been suggested that in typical synthetic organic semiconductors designed for photovoltaic devices, the existance of delocalized states may also facilitate charge separation following initial light absorption.[11] As a consequence, materials that support delocalized electronic states in well-defined arrays of chromophores make excellent components for next-generation carbon-based solar cells.[12,13] As such, the naturally occurring photosystems provide

tremendous inspiration for scientists striving to create new molecular light-harvesting materials.

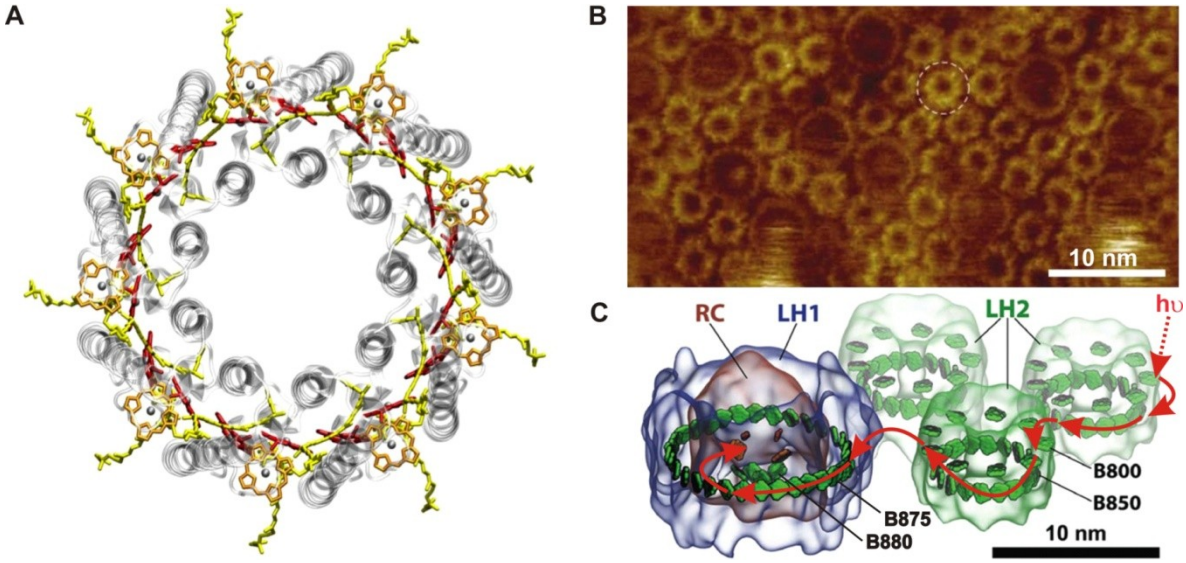

Figure 1.2. (a) Top view of the LH2 of purple bacteria. Model reprinted from *http://commons.wikimedia.org/wiki/File:LH2_top.jpg*. (b) AFM image of a native membrane of Rs. photometricum (scale bar = 10 nm). Reprinted from permission from ref. 14. Copyright 2013. American Association for the Advancement of Science. (c) The model of the one LH1-RC complex with LH2 complexes nearby. The red arrows indicate the flow of energy from absorption to charge-separation. Adapted with permission from ref.15. Copyright 2013 American Chemical Society.

1.2 Linear Porphyrin Oligomers

1.2.1 Optoelectronic Properties

All porphyrins are intensely coloured which gives rise to the name: the word *porphyrin* is derived from Greek word *porphura* meaning purple.[16] The electronic absorption spectrum of a typical porphyrin monomer consists of two strong transitions: one to the second excited state ($S_0 \rightarrow S_2$) at about 400 nm (the Soret or B band) and a weaker transition to the first excited state ($S_0 \rightarrow S_1$) at about 550 nm (the Q band). Internal conversion from S_2 to S_1 is rapid so fluorescence is only detected from S_1. The B and Q bands arise from π– π* transitions and can be explained using Gouterman's four orbital model (Figure 1.3a). The four frontier orbitals in the D_{4h} symmetrical porphyrins are: two π orbitals (a_{1u} (HOMO) and a_{2u} (HOMO-1)) and a degenerate pair of π* orbitals (e_{gx} and e_{gy}, both LUMO). The a_{1u} and a_{2u} orbitals have about the same energy and the transition to the degenerate LUMOs should result in two almost coincident absorption bands. However, due to the configurational interaction, the two bands mix together resulting in the two bands with significantly different intensities and energies: one, the B band ($S_0 \rightarrow S_2$), of the higher intensity and the Q band ($S_0 \rightarrow S_1$) of the lower intensity (Figure 1.3b,c).[17] The modification of the porphyrins at the β or *meta*-positions can significantly affect porphyrin electronic properties and the extent of such influence depends on the extent of the π–overlap. It has also been shown that the introduction of substituents through β positions affects electronic properties of the porphyrin core less than when they are connected through *meso*-positions in accordance with the smaller frontier orbital coefficients in the former.[17] Of

particular importance are porphyrins having *meso*-aryl substituents, which, due to the large aryl–porphyrin dihedral angles, only slightly perturbate electronic structure of the porphyrin core.[17]

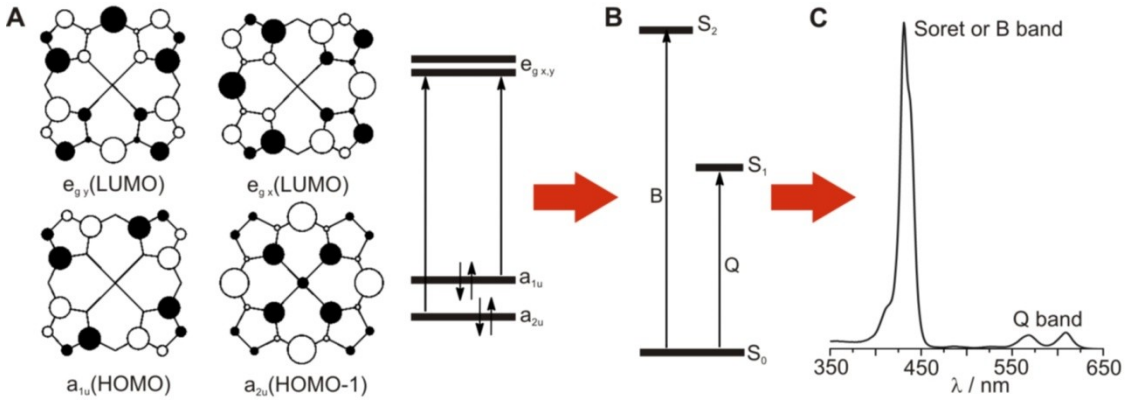

Figure 1.3. (a) The four Gouterman molecular orbitals of the typical D_{4h} symmetrical porphyrin monomer. (b) Configurational interaction between $a_{1u} \rightarrow e_{gy}$ and $a_{2u} \rightarrow e_{gx}$ results in (c) two absorption bands of very different intensities.

The electronic properties of the covalent or non-covalent porphyrin arrays may be significantly different as compared to the monomers, depending on the proximity of the individual porphyrin units, as well as on whether they are conjugated. In D_{4h} symmetrical porphyrin monomers, the components B_x and B_y of the Soret band are degenerate and the Q band is of low intensity. However, in porphyrin arrays, these components may become non-degenerate because of the interaction between *x* and *y* components of the transitions and thus the B and Q bands will be altered. The point-dipole theory describing interaction of transition moments of two dipoles, such as in the porphyrin dimer linked by a general bridge (Figure 1.4a), has been developed by Kasha[18] and is summarized in Figure 1.4b,c. If the porphyrin monomer units are aligned along the *x* axis, the B_x transitions are arranged head-to-tail and the B_y transitions lie parallel and face-to-face. The transitions to the states with alternative arrangements of two components of B_x (head-to-head) and B_y (anti-parallel and face-to-face) are not allowed due to symmetry (Figure 1.4b,c). In electrostatic terms, the head-to-tail arrangement of B_x is an attractive interaction, in contrast to parallel face-to-face arrangement of B_y which is a repulsive interaction. As a result, the transitions are only allowed to the lower energy of the two B_x states and to the higher energy of the two B_y states, and the B band of a porphyrin dimer is split into a low energy (red shifted) B_x component and a higher energy (red shifted) B_y component, in accordance with the data of the polarized spectroscopy (Figure 1.5a).[19]

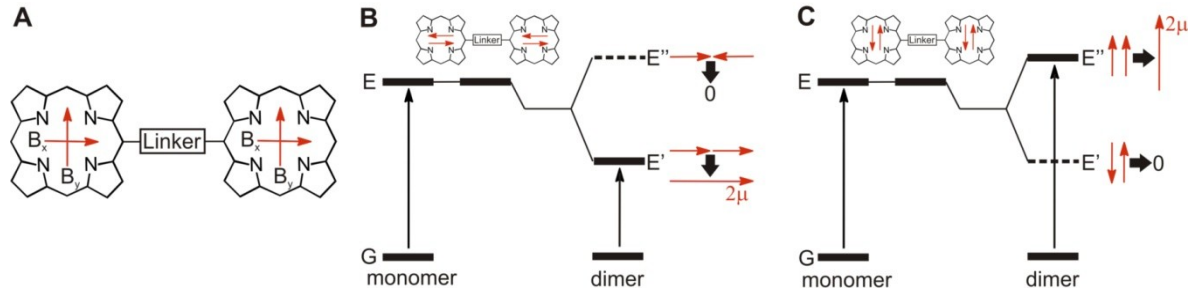

Figure 1.4. (a) Transition dipole moments of B band transitions in the planarized porphyrin dimer. (b) Exciton band energy diagram for a porphyrin dimer with in-line transition dipoles. (c) Exciton band energy diagram for a planarized porphyrin dimer with parallel transition dipoles.

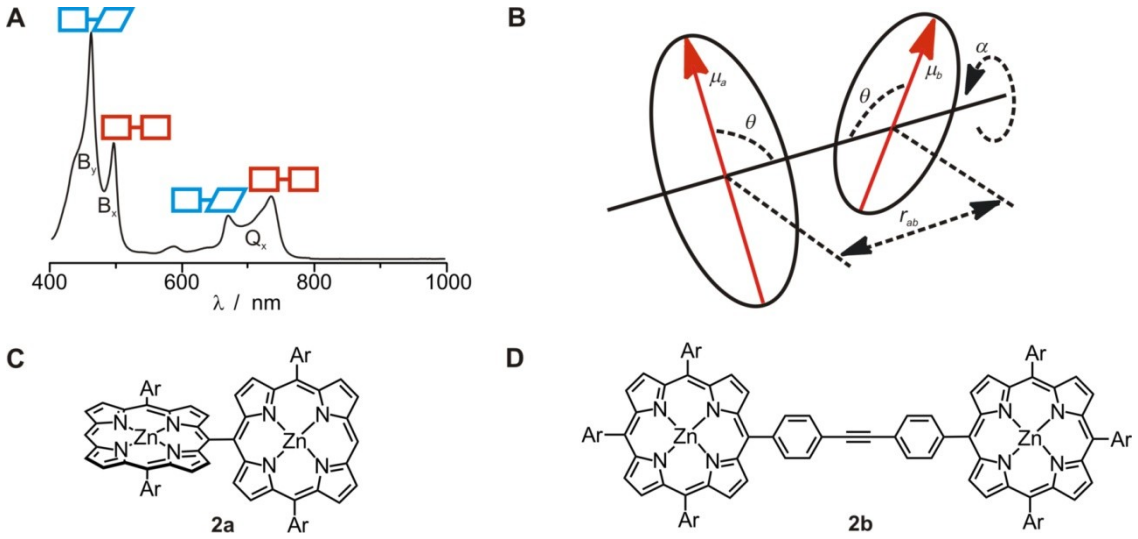

Figure 1.5. (a) Absorption spectrum of the butadiyne linked porphyrin dimer **3c** in $CHCl_3$/1% pyridine. (b) Model for the coupling of two transition dipole moments. (c) Osuka's *meso-meso* linked porphyrin dimer **2a**[20] and (d) Lindsey's *para*-phenylene-ethyne bridged porphyrin dimer **2b**.[23]

In the general case, the exciton splitting energy of two adjacent transition dipole moments μ_a and μ_b is described by the equation:

$$\Delta E = E'' - E' = \frac{2|\mu_a \mu_b|}{r_{ab}^3}\left(\cos\alpha + 3\cos^2\theta\right)$$

where, μ_a and μ_b are the transition dipole moments for the singlet-singlet transitions of monomers *a* and *b*, r_{ab} is the centre-to-centre distance, α is the torsional angle between two molecular planes of the chromophores and θ is the angle between polarization axes and the centre-to-centre line assuming the same angles for both dipoles for simplicity (Figure 1.5b).[18] From the equation above, it follows that for the considered porphyrin dimer the maximum exciton coupling is achieved when the porphyrin dimer is planarized ($\alpha = 0°$, $\cos\alpha = 1$) and the dipoles are oriented along the centre-to-centre line ($\theta = 0°$, $\cos\theta = 1$). The important factor is the proximity of the porphyrin units (so that the linker is not too long) as the extent of the exciton coupling is also proportional to $1/r_{ab}^3$. For example, Osuka's porphyrin dimer directly-linked through *meso*- positions **2a** (Figure 1.5c) and longer oligomers of this type exhibit pronounced splitting of their Soret bands.[20-22] In contrast, in the case of the Lindsey's porphyrin dimer such as **2b** linked through long *para*-phenylene-ethyne bridges (Figure 1.5d), the absorption spectra are all nearly the same as that of the monomer.[23,24]

Exciton coupling theory does not take into account the effect of electronic overlap between different chtomophores. It works best when applied to the non-conjugated porphyrin oligomers such as those shown in Figure 1.5c,d, where electronic overlap is excluded due to unfovourable torsional angles between planes of porphyrins. The possibility of electronic overlap afforded by the use of sterically less demanding bridges, such as ethylene in **3a**,[25] acetylene in **3b**,[26] butadiyne in **3c**,[27] by fusing the porphyrin moieties directly at *meso* and one or two nearby β positions such as in **3d**,[28,29] or by connecting β positions by 1,4,5,8-tetraazaanthracene bridges as in **3e**,[30] (Figure 1.6a) leads to

strong electronic coupling as indicated by the very large red shifts of the Q bands (see for example, Figure 1.6b). Further enhancement in electronic coupling can be achieved by the use of the substituent groups that can stabilize quinoidal resonance structures such as anthracene in **3f**,[31] pentacene in **3g**,[32] thiophene in **3h**,[31] benzo-*bis*(thiadiazole) in **3i**,[32] benzo-thiodiazole-quinoxaline derivative in **3j**,[32] cyanine-like in **3k**,[33,34] *etc* moieties (Figure 1.6a). The shift of the Q band achieved upon insertion of the latter group reaches the region of 1300 nm. Extending porphyrin oligomers beyond the dimer is yet another approach for increasing the electronic coupling between porphyrin units which dramatically affects the energy and intensity of the Q band (Figure 1.6b). This has been realized so far using acetylene,[26,35] butadiyne[17,36] and fusion of porphyrin units.[28] Comparison of *meso–meso*, *meso*–β and β–β linked dimers of the type **3c** shows that *meso-meso* connectivity confers maximum electronic coupling attributed to the smaller frontier orbital coefficients at the β–positions (Figure 1.3a).[17,37]

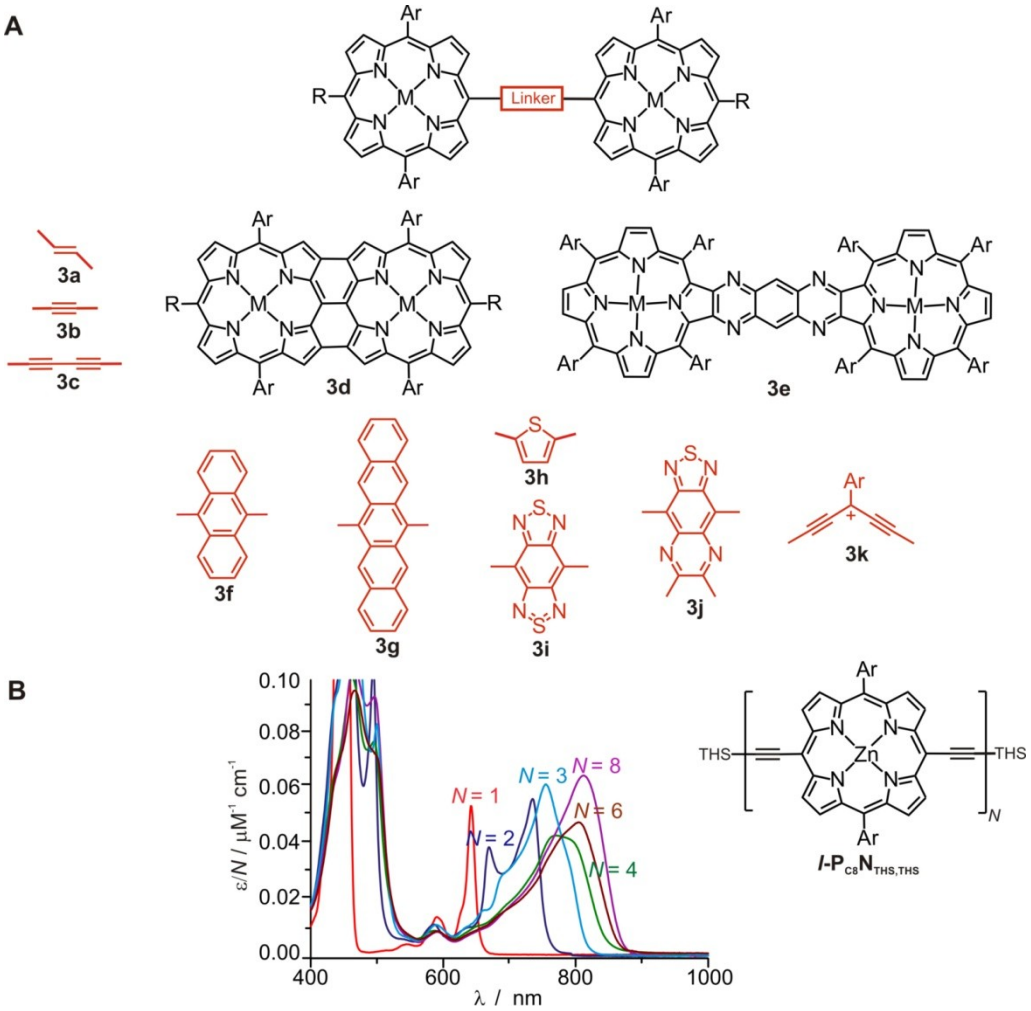

Figure 1.6. (a) Some common porphyrin dimer linkers used to provide electronic coupling between porphyrin moieties. Absorption spectra in $CHCl_3$/1% pyridine of the series ***l*-P$_{C8}$N$_{THS,THS}$**.

Theoretical studies at the DFT level of theory shed some light on the origin of the large shift of the Q band observed in the butadiyne linked porphyrin dimers such as **3c**.[38] The frontier orbitals responsible for the Q band (HOMO and LUMO) spread over the butadiyne linker and the corresponding HOMO-LUMO gaps are lowered as compared to the monomer (Figure 1.7a).[38]

According to calculations, in a planarized conformer of **3c** the Q band is not split in contrast to the B band, and is polarized along *x* axes (axes connecting the centres of porphyrin). The energies of these orbitals show strong dependence on the dihedral angle between the planes of porphyrins and blue shift by almost 100 nm upon changing the dihedral angle from 0º to 90º. Thus the observed experimental splitting of the Q band in Figure 1.5a is probably due to the presence of different conformers. The shape of the spectra also suggests a wide distribution of dihedral angles at room temperature consistent with the very low theoretical rotational barrier of only 0.67 kcal/mol (RT = 0.59 kcal/mol).[38] Interestingly, the first excited state the rotational barrier is significantly higher (3.9 kcal/mol) and the rotation should be more constrained.[38] Dimers like **3c** can be easily fixed in one conformation using tools of supramolecular chemistry (Figure 1.7b): by complexation with rigid bidentate ligand such as in the complex **3c•T2**,[38] by forming ladder complexes with DABCO such as **(3c)**$_2$•(DABCO)$_2$,[27] or by simple aggregation[27] which all result in simplification of the Q band.

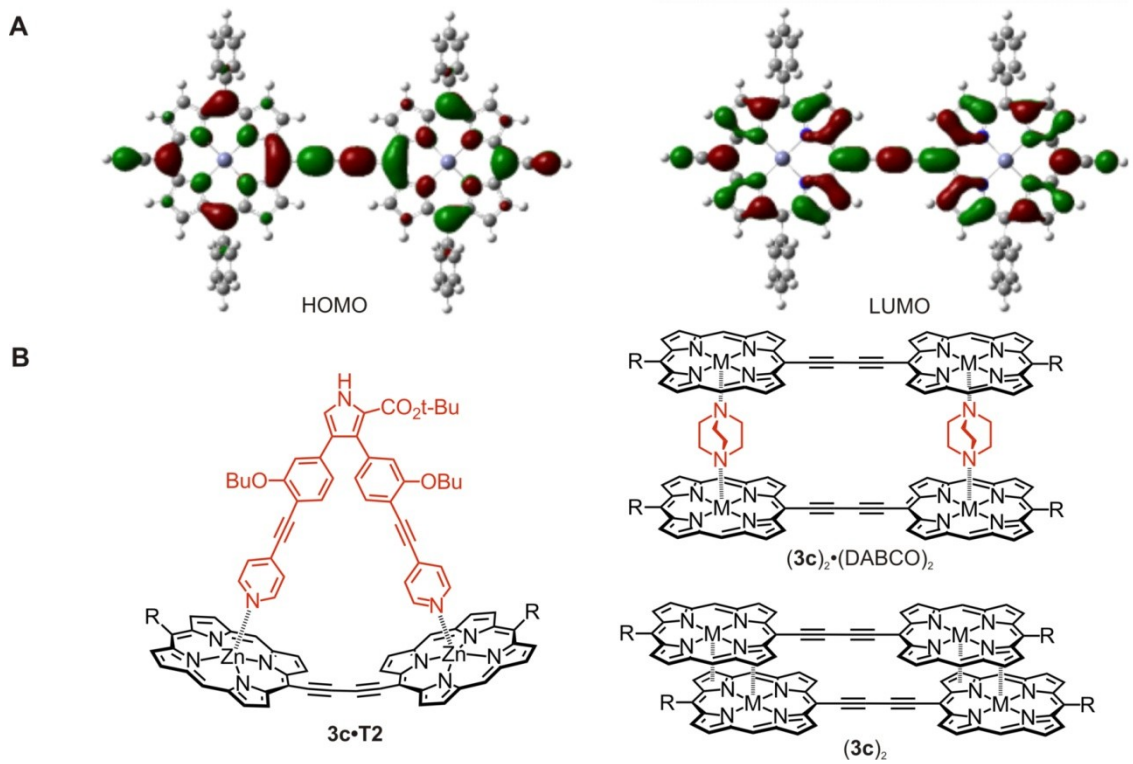

Figure 1.7. (a) HOMO and LUMO of a butadiyne-linked porphyrin dimer as calculated by DFT.[38] (b) Different strategies applied to restrict free internal rotation around butadiyne bond is porphyrin dimer **3c**.

1.2.2 Synthesis of Linear Porphyrin Oligomers

1,3-Butadiyne linkers provide convenient tools to building up fully conjugated porphyrin oligomers beyond a dimer. Strong electronic coupling between individual porphyrins in such oligomers give rise to unusual optoelectronic properties and makes them promising models for natural photosynthetic systems. In addition to providing full conjugation, 1,3-butadiynes add shape-persistence to the molecules, which, combined with the coordinating properties of the porphyrins themselves, lead to unusual self-assembly properties. This also opens up the possibility of tuning electronic properties

using supramolecular chemistry, just as in natural systems.

With increasing the size of the porphyrin oligomers, their solubility drops. The first generation of the butadiyne-linked porphyrin dimers, prepared by Arnold[39] and Anderson,[27] had alkyl and alkyl-ester subsituents in the β positions which provided enough solubility to the corresponding linear porphyrin polymer. The second generation of porphyrin dimers and longer oligomers, introduced by Anderson[36,40-42] and Ogawa,[43] had substituents in the *meso*-positions not involved in connecting porphyrin subunits. Some of the most common substituents of this type are shown in Figure 1.8. Of these, *meso*-aryl side groups have found most application because of their perpendicular orientation to the porphyrin plane. Because of such orientation, these groups reduce aggregation and also have a minute effect on the electronic properties of the porphyrin core. In this thesis, two main side groups have been employed: 3,5-*bis*-*tert*-butyl phenyl and 3,5-*bis*-octyloxy phenyl (Figure 1.8). The porphyrin oligomers bearing the former side groups tend to crystallize better and provide enough solubility for up to the linear 8-mer. In the case of the latter side groups, oligomers are much less ordered in the solid state and tend to aggregate, but provide ample solubility to oligomers having at least 40-50 units.

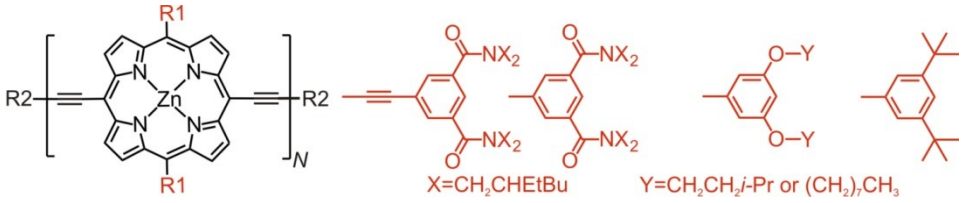

Figure 1.8. Second generation of side groups used by Anderson and Ogawa to solubilize porphyrin oligomers beyond dimer.

The synthesis of the 1,3-butadiyne linked porphyrin oligomers (for both side groups) is achieved through sequential trihexylsilyl (THS) deprotection and acetylene-homo coupling steps. The starting porphyrin free base cores can be easily assembled by condensation and following oxidation of the dipyrromethane **4**[44] with corresponding benzaldehyde derivatives **5**[45] and **6**[46] using Lindsey's conditions to give porphyrins ***l*-P$_{t\text{-Bu}}$1$_{FB}$/*l*-P$_{C8}$1$_{FB}$** in nearly 50% yield (Figure 1.9a).[47] Free base porphyrins are then quantitatively converted to the corresponding zinc porphyrins ***l*-P$_{t\text{-Bu}}$1$_{Zn}$/*l*-P$_{C8}$1$_{Zn}$** by treatment with $Zn(OAc)_2$. Electrophilic bromination of ***l*-P$_{t\text{-Bu}}$1$_{Zn}$/*l*-P$_{C8}$1$_{Zn}$** in the *meso*-position by treatment with *N*-bromosuccinimide (NBS) affords dibromoporphyrins ***l*-P$_{t\text{-Bu}}$1$_{Br,Br}$/*l*-P$_{C8}$1$_{Br,Br}$** in good yield. Sonogashira coupling of the dibromoporphyrins ***l*-P$_{t\text{-Bu}}$1$_{Br,Br}$/*l*-P$_{C8}$1$_{Br,Br}$** with mono THS-protected acetylene affords THS-protected porphyrin monomers ***l*-P$_{t\text{-Bu}}$1$_{THS,THS}$/*l*-P$_{C8}$1$_{THS,THS}$** in quantitative yields.

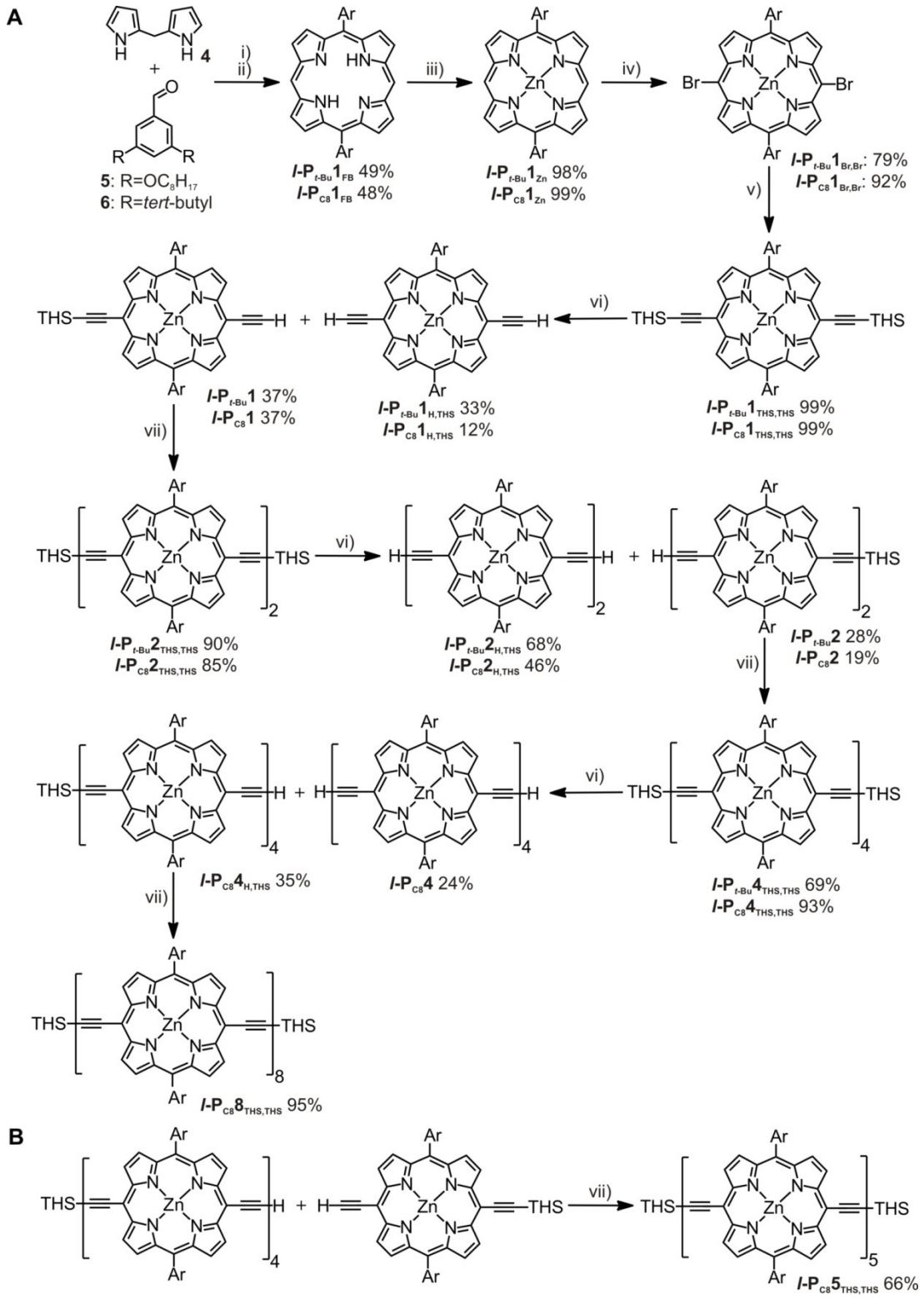

Figure 1.9. (a) Synthesis of butadiyne-linked porphyrin oligomers up to octamer. (b) Cross coupling of the half-protected monomer and tetramer for preparation of ***l*-P$_{C8}$5$_{THS,THS}$**. Reagents: i) TFA; ii) DDQ; iii) $Zn(OAc)_2$; iv) NBS; v) THS-acetylene, $Pd_2(DBA)_3$, PPh_3, CuI, *i*-Pr_2NH; vi) TBAF; vii) 1,4-benzoquinone, $Pd(PPh_3)_2Cl_2$, CuI, *i*-Pr_2NH. Ar=3,5-bis(*tert*-butyl)phenyl and 3,5-bis(octyloxy)phenyl.

Statistical deprotection of monomers ***l*-P$_{t\text{-}Bu}$1$_{THS,THS}$/*l*-P$_{C8}$1$_{THS,THS}$** with tetra *n*-butylammonium fluoride (TBAF) gives a mixture of the unreacted starting material, half-protected monomers ***l*-P$_{t\text{-}Bu}$1$_{H,THS}$/*l*-P$_{C8}$1$_{H,THS}$** and fully deprotected monomers ***l*-P$_{t\text{-}Bu}$1/*l*-P$_{C8}$1**. Pd-catalyzed Glaser coupling

of ***l*-P$_{t\text{-Bu}}$1$_{H,THS}$/*l*-P$_{C8}$1$_{H,THS}$** gives dimers ***l*-P$_{t\text{-Bu}}$2$_{H,THS}$/*l*-P$_{C8}$2$_{H,THS}$** in good yields. Applying the same sequence of reactions iteratively tetramers ***l*-P$_{t\text{-Bu}}$4$_{H,THS}$/*l*-P$_{C8}$4$_{H,THS}$** and octamer ***l*-P$_{C8}$8$_{H,THS}$** can be prepared. The same approach also works for cross coupling of half-protected porphyrin oligomers of different lengths such as in the synthesis of porphyrin pentamer ***l*-P$_{C8}$5$_{THS,THS}$** by coupling of half-protected monomer ***l*-P$_{C8}$1$_{H,THS}$** and tetramer ***l*-P$_{C8}$4$_{H,THS}$** (Figure 1.9b). The resulting mixture of protected dimer ***l*-P$_{C8}$2$_{THS,THS}$**, pentamer ***l*-P$_{C8}$5$_{THS,THS}$** and octamer ***l*-P$_{C8}$8$_{THS,THS}$** can be separated by preparative GPC system.

For oligomers higher than a tetramer, half- and fully-deprotected porphyrins are inseparable by column chtomatography and an alternative approach is needed to controllably synthesize longer oligomers.[44] This can been achieved by coupling the corresponding full-deprotected forms with excess of the porphyrin monomer or dimer (Figure 1.10); the resulting mixtures of oligomers are separable by GPC chromatography. Thus, the porphyrin trimer ***l*-P$_{C8}$3$_{THS,THS}$** has been synthesized by coupling of the fully-deprotected monomer ***l*-P$_{C8}$1** with the excess of ***l*-P$_{C8}$1$_{H,THS}$** (Figure 1.10). After statistical half-deprotection of the trimer and coupling of the resulting half-deprotected form hexamer ***l*-P$_{C8}$6$_{THS,THS}$** can be prepared.

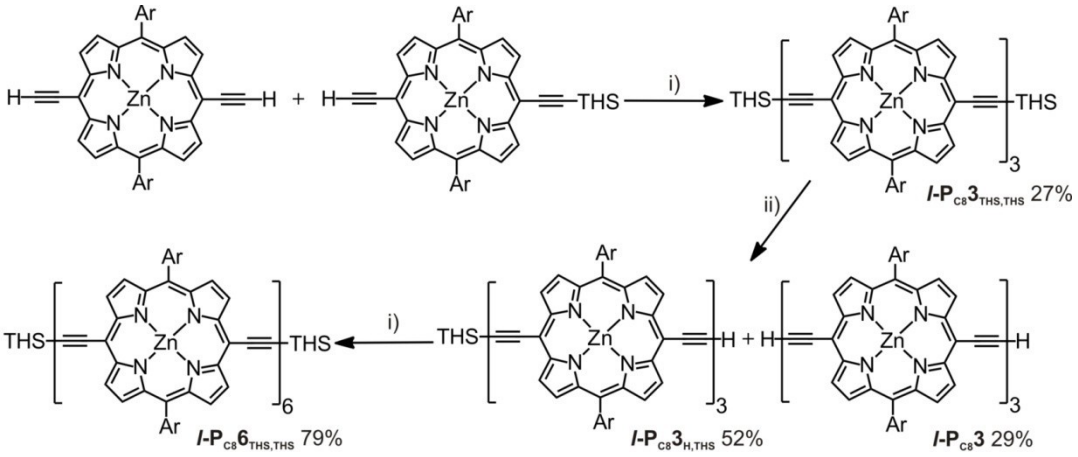

Figure 1.10. Synthetic scheme for preparation of linear porphyrin trimer ***l*-P$_{C8}$3$_{THS,THS}$** and hexamer ***l*-P$_{C8}$6$_{THS,THS}$**. Reagents: i) 1,4-benzoquinone, $Pd(PPh_3)_2Cl_2$, CuI, *i*-Pr_2NH; ii) TBAF. Ar=3,5-bis(octyloxy)phenyl.

Porphyrin pentamer ***l*-P$_{C8}$5$_{THS,THS}$** has been alternatively synthesized by coupling of the fully-deprotected porphyrin trimer ***l*-P$_{C8}$3** with the excess of ***l*-P$_{C8}$1$_{H,THS}$** in yield comparable with that by coupling half-deptrotected tetramer and monomer (Figure 1.11a). Porphyrin hexamer ***l*-P$_{t\text{-Bu}}$6$_{THS,THS}$** can be prepared by coupling of the fully-deprotected porphyrin dimer ***l*-P$_{t\text{-Bu}}$2** with the excess of ***l*-P$_{t\text{-Bu}}$2$_{H,THS}$** (Figure 1.11b). Similarly, coupling of the fully-deprotected porphyrin octamer ***l*-P$_{C8}$8** with the excess of ***l*-P$_{C8}$1$_{H,THS}$** proceeds with formation of porphyrin decamer ***l*-P$_{C8}$10$_{THS,THS}$** as well as small amounts of 18-mer ***l*-P$_{C8}$18$_{THS,THS}$** (as a result of coupling of two molecules of ***l*-P$_{C8}$8** and capping of the ***l*-P$_{C8}$16** with the excess of ***l*-P$_{C8}$1$_{H,THS}$**) all of which can be separated and purified by the recycling GPC system (Figure 1.11c).

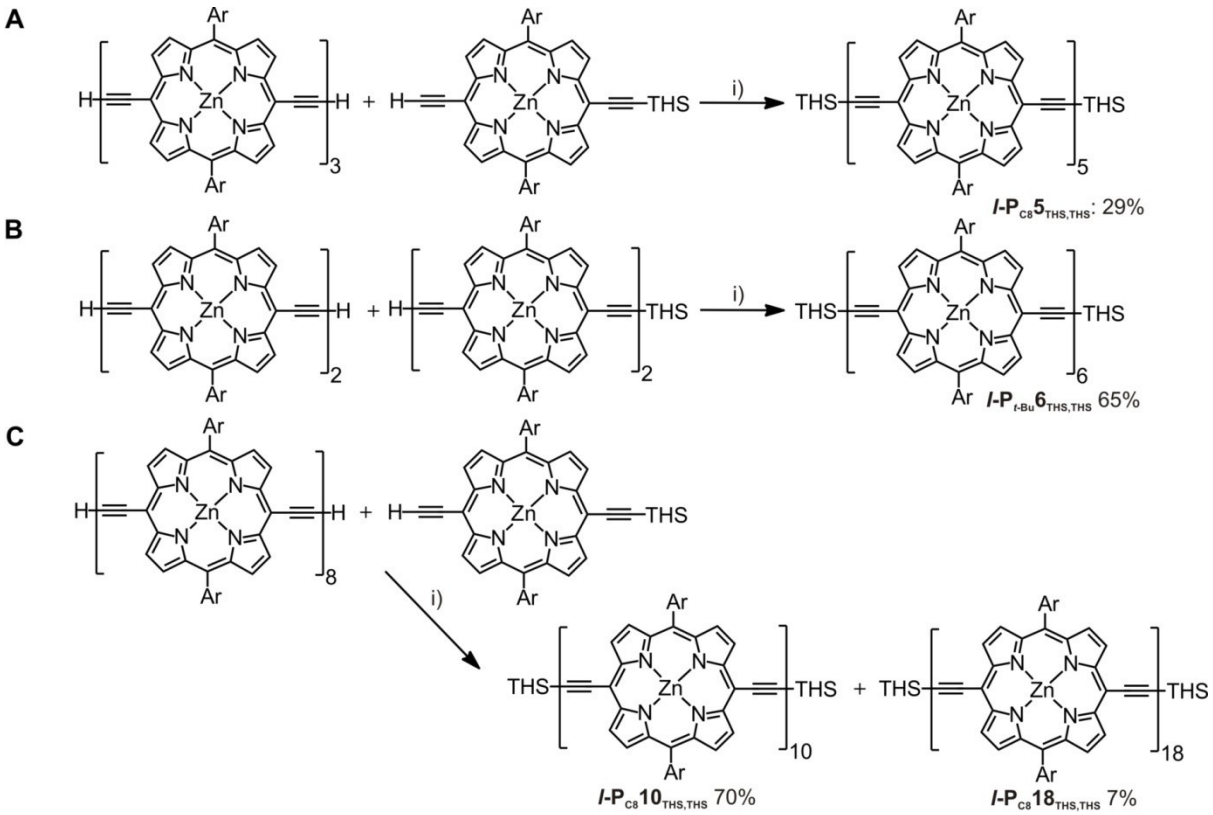

Figure 1.11. Synthetic schemes for preparation of linear porphyrin pentamer (a) ***l*-P$_{C8}$5$_{THS,THS}$**, hexamer (b) ***l*-P$_{t\text{-}Bu}$6$_{THS,THS}$**, decamer (c) ***l*-P$_{C8}$10$_{THS,THS}$** and 18-mer ***l*-P$_{C8}$18$_{THS,THS}$**. Reagents: i) 1,4-benzoquinone, $Pd(PPh_3)_2Cl_2$, CuI, *i*-Pr_2NH; ii) TBAF. Ar=3,5-bis(*tert*-butyl)phenyl and 3,5-bis(octyloxy)phenyl.

1.3 Properties and Synthesis of Cyclic Polymers

1.3.1 Some Properties of Cyclic Polymers Distinct from Linear Analogues

Many of the physical properties of linear polymers, such as crystallinity, glass transition temperature, and flow dynamics, result from the diffusion of the chain ends.[48,49] In cyclic polymers there are no ends and as such they inevitably exhibit different physical properties under bulk and dilute conditions. For example, in a polymer melt or concentrated polymer gel solution, linear polymers tend to diffuse in a snake-like manner (*i.e. via* reptation) as their chain-ends can explore a much greater volume than the interior of the chain (Figure 1.12a).[50,51] In contrast, cyclic polymers cannot reptate like their linear counterparts and tend to move with an amoebae-like motion (Figure 1.12b).[52] Another crucial difference between linear and cyclic polymers is greater intramolecular interactions of the latter. These two distinctive features of cyclic polymers together result in different physical properties as compared to their linear analogues. These include cyclic polymers' higher density,[53] lower intrinsic viscosity,[54] lower translational friction coefficients,[49,53] higher glass transition temperatures,[54] higher critical solution temperature,[55] increased rate of crystallization,[56] higher refractive index[57] *etc*. The statistical model developed by Casassa predicts that in the dilute solution the ratio of the radii of gyration for a cyclic to linear (*i.e.*$\langle R_g^2\rangle_{Cyclic}/\langle R^2_g\rangle_{Linear}$) equals 0.5 in a *theta* solvent (in which polymer

chains act like ideal coils) and 0.526 in a good solvent (in which polymer chains are more expanded as in a *theta* solvent).[58] The latter values have been shown to be in good agreement with experiment.[59] The more compact nature of cyclic polymers compared to their linear counterparts, as follows from their lower hydrodynamic diameter, is widely used to identify the presence of cyclic polymers by size exclusion chromatography (SEC).[60] The SEC elution volume is directly related to the molecular weight of the polymer in question and its intrinsic viscosities.[61] Fukatsu and Kurata[62] have calculated numerically the so-called *g'* factor defined by the ratio of the intrinsic viscosities of the cyclic and linear polymer chains at the same contour length to be 0.645, close to experimentally determined values.[59]

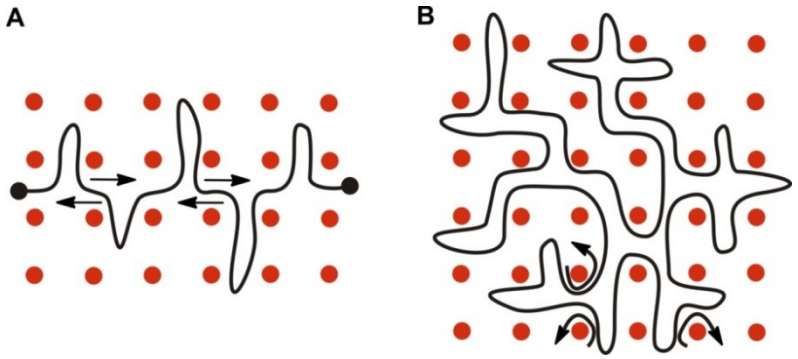

Figure 1.12. Two models of movement dynamics of a linear and cyclic polymer entangled with a mesh of obstacles. The obstacles arise from the presence of other loops. The linear polymer (a) moves in a snake-like manner whereas in the case of the cyclic polymer (b) the movement occurs *via* retraction and reconfiguration of the constituent loops. In both cases polymer is shown as self-avoiding and in two dimensions for the sake of clarity.

As compared to their linear counterparts, cyclic fully conjugated oligomers have an "end-free" π-conjugated system combined with well-defined shape and size. Such structures (in particular in relatively short oligomers) may be accompanied by a high extent of bending of the fully conjugated pathways and lead to intriguing and unexpected optoelectronic properties. In addition, the non-collapsible and electron rich surface of the cyclic fully π-conjugated backbones should affect their flow, redox, aggregation and self-assembly properties which may be useful for creating of various functional 1D, 2D and 3D molecular systems.[63]

Wong studied theoretically at the DFT level of theory the effect of bending on the electronic properties of the π-conjugated cyclic *para*-phenylenes containing 6–18 phenylene units (Figure 1.13).[64] He discovered that the computed optical gaps of the cyclic *para*-phenylenes are always lower than their linear counterparts. This effect is the strongest for the smallest, most strained ring systems such as [5] and [6] cyclic *para*-phenylenes (Figure 1.13a) and was observed experimentally for cyclic *para*-phenylenes[65,66] and cyclic oligothiophenes.[66] However, the first time this counter-intuitive enhancement of conjugation upon bending has been observed experimentally in a 6-porphyrin nanoring by Anderson.[68-70] Based on the data of absorption and emission spectroscopy it has been established that linear and cyclic porphyrin oligomers exhibit the similar trends for the dependence of the HOMO-LUMO gap as predicted and observed for cyclic *para*-phenylenes and cyclic oligothiophenes (Figure 1.13b).

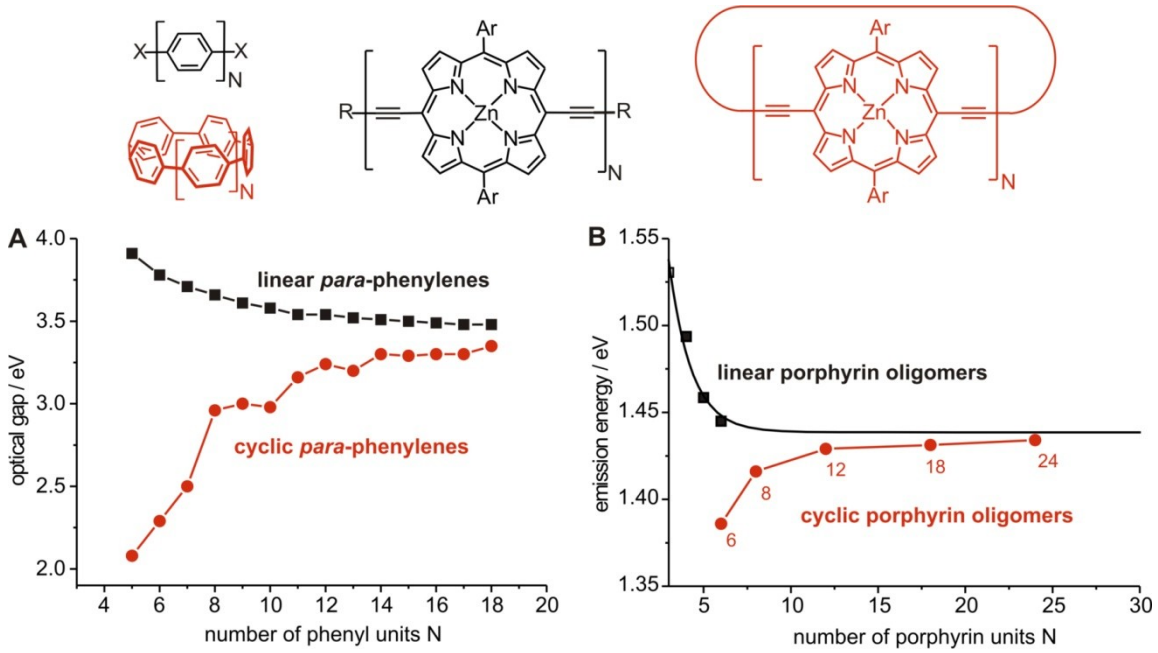

Figure 1.13. Trends in optical gaps in linear (black squares) and cyclic (red circles) (a) paraphenylenes as calculated in ref. 63 and (b) porphyrin oligomers measured in toluene/1% pyridine (cyclic) and dichloromethane/1% pyridine (linear). Emission data from linear oligomers is from ref. 68 and a Meier[71] fit to these data is shown to extrapolate the trend for longer oligomers. Figure reprinted from the D.Phil. thesis of Dr. J. K. Sprafke.[70] The synthesis of 18 and 24 porphyrin nanorings will be presented in Chapter 3.

1.3.2 Synthesis of Cyclic Polymers

It has been shown in the previous section that incorporation of the cyclic motif into polymer architectures can dramatically affect their properties, and even trace amounts of linear polymer materials can jeopardize the validity of the physical measurements on cyclic polymers. For this reason, synthetic techniques that yield high-purity cyclic polymers are of great importance. This section aims at summarizing the most common and successful approaches to the synthesis of cyclic polymers. Two principally different classes of cyclic structures are considered: non-conjugated and conjugated cyclic polymers.

1.3.2.1 Synthesis of Non-Conjugated Cyclic Polymers

According to Grayson's classification, all synthetic strategies for the formation of cyclic polymers can be divided into two main categories: ring-closure techniques (Figure 1.14a-c) and ring-expansion techniques (Figure 1.14d).[72] In the former approach, the reaction involves the coupling of ends of the linear polymer together to yield a cyclic polymer whereas in the case of the ring-expansion approach, cyclic chain growth occurs through the insertion of small cyclic monomer. The ring-closure techniques can be further divided into three major categories: bimolecular homodifunctional, unimolecular homodifunctional, unimolecular heterofunctional approaches represented schematically in Figure 1.14a-c. The critical feature of all ring-closure techniques is that they require high dilution to favour intramolecular cyclization over intermolecular coupling.

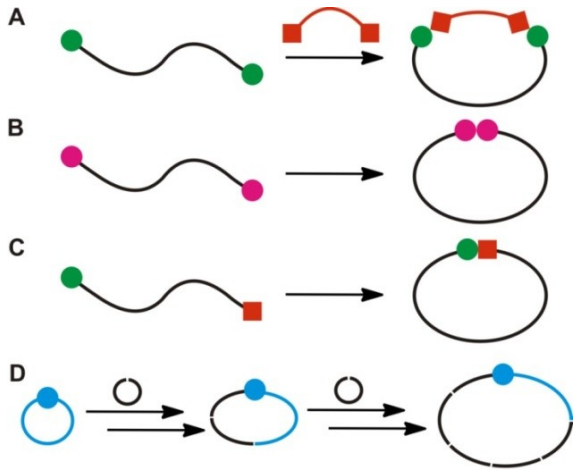

Figure 1.14. Schematic representation of the bimolecular homodifunctional (a), unimolecular homodifunctional (b), unimolecular heterofunctional (c) and ring-expansion (d) approaches for the preparation of cyclic polymers.

When preparing cyclic polymers *via* the bimolecular homodifunctional route (Figure 1.14a), it is common to employ linear polymers produced by living anionic polymerization. This affords linear precursors of well-defined molecular weights and low polydispersities which are then cyclized by treatment with dihalogen-derivatives. This approach has been used for the synthesis of the cyclic polystyrene (Figure 1.15). The authors used sodium naphthalenide **7** to generate *bis*-anionic initiator **8** for polymerizing styrene to the linear precursor **9**. Following cyclization by addition of dichloro or dibromo *para*-xylene **10** yields corresponding cyclic polystyrenes **11**.[73-75] The same approach also works for cyclopolymerization of vinylpyridines, ethyleoxide, dienes *etc*.

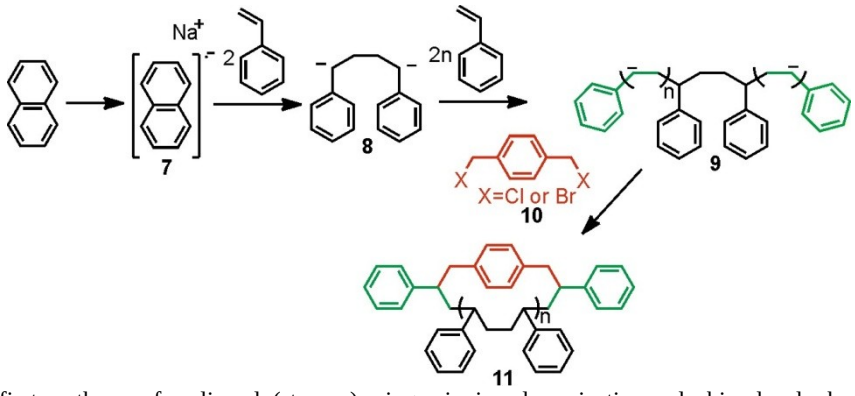

Figure 1.15. The first syntheses of cyclic poly(styrene) using anionic polymerization and a bimolecular homodifunctional coupling with dihalo-*para*-xylene linking agents.[72-75]

Oike *et al.* used an electrostatic interaction with oppositely charged template to promote cyclization.[76] First, using anionic polymerization and subsequent end-group modification, polymers with reactive cationic ends, such as *N*-phenylpyrrolidinium groups, are obtained (Figure 1.16). Using coordination with short dianionic molecules, such as dicarboxylate **12**, it is possible to bring together the ends of the linear polymer in a dimeric pair. Heating of the reaction mixture under high dilution initiated nucleophilic attack of the carboxylate on the pyrrolidinium salts to produce the neutral cyclic diester species **13**. The power of templating effect demonstrated by this work has found wide application for the ring closure approaches and will be discussed further in the section related to the

synthesis of fully conjugated macrocyclic structures.

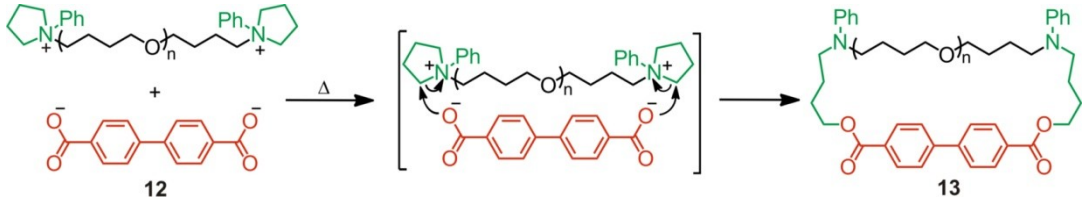

Figure 1.16. Cyclization via ionic pre-assembly followed by a covalent fixation used by Tezuka and co-workers to minimize intermolecular oligomerization during bimolecular coupling.[76]

Under the homodifunctional unimolecular cyclization approach (Figure 1.14b), in contrast to the case above, dilution represses only oligomerization, but not cyclization since reactive groups in this case are connected to each other. Under proper dilution very well defined cyclic species can be obtained. In this type of cyclization, ring closing metathesis has found wide application. An example is shown in Figure 1.17. First acrylate monomers are polymerized *via* atom transfer radical polymerization (ATRP) using a bifunctional ATRP initiator **14**. Subsequently, the halide end groups were converted with allyl tributyl tin **15** to the linear polymer **16** functionalized with allylic end groups. Performing on it the ring-closing metathesis leads to formation of the cyclic polymer **17**.[77] Similar unimolecular cyclization approach has been realized using reversible formation of disulfide bonds,[78] Glaser coupling,[79] radical coupling of bromobenzyl groups[80] *etc*.

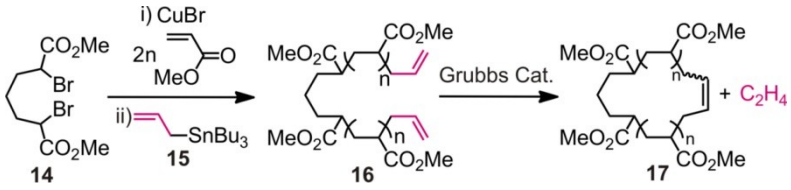

Figure 1.17. The homodifunctional unimolecular cyclization of poly-(methyl acrylate) used by Tezuka and co-workers *via* an olefin metathesis coupling.[77]

Unimolecular heterodifunctional polymers bear different functional groups on the opposite chain ends. Like in the case of unimolecular homodifunctional approach, high dilution suppresses formation of linear oligomers, but not cyclic ones. A typical example of unimolecular difunctional cyclization using acetylene-azide "click" reaction is shown in Figure 1.18. Firstly, a linear polymer precursor **18** is obtained by ATRP using a functionalized initiator. The bromide is then substituted with an azide group to access heterofunctionalized linear polymer **19**, which is subsequently converted into cyclic polymer **20** by initiating a "click" process under high dilution.[81] This unimolecular process has been extended by employing different chemistries, such as amide formation from a carboxylic group and an amino group,[82] Diels-Alder reaction between end-capped maleimide cyclopentadienyl groups[83] *etc*.

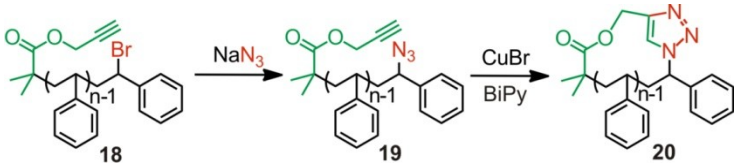

Figure 1.18. Synthesis of cyclic poly(styrene) via atom transfer radical polymerization followed by a "click-coupling by Laurent and Grayson.[81] BiPy=2,2'-bipyridyl.

In the case of ring-expansion polymerizations (Figure 1.14d), there is typically a catalyst or initiator linked by a relatively weak bond (organometallic or electrostatic) with a growing cyclic polymer chain. Propagation by insertion of new monomer units into this weak bond is driven by energy accumulated in the strained cyclic monomer. The formed cyclic polymer will either retain this initiating species, or in some cases, expel the catalyst by "intramolecular chain transfer" reaction. The main advantage of the ring-expansion technique over ring-closure approaches is that high dilution is not required to yield cyclic polymers and the technique can be used on a relatively large scale. Because the cyclic structure is maintained throughout propagation, formation of linear structures is not expected as long as the monomer and initiator are pure from any linear contaminants. However, it is not always easy to remove the initiator from the cyclic structure. Also, fine tuning of the catalyst activity is necessary to achieve low polydispersity of the cyclic polymer obtained.

Ring expansion polymerization has been pioneered by Kricheldorf and Lee using cyclic β-butyrolactone as a strained monomer unit and a cyclic tin oxide initiator 2,2-dibutyl-5,5-dimethyl-1,3-dioxa-2-stannane **21** (Figure 1.19).[84] Here, propagation occurs by the insertion of monomer into the tin-oxygen bond which produces expanded macrocycle **22**. The main disadvantage of this approach is that the labile tin oxide functionality is difficult to substitute for more stable linkers.

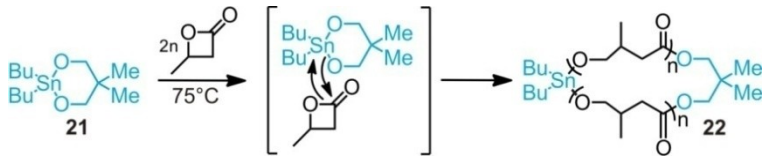

Figure 1.19. First example of the ring-expansion polymerization *via* β-butyrolactone insertion into a cyclic tin initiator by Kricheldorf and co-workers.[84]

A ring expansion approach has also been realized using ring opening metathesis using a Ru catalyst with a cyclic ligand (Figure 1.20).[85] In this case, the cyclic Ru catalyst **23** inserts into the strained monomer **24** and the propagation occurs through repetition of the catalyst insertion process followed by expulsion of the catalyst by intramolecular chain transfer to yield cyclic polymer **25**. This approach produced some of the highest molecular weight cyclic polymers to date (145 kDa), although of high polydispersity (PDI=1.8-2.0).

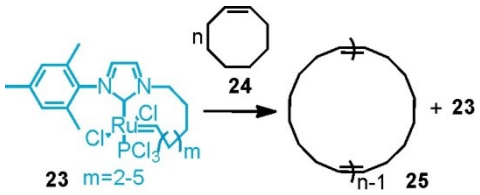

Figure 1.20. Olefin metathesis by Grubbs and co-workers utilizing a cyclic Ru-catalyst to produce macrocyclic *poly*(octene).[85]

1.3.2.2 Synthesis of Fully Conjugated Cyclic Oligomers

Introducing a full conjugation pathway into a cyclic motif further complicates the challenging task of preparing cyclic polymers. The conjugated linear precursors are usually stiffer and thus the enthalpic price for closure is much higher than in the case of flexible chains. The building blocks constituting a

cycle may internally rotate or even sit perpendicular to each other, thus disrupting or limiting π-conjugation, as in cyclic porphyrin arrays prepared by Osuka,[86] Gossauer,[87] Sanders,[88] Lindsey[89] and others. Besides directly fixing the dynamic conjugated moieties in planar configuration by means of installing additional bonds or using a template, it is sometimes beneficial to synthesize smaller cycles in which the internal rotation is more hindered. However, both these synthetic modifications make the synthesis more challenging due to higher strain. This section lists the most successful approaches to the synthesis of large π-conjugated cyclic polymers, also called here *nanorings*, which preserve some extent of conjugation while being cyclic.

Of the four most common approaches to the synthesis of non-conjugated cyclic polymers (Figure 1.14), both unimolecular homodifunctional (Figure 1.14b) and unimolecular heterodifunctional (Figure 1.14c) have been applied to the synthesis of π-conjugated cyclic polymers by a cyclization of a corresponding linear precursor. As with the non-conjugated versions, high dilution is necessary to achieve cyclization and suppress formation of linear side products, although in all of the reported cases, the formation of the linear side products could not be avoided completely. Another crucial factor is to use kinked starting materials that significantly restrict rotational freedom of the ends and thus facilitate cyclization.

Mayor applied a unimolecular homodifunctional approach to synthesize a 12 nm fully conjugated macrocycle **26** by Glaser coupling of the terminal acetylene moieties of the corresponding linear precursor **27** in 38% yield.[90] Very high dilution (8.3×10^{-6} M) was necessary to perform the reaction. The absorption maxima of **26** (461 nm) is very close to the predicted value for the corresponding linear polymer (462 nm).

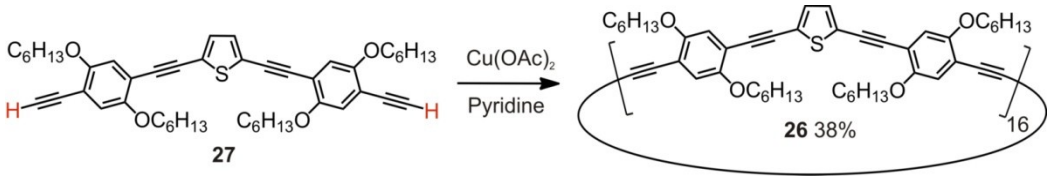

Figure 1.21. Mayor's synthesis of the 11.8 nm macrocycle **26** by Glazer coupling.[90]

Cyclooligomerization of small kinked linear precursors presents a third common approach to the synthesis of fully conjugated cyclic polymers. As before, high dilution is required to achieve cyclization. In this case libraries of rings of various sizes tend to form and side products include linear oligomers. An example of the application of this approach is Iyoda's synthesis of π-conjugated cyclic oligothiophenes **28a-e** (Figure 1.22) using McMurry coupling of a kinked thiophene pentamer dialdehyde **29**.[91] The main product of the cyclization is dimer **28a** (32%), however significant amounts of trimeric **28b** (9%), tetrameric **28c** (6%), pentameric **28d** (4%) and even hexameric **28e** (2%) products are also formed. The latter macrocycle reaches in size 6 nm. Similarly, cyclic oligothiophenes **30a-d** are obtained by coupling thiophene hexamer derivative **31** in 39% (**30a**), 8% (**30b**), 3% (**30c**) and 1% (**30d**) yields.[92] In **28a-e** and **30a-d** the longest wavelength absorption maxima continuously red shift with increasing ring size. This reflects efficient conjugation between individual

thiophene units. The authors also connect electronic coupling between thiophene units with large increases in the two-photon absorption (TPA) cross sections in **30a-d**.[92] Exciton delocalization studies performed on **30a-d** show formation of the 18-thiophene delocalized excited state upon excitation.[93]

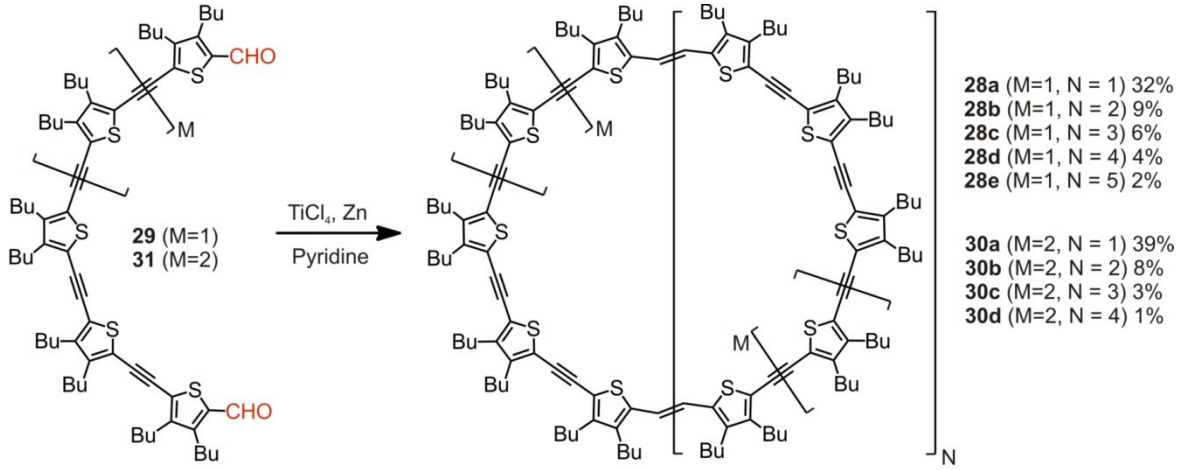

Figure 1.22. Iyoda's synthesis of giant macrocycles **28a-e** and **30a-d** by cyclooligomerization of the linear oligothiophene precursors **29** and **31**.[91,92]

The rectangular position of terminal acetylene groups in the porphyrin "corner" **32** allowed Sugiura and Yamashita to prepare π-conjugated porphyrin square **33** in one step via trimerization of **32**, though in only 9% yield (Figure 1.23).[94] Ultrahigh-vacuum scanning tunnelling microscopy (STM) on a Cu(111) surface was used to study the shape of **33**. The STM imaging confirmed the square shape of the molecule and also that it contained a hole in the centre. The size determined by STM (5 nm) was consistent with that obtained from molecular geometry calculations (5.1 nm).

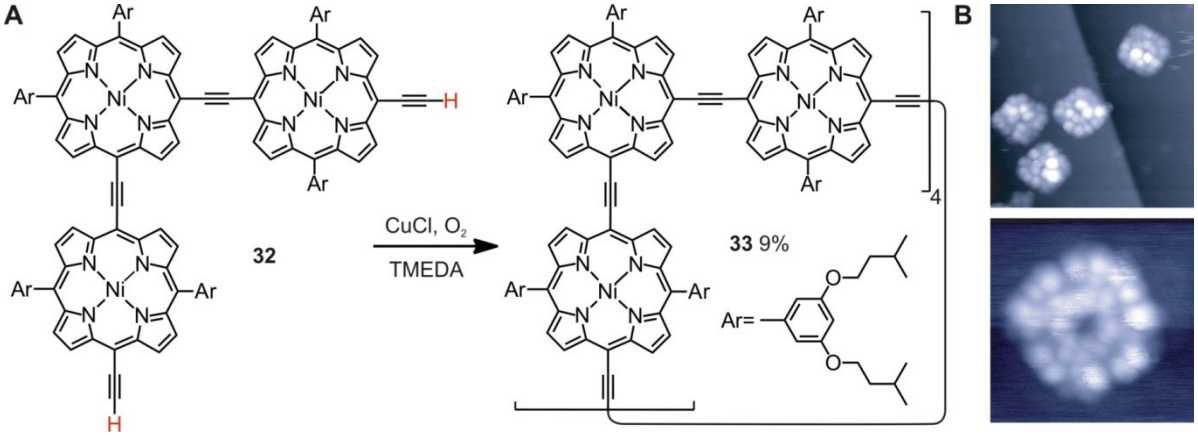

Figure 1.23. (a) Synthesis of the π-conjugated square porphyrin oligomer **33** prepared by Glaser coupling of the porphyrin trimer **32** and (b) its STM images (reprinted from ref. 93).[94]

In three cases of π-conjugated cycles described so far, favourable geometry or possibility of rotation around linkers kept the structures relatively unstrained. Highly strained structures were only obtained by preparing the non-strained cycle first using the approaches described above, followed by introducing strain by means of an additional chemistry. Thus, highly strained cyclic [*n*]p*ara*-phenylenacetylenes ([n]-*c*-PPAs) **34a,b** (*n* = 6 and 8) were prepared both in 85 % yields over two steps from their reduced versions **35b,c** by bromination and treatment with *t*-BuOK

(Figure 1.24a).[95,96] The precursors **35b** (11-16 %) and **35c** (3-5 %) are side products of condensing dialdehyde **36** using McMurry conditions which produces, as a main product, dimer **35a** (30-35%). A similar approach also works for the synthesis of [*n*]-*c*-PPAs with *n* = 7 and 9.[97] A rigid belt-shaped structure of **35a,b** and its radially oriented p-orbitals pointing towards the centre of the ring, allow the formation of inclusion complexes with molecules having a curved π-surface such as fullerenes (Figure 1.24b)[95,98] or even other *c*-PPAs such as in the Russian Matrioshka type inclusion complex of **34a**, [9]-*c*-PPA and C_{60}.[95,99] According to the authors, in the latter complex, inclusion of C_{60} does not affect interaction [6]-*c*-PPA and [9]-*c*-PPA.[99]

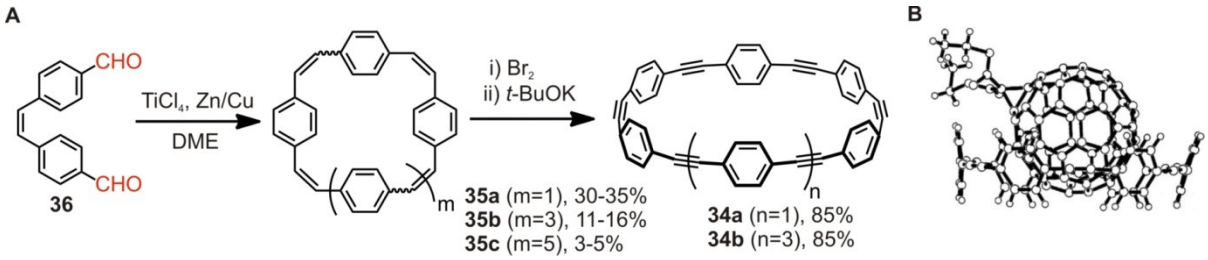

Figure 1.24. (a) Synthesis of the strained cyclic *para*-phenyleneacetylenes **35** and (b) crystal structure of the inclusion comples of **34a** with a fullerene derivative (reprinted from ref. 94).[95,98]

Bäuerle's synthesis of highly symmetrical directly-linked cyclic oligothiophenes **37a-e** (of which **37a** and **37b** are significantly strained) exploited formation of the expanded multinuclear metallocomplexes **38** which then underwent elimination of the metallocentres (Figure 1.25).[67] First, by reacting a kinked pentathiophene derivative **39** with a platinum(II) complex [Pt(cod)Cl_2] a statistical library of complexes **38** of various sizes were obtained in good yields. Subsequent C-C bond formation through reductive elimination of platinum centres afforded **37a-f** in 4% (**37a**), 25% (**37b**), 15% (**37c**), 9% (**37d**), 3% (**37e**) and 2% (**37f**). **37a-f** exhibited red shift in absorption as well as increase of oxidation potential as the ring sizes increase. The emission maxima for **37c–f** are not significantly different whereas the smaller cycles **37a** and **37b** show a much weaker fluorescence band that is shifted to longer wavelengths, as a result of the high ring strain. The determined optical band gaps for **37a-f** (2.26-2.63 eV) are within the range of linear semiconducting oligo- and polythiophenes.

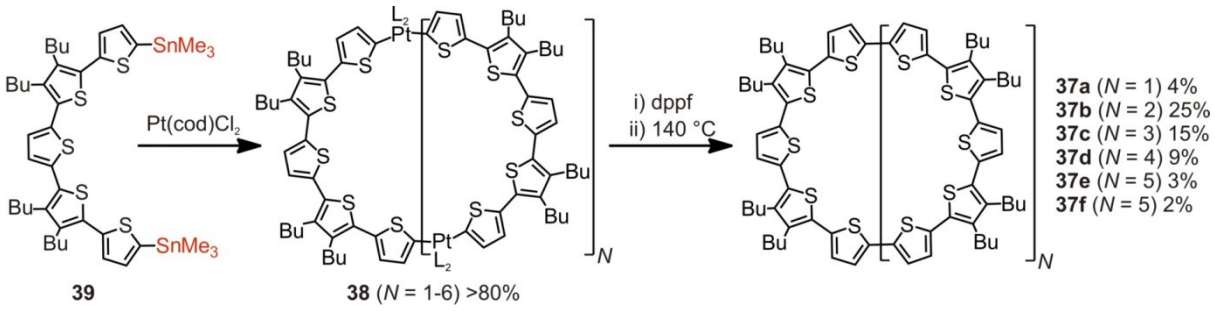

Figure 1.25. Bäuerle's synthesis of directly-linked cyclic oligothiophenes **37**.[67] L_2: cod=1,5-cyclooctadiene; dppf=1,1'-*bis*(diphenylphosphino)ferrocene.

Both of the approaches to the synthesis of strained π-conjugated macrocycles described above

(using a reduced intermediate as in Figure 1.24 or using an expanded platinum(II) complex as in Figure 1.25) were applied to prepare elusive cycloparaphenylenes (*c*-PPs) such as **40a-d** (Figure 1.26). Bertozzi's procedure relied on preparing non-strained macrocyclic precursors **41a-c** by statistical Suzuki coupling of intermediates **42** and **43**.[100] Intermediates **41a-c** contain a 3,6-*syn*-dimethoxycyclohexa-1,4-diene moiety which is a masked aromatic ring. Treatment with lithium naphthalenide leads to aromatization of **41a-c** to give the corresponding *c*-PPs in 43% (**40a**), 10% (**40b**) and 10% (**40c**) yields. Itami used a similar approach to selectively prepare [12]-, [14]-, [15]- and [16]-*c*-PPs using a *cis*-1,4-dihydroxycyclohexane-1,4-diyl unit as a masked *para*-phenylene group.[101,102] In contrast, Yamago used an approach similar to Bäuerle's synthesis of cyclic thiophenes **37a-b**.[103] First, a square platinum complex **44** was obtained in 52% yield from a biphenyl derivative **45**. This was then converted into **40d** in 49% yield by treatment with elemental bromine to initiate a reductive elimination of the platinum centres (Figure 1.26). The size of *c*-PPs strongly influences their fluorescence spectra and smaller *c*-PPs exhibit a larger Stokes shift. In accordance with theoretical prediction,[64] strain enhances π-conjugation in *c*-PPs.[66] Similarly to *c*-PPAs, cavity of *c*-PPs can accommodate guests with curved π-surfaces such as C_{60} which can be selectively complexed by [10]-*c*-PP.[104] Finally, Itami has recently showed that *c*-PPs can be used as templates for size-selective bottom-up growth of carbon nanotubes (CNTs).[1045] However, it is still not possible to precisely control size and chirality of CNTs using *c*-PPs as templates.

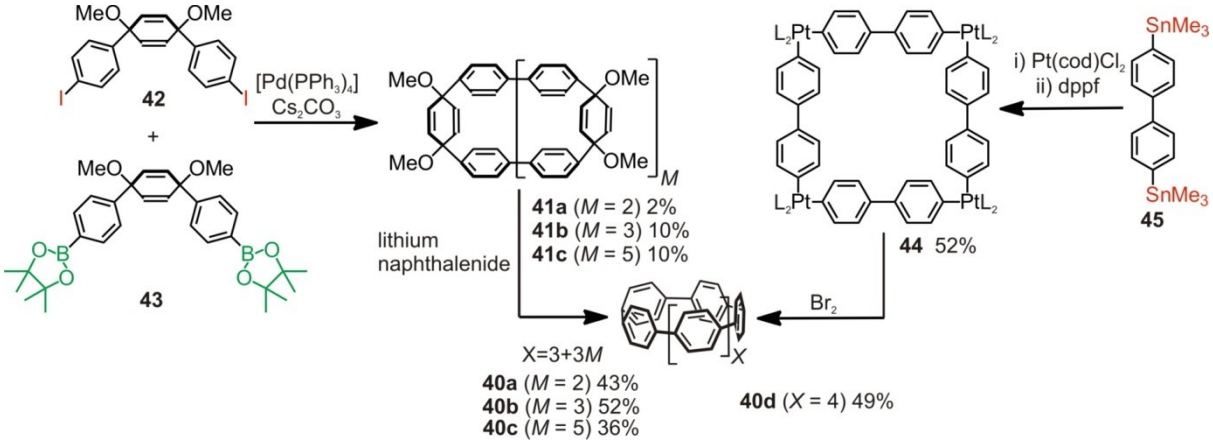

Figure 1.26. Bertozzi's and Itami's synthesis of cyclic *para*-phenylenes using less strained precursors.

Template-directed synthesis has found wide application in the preparation of conjugated unstrained and strained macrocycles. Müllen used the geometry of a fully *meso*-substituted porphyrin to favourably arrange four tricarbazole units for cyclization into a carbazole nanoring **45** (Figure 1.27).[106] The ends of the tricarbazole moieties were coupled into a nanoring using Yamamoto conditions. This was followed by removal of the covalently linked template by hydrolysis. The yield of **45** from **46** over two steps was only 2%, which the authors attributed to the high flexibility of hexyl spacers connecting tricarbazole units to the porphyrin core. The authors managed to image molecules of **46** on a highly oriented pyrolytic graphite (HOPG) surface by STM, which confirmed the perfect round shape of **46** consistent with the presence of a conjugated π-system.

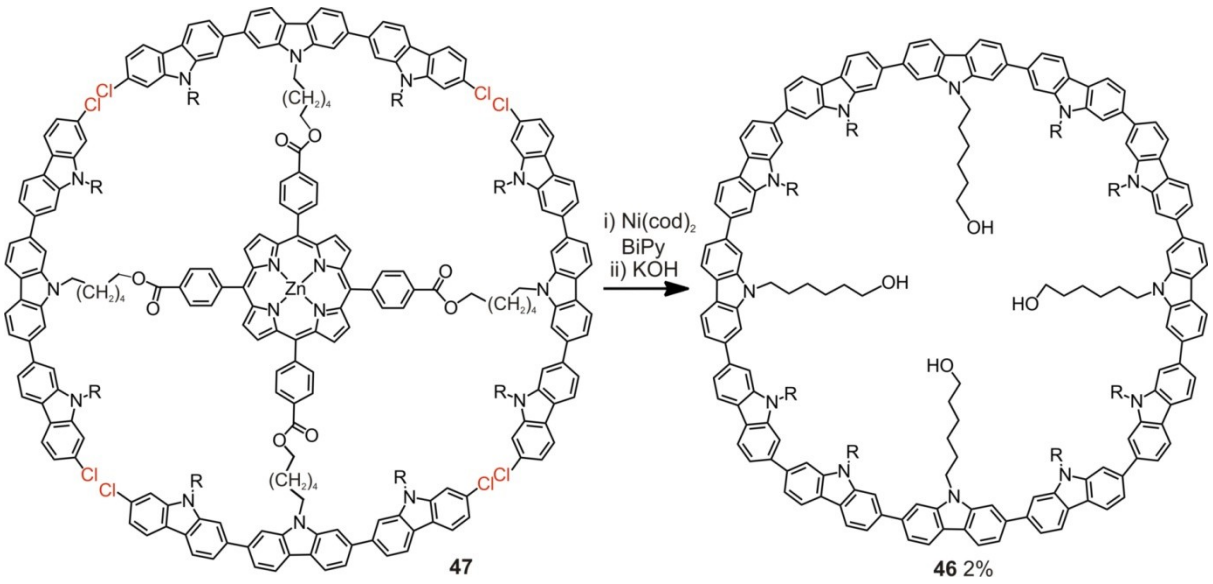

Figure 1.27. Template-directed synthesis of Müllen's oligocarbazole macrocycle.[106]

Anderson has used non-covalent binding of templates to direct formation of fully conjugated cyclic porphyrin oligomers comprised of 6, 8 or 12 porphyrin moieties. This approach uses the interaction of Zn-porphyrin subunits with pyridine residues to arrange linear porphyrin building blocks around a circular template before their terminal acetylene ends are Glaser coupled to yield a nanoring-template complex. Treatment of the latter with a competing ligand, such as pyridine or DABCO, leads to formation of the corresponding free porphyrin nanorings. Thus, Hoffmann, Wilson, O'Sullivan and Anderson prepared cyclic porphyrin octamers ***c*-P$_{t\text{-Bu}}$8** and ***c*-P$_{C8}$8** by coupling linear porphyrin dimer ***l*-P$_{t\text{-Bu}}$2** (***c*-P$_{t\text{-Bu}}$8**), tetramer ***l*-P$_{t\text{-Bu}}$4** (***c*-P$_{t\text{-Bu}}$8**) or octamer ***l*-P$_{C8}$8** (***c*-P$_{C8}$8**) in the presence of a complementary octadentate template **T8** in 25%, 22% and 14% yields respectively, followed by efficient removal of **T8** by treatment with pyridine (Figure 1.28).[42,107] A similar approach, but using a hexadentate template **T6**, was applied to the synthesis of the cyclic porphyrin hexamers ***c*-P$_{t\text{-Bu}}$6** and ***c*-P$_{C8}$6** from linear porphyrin dimers ***l*-P$_{t\text{-Bu}}$2** (***c*-P$_{t\text{-Bu}}$6**) and ***l*-P$_{C8}$2** (***c*-P$_{C8}$6**) by Hoffmann and Anderson (Figure 1.29a).[68] Further optimization of the coupling conditions allowed Sprafke and Anderson to increase the yields of ***c*-P$_{t\text{-Bu}}$6** and ***c*-P$_{C8}$6** made from dimers, afforded their synthesis directly from corresponding porphyrin monomers in moderate yields, and also led to isolation of the [12]-porphyrin nanorings ***c*-P$_{C8}$12** and ***c*-P$_{t\text{-Bu}}$12** as side products in the cyclooligomerization of both linear porphyrin dimers and monomers.[69,70]

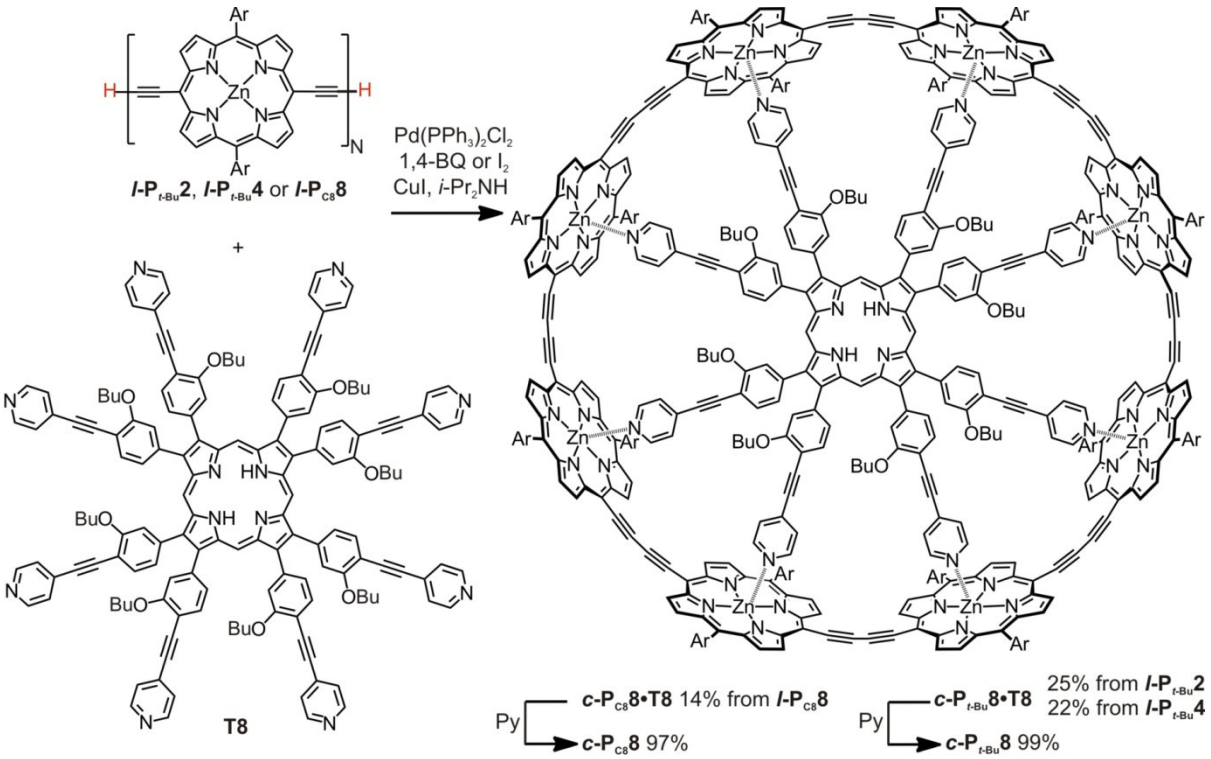

Figure 1.28. Template-directed synthesis of cyclic porphyrin octamers ***c*-P$_{t\text{-Bu}}$8** and ***c*-P$_{C8}$8** from various linear porphyrin precursors. Ar=3,5-bis(*tert*-butyl)phenyl (***c*-P$_{t\text{-Bu}}$8**) and 3,5-bis(octyloxy)phenyl (***c*-P$_{C8}$8**). 1,4-BQ=1,4-benzoquinone.

Selective synthesis of ***c*-P$_{C8}$12** and ***c*-P$_{t\text{-Bu}}$12** was achieved by Sprafke, O'Sullivan, Kondratuk[†] and Anderson via the novel concept of Vernier templating.[70,107,108] It uses formation of Vernier complexes with more binding sites than in either a template (n_T) or a ligand (n_L) when these numbers are not multiple of each other. The number of the binding sites in the Vernier complex is the lowest common multiple of n_T and n_L. Thus, Vernier complexes, containing 12 porphyrin units, form when mixing a linear porphyrin tetramer and a hexa-dentate template **T6** (Figure 1.29b). Following cyclization using Glaser coupling and removal of template molecules with pyridine yield cyclic porphyrin dodecamers ***c*-P$_{C8}$12** and ***c*-P$_{t\text{-Bu}}$12** in 37% and 30% yields respectively (over two steps from corresponding tetramers). Molecules of ***c*-P$_{C8}$12** were imaged on an Au (111) surface using STM, which directly confirmed the presence of 12 porphyrin subunits (Figure 1.30a).

Steady-state absorption and emission spectra, as well as theoretical studies at the DFT level of theory, indicate a decrease of the HOMO-LUMO gap and enhancement of conjugation in ***c*-P$_{t\text{-Bu}}$6•T6** as compared to linear porphyrin hexamer and even linear porphyrin polymer in the result of the bending of the π-surface.[68-70] Ultrafast fluorescence measurements on the ***c*-P$_{t\text{-Bu}}$6•T6** showed that the excited state is delocalized around the whole ring.[69]

[†]Scaled-up synthesis of starting materials and ***c*-P$_{t\text{-Bu}}$12** was performed by me.

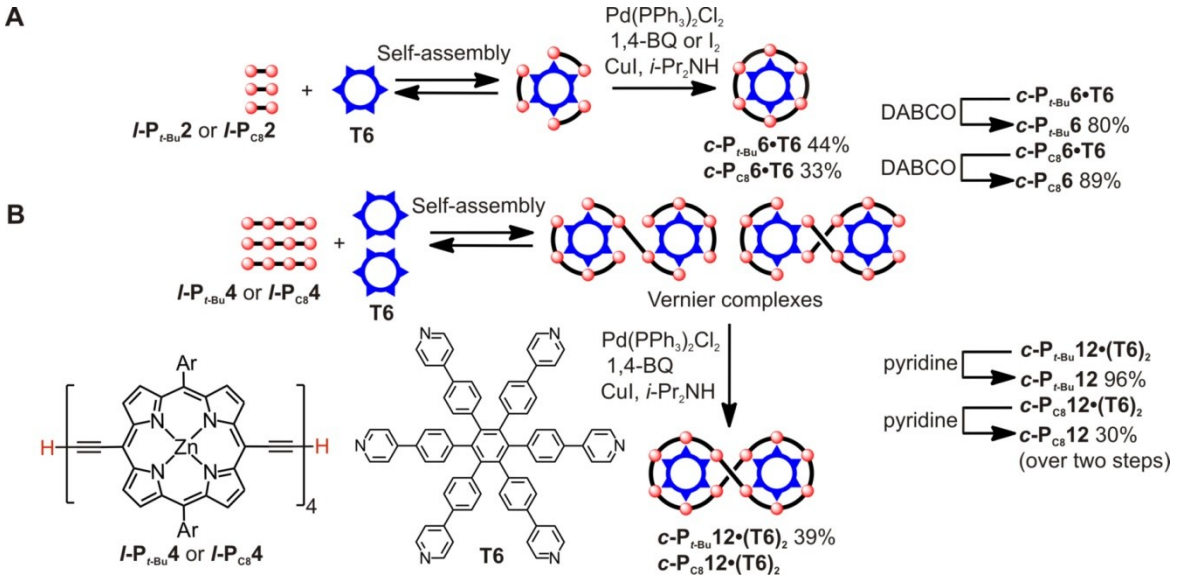

Figure 1.29. (a) Template-directed synthesis of cyclic hexamers ***c*-P$_{t\text{-Bu}}$6** and ***c*-P$_{C8}$6** from dimers ***l*-P$_{C8}$4** and ***l*-P$_{t\text{-Bu}}$4**. (b) Vernier templating for the synthesis of cyclic porphyrin dodecamers ***c*-P$_{t\text{-Bu}}$12** and ***c*-P$_{C8}$12** from linear porphyrin tetramers ***l*-P$_{C8}$4** and ***l*-P$_{t\text{-Bu}}$4**. Ar = 3,5-bis(*tert*-butyl)phenyl and 3,5-bis(octyloxy)phenyl.

As evidenced by data of absorption spectroscopy, removal of a template from template complexes or increasing the ring size led to higher flexibility of the rings and hence disrupted conjugation between porphyrin units. Sprafke and Anderson showed that in the presence of DABCO, the semi-flexible nanoring ***c*-P$_{C8}$12** planarizes to form a much more rigid sandwich complex in an all-or-nothing process (Figure 1.30b).[70,109] Planarization of the nanoring in the sandwich complex led to enhanced conjugation between porphyrin units as evidenced by significant sharpening and red-shift of the Q band.

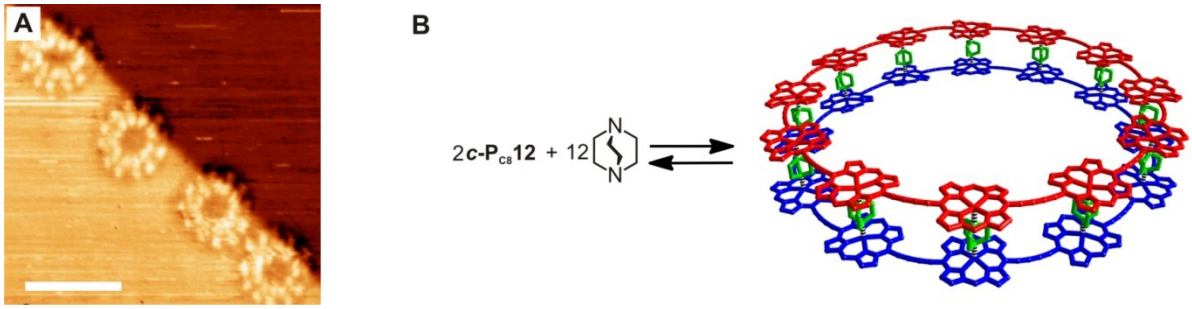

Figure 1.30. (a) STM image of ***c*-P$_{C8}$12** on an Au (111) surface. Scale bar, 5 nm. (b) Formation of a double strand sandwich complex between ***c*-P$_{C8}$12** and DABCO. Aryl side groups and hydrogen atoms are omitted for clarity. STM images and sandwich complex cartoon are reprinted from ref. 70.

1.4 Project Aims

Esthetic beauty and unique fully π-conjugated system of porphyrin nanorings make them non-trivial and intriguing compounds to prepare and study. Equaly important is their similarity with naturally occurring light harvesting systems.

The work presented herein investigates the application of different synthetic approaches developed by the Anderson group to the synthesis of porphyrin nanorings beyond 12-porphyrin

nanoring. A particular emphasis was put on understanding the mechanism and scope of Vernier templating.

In addition, this project aimed at improving our understanding of unusual supramolecular, optoelectronic and structural properties of known and novel porphyrin nanorings. A key question is the similarity between their electronic properties (in particular, in terms of ultrafast energy delocalization) and those of the naturally occurring light-harvesting systems.

1.5 References

[1] E. Vogel, *Pure & Appl. Chem.*, **1993**, *65*, 143–152.
[2] J. Braun, C. Hasenfratz, R. Schwesinger, H.-H. Limbach, *Angew. Chem., Int. Ed.,* **1994**, *33*, 2215–2217.
[3] T. Pullerits, V. Sundström, *Acc. Chem. Res.* **1996**, *29*, 3811–389.
[4] G. McDermott, S. M. Prince, A. A. Freer, A. M. Hawthornthwaite-Lawless, M. Z. Papiz, R. J. Cogdell, N. W. Isaacs, *Nature* **1995,** *374*, 517–521.
[5] M. Z. Papiz, S. M. Prince, T. Howard, R. J. Cogdell, N. W. Isaacs, *J. Mol. Biol.* **2003,** *326*, 1523–1538.
[6] M. Sener, J. Strumpfer, J. Hsin, D. Chandler, S. Scheuring, C. N. Hunter, K. Schulten, *ChemPhysChem*, **2011**, *12*, 518–531.
[7] J. L. Herek, W. Wohlleben, R. J. Cogdell, D. Zeidler, M. Motzkus, *Nature* **2002**, *417*, 533–535.
[8] R. Jimenez, S. N. Dikshit, S. E. Bradforth, G. R. Fleming, *J. Phys. Chem.* **1996**, *100*, 6825-6834.
[9] M. Dahlbom, T. Pullerits, S. Mukamel, V. J. Sandstrom, *Phys. Chem. B* **2001**, *105*, 5515–5524.
[10] J. T. M. Kennis, A. M. Streltsov, S. I. E. Vulto, T. J. Aartsma, T. Nozawa, J. J. Amesz, *J. Phys. Chem. B* **1997**, *101*, 7827–7834.
[11] A. A. Bakulin, A. Rao, V. G. Pavelyev, P. H. M. van Loosdrecht, M. S. Pshenichnikov, D. Niedzialek, J. Cornil, D. Beljonne, R. H. Friend, *Science* **2012**, *335*, 1340–1344.
[12] Y. Kim, S. Cook, S. M. Tuladhar, S. A. Choulis, J. Nelson, J. R. Durrant, D. C. Bradley, M. Giles, I. McCulloch, C. S. Ha, M. Ree, *Nat. Mater.* **2006**, *5*, 197–203.
[13] S. H. Park, A. Roy, S. Beaupre, S. Cho, N. Coates, J. S. Moon, D. Moses, M. Leclerc, K. Lee, A. J. Heeger, *Nat. Photonics* **2009**, *3*, 297–303.
[14] S. Scheuring, J. N. Sturgis, *Science* **2005**, *309*, 484–487.
[15] J. Strumpfer, M. Sener, K. Schulten, *J. Phys. Chem. Lett.* **2012**, *3*, 536–542.
[16] L. R. Milgrom, *The Colours of Life: An Introduction to the Chemistry of Porphyrins and Related Compounds*, OUP, Oxford, **1997**.
[17] H. L. Anderson, *Chem. Comm.* **1999**, 2323–2330.
[18] M. Kasha, H. R. Rawls, M. Ashraf El–Bayoumi, *Pure Appl. Chem.* **1965**, *11*, 371–392.
[19] H. L. Anderson, *Adv. Mater.* **1994**, *6*, 834–836.
[20] Y. H. Kim, D. H. Jeong, D. Kim, S. C. Jeoung, H. S. Cho, S. K. Kim, N. Aratani, A. Osuka, *J. Am. Chem. Soc.* **2001**, *123*, 76–86.
[21] A. Osuka, H. Shimidzu, *Angew. Chem., Int. Ed.*, **1997**, *36*, 135–137.
[22] N. Aratani, A. Takagi, Y. Yanagawa, T. Matsumoto, T. Kawai, Z. S. Yoon, D. Kim, A. Osuka *Chem. Eur. J.* **2005**, *11*, 3389–3404.
[23] J. Seth, V. Palaniappan, T. E. Johnson, S. Prathapan, J. S. Lindsey, D. F. Bocian, *J. Am. Chem. Soc.*, **1994**, *116*, 10578–10592.
[24] R. W. Wagner, T. E. Johnson, J. S. Lindsey, *J. Am. Chem. Soc.*, **1996**, *118*, 11166–11180.
[25] M.J. Frampton, H. Akdas, A.R. Cowley, J.E. Rogers, J.E. Slagle, P.A. Fleitz, M. Drobizhev, A. Rebane, H.L. Anderson, *Org. Lett.* **2005**, *7*, 5365–5368.
[26] V. S. Lin, S. G. DiMagno, M. J. Therien, *Science* **1994,** *264*, 1105–1111.
[27] H. L. Anderson, *Inorg. Chem.* **1994**, *33*, 972–981.
[28] A. Tsuda, A. Osuka, *Science* **2001,** *293*, 79–82.

[29] A. Tsuda, H. Furuta, A. Osuka, *J. Am. Chem. Soc.* **2001,** *123*, 10304–10321.
[30] M. J. Crossley, P. L. Burn, *J. Chem. Sos., Chem. Comm.* **1987**, 39-40.
[31] P. N. Taylor, A. P. Wylie, J. Huuskonen, H. L. Anderson, *Angew. Chem., Int. Ed.* **1998,** *37*, 986–989.
[32] K. Susumu, T. V. Duncan, M. J. Therien, *J. Am. Chem. Soc.* **2005,** *127*, 5186–5195.
[33] K. J. Thorley, J. M. Hales, H. L. Anderson, J. W. Perry, *Angew. Chem., Int. Ed.* **2008**, *47*, 7095–7098.
[34] S. Ohira, J. M. Hales, K. J. Thorley, H. L. Anderson, J. W. Perry, J.-L. Brédas, *J. Am. Chem. Soc.* **2009**, *131*, 6099–6101.
[35] K. Susumu, M. J. Therein, *J. Am. Chem. Soc.* **2002**, *124*, 8550–8552.
[36] P. N. Taylor**,** J. Huuskonen**,** R. T. Aplin**,** H. L. Anderson**,** J. Huuskonen**,** G. Rumbles**,** E. Williams**,** *Chem. Comm.* **1998**, 909-910.
[37] V. S.-Y. Lin, M. J. Therien, *Chem. Eur. J.*, **1995**, ***1***, 645–651.
[38] M. U. Winters, J. Kornbratt, M. Eng, C. J. Wilson, H. L. Anderson, B. Albinsson, *J. Phys. Chem. C* **2007**, *111*, 7192-7199.
[39] D. P. Arnold, A. W. Johnson, M. Mahendran, *J. Chem. Soc., Perkin Trans. 1* **1978**, 366–370.
[40] T. E. O. Screen, K. B. Lawton, G. S. Wilson, N. Dolney, R. Ispasoiu, T. Goodson III, S. J. Martin, D. D. C. Bradley, H. L. Anderson, *J. Mater. Chem.* **2001**, *11*, 312–320.
[41] T. E. O. Screen, J. R. G. Thorne, R. G. Denning, D. G. Bucknall, H. L. Anderson, *J. Am. Chem. Soc.* **2002**, *124*, 9712–9713.
[42] M. Hoffmann, C. J. Wilson, B. Odell, H. L. Anderson, *Angew. Chem. Int. Ed.* **2007**, *46*, 3122–3125.
[43] M. Kawao, H. Ozawa, H. Tanaka, T. Ogawa, *Thin Solid Films*, **2006**, *499*, 23–28.
[44] B. J. Littler, M. A. Miller, C.-H. Hung, R. W. Wagner, D. F. O'Shea, P. D. Boyle, J. S. Lindsey, *J. Org. Chem.* **1999**, *64*, 1391–1396.
[45] C. J. Wilson, *Large Porphyrin Based π-Systems*, DPhil Thesis, University of Oxford, Oxford, **2006**.
[46] M. S. Newman, L. F. Lee, *J. Org. Chem.* **1972**, *37*, 4468–4469.
[47] J. S. Lindsey, *Acc. Chem. Res.* **2010**, *43*, 300–311.
[48] T. McLeish, *Science* **2002**, *297*, 2005–2006.
[49] Z. Jia, M. J. Monteiro, *J. Pol. Science A: Pol. Chem.* **2012**, *50*, 2085–2097.
[50] P.-G. De Gennes, *J. Chem. Phys.* **1971**, *55*, 572–579.
[51] M. Doi, S. F. Edwards, *J. Chem. Soc. Faraday Trans. 2* **1978**, *74*, 1789–1801.
[52] S. P. Obhukov, M. Rubinstein, T. Duke, *Phys. Rev. Lett.* **1994**, *73*, 1263–1266.
[53] D. J. Orrah, J. A. Semlyen, S. B. Ross-Murphy, *Polymer* **1988**, *29*, 1455–1458.
[54] S. J. Clarson, J. A. Semlyen, *Polymer* **1986**, *27*, 1633–1636.
[55] X.-P. Qiu, F. Tanaka, F. M. Winnik, *Macromolecules* **2007**, *40*, 7069–7071.
[56] E. J. Shin, W. Jeong, H. A. Brown, B. J. Koo, J. L. Hedrick, R. M. Waymouth, *Macromolecules* **2011**, *44*, 2773–2779.
[57] D. J. Bannister, J. A. Semlyen *Polymer* **1981**, *22*, 377–381.
[58] E. F. Casassa, *J. Pol. Sci. A* **1965**, *3*, 605–614.
[59] J. Roovers, *J. Pol. Sci. Pol. Phys.* **1985**, *23*, 1117–1126.
[60] D. E. Lonsdale, C. A. Bell, M. J. Monteiro, *Macromolecules*, **2010**, *43*, 3331–3339.
[61] J. M. G. Cowie, V. Arrighi, *Polymers: Chemistry & Physics of Modern Materials*, 3rd edition, CRC Press, **2007**.
[62] M. Fukatsu, M. Kurata, *J. Chem. Phys.* **1966**, *44*, 4539–4545.
[63] M. Iyoda, J. Yamakawa, M. J. Rahman, *Angew. Chem., Int. Ed.*, **2011**, *50*, 10522–10553.
[64] B. M. Wong, *J. Phys. Chem. C* **2009**, *113*, 21921–21927.
[65] Y. Segawa, A. Fukazawa, S. Matsuura, H. Omachi, S. Yamaguchi, S. Irle, K. Itami, *Org. Biomol. Chem.* **2012**, *10*, 5979–5984.
[66] T. Iwamoto, Y. Watanabe, Y. Sakamoto, T. Suzuki, S. Yamago, *J. Am. Chem. Soc.* **2011**, *133*, 8354–8361.
[67] F. Zhang, Gunther Gotz, H. D. F. Winkler, C. A. Schalley, P. Bäuerle, *Angew. Chem., Int. Ed.* **2009**, 48, 6632–6635.
[68] M. Hoffmann, J. Kärnbratt, M.-H. Chang, L. M. Herz, B. Albinsson, H. L. Anderson,

Angew. Chem., Int. Ed. **2008**, *47*, 4993–4996.
[69] J. K. Sprafke, D. V. Kondratuk, M. Wykes, A. L. Thompson, M. Hoffmann, R. Drevinskas, W.-H. Chen, C. K. Yong, J. Kärnbratt, J. E. Bullock, M. Malfois, M. R. Wasielewski, B. Albinsson, L. M. Herz, D. Zigmantas, D. Beljonne, H. L. Anderson, *J. Am. Chem. Soc.* **2011**, *133*, 17262–17273.
[70] J. K. Sprafke, *Supramolecular Control of Synthesis and Electronic Structure of Porphyrin Oligomers*, D.Phil. thesis, University of Oxford, Oxford, 2011.
[71] H. Meier, U. Stalmach, H. Kolshorn, *Acta Polymer.* **1997**, *40*, 379–384.
[72] B. A. Laurent, S. M. Grayson, *Chem. Soc. Rev.* **2009**, *38*, 2202–2213.
[73] D. Geiser and H. Hocker, *Macromolecules* **1980**, *13*, 653–657.
[74] G. Hild, A. Kohler and P. Rempp, *Eur. Polym. J.* **1980**, *16*, 525–527.
[75] B. Vollmert, J. Huang, *Makromol. Chem., Rapid Commun.* **1980**, *1*, 333–339.
[76] H. Oike, H. Imaizumi, T. Mouri, Y. Yoshioka, A. Uchibori, Y. Tezuka, *J. Am. Chem. Soc.* **2000**, *122*, 9592-9599.
[77] S. Hiyashi, K. Adachi, Y. Tezuka, *Chem. Lett.*, **2007**, *36*, 982-983.
[78] M. R. Whittaker, Y. Goh, H. Gemici, T. M. Legge, S. Perrier, M. J. Monteiro, *Macromolecules* **2006**, *39*, 9028-9034.
[79] Y. Zhang, G. Wang, J. Huang, *Macromolecules* **2010**, *43*, 10343–10347.
[80] A. F. Voter, E. S. Tillman, *Macromolecules* **2010**, *43*, 10304–10310.
[81] B. A. Laurent, S. M. Grayson, *J. Am. Chem. Soc.* **2006**, *128*, 4238–4239.
[82] M. Kubo, T. Hayashi, H. Kobayashi, T. Itoh, *Macromolecules* **1998**, *31*, 1053–1057
[83] M. Glassner, J. P. Blinco, C. Barner–Kowollik, *Macromol. Rapid Commun.* **2011**, *32*, 724–728.
[84] H. R. Kricheldorf, S. Lee, *Macromolecules* **1995**, *28*, 6718-6725.
[85] C. W. Bielawski, D. Benitez, R. H. Grubbs, *Science* **2002**, *297*, 2041-2044.
[86] T. Hori, N. Aratani, A. Takagi, T. Matsumoto, T. Kawai, M.-C. Yoon, Z. S. Yoon, S. Cho,D. Kim, A. Osuka, *Chem. Eur. J.* **2006,** *12*, 1319-1327.
[87] S. Rucareanu, A. Schuwey, A. Gossauer *J. Am. Chem. Soc.* **2006,** *128*, 3396-3413.
[88] H. L. Anderson, J. K. M. Sanders, *J. Chem. Soc., Chem. Commun.* **1989**, *22*, 1714-1715.
[89] J. Li, A. Ambroise, S. I. Yang, J. R. Diers, J. Seth, C. R. Wack, D. F. Bocian, D. Holten, J. S. Lindsey, *J. Am. Chem. Soc.* **1999,** *121*, 8927-8940.
[90] M. Mayor, C. Didschies, *Angew. Chem., Int. Ed.* **2003**, *42*, 3176–3179.
[91] K. Nakao, M. Nishimura, T. Tamachi, Y. Kuwatami, H. Miyasaka, T. Nishinaga, M. Iyoda, *J. Am. Chem. Soc.* **2006**, *128*, 16740–16747.
[92] M. Williams-Harry, A. Bhaskar, G. Ramakrishna, T. Goodson III, M. Imamura, A. Mawatari, K. Nakao, H. Enozawa, T. Nishinaga, M. Iyoda, *J. Am. Chem. Soc.* **2008**, *130*, 3252–3253.
[93] J. E. Donehue, O. P. Varnavski, R. Cemborski, M. Iyoda, T. Goodson III, *J. Am. Chem. Soc* **2011**, *133*, 4819–4828.
[94] A. Kato, K.-I. Sugiura, H. Miyasaka, H. Tanaka, T. Kawai, M. Sugimoto, M. Yamashita, *Chem. Lett.* **2004**, *33*, 578-579.
[95] T. Kawase, Synlett **2007**, 2609-2626.
[96] T. Kawase, H. R. Darabi, M. Oda, *Angew. Chem., Int. Ed.* **1996**, *35*, 2664–2666.
[97] T. Kawase, N. Ueda, K. Tanaka, Y. Seirai, M. Oda, *Tetr Lett.* **2001**, 42, 5509–5511.
[98] T. Kawase, K. Tanaka, N. Fujiwara, H. R. Darabi, M. Oda, *Angew. Chem., Int. Ed.* **2003**, *42*, 1624–1628.
[99] T. Kawase, K. Tanaka, N. Shiono, Y. Seirai, M. Oda, *Angew. Chem., Int. Ed.* **2004**, *43*, 1722-1724.
[100] R. Jasti, J. Bhattacharjee, J. B. Neaton, C. R. Bertozzi, *J. Am. Chem. Soc.* **2008**, *130*, 17646–17647.
[101] H. Takaba, H. Omachi, Y. Yamamoto, J. Bouffard, K. Itami, *Angew. Chem. Int. Ed.* **2009**, *48*, 6112–6116.
[102] H. Omachi, S. Matsuura, Y. Segawa, K. Itami, *Angew. Chem. Int. Ed.* **2010**, *49*, 10202–10205.
[103] S. Yamago, Y. Watanabe, T. Iwamoto, *Angew. Chem. Int. Ed.* **2010**, *49*, 757–759.
[104] T. Iwamoto, Y. Watanabe, T. Sadahiro, T. Haino, S. Yamago, *Angew. Chem.* **2011**, *123*, 8492-8494.
[105] H. Omachi, T. Nakayama, E. Takahashi, Y. Segawa, K. Itami, *Nat. Chem.* **2013**, DOI: 10.1038/

NCHEM.1655.
[106] S.-H. Jung, W. Pisula, A. Rouhanipour, H. J. Räder, J. Jacob, K. Müllen, *Angew. Chem. Int. Ed.* **2006**, *45*, 4685–4690.
[107] M. C. O'Sullivan, *Template Directed Synthesis of Porphyrin Nanorings*, DPhil Thesis, University of Oxford, Oxford, **2011**.
[108] M. C. O'Sullivan, J. K. Sprafke, D. V. Kondratuk, C. Rinfray, T. D. W. Claridge, A. Saywell, M. O. Blunt, J.. N. O'Shea, P. H. Beton, M. Malfois, H. L. Anderson *Nature* **2011**, *469*, 72–75.
[109] J. K. Sprafke, B. Odell, T. D. W. Claridge, H. L. Anderson *Angew. Chem. Int. Ed.* **2011**, *50*, 5572–5575.

Chapter 2

Synthesis of 6- and 12-Porphyrin Nanorings: a Detailed Study

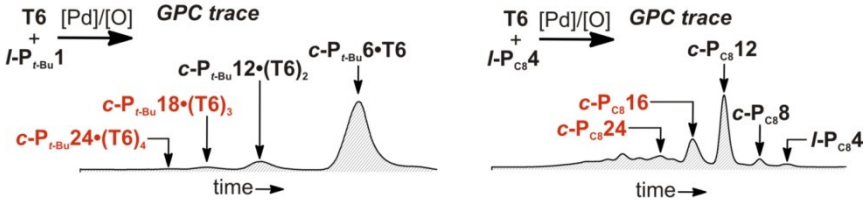

This chapter presents further advances in classical synthesis of 6-porphyrin nanoring from porphyrin monomer and Vernier-templated synthesis of 12-porphyrin nanorings from linear porphyrin tetramer. Careful investigation of these reactions confirms formation of cyclic species bigger than 12-porphyrin nanoring as side-products.

Parts of the results in this chapter have been published in the following articles:

Vernier templating and synthesis of a 12-porphyrin nanoring
M. C. O'Sullivan, J. K. Sprafke, D. V. Kondratuk, C. Rinfray, T. D. W. Claridge, A. Saywell, M. O. Blunt, J. N. O'Shea, P. H. Beton, M. Malfois, H. L. Anderson, *Nature* **2011,** *469*, 72–75**.**

Belt-Shaped π-Systems: Relating Geometry to Electronic Structure in a Six-Porphyrin Nanoring
J. K. Sprafke, D. V. Kondratuk, M. Wykes, A. L. Thompson, M. Hoffmann, R. Drevinskas, W.-H. Chen, C. K. Yong, J. Kärnbratt, J. E. Bullock, M. Malfois, M. R. Wasielewski, B. Albinsson, L. M. Herz, D. Zigmantas, D. Beljonne, H. L. Anderson, *J. Am. Chem. Soc.* **2011,** *133*, 17262–17273**.**

2.1 Background

Pioneering work on the classical template-directed synthesis of cyclic porphyrin 6-mer and 8-mer by Dr. Craig Wilson and Dr. Markus Hoffmann established porphyrin nanorings as a new class of cyclic π-conjugated systems.[1,2] Further work by Dr. Johannes Sprafke and Dr. Melanie O'Sullivan, which resulted in the development of the Vernier templating strategies led to the synthesis of cyclic porphyrin 12-mer.[3] This short chapter describes the thorough study of the coupling of porphyrin monomer or linear porphyrin tetramer in the presence of **T6**.

2.2 Classical Cyclization of *l*-$P_{t\text{-}Bu}$**1** in the Presence of T6: a Detailed Study

It was shown by Dr. Johannes Sprafke that the palladium-catalyzed oxidative coupling of the deprotected porphyrin monomer ***l*-P$_{t\text{-}Bu}$1** in the presence of **T6** leads to formation, in addition to the target ***c*-P$_{t\text{-}Bu}$6•T6** and insoluble linear polymeric materials, of a figure-of-eight complex ***c*-P$_{t\text{-}Bu}$12•(T6)$_2$** in 9% analytical yield (Figure 2.1a).[4] The GPC analysis of the crude reaction mixture from coupling ***l*-P$_{t\text{-}Bu}$1** in the presence of **T6** (after removal of linear polymeric materials by a short alumina column in toluene) using THF as an eluent showed the presence of only two cyclic species, ***c*-P$_{t\text{-}Bu}$6•T6** and ***c*-P$_{t\text{-}Bu}$12•(T6)$_2$**, and no signs of the templated complexes of higher order such as ***c*-P$_{t\text{-}Bu}$18•(T6)$_3$** and ***c*-P$_{t\text{-}Bu}$24•(T6)$_4$** which should form at the same time (Figure 2.1b). A representation of ***c*-P$_{t\text{-}Bu}$18•(T6)$_3$** and ***c*-P$_{t\text{-}Bu}$24•(T6)$_4$** in Figure 2.1a neglects the fact that these higher order complexes may be mixtures of stereoisomers such as those of ***c*-P$_{t\text{-}Bu}$24•(T6)$_4$** depicted in Figure 3.1b of Chapter 3. The possibility of their formation is discussed in more detail in Section 3.2 of Chapter 3. A distribution of products similar to that of cyclooligomerizing ***l*-P$_{t\text{-}Bu}$1** was also obtained when coupling linear porphyrin dimer ***l*-P$_{t\text{-}Bu}$2** in the presence of **T6** (Figure 2.1c), however in that case the efficiency of formation of ***c*-P$_{t\text{-}Bu}$12•(T6)$_2$** is slightly higher (12% analytical yield). As expected, the coupling of ***l*-P$_{t\text{-}Bu}$4** in the presence of **T6** leads to formation of ***c*-P$_{t\text{-}Bu}$12•(T6)$_2$** as a main cyclic species in 39% analytical yield (Figure 2.1d).

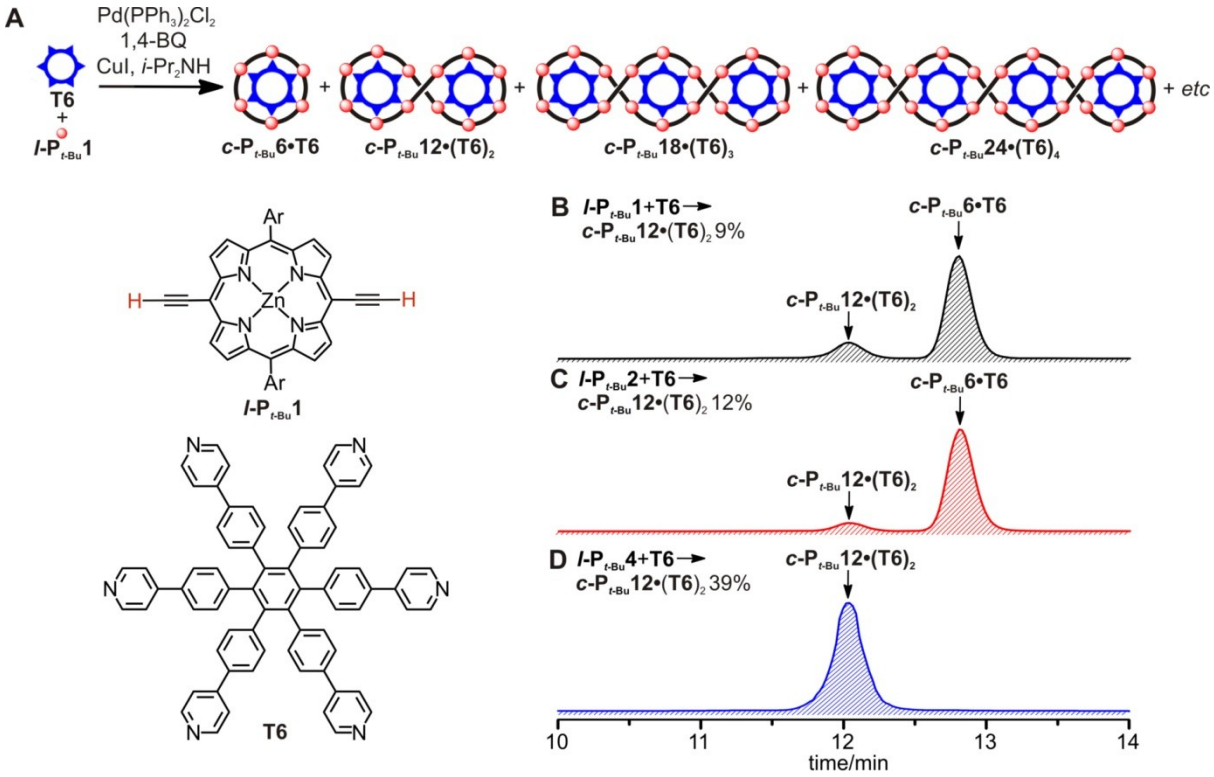

Figure 2.1. (a) Expected products for the cyclooligomerization of the deptrotected porphyrin monomer ***l*-P$_{t\text{-Bu}}$1** in the presence of a hexapyridyl template **T6**. Ar = 3,5-bis(*t*-butyl)phenyl. Analytical GPC traces (PLGel columns, THF, detection at 360 nm) of the crude reaction mixtures of coupling ***l*-P$_{t\text{-Bu}}$1** (b) ***l*-P$_{t\text{-Bu}}$2** (c) and ***l*-P$_{t\text{-Bu}}$4** (d) in the presence of **T6** in toluene and the corresponding analytical yields. The analytical yields shown were determined by comparing the areas of ***c*-P$_{t\text{-Bu}}$12•(T6)$_2$** with the area of standard injection of ***c*-P$_{t\text{-Bu}}$12•(T6)$_2$**. The coupling reagents (the catalysts and 1,4-benzoquinone) and insoluble polymers have been removed by passing through a short alumina column in $CHCl_3$. The GPC traces were recorded by Dr. Johannes Sprafke.

One possible reason for not seeing the higher order templated complexes in all of the above cases may be their low solubility under the conditions used for GPC analysis. Alternatively, they could dissociate to insoluble free rings in the presence of THF used as an eluent, which can compete with template molecules for coordination to the zinc-centres of porphyrin units. The third possible reason may be that the cyclic species are removed at the same time with linear porphyrin oligomers using alumina column. I started my work by analysing reaction mixtures of coupling ***l*-P$_{t\text{-Bu}}$1** in the presence of **T6** usign toluene (non-coordinating solvent) as eluent. When the GPC analysis, after passing the sample through alumina in toluene, was performed using toluene the presence of two more species of higher molecular weight was identified (Figure 2.2a) and they were isolated (Figure 2.2d,e) and analysed. The ^{1}H NMR spectra of these fractions (‘***c*-P18**’ and ‘***c*-P24**’) are inconclusive, as they only contain broad peaks. Matrix-assisted laser desorption/ionization mass spectrometry (MALDI-ToF) (acquired by the EPSRC National Mass Spectrometry Centre at Swansea University in toluene using DCTB as a matrix) of the ‘***c*-P18**’ fraction identified the presence of the expected molecular ion of ***c*-P$_{t\text{-Bu}}$18•(T6)$_3$** (*m/z* 17,401, *calc* 17,327) as a dominant peak, as well as a minor peak of ***c*-P$_{t\text{-Bu}}$12•(T6)$_2$** (*m/z* 11,583, *calc* 11,551) (Figure 2.2f). Similar analysis on the ‘***c*-P24**’ fraction revealed the presence of the expected molecular ion of ***c*-P$_{t\text{-Bu}}$24•(T6)$_4$** (*m/z* 23,979, *calc* 23,102) as a major peak, as well as minor peaks corresponding to ***c*-P$_{t\text{-Bu}}$18•(T6)$_3$** (*m/z* 17,915, *calc* 17,327) and

***c*-P$_{t\text{-Bu}}$12•(T6)$_2$** (*m/z* 11,563, *calc* 11,551) (Figure 2.2g).

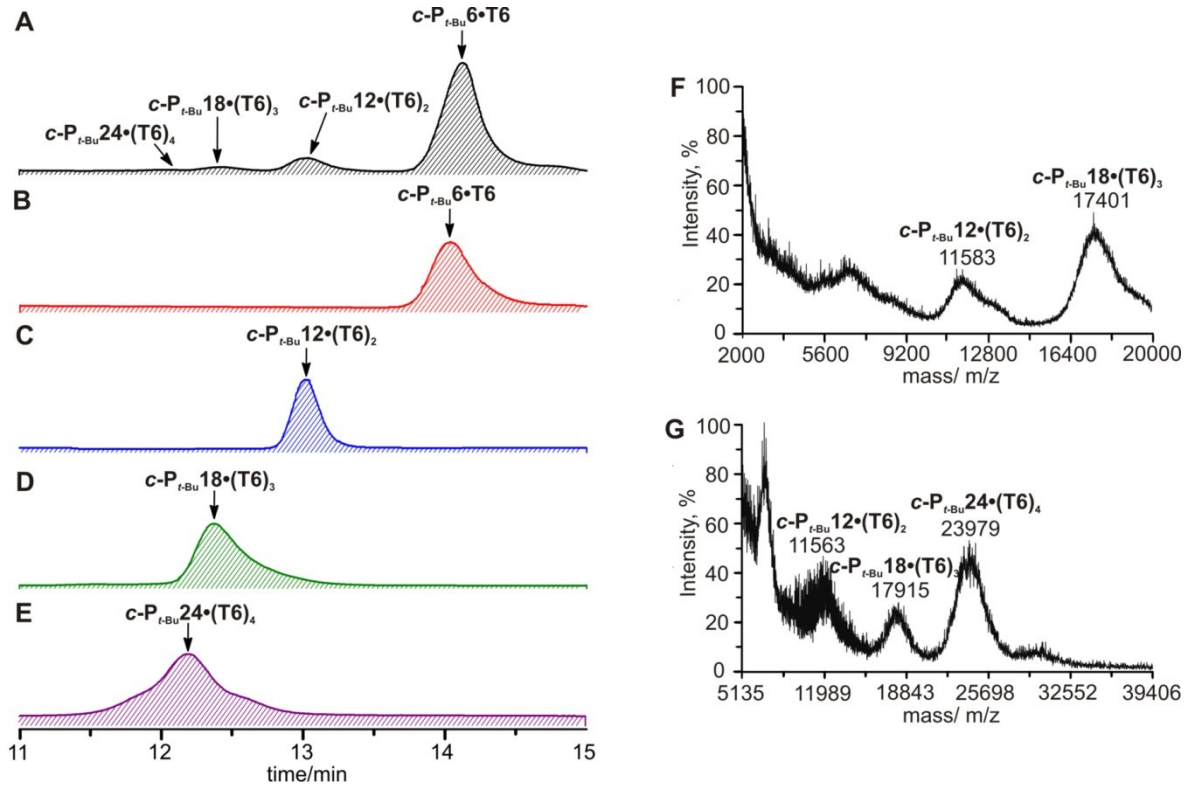

Figure 2.2. Analytical GPC traces (PLGel columns, toluene, detection at 500 nm) of the crude reaction mixtures of coupling ***l*-P$_{t\text{-Bu}}$1** in the presence of **T6** in toluene (a) and the purified samples of ***c*-P$_{t\text{-Bu}}$6•T6** (b), ***c*-P$_{t\text{-Bu}}$12•(T6)$_2$** (c), ***c*-P$_{t\text{-Bu}}$18•(T6)$_3$** (d) and ***c*-P$_{t\text{-Bu}}$24•(T6)$_4$** (e). The linear polymeric materials, catalysts and 1,4-benzoquinone have been removed by passing a sample of the crude reaction mixture through a short alumina column in toluene as eluent prior to analysis. MALDI-ToF analysis of samples of (f) ***c*-P$_{t\text{-Bu}}$18•(T6)$_3$** and (g) ***c*-P$_{t\text{-Bu}}$24•(T6)$_4$**. DCTB was used as a matrix in the linear mode. Both spectra were acquired by the EPSRC National Mass Spectrometry Centre at Swansea University.

SAXS analysis on the samples of '***c*-P18**' and '***c*-P24**' fractions was performed to further confirm their identity (Figure 2.3). The scattering data were acquired at Diamond Light Source, UK with the assistance of Dr. Marc Malfois. In both cases, the simulated data are in good agreement with the experimental data (Figure 2.3). In the case of the '***c*-P18**' sample, the pair-distribution function (PDF) from raw scattering data (Figure 2.3a) features 25 Å and 78 Å peaks close to the zinc-zinc distance across one 6-cycle (24 Å) and the longest calculated zinc-zinc distance in ***c*-P$_{t\text{-Bu}}$18•(T6)$_3$** (78 Å). The molecular weight calculated from scattering intensity at zero angle *I*(0) (16.0 kDa), with a solution of ***c*-P$_{t\text{-Bu}}$6·T6** as a standard, is in good agreement with the calculated mass of 17.3 kDa (Figure 2.3a). Similarly, the PDF from the scattering data of the '***c*-P24**' sample features 25 Å and 109 Å peaks that match these distances in ***c*-P$_{t\text{-Bu}}$24•(T6)$_4$** (Figure 2.3b). However, in this case the molecular weight calculated from scattering intensity at zero angle *I*(0) (26.9 kDa) is significantly higher than the expected mass of 23.1 kDa (Figure 2.3b) which might reflect the presence in the sample of even higher molecular weight species. The latter is consistent with the obvious shouldering at low retention time of the '***c*-P24**' peak in Figure 2.2e.

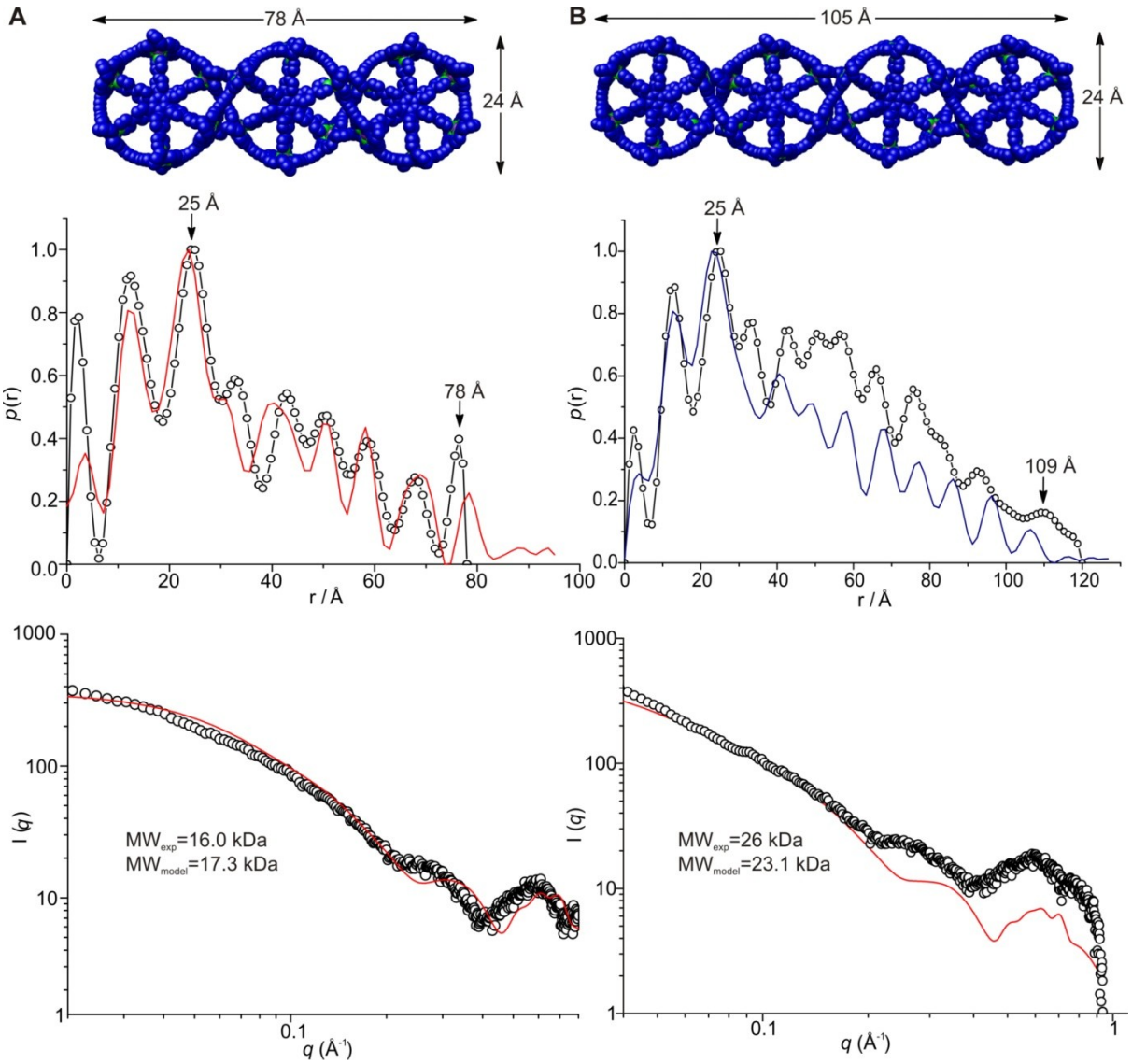

Figure 2.3. SAXS analysis of ***c*-P$_{t\text{-Bu}}$18•(T6)$_3$** (a) and ***c*-P$_{t\text{-Bu}}$24•(T6)$_4$** (b) in toluene acquired at 298 K at the beamline I22 at the Diamond Light Source, UK. The top row contains molecular models that were used to simulate experimental SAXS data. Side chains and hydrogen atoms are removed for clarity. Energy minimized structures were obtained using the MM+ force field implemented in the package HyperChem™. The middle row shows pair-distribution functions determined experimentally (black circles) and from models (lines). The bottom row shows the raw scattering data (black circles) together with the simulated curves based on calculated models (lines).

Treatment of the sample of '***c*-P24**' fraction with pyridine leads to precipitation of the corresponding free porphyrin oligomers which are also insoluble under conditions used for GPC chtromatography. This is consistent with the recent attempts of Dr. Melanie O'Sullivan to synthesize ***c*-P$_{t\text{-Bu}}$24** by the Vernier templated coupling of ***l*-P$_{t\text{-Bu}}$6** in the presence of **T8**, which also failed because of the low solubility and inability to purify ***c*-P$_{t\text{-Bu}}$24**.[5] The data presented above suggest that a more promising strategy to prepare the bigger rings may be to use porphyrin oligomers ***l*-P$_{C8}$N** bearing octyloxy side chains, instead of *t*-butyl series ***l*-P$_{t\text{-Bu}}$N** (Figure 2.4). This should help to improve the solubility of the targeted cyclic porphyrin oligomers, resulting in their easier separation using GPC chromatography.

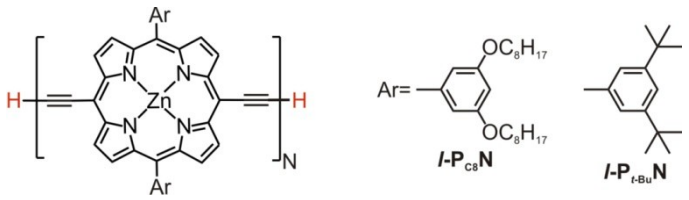

Figure 2.4. Molecular structures of porphyrin oligomers ***l*-P$_{C8}$N** and ***l*-P$_{t\text{-}Bu}$N**.

2.3 Vernier Cyclization of *l*-P$_{C8}$4 in the Presence of T6: a Detailed Study

The expected course of Vernier cyclization of ***l*-P$_{C8}$4** in the presence of **T6** is shown in Figure 2.5a. Palladium-catalyzed oxidative coupling of the deprotected linear porphyrin tetramer ***l*-P$_{C8}$4** in the presence of **T6** leads to formation of a mixture of linear and cyclic porphyrin oligomers. As before, it was possible to remove most of the linear species using a short alumina column in $CHCl_3$ followed by passing the cyclic species templated complexes mixture through a size exclusion column in the presence of pyridine to remove the template **T6**. The GPC analysis of the reaction mixtures shows that using the octyloxy modification of porphyrin subunits adds enough solubility to the oligomers to analyse template-free mixtures of oligomers (Figure 2.5b-d).

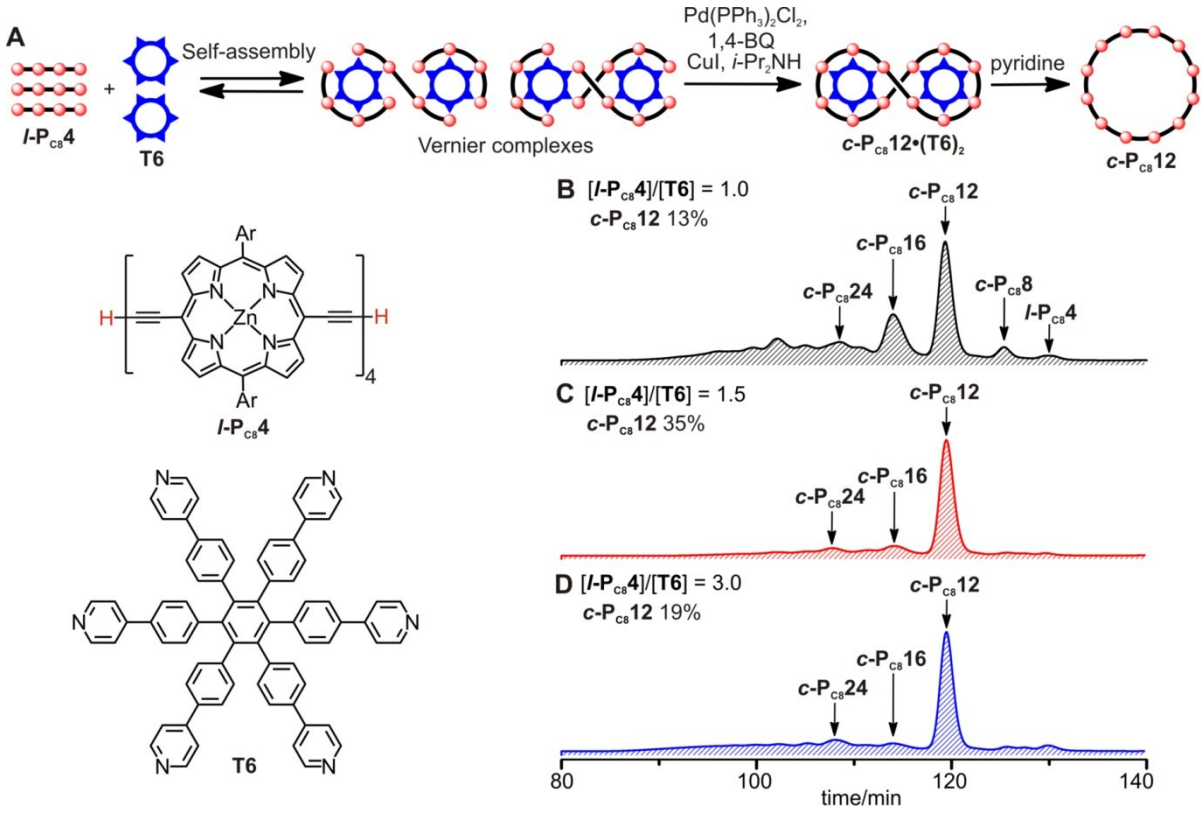

Figure 2.5. (a) Vernier templating for the synthesis of cyclic porphyrin dodecamer ***c*-P$_{C8}$12** from linear porphyrin tetramer ***l*-P$_{C8}$4**. Ar=3,5-bis(*t*-butyl)phenyl and 3,5-bis(octyloxy)phenyl. Recycling GPC traces (JAIGEL columns, 2^d cycle shown, toluene / 1% pyridine, detection at 500 nm) of the crude reaction mixtures of coupling ***l*-P$_{C8}$4** in the presence of **T6** under 1.0 (b), 1.5 (c) and 3.0 (d) ratios ***l*-P$_{C8}$4/T6** and the corresponding analytical yields of ***c*-P$_{C8}$12**.The mixtures were subjected to two recycling cycles and only the final traces are shown. The analytical yields shown were determined by comparing the areas of ***c*-P$_{C8}$12** with the area of standard injection of ***c*-P$_{C8}$12**. The coupling reagents (the catalysts and 1,4-benzoquinone) and **T6** were removed by passing through a short alumina column in $CHCl_3$ and the size exclusion column in $CHCl_3$/10% pyridine respectively.

As seen from the analytical traces in Figure 2.5b-c, the main cyclic species formed is ***c*-P$_{C8}$12**. However, in this case formation of significant amounts of other, bigger and smaller, cyclic species is observed (Figure 2.5). The ratio between the cyclic species appeared to be sensitive to the ratio between starting components. Using the recycling GPC chromatography it was possible to analyse the distribution of the porphyrin oligomer species in the crude product mixtures varying the mole ratio between starting components (***l*-P$_{C8}$4/T6**, Figure 2.5). In all cases studied (***l*-P$_{C8}$4/T6** = 1.0, 1.5, 3.0) the major cyclic product in the mixture was ***c*-P$_{C8}$12** and, as expected, its formation was most efficient when using the stoichiometric amount of the template (***l*-P$_{C8}$4/T6** = 1.5). However, the ***c*-P$_{C8}$12** is never the only product formed in the system and the traces of smaller (***c*-P$_{C8}$8**), various identifed larger (***c*-P$_{C8}$16** and ***c*-P$_{C8}$24**) and unidentified linear and cyclic species were detected. It implies that ***l*-P$_{C8}$4** couples in a variety of states, not just in the form of Vernier complexes shown in Figure 2.5a.

In accordance with GPC analysis, the 35% analytical yield of ***c*-P$_{C8}$12** was achieved by using the stoichiometric amount of **T6** and is comparable to the analytical yield achieved in the Vernier synthesis of the ***c*-P$_{t\text{-}Bu}$12** (39 %). Under 1:1 mole ratio between ***l*-P$_{C8}$4** and **T6** the analytical yield of ***c*-P$_{C8}$12** (13%) decreased, and a significant amount of ***c*-P16$_{C8}$** (isolated yield 6 %) was formed.

2.4 Conclusions and Outlook

The aforementioned results demonstrated that the cyclooligomerization of porphyrin monomer in the presence of template **T6** leads to formation of not only 6- and 12-porphyrin nanorings, as believed before, but also higher order species such as 18- and 24-porphyrin nanorings. Similarly, coupling of the linear porphyrin tetramer in the presence of **T6** leads to formation, in addition to the expected 12-porphyrin nanoring, of the species as large as 16- and 24-porphyrin nanorings. It is crucial to use the porphyrin oligomers bearing appropriate solubilizing groups to be able to analyse and separate the higher order species. This will prove important for the Vernier synthesis of cyclic porphyrin arrays larger than 12-porphyrin nanoring, as discussed in the following chapters.

2.5 References

[1] M. Hoffmann, C. J. Wilson, B. Odell, H. L. Anderson, *Angew. Chem., Int. Ed.* **2007**, *46*, 3122–3125.

[2] M. Hoffmann, J. Kärnbratt, M.-H. Chang, L. M. Herz, B. Albinsson, H. L. Anderson, *Angew. Chem., Int. Ed.* **2008**, *47*, 4993–4996.

[3] M. C. O'Sullivan, J. K. Sprafke, D. V. Kondratuk, C. Rinfray, T. D. W. Claridge, A. Saywell, M. O. Blunt, J. N. O'Shea, P. H. Beton, M. Malfois, H. L. Anderson, *Nature* **2011**, *469*, 72–75.

[4] J. K. Sprafke, D. V. Kondratuk, M. Wykes, A. L. Thompson,M. Hoffmann, R. Drevinskas, W. H. Chen, C. K. Yong, J. Kärnbratt,J. E. Bullock, M. Malfois, M. R. Wasielewski, B. Albinsson, L. M. Herz, D. Zigmantas, D. Beljonne, H. L. Anderson, *J. Am. Chem. Soc.* **2011**, *133*, 17262–17273.

[5] M. C. O'Sullivan, *Template Directed Synthesis of Porphyrin Nanorings*, D.Phil. thesis, University of Oxford, Oxford, **2011**.

Chapter 3

Vernier Synthesis and Characterization of a 24-porphyrin Nanoring

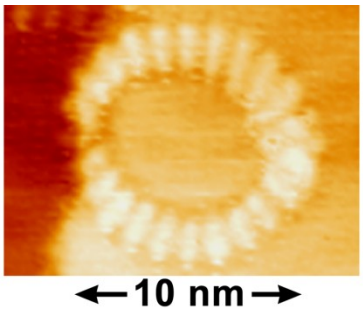

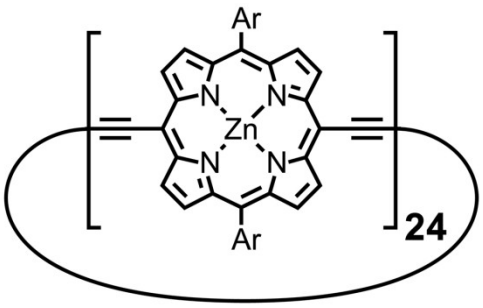

Established for the synthesis of 12-porphyrin nanoring, Vernier templating can be generalized for the synthesis of other challenging macrocycles. This chapter describes how, using this concept, it is possible to synthesize the 24-porphyrin nanoring, a giant π-conjugated macrocycle with a diameter close to 10 nm – larger than many enzymes. Three possible Vernier routes are considered (starting with a linear porphyrin trimer, hexamer or octamer). The structure of this 24–porphyrin nanoring is investigated by means of ^{1}H NMR, MALDI-ToF and STM imaging.

Parts of the results in this chapter have been published in the following article:

Two Vernier-Templated Routes to a 24-Porphyrin Nanoring
D.V. Kondratuk, L. M. A. Perdigao, M. C. O'Sullivan, S. Svatek, G. Smith, J. N. O'Shea, P. H. Beton, H. L. Anderson, *Angew. Chem. Int. Ed.* **2012**, *51*, 6696–6699

3.1 Background

The successful synthesis of a 12-porphyrin nanoring from a linear zinc porphyrin tetramer and a hexapyridyl template, **T6**, establishes Vernier-templating as a new templating strategy which uses non-commensurate combinations of templates and building blocks to direct the formation of cyclic oligomers. This new principle allows a small template to direct the formation of a much larger macrocycle, such that the number of binding sites in the product is the lowest common multiple of the numbers of sites in the template and the starting material. This distinguishes Vernier templating from the classical templating approaches where to address the synthesis of a bigger macrocycle a bigger template is necessary.[1-3] The "road-map" in the Table 3.1 shows how Vernier templating approach can be generalized to address the synthesis of the porphyrin nanorings beyond a 12-porphyrin cycle using readily available linear porphyrin oligomers, a hexapyridyl template, **T6**, and octapyridyl template, **T8**. Of these rings, the 24-porphyrin nanoring is the logical next challenge: there are only a few reports of larger π-conjugated macrocycles, namely Mayor's 11.8 nm conjugated cycle,[4] and larger cyclic porphyrin oligomers, namely Osuka's cyclic array of 32 porphyrins,[5] and if prepared the 24-porphyrin nanoring would be the largest molecular ring to have been synthesized by a template-directed strategy. As was shown in Section 2.2 of Chapter 2, using porphyrin oligomers ***l*-P$_{C8}$N,** bearing octyloxy side chains, should provide enough solubility of the rings above 12-porphyrin.

Table 3.1. "Road map" for Vernier templating using easily available linear porphyrin oligomers ***l*-PN**, where N = 1–10, hexapyridyl template, **T6**, and octapyridyl template, **T8**. The Vernier combinations are shown in blue and underlined.

Linear Porphyrin Oligomer	Product from T6	Product from T8
***l*-P1**	***c*-P6**	***c*-P8**
***l*-P2**	***c*-P6**	***c*-P8**
***l*-P3**	***c*-P6**	***c*-P24**
***l*-P4**	***c*-P12**	***c*-P8**
***l*-P5**	***c*-P30**	***c*-P40**
***l*-P6**	***c*-P6**	***c*-P24**
***l*-P7**	***c*-P42**	***c*-P56**
***l*-P8**	***c*-P24**	***c*-P8**
***l*-P9**	***c*-P54**	***c*-P72**
***l*-P10**	***c*-P30**	***c*-P40**

3.2 Oligomerization of *l*-P_{C8}8

Figure 3.1a shows three possible Vernier routes to a 24-porphyrin ring, ***c*-P_{C8}24** in accordance with Table 3.1. The representation of the three routes in Figure 3.1a overlooks the fact that complexes such as ***c*-P_{C8}24•(T6)$_4$** and ***c*-P_{C8}24•(T8)$_3$** have many possible stereoisomers, some of which are illustrated for ***c*-P_{C8}24•(T6)$_4$** in Figure 3.1b. Nonetheless, formation of these isomeric intermediates does not detract from the efficiency of the Vernier-templated synthesis because removal of the template will convert all these isomers to the same ***c*-P_{C8}24** open ring. The only exception would be formation of knotted products which have never been detected.

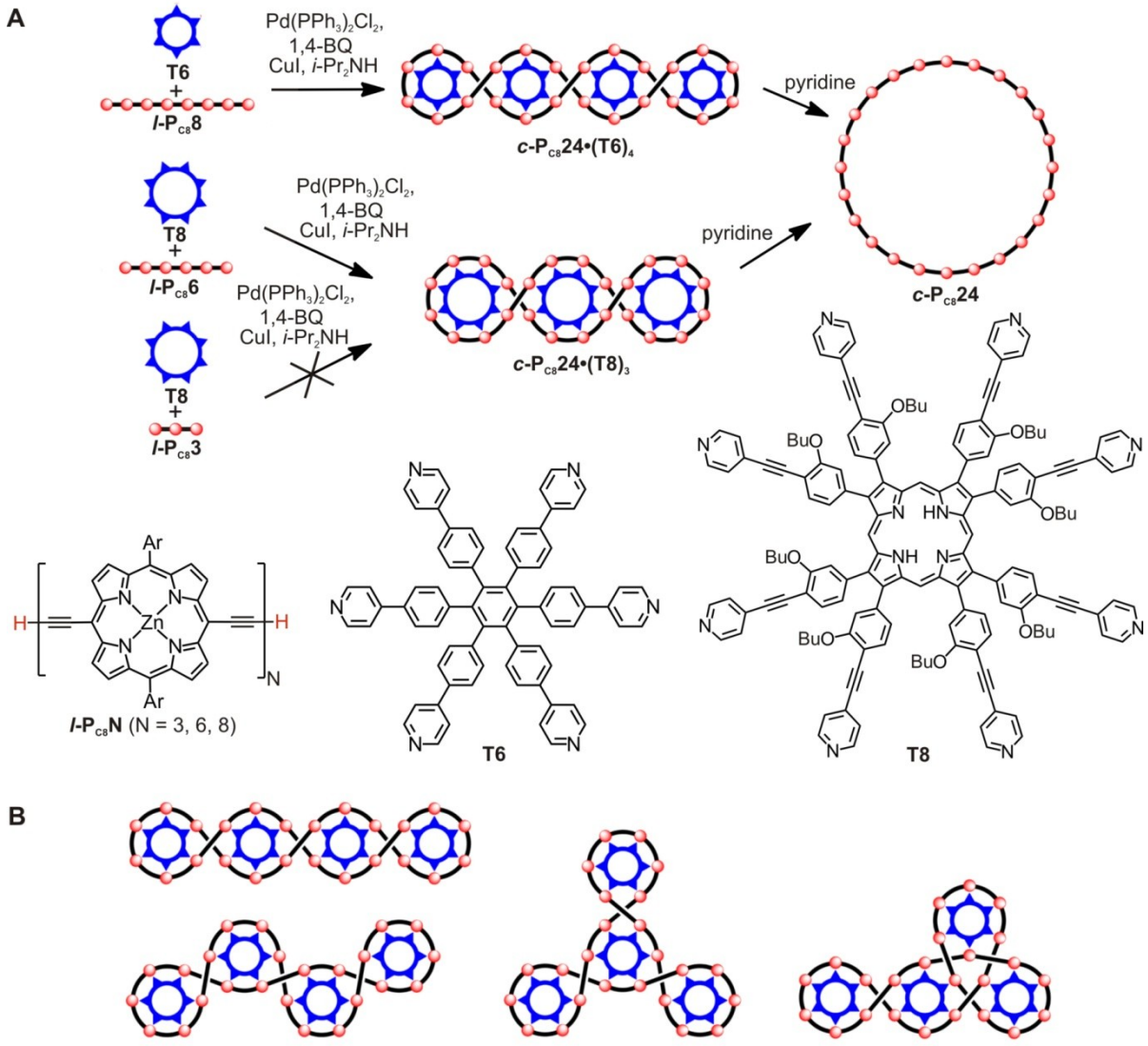

Figure 3.1. (a) Three possible Vernier templated routes for the synthesis of the nanoring ***c*-P_{C8}24**. (b) Four examples of possible stereoisomers of ***c*-P_{C8}24·(T6)$_4$**.

Palladium-catalyzed oxidative coupling of the linear porphyrin octamer ***l*-P_{C8}8** in the presence of the hexapyridyl template **T6** gives the expected product ***c*-P_{C8}24**, together with the 16-porphyrin ring ***c*-P_{C8}16**, and linear polymers, all as complexes with **T6**. The linear polymeric byproducts can be

removed using a short alumina column in $CHCl_3$. The resulting mixture of ring complexes separates well by preparative size-exclusion chromatography on Plgel (Polymer Laboratories Ltd.) columns in toluene (Figure 3.2).

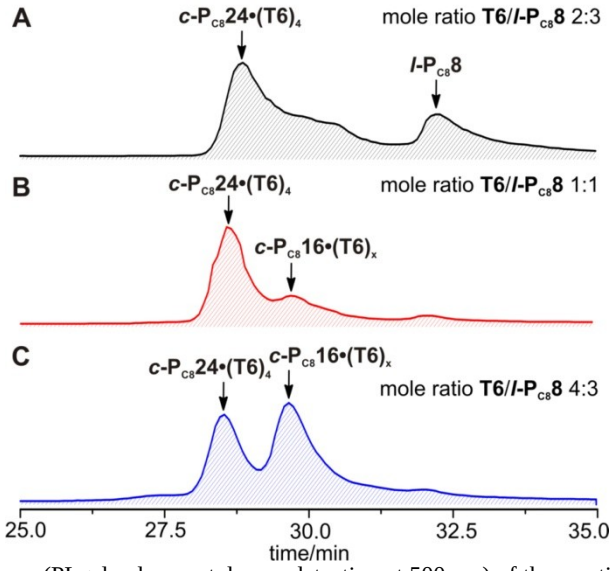

Figure 3.2. Analytical GPC traces (PLgel columns, toluene, detection at 500 nm) of the reaction mixtures of coupling ***l*-P$_{C8}$8** in toluene in the presence of **T6** using (a) 2:3, (b) 1:1 and (c) 4:3 ratios between **T6** and ***l*-P$_{C8}$8**. The rings are in the form of corresponding template complexes ***c*-P$_{C8}$16(T6)$_x$** and ***c*-P$_{C8}$24(T6)$_4$**. The linear polymeric materials, catalysts and 1,4-benzoquinone were removed by passing through short alumina column in $CHCl_3$ as eluent prior to GPC analysis.

Alternatively, reaction mixtures can be analysed and separated directly as template-free polymer oligomers via semi-preparative GPC on Plgel columns in THF/1% pyridine using analytical variation of the columns. Prior to GPC analysis/separation removal of **T6**, catalysts and 1,4-benzoquinone was performed by passing a sample of reaction mixture through a short SEC column. In this case, the GPC trace shows that coupling of ***l*-P$_{C8}$8** in the presence of **T6** occurs with formation, apart from target ***c*-P$_{C8}$16** and ***c*-P$_{C8}$24**, of some amounts of ***c*-P$_{C8}$8** and unidentified high molecular weight species (Figure 3.3a).[‡]

[‡] As was shown in Chapter 2 and will be shown in Chapter 5, JAIGEL (Japan Analytical Industry Co.,Ltd.) columns in combination with recycling GPC provide most efficient and quick separation conditions for mixtures of template-free linear and cyclic porphyrin oligomers. However, at the time when the research program described in this chapter was performed, such equipment had not yet become available in our laboratory and combinations of Plgel columns were used instead.

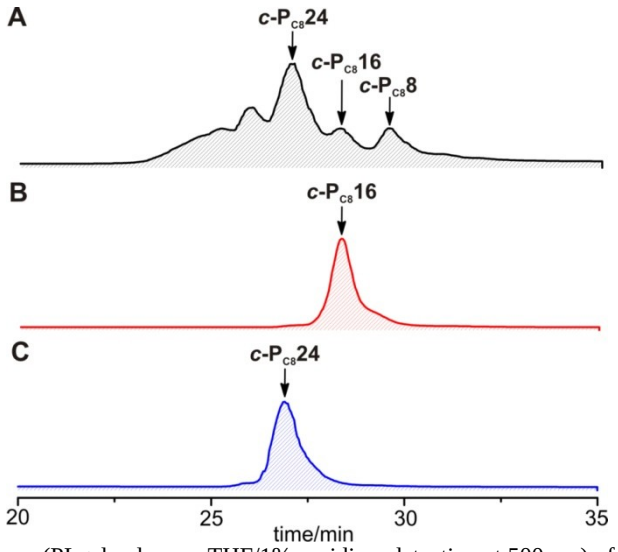

Figure 3.3. Analytical GPC traces (PLgel columns, THF/1% pyridine, detection at 500 nm) of (a) the crude reaction mixture of coupling ***l*-P$_{C8}$8** in the presence of **T6** overlaid with the purified samples of (b) ***c*-P$_{C8}$16** and (c) ***c*-P$_{C8}$24**. The starting mole ratio **T6**/***l*-P$_{C8}$8** = 1:1. **T6**, catalysts and 1,4-benzoquinone were removed by passing through SEC column in $CHCl_3$/10% pyridine as eluent prior to GPC analysis and separation.

The ratio ***c*-P$_{C8}$24**/***c*-P$_{C8}$16** depends on the amount of **T6** present during the reaction (Figure 3.2). Use of a slightly sub-stoichiometric amount of template ([**T6**]/[***l*-P$_{C8}$8**]<4/3) shifts the product distribution towards ***c*-P$_{C8}$24·(T6)$_4$**, while use of more than 4/3 equivalents of **T6** favours formation of ***c*-P$_{C8}$16**. Coupling ***l*-P$_{C8}$8** in the presence of one equivalent of **T6** gives ***c*-P$_{C8}$24·(T6)$_4$** as the main cyclic product (14% isolated yield). Treatment of the template complexes with an excess of pyridine results in quantative conversion to the free nanorings ***c*-P$_{C8}$16** and ***c*-P$_{C8}$24**.

When the starting material ***l*-P$_{C8}$8** is coupled under the same conditions, except in the absence of any template, only high molecular weight linear polymers are formed. These, apparently due to their high molecular weight, cannot be analysed by GPC using Plgel columns as they stick to them.

3.3 Oligomerization of *l*-P$_{C8}$6

A second possible Vernier route to ***c*-P$_{C8}$24** starts with linear porphyrin hexamer ***l*-P$_{C8}$6** (Figure 3.1a). Coupling of ***l*-P$_{C8}$6** in the presence of the octapyridyl template **T8** gives a mixture of templated complexes of cyclic products ***c*-P$_{C8}$12**, ***c*-P$_{C8}$18** and ***c*-P$_{C8}$24** and linear polymers. In contrast to the case of **T6**, complexes based on **T8** cannot be analysed and separated using PLgel GPC as these templated complexes permanently stick to such columns. Consequently, removal of **T8** by size-exclusion chromatography in the presence of pyridine is necessary before the analysis and separation. This affords mixtures of ***c*-P$_{C8}$12**, ***c*-P$_{C8}$18**, ***c*-P$_{C8}$24** and linear polymers, which are then easily separated via semi-preparative GPC using analytical PLgel columns (Figure 3.4).

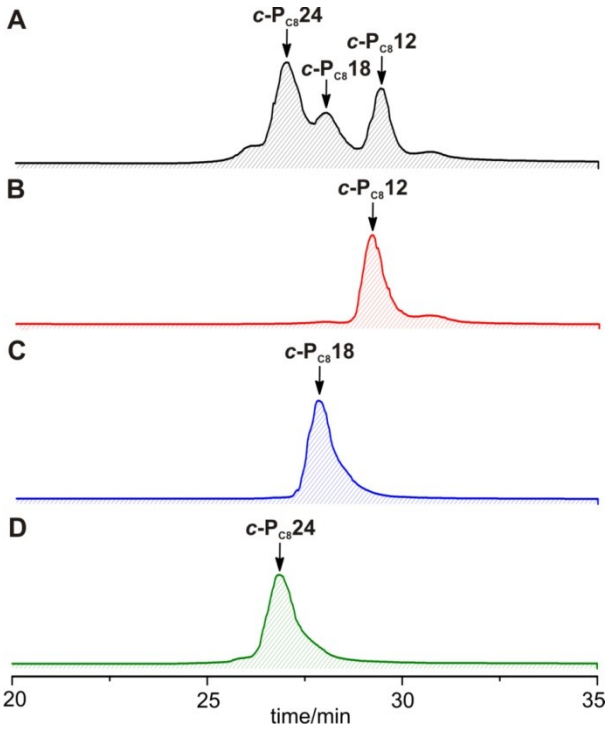

Figure 3.4. Analytical GPC traces (PLgel columns, THF/1% pyridine, detection at 500 nm) of (a) the crude reaction mixture of coupling ***l*-P$_{C8}$6** in the presence of **T8** (a) overlaid with the purified samples of (b) ***c*-P$_{C8}$12**, (c) ***c*-P$_{C8}$18** (c) and (d) ***c*-P$_{C8}$24**. The starting ratio **T6/*l*-P8** = 1:1. **T8**, catalysts and 1,4-benzoquinone were removed using short SEC column in $CHCl_3$/10% pyridine as eluent prior to GPC analysis and separation.

As before, the ratio between the rings depends on the amount of **T8** in the reaction mixture. Using less of **T8** over required by stoichiometry (***l*-P$_{C8}$6/T8** = 4:3) favours formation of ***c*-P$_{C8}$18**; using significant excess of **T8** (more than 1 eqv of **T8** per 1 eqv of ***l*-P$_{C8}$6**) favours formation of ***c*-P$_{C8}$12** (Figure 3.5). The ***c*-P$_{C8}$24** is the major product when coupling a 1:1 mixture of **T8** and ***l*-P$_{C8}$6** (25% isolated yield). It is surprising and unclear that, as opposed to the ***l*-P$_{C8}$8/T6** case, most efficient formation of ***c*-P$_{C8}$24** is observed under slight excess (over stoichiometry) of **T8** in the system.

Coupling of ***l*-P$_{C8}$6** in the absence of any template only gives high molecular weight linear polymers which cannot be analysed by PLgel columns as they stick to them.

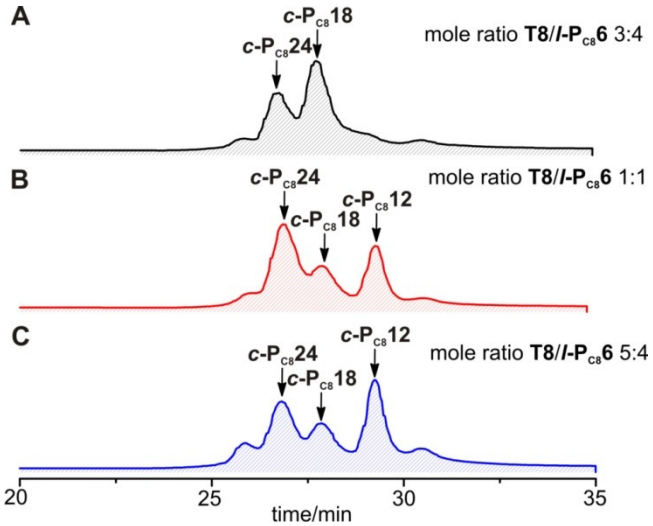

Figure 3.5. Analytical GPC traces (PLgel columns, THF/1% pyridine, detection at 500 nm) of the reaction mixtures of coupling ***l*-P$_{C8}$6** in the presence of **T8** using 3:4 (a), 4:4 (b) and 5:4 (c) ratio between **T8** and ***l*-P$_{C8}$6**. **T8**, catalysts and 1,4-benzoquinone have been removed by passing through SEC column in $CHCl_3$/10% pyridine prior to GPC analysis.

3.4 Oligomerization of *l*-P$_{C8}$3

The most convenient way of preparing ***c*-P$_{C8}$24** would be coupling of the simple linear porphyrin trimer ***l*-P$_{C8}$3** in the presence of template **T8** (Figure 3.6). However, when applying the reaction conditions of Sections 3.2 and 3.3 to ***l*-P$_{C8}$3** in the presence of **T8**, formation of only small amount of high molecular weight polymeric materials of unknown composition (Figure 3.6) is observed.

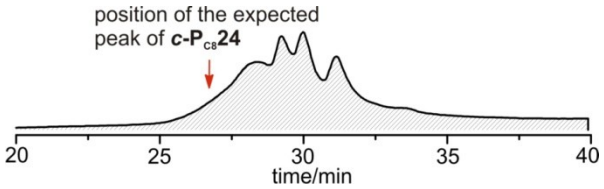

Figure 3.6. Analytical GPC trace (PLgel columns, THF/1% pyridine, detection at 500 nm) of the crude reaction mixture of coupling ***l*-P$_{C8}$3** in the presence of **T8**. The starting ratio **T8/*l*-P$_{C8}$3** = 1:2. **T8**, catalysts and 1,4-benzoquinone were removed by passing through SEC column in $CHCl_3$/10% pyridine prior to GPC analysis.

Figure 3.7 shows semilogarithmic plot of molecular weight *vs* retention times for reported and novel linear (***l*-P$_{C8}$1$_{THS,THS}$, *l*-P$_{C8}$2$_{THS,THS}$, *l*-P$_{C8}$3$_{THS,THS}$, *l*-P$_{C8}$4$_{THS,THS}$, *l*-P$_{C8}$6$_{THS,THS}$** and ***l*-P$_{C8}$8$_{THS,THS}$**) and cyclic (***c*-P$_{C8}$12**, ***c*-P$_{C8}$16**, ***c*-P$_{C8}$18** and ***c*-P$_{C8}$24**) porphyrin oligomers. The data for linear and cyclic species form two separate straight lines. Based on the calibration plot in Figure 3.7, the highest molecular weight peak in Figure 3.6 is most likely either linear porphyrin decamer ***l*-P$_{C8}$10** or cyclic porphyrin 15-mer ***c*-P$_{C8}$15**. Most of the product, however, is an insoluble polymer.

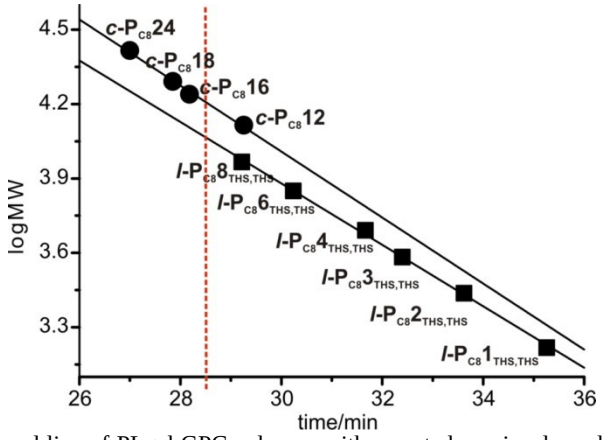

Figure 3.7. Calibration of the used line of PLgel GPC columns with reported previously and new cyclic (circles) and linear (squares) porphyrin oligomers. The red vertical line corresponds to the retention time of the higher molecular weight peak in the trace in Figure 3.6. The points were collected using the line of PLgel 3 μm Mixed-E columns (2 × 300 mm length, 7.5 mm diameter) and Plgel 5 μm Mixed-D columns (3 × 300 mm length, 7.5 mm diameter) in THF/1%Py with a flow rate of 1.0 mL/min.

3.5 Efficiency of Vernier Templating: Toluene *vs* $CHCl_3$, T6 *vs* T8.

Coupling of ***l*-P$_{C8}$8** in the presence of **T6** (mole ratio **T6/*l*-P$_{C8}$8** = 1:1) is equally efficient when using toluene or $CHCl_3$ as a solvent (see Table 3.2); coupling of ***l*-P$_{C8}$6** in the presence of **T8** (mole ratio **T8/ *l*-P$_{C8}$6** = 1:1) is slightly more efficient when performed in $CHCl_3$. **T6** directs formation of ***c*-P$_{C8}$24**

more efficiently than **T8** in toluene; templating by **T8** is better and gives the highest yield of ***c*-P$_{C8}$24** when performed in $CHCl_3$.

Table 3.2. Yields of ***c*-PC$_8$24** synthesized from coupling ***l*-P$_{C8}$8** or ***l*-P$_{C8}$6** in toluene or $CHCl_3$. The yields are determined by analytical GPC from comparison of the areas of the deconvoluted peaks of ***c*-P$_{C8}$24** with an area of the peak of pure ***c*-P$_{C8}$24** at known concentration assuming no adsorption of the porphyrin oligomer. The error in the yields comes from deconvolution.

Starting Materials	Reaction in Toluene	Reaction in $CHCl_3$
***l*-P$_{C8}$8+T6**	17%±1%	17%±1%
***l*-P$_{C8}$6+T8**	14%±1%	22%±1%

The yields mentioned in the Table 3.2 were determined by analytical GPC from comparison of the areas of the deconvoluted peaks of ***c*-P$_{C8}$24** with an area of the peak of pure ***c*-P$_{C8}$24** at known concentration. Deconvolution and integration of the peaks were performed using Origin 8.1 software package (see Figure 3.8 showing an example).

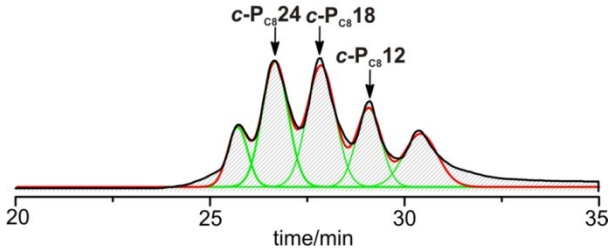

Figure 3.8. Deconvoluted analytical GPC trace (PLgel columns, THF/1% pyridine, detection at 500 nm) of the crude reaction mixture of coupling ***l*-P$_{C8}$6** in the presence of **T8**. A GPC of an unoptimized reaction is shown (***c*-P$_{C8}$24** is not the main product). The figure features the starting GPC trace (black), the deconvoluted peaks of individual components (light green) and the sum of the deconvoluted peaks (red). **T8**, catalysts and 1,4-benzoquinone have been removed by passing through SEC column in $CHCl_3$/10% pyridine prior to GPC analysis.

3.6 Characterization of Cyclic Species

3.6.1 ^{1}H NMR Spectroscopy

^{1}H NMR spectra of ***c*-P$_{C8}$16**, and ***c*-P$_{C8}$24** shows just two β-proton doublets, reflecting the high symmetry of the molecules (Figure 3.9a,c). In contrast, ^{1}H NMR of ***c*-P$_{C8}$18** contains two sets of β-proton doublets of unknown origin (Figure 3.9b).

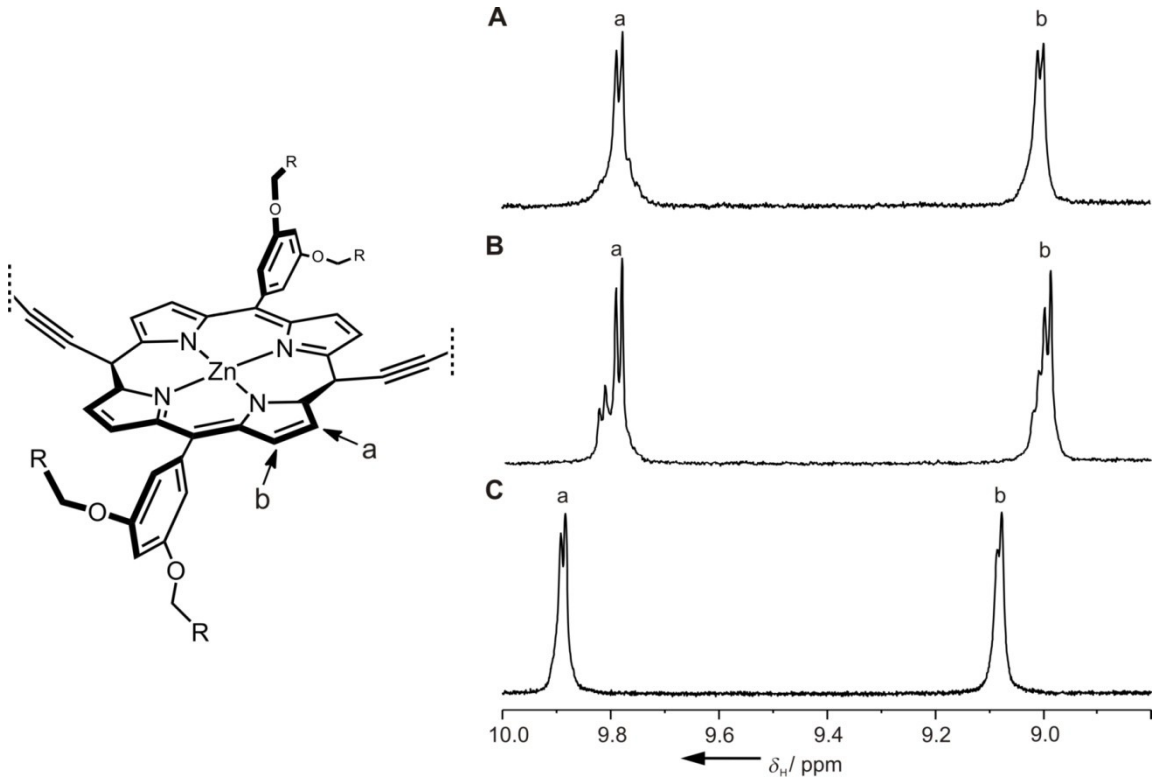

Figure 3.9. ^{1}H NMR spectra of (a) ***c*-P$_{C8}$16**, (b) ***c*-P$_{C8}$18** and (c) ***c*-P$_{C8}$24** showing the β-pyrrole region. The spectra were recorded in $CDCl_3$/1%C_5D_5N (298 K) at 400 MHz (a,b) and 500 MHz (c).

3.6.2 MALDI-ToF Mass Spectrometry

The isolated cyclic porphyrin oligomers were characterized by matrix-assisted laser desorption/ionization mass spectrometry. The experiments were run using toluene/5% pyridine mixture as a solvent for deposition of the samples to prevent aggregation, in the presence of DCTB as a matrix. The spectra were acquired by the EPSRC National Mass Spectrometry Centre at Swansea University or with the help of Mr. Gareth Smith at the University of Manchester. In all cases the spectra show the presence of the expected molecular ions of ***c*-P$_{C8}$16** (*m/z* 17,323; *calc* 17,357), ***c*-P$_{C8}$18** (*m/z* 19,477; *calc* 19,526) and ***c*-P$_{C8}$24** (*m/z* 26,124; *calc* 26,035) as the dominant peaks (Figure 3.10). The MALDI-ToF spectra in Figure 3.10 in all cases exhibit minor peaks at half and twice the expected mass. The resolution is not sufficient to determine whether these peaks arise from M^{2+} and M_2^+ of the corresponding rings, or from traces of the other rings in the sample such as ***c*-P$_{C8}$12** and ***c*-P$_{C8}$48** in the case of ***c*-P$_{C8}$24**. However, because in the case of ***c*-P$_{C8}$18** a peak at half expected mass corresponding to ***c*-P$_{C8}$9** or ***l*-P$_{C8}$9** (neither of which could form from ***l*-P$_{C8}$6**) is also observed, the half mass peaks most likely arise from M^{2+}.

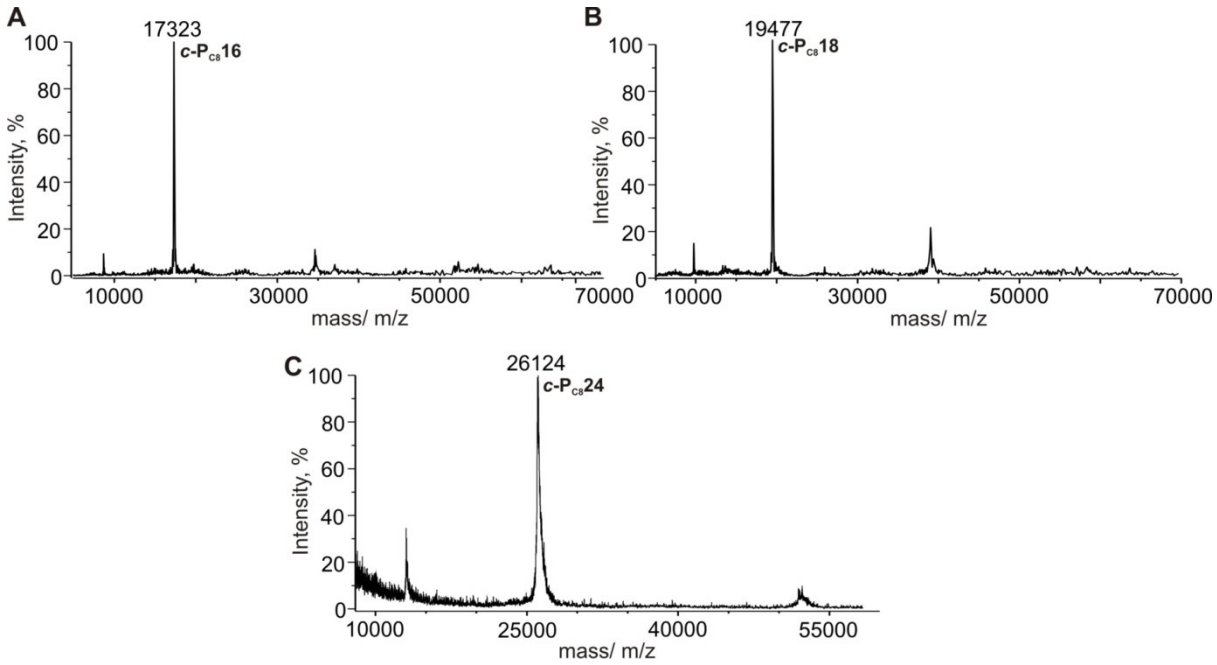

Figure 3.10. MALDI-ToF analysis of (a) ***c*-P$_{C8}$16**, (b) ***c*-P$_{C8}$18** and (c) ***c*-P$_{C8}$24** samples. DCTB was used as a matrix. Spectra (a) and (b) were acquired by Mr. Gareth Smith (University of Manchester) and spectrum (c) was acquired by the EPSRC National Mass Spectrometry Centre at Swansea University

3.6.3 STM Imaging

Scanning tunneling microscopy (STM) of samples of ***c*-P$_{C8}$16**, ***c*-P$_{C8}$18** and ***c*-P$_{C8}$24** was performed by Dr. Luis Perdigao, Simon Svatek, Dr. James O'Shea and Prof. Peter Beton (University of Nottingham, UK). The molecules were deposited using an electrospray source on an Au(111) surface in ultrahigh vacuum,[8] from solutions in a toluene/MeOH (3:1) solvent mixture containing 5% of pyridine to prevent aggregation. The sample of ***c*-P$_{C8}$24** used in this experiment was synthesized from linear porphyrin hexamer ***l*-P$_{C8}$6**.

The STM of the samples of ***c*-P$_{C8}$16** and ***c*-P$_{C8}$18** used for imaging show the presence of many nanometer-sized rings, however the resolution of the images is not enough to count directly the number of porphyrin subunits (Figure 3.11a, b). In contrast, individual porphyrin subunits are clearly resolved on the small area STM images of ***c*-P$_{C8}$24** (Figure 3.11c,d). In Figure 3.11d two nearly circular ***c*-P$_{C8}$24** molecules are shown adsorbed on a gold surface and it is possible to count 24 porphyrin subunits. The average diameter of the nanorings (about 10 nm) matches the calculated Zn···Zn diameter of 9.7 nm. As expected, ***c*-P$_{C8}$24** is the main component present in the sample indicating its high purity.

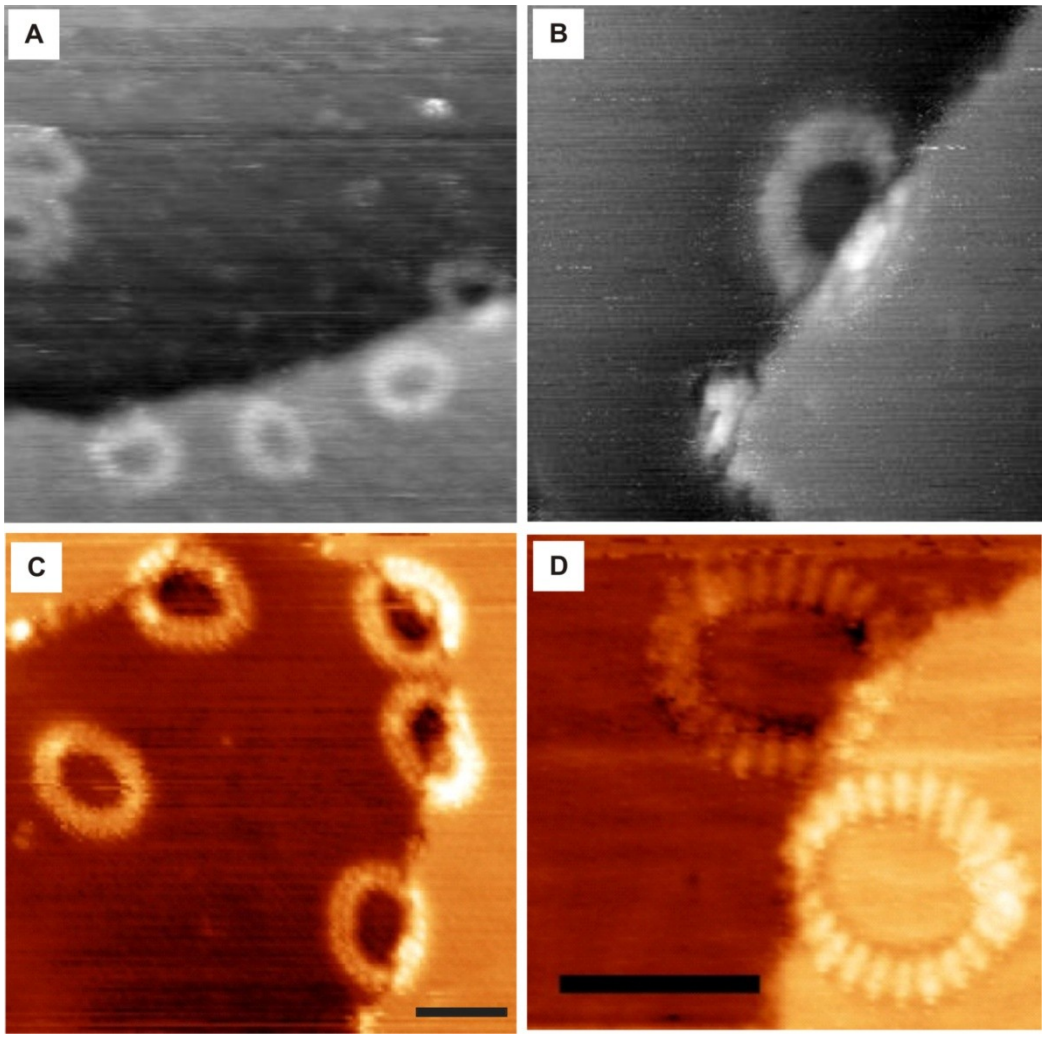

Figure 3.11. STM images of (a) ***c*-P$_{C8}$16**, (b) ***c*-P$_{C8}$18** and (c,d) ***c*-P$_{C8}$24** single molecules on an Au (111) surface (scale bar, 10 nm). The samples were deposited from toluene/MeOH (3:1) solvent mixtures containing 5% pyridine.

3.7 Conclusions and Outlook

In this chapter a butadiyne-linked π-conjugated 24-porphyrin nanoring ***c*-P$_{C8}$24** with a diameter of 10 nm has been prepared by Vernier templated synthesis from a linear porphyrin octamer ***l*-P$_{C8}$8** and from a linear porphyrin hexamer ***l*-P$_{C8}$6**. However, it proved impossible to synthesize the same ring by Vernier templated polymerization of the linear porphyrin trimer ***l*-P$_{C8}$3**. As compared to the Vernier synthesis of a 12-porphyrin nanoring ***c*-P$_{C8}$12** from a linear porphyrin tetramer ***l*-P$_{C8}$4**, ***c*-P$_{C8}$24** synthesis occurs with formation of significant amounts of the mismatched products such as ***c*-P$_{C8}$16** (in the case of ***l*-P$_{C8}$8**) and ***c*-P$_{C8}$12** and ***c*-P$_{C8}$18** (in the case of ***l*-P$_{C8}$6)** with the yield of the ***c*-P$_{C8}$24** being sensitive to the amount of a template in the reaction.

All isolated rings have been characterized using ^{1}H NMR spectroscopy, MALDI-ToF and STM imaging. Although there are a few reports of larger π-conjugated macrocycles,[5] and larger cyclic porphyrin oligomers,[9] ***c*-P$_{C8}$24** is the largest molecular ring to have been synthesized by a template

directed strategy, and these nanorings have possible application for exploring molecular Aharonov-Bohm effects.[9-11]

The results in this chapter suggest that this strategy should be applicable to the selective synthesis of even larger macrocycles.

3.8 References

[1] M. Hoffmann, C. J. Wilson, B. Odell, H. L. Anderson, *Angew. Chem., Int. Ed.* **2007**, *46*, 3122–3125.

[2] M. Hoffmann, J. Kärnbratt, M.-H. Chang, L. M. Herz, B. Albinsson, H. L. Anderson, *Angew. Chem. Int. Ed.* **2008**, *47*, 4993–4996.

[3] M. C. O'Sullivan, J. K. Sprafke, D. V. Kondratuk, C. Rinfray, T. D. W. Claridge, A. Saywell, M. O. Blunt, J. N. O'Shea, P. H. Beton, M. Malfois, H. L. Anderson, *Nature* **2011**, *469*, 72–75.

[4] M. Mayor, C. Didschies, *Angew. Chem., Int. Ed.* **2003**, *42*, 3176–3179.

[5] T. Hori, X. Peng, N. Aratani, A. Takagi, T. Matsumoto, T. Kawai, Z. S. Yoon, M.-C. Yoon, J. Yang, D. Kim, A. Osuka, *Chem. Eur. J.* **2008**, *14*, 582–595.

[6] J. K. Sprafke, D. V. Kondratuk, M. Wykes, A. L. Thompson, M. Hoffmann, R. Drevinskas, W. H. Chen, C. K. Yong, J. Kärnbratt, J. E. Bullock, M. Malfois, M. R. Wasielewski, B. Albinsson, L. M. Herz, D. Zigmantas, D. Beljonne, H. L. Anderson, *J. Am. Chem. Soc.* **2011**, *133*, 17262–17273.

[7] M. C. O'Sullivan, *Template Directed Synthesis of Porphyrin Nanorings*, D.Phil. thesis, University of Oxford, Oxford, 2011.

[8] A. Saywell, J. K. Sprafke, L. J. Esdaile, A. J. Britton, A. Rienzo, H. L. Anderson, J. N. O'Shea, P. H. Beton, *Angew. Chem. Int. Ed.* **2010**, *49*, 9136–9139.

[9] M. Mayor, C. Didschies, *Angew. Chem. Int. Ed.* **2003**, *42*, 3176–3179.

[10] S. Zaric, G. N. Ostojic, J. Kono, J. Shaver, V. C. Moore, M. S. Strano, R. H. Hauge, R. E. Smalley, X. Wei, *Science* **2004**, *304*, 1129–1131.

[11] N. A. J. M. Kleemans, I. M. A. Bominaar-Silkens, V. M. Fomin, V. N. Gladilin, D. Granados, A. G. Taboada, J. M. García, P. Offermans, U. Zeitler, P. C. M. Christianen, J. C. Maan, J. T. Devreese, P. M. Koenraad, *Phys. Rev. Lett.* **2007**, *99*, 146808.

Chapter 4

Covalent and Non-Covalent Locking of Conformation of a 24-Porphyrin Nanoring

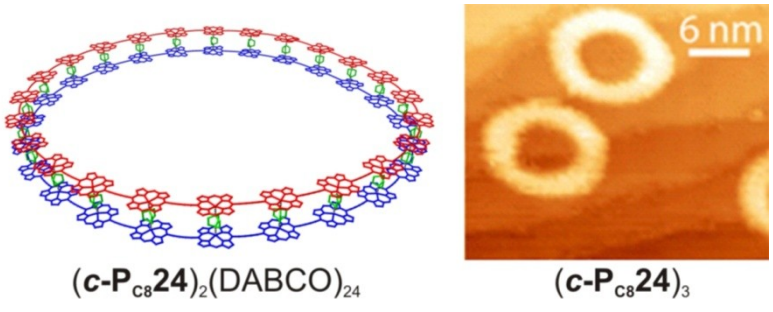

Increasing the size of porphyrin nanorings affects their structural and electronic properties drastically. Established for the case of 12-porphyrin nanoring, self-assembly of a 2:24 double-strand sandwich complex with DABCO can be also realized in the case of 24-porphyrin nanoring. An alternative non-covalent approach is the solvent induced formation of aggregates of nanorings which can be transferred to a gold surface and studied in detail by STM.

Parts of the results in this chapter have been published in the following articles:

Two Vernier-Templated Routes to a 24-Porphyrin Nanoring
D. V. Kondratuk, L. M. A. Perdigao, M. C. O'Sullivan, S. Svatek, G. Smith, J. N. O'Shea, P. H. Beton, H. L. Anderson, *Angew. Chem., Int. Ed.* **2012,** *51*, 6696–6699**.**

Mechanical Stiffening of Porphyrin Nanorings through Supramolecular Columnar Stacking
S. A. Svatek, L. M. A. Perdigão, A. Stannard, M. B. Wieland, D. V. Kondratuk, H. L. Anderson, J. N. O'Shea, P. H. Beton, *Nano Lett*, **2013**, *13*, 3391–3395.

4.1 Background

Large π-conjugated macrocycles attract widespread interest due to their intriguing optoelectronic properties[1-5] and unusual complexation abilities with substrates featuring π-surfaces.[6-8] As the size of such macrocycles is increased, they inevitably become more flexible and less shape-persistent. This effect is clearly visible, for example, when comparing shapes of ***c*-P$_{t\text{-Bu}}$6** and ***c*-P$_{t\text{-Bu}}$12** by small angle X-ray scattering (SAXS)[2,9] and can be detrimental to the host-guest properties of such macrocycles due to the lack of preorganization. The π-conjugation in such systems is also sensitive to conformational distortion.[5,10] As was shown before for the cases of ***c*-P$_{t\text{-Bu}}$6** (see references 2 and 3) and cycloparaphenylenes,[10,11] π-conjugation in the smaller strained macrocycles is higher than in the non-strained linear and cyclic analogues.

In the case of ***c*-P$_{t\text{-Bu}}$6**, complexation with radial templates through Zn-N bonding can effectively rigidify the macrocycle.[2,3] However, this approach has the same limitations as the classical templated synthesis of the macrocycles: the radial templates necessary to lock the conformation of ***c*-P$_{C8}$24** ring are too challenging to prepare. A convenient supramolecular approach to rigidification of such structures has been established by Dr. Johannes Sprafke (Chapter 1).[3,12] He showed that the 12-porphyrin nanoring can be easily locked into a double-strand sandwich complex by self-assembly with DABCO and this should be extendable to the 24-porphyrin nanoring. The formation of double-strand complexes also works in the case of linear porphyrin oligomers, such as the porphyrin dimer and tetramer, which in the presence of stoichiometric amounts of DABCO form corresponding ladder complexes.[13,14] In some cases the conformational freedom of linear porphyrin dimers and tetramers can also be restricted through aggregation of porphyrin subunits using π-π interactions.[13,15,16] The latter non-covalent approach should be transferable to the porphyrin nanorings such as ***c*-P$_{C8}$24**. In the case of ***c*-P$_{C8}$24** aggregation is expected to be particularly favoured due to cooperative effect of 24 porphyrin subunits as well as the presence of non-hindering octyloxy side chains.

Two of the aforementioned approaches to rigidification of ***c*-P$_{C8}$24** are investigated in this chapter.

4.2 Sandwich-complex formation by *c*-P$_{C8}$24

Dr. Johannes Sprafke found that the formation of a sandwich complex of ***c*-P$_{C8}$12** was most easily observed when using DABCO as a bidentate ligand.[3,12] Formation of such complexes with other bidentate ligands such as 4,4'-bipyridine (BiPy) was less clear-cut, even though ladder complexes of other linear porphyrin oligomers with BiPy are known.[14] It is possible that only in the case of DABCO can the binding energy compensate for the locking ***c*-P$_{C8}$12** in the planar conformation.[3] Planarization of a more flexible ***c*-P$_{C8}$24** ring with DABCO (Figure 4.1) should require compensation with even less binding energy as compared to ***c*-P$_{C8}$12**. On the other hand, the higher flexibility of ***c*-P$_{C8}$24** may

disfavour sandwich formation due to a higher entropic barrier as compared to ***c*-P$_{C8}$12**.

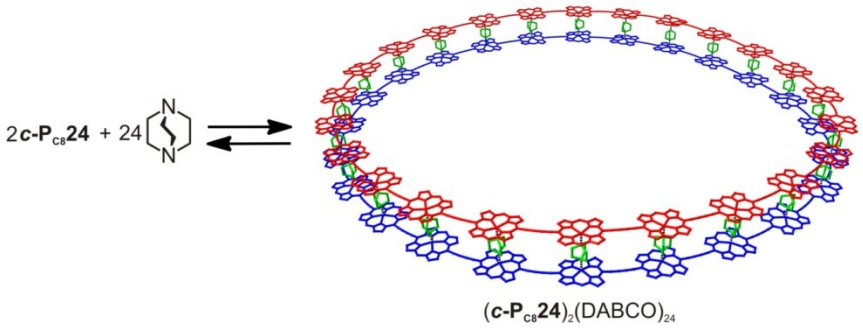

Figure 4.1. Formation of the sandwich complex (***c*-P$_{C8}$24**)$_2$•(DABCO)$_{24}$ by addition of DABCO to ***c*-P$_{C8}$24.** The molecular structure of the sandwich complex was calculated using the MM$^+$ force field (HyperChem^{TM}). Aryl side groups and hydrogen atoms are omitted for clarity.

According to the data of ^{1}H NMR titration, addition of the stoichiometric amount of DABCO to a solution of ***c*-P$_{C8}$24** in $CDCl_3$ leads to formation of a similar complex to that which was observed in the case of ***c*-P$_{C8}$12** (Figure 4.2).[3,12] Formation of (***c*-P$_{C8}$24**)$_2$•(DABCO)$_{24}$ is in slow exchange on the ^{1}H NMR timescale and the complex exhibits the expected singlet at -4.1 ppm, due to DABCO molecules sandwiched between two porphyrin units. The inequivalence between the two faces of the porphyrins is evident from splitting in the *ortho*-protons of the *meso*-aryl substituents, but the inequivalence between the inner and outer rims of the nanorings is unresolved, in contrast to (***c*-P$_{C8}$12**)$_2$•(DABCO)$_{12}$, probably because the ring is so large that the environments of its inside and outside rims are similar.[3,12]

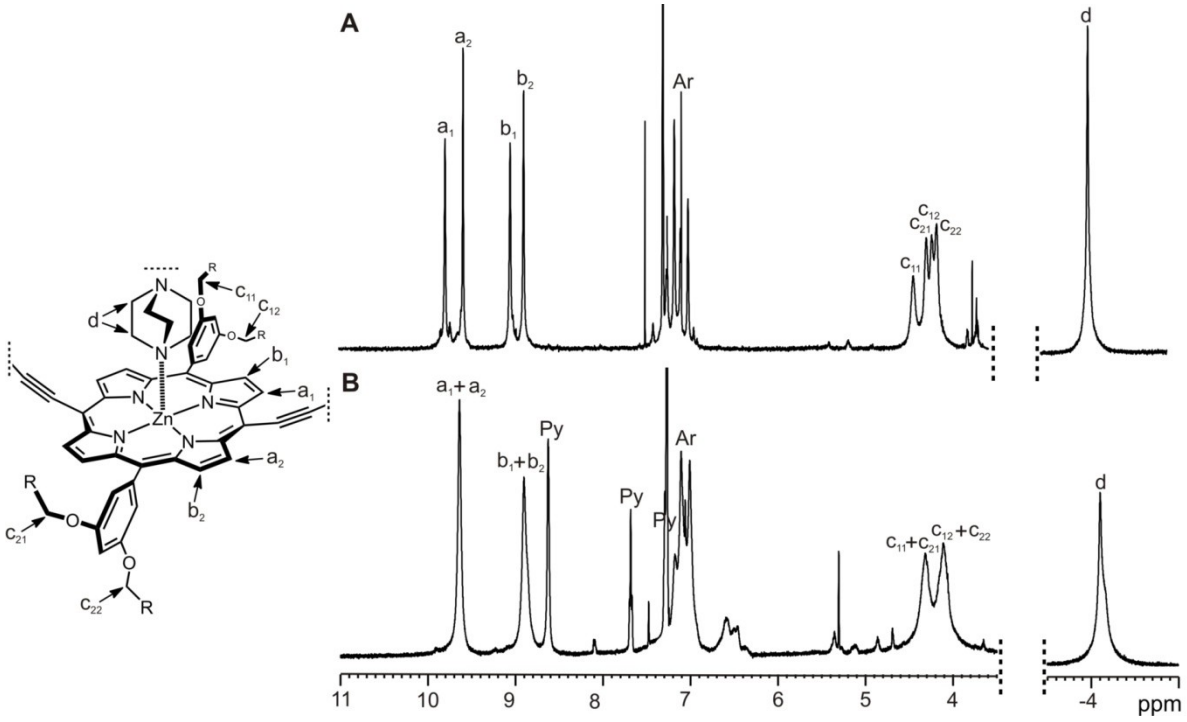

Figure 4.2. (a) ^{1}H-NMR of (***c*-P$_{C8}$12**)$_2$•(DABCO)$_{12}$[3] and (b) (***c*-P$_{C8}$24**)$_2$•(DABCO)$_{24}$ in $CDCl_3$ at 298 K, 500 MHz. The assignments of peaks are shown. The stoichiometric amount (12 eqv of DABCO) was added. Signals of pyridine are from the pyridine added initially to prevent aggregation.

UV-*vis*-IR titration of ***c*-P$_{C8}$24** with DABCO confirms formation of a very stable 2:24 sandwich complex (Figure 4.3a,c). It gives an end-point after addition of 12 equivalents of DABCO (Figure 4.3c). Similar clear-cut end point, but after addition of 6 equivalents of DABCO, was observed in the case of titration ***c*-P$_{C8}$12** with DABCO (Figure 4.3d). As in the case of ***c*-P$_{C8}$12**, addition of a large excess of DABCO to the complex causes its disassembly into two single-strand rings. The spectral changes associated with formation of (***c*-P$_{C8}$24)$_2$•(DABCO)$_{24}$ are similar to those for formation of (***c*-P$_{C8}$12)$_2$•(DABCO)$_{12}$, (Figure 4.3b) however the peak for (***c*-P$_{C8}$24)$_2$•(DABCO)$_{24}$ at λ_{max} = 864 nm is red-shifted compared with that of (***c*-P$_{C8}$12)$_2$•(DABCO)$_{12}$ at λ_{max} = 850 nm, reflecting the greater π-conjugation in the larger ring. The absorption band of (***c*-P24)$_2$•(DABCO)$_{24}$ is also broader, indicating that the larger nanoring is more flexible.

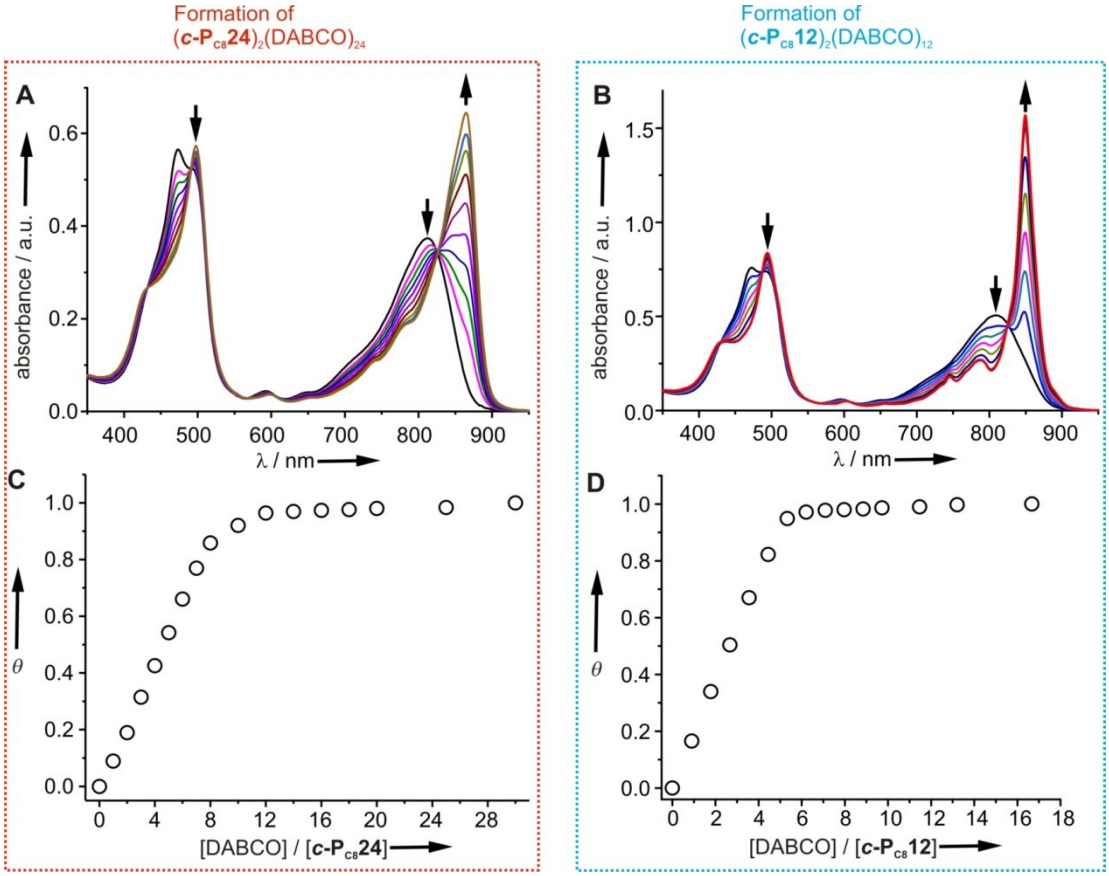

Figure 4.3. UV-*vis*-NIR titration of DABCO into solution of (a) ***c*-P$_{C8}$24** (0.54 μM in $CHCl_3$ at 298 K) and (b) ***c*-P$_{C8}$12** (0.69 μM in $CHCl_3$ at 298 K) . Black arrows indicate the spectral change with increasing DABCO concentration. The mole fraction of (c) (***c*-P$_{C8}$24)$_2$•(DABCO)$_{24}$ (%, from absorption data at 865 nm) and (d) (***c*-P$_{C8}$12)$_2$•(DABCO)$_{12}$ (%, from absorption data at 850 nm) plotted against the molar ratio of DABCO to the ring (***c*-P$_{C8}$24** or ***c*-P$_{C8}$12**) in the cuvette (black circles). The data for (***c*-P$_{C8}$12)$_2$•(DABCO)$_{12}$ were recorded and analysed by Dr. Johannes Sprafke.[3] All spectra were recorded in the presence of a low concentration of pyridine (2.0×10^{-3} M in the case of ***c*-P$_{C8}$24** and 6.1×10^{-4} M in the case of ***c*-P$_{C8}$12**) to prevent aggregation.

Similarly to (*c*-P$_{C8}$12)$_2$·(DABCO)$_{12}$,[3,12] the break-up experiments using the thermodynamic cycle in Figure 4.4 allow one to determine the number of binding sites involved in formation of (*c*-P$_{C8}$24)$_2$·(DABCO)$_{24}$, to assess the cooperativity of the process. The almost isosbestic behavior (Figure 4.5a) and the sharp, sigmoidal denaturation curve (Figure 4.5b) suggest a two-state

equilibrium between (***c*-P$_{C8}$24**)$_2$•(DABCO)$_{24}$ and (***c*-P$_{C8}$24)**•(DABCO)$_{24}$. Equation 4.1 shows how the mole fraction of the complex formed can be deduced from this cycle, where N is the number of binding sites (24), K_b is the denaturation equilibration constant, $[A]_0$ is the total concentration of ***c*-P$_{C8}$24** and $[B]_0$ is the total concentration of DABCO.[3,12] When deriving equitation 4.1 it is assumed that $[B]=[B]_0$ and any other possible intermediates are not significantly populated.

$$\theta = \frac{-K_b[B]_0^N + \sqrt{K_b^2[B]_0^{2N} + 8K_b[B]_0^N[A]_0}}{4[A]_0} \qquad (4.1)$$

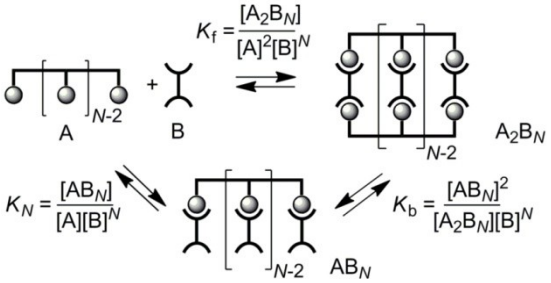

Figure 4.4. Generic thermodynamic cycle for the formation of double-strand complexes using a bidentate linker. In the case of (***c*-P$_{C8}$24**)$_2$·(DABCO)$_{24}$, A is a porphyrin oligomer with N binding sites and B is DABCO.[3,12]

Fitting the experimental data from the break-up titration to Equation 4.1 using Origin 8.1 "non-linear curve fit" function (assuming that $[B]_0 = [B]$ and $[A]_0 = 0.2$ μm) reveals that the best fit could be achieved when assuming N = 16-18 (Figure 4.5), suggesting less cooperativity involved in the formation of a sandwich complex by ***c*-P$_{C8}$24** compared to ***c*-P$_{C8}$12**.

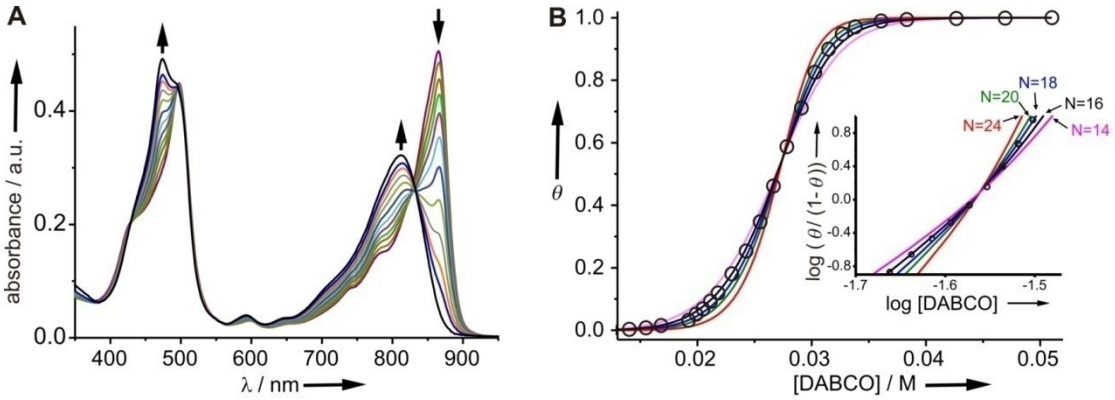

Figure 4.5. UV-*vis*-IR titration of DABCO into (***c*-P$_{C8}$24**)$_2$•(DABCO)$_{24}$ (c = 0.2 μM, $CHCl_3$, 298 K). (a) Absorption spectra over the course of the titration. Arrows indicate changes on addition of DABCO. (b) Mole fraction of single-strand (***c*-P$_{C8}$24)**•(DABCO)$_{24}$ (θ) derived from the absorption at 864 nm (black dots), fitted to the calculated curves for N = 14 (pink line), 16 (black line), 18 (blue line), 20 (green line) and 24 (red line) binding sites. The inset shows the Hill plot with fits for the same values of N.

The denaturation of ***c*-P$_{C8}$24**)$_2$•(DABCO)$_{24}$ is extremely cooperative, with a Hill coefficient of n_H = 11.7 and a switching window of c_R = 1.5.[17] The switching window, c_R, is defined as the factorial increase in ligand concentration required to change the bound/free ratio from 1:10 to 10:1. Compared with denaturation of (***c*-P$_{C8}$24)**•(DABCO)$_{24}$, denaturation of (***c*-P$_{C8}$12)**•(DABCO)$_{12}$ is less cooperative, giving a Hill coefficient of n_H = 9.5 and a switching widow of c_R = 1.8. The cooperativity of formation

of (***c*-P$_{C8}$24)**•(DABCO)$_{24}$ appears to be higher than that observed for any synthetic supramolecular system. However, as noted above, the cooperativity is not as high as would be expected for a two-state equilibrium with this stoichiometry. The simulated Hill coefficient for a process of the type shown in Figure 4.4 with $N = 24$ is $n_H = 15.9$, and the experimental value of 11.7 also correspond to an apparent number of binding sites of $N = 16–18$, as shown in Figure 4.5b. Thus denaturation of the (***c*-P$_{C8}$24)**$_2$•(DABCO)$_{24}$ complex appears to be not completely an all-or-nothing process, with some population of partially bound species leading to a broadening of the denaturation curve. The (***c*-P$_{C8}$12)**$_2$•(DABCO)$_{12}$ complex is also less stable that that based on ***c*-P$_{C8}$24**; the DABCO concentration required to achieve 50% denaturation is 5.8 mM, compared with 27 mM for (***c*-P$_{C8}$24)**$_2$•(DABCO)$_{24}$.

4.3 Solvent-Induced Aggregation of *c*-P$_{C8}$24

The idea of using non-covalent interactions to control the position of molecules in solution or on surfaces is not new and has been exploited for the formation of a wide variety of supramolecular networks with tailored dimensions, symmetry and functionality.[18-22] It was previously well established by Anderson that under some solvent conditions linear porphyrin dimer spontaneously self-assembles into a stable bimolecular aggregate (see Figure 1.7 of Chapter 1) as confirmed by the data of ^{1}H NMR and UV-*vis*-IR spectroscopies.[13] Most recently, aggregation of butadiyne-linked zinc porphyrin tetramer ***l*-P$_{C8}$4$_{THS,THS}$** was studied by Anderson and Hutin.[15] It was shown by combination of NMR, UV and SAXS data analysis, that ***l*-P$_{C8}$4$_{THS,THS}$** forms remarkably well-defined aggregate, consisting of exactly three molecules, in a parallel stacked arrangement (in chloroform and toluene at r.t.; concentration 1 mM–0.1 μM) (Figure 4.6). This geometry maximizes van der Waals contact between the porphyrins,[16] while avoiding clashes between side chains. The need for interdigitation of the sidechains of ***l*-P$_{C8}$4$_{THS,THS}$** prevents formation of stacks consisting of more than three layers (Figure 4.6). Although a detailed analysis has only been carried out for one compound (***l*-P$_{C8}$4$_{THS,THS}$**), comparison with the NMR spectra of other longer oligomers indicated that they also form similar three-layer stacks. In all cases, aggregation can be prevented by addition of pyridine, although at low pyridine concentrations, disaggregation takes many hours to reach equilibrium. It was assumed that this non-covalent approach to rigidification using π-π interaction between porphyrin surfaces should also be applicable to porphyrin nanorings such as ***c*-P$_{C8}$24**.

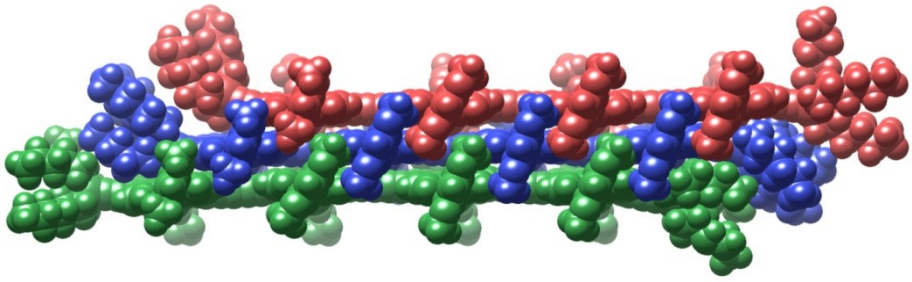

Figure 4.6. Calculated (MM+ force field, HyperChem™) molecular model of the (***l*-P$_{C8}$4$_{THS,THS}$)$_3$** aggregate (with octyloxy sidechains replaced by methoxy groups for clarity). Reprinted from ref. 15.

Initially formation of aggregates of ***c*-P$_{C8}$24** was probed in solution using non-coordinating solvents such as toluene and $CHCl_3$ in the absence of pyridine. ^{1}H NMR spectra of solutions of ***c*-P$_{C8}$24** in $CDCl_3$ are inconclusive and contain only broad peaks. Due to the extremely low solubility of ***c*-P$_{C8}$24** in the absence of pyridine, it was not impossible to perform SAXS analysis of its aggregates. UV-*vis*-NIR titrations of solution ***c*-P$_{C8}$24** in toluene with pyridine show that the Q-band shifts to shorter wavelengths (from 850 to 820 nm) and that the B-band becomes narrower (at around 480 nm) on addition of pyridine (Figure 4.7); both these spectral changes indicate that pyridine causes dissociation of stacked aggregates.[13,23] The spectra in Figure 4.7 were acquired with an equilibration time of 1 hour after each addition of pyridine, however even with this long delay, the system did not completely reach equilibrium during the early stages of the titration. The slow kinetics is another indication of a disaggregation process because coordination of pyridine to a zinc porphyrin is normally very rapid.

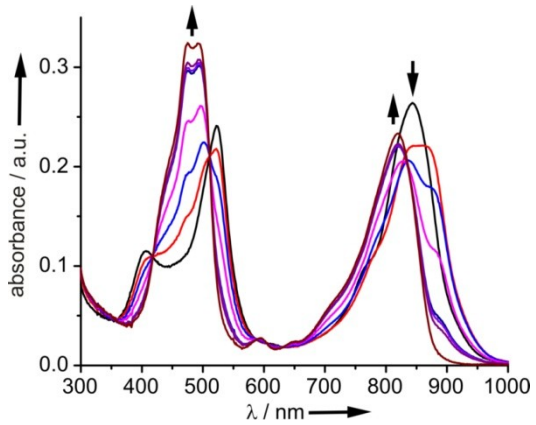

Figure 4.7. UV-*vis*-NIR absorption spectra of ***c*-P$_{C8}$24** in toluene at increasing concentrations of pyridine (concentration: 0 to 7 mM). Spectra recorded at 298 K in a 1 cm quartz cuvette with a 1 hour equilibration delay after addition of each aliquot of pyridine.

Structure of aggregates of ***c*-P$_{C8}$24** was investigated by STM in collaboration with Simon Svatek, Dr. Luis Perdigao, Dr. James O'Shea and Prof. Peter Beton at the University of Nottingham, UK.[24] The aggregates of ***c*-P$_{C8}$24** were deposited on a Au (111) using electrospray under ultra high vacuum (UHV). This technique permits the direct transfer of large molecules which are not compatible with sublimation from solution into an ultra-high vacuum.

Figure 4.8a shows an STM image following the deposition of ***c*-P$_{C8}$24** from the toluene/MeOH (3:1) solvent mixtures containing 5% pyridine. Under these conditions no aggregates are expected to form. The 24 individual porphyrin units are clearly resolved (see inset to Figure 4.8a) and, in common with nearly all adsorbed ***c*-P$_{C8}$24** at low coverage, the adsorption occurs preferentially with the nanoring overlapping one or more step edges on the Au(111) surface. The topographic height (typically 0.1 nm) and uniformity of contrast of the nanorings indicate that the porphyrin units are adsorbed parallel to the surface, although some distortion of the porphyrin macrocycle cannot be ruled

out from these images. The conformation for ***c*-P$_{C8}$24** shows a significant deviation from a circular shape; for example the nanoring in Figure 4.8a inset has long and short axes equal to 12 nm and 7 nm respectively. This flexibility is similar to that of linear porphyrin oligomers (average lengths ~ 50nm) which exhibit bending with a radius of curvature as small as 1.3 nm, equivalent to a 180° degree turn over a circumference of ~ 3 porphyrin repeat units.[25]

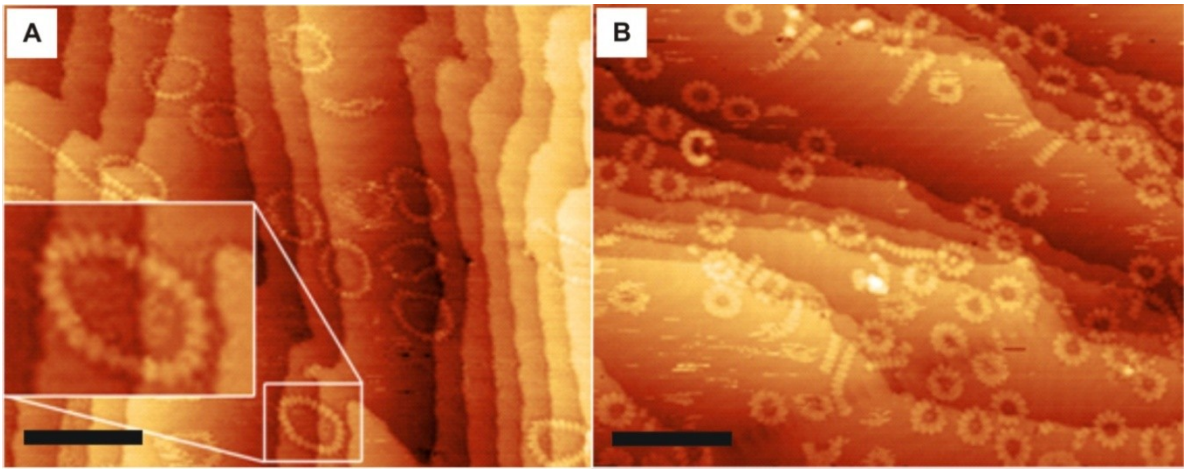

Figure 4.8. (a) ***c*-P$_{C8}$24** on a Au(111) deposited from the toluene/MeOH (3:1) solvent mixtures containing 5% pyridine. (b) ***c*-P$_{C8}$12** on Au(111) deposited from the toluene/MeOH (3:1) solvent mixtures. Scale bar is 20 nm. All images acquired and all figures are made by S. Svatek and Dr. L. Perdigao and reprinted from ref. 24.

The surface topography is significantly different if the ***c*-P$_{C8}$24** is deposited without the addition of pyridine to the toluene/methanol mixture (see Figure 4.9). In this case, formation of nanorings of various heights is observed such as 0.1 nm and 0.8 nm respectively for the left and right nanoring in Figure 4.9a. Nonetheless, in the latter case 24 porphyrin sub-units may still be resolved. Large area images (Figure 4.9c) also show the presence of many rings with different heights and also many which are partially overlapping.

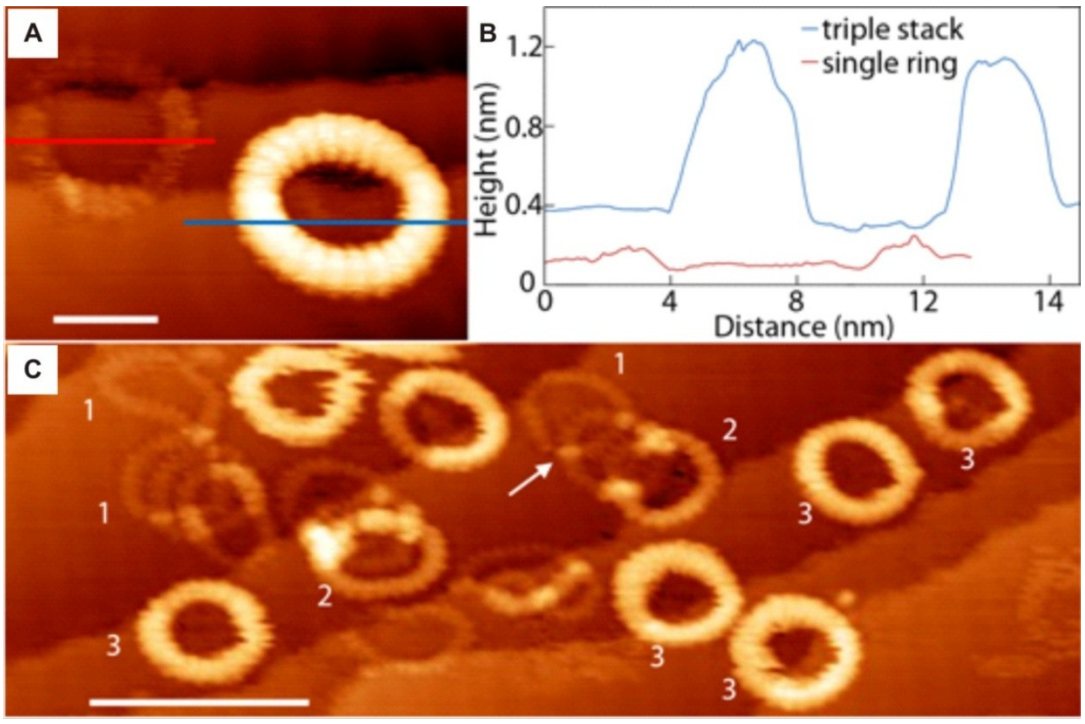

Figure 4.9. (a) STM images of a single (left) and stacked (right) porphyrin nanoring ***c*-P$_{C8}$24** deposited on a Au(111) from the toluene/MeOH (3:1) solvent mixtures. Scale bar is 6 nm. (b) Height profile of the blue and red marked traces shows the different ring heights. (c) Larger area shows different ring heights for triple (3), double (2) and single (1) rings. Scale bar is 20 nm. All images acquired and all figures are made by S. Svatek and Dr. L. Perdigao and reprinted from ref. 24.

A histogram (Figure 4.10a) shows that nanoring heights are clustered around discrete values, and the higher features were therefore ascribed to stacks of two and three nanorings. When images of ***c*-P$_{C8}$24** were acquired using a solution with added THF (5%), the distribution of species changed and the relevant histogram is also shown in Figure 4.10a. Heights are clustered at similar values, although in this case formation of a structure with apparent height of 1.1 nm, corresponding to four layers is observed. In Figure 4.10b the histogram peak position is plotted *vs* peak number and is found to be linear with a gradient, corresponding to the layer spacing in the stacks, of 0.32 ± 0.04 nm. This value is consistent with parallel alignment of porphyrin groups and stabilization of the stacked nanorings by π–π interactions.[16]

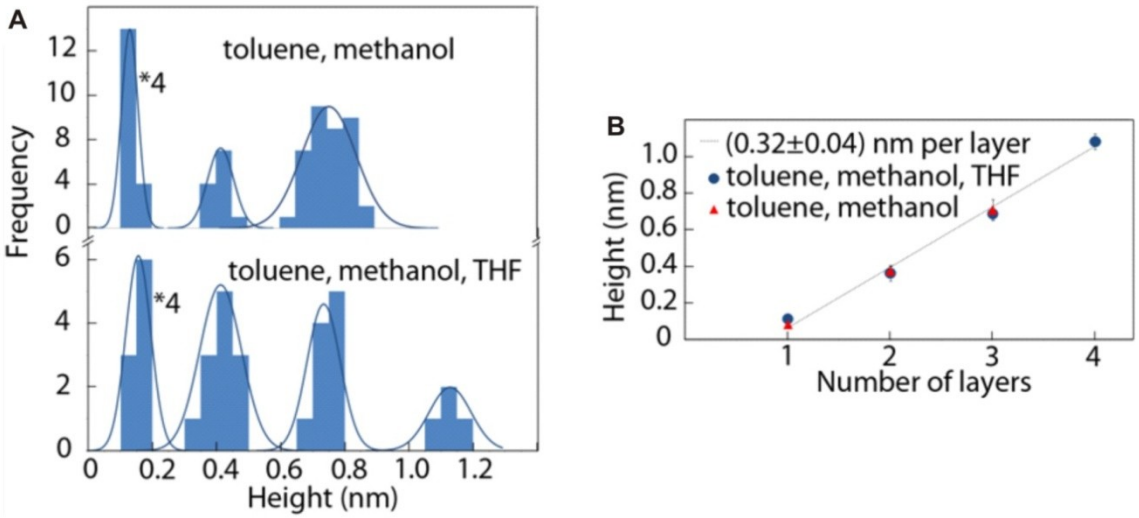

Figure 4.10. (a) Histogram of the heights of ***c*-P$_{C8}$24** stacks deposited from different solvent combinations. Groups around discrete numbers are associated with the number of rings per stack. The peaks for heights <0.2 nm have been scaled down (by a factor of 4) for clarity. (b) The peak position in the histogram *vs* the peak number. Both figures are made by S. Svatek and Dr. L. Perdigao and reprinted from ref. 24.

Also present on the surface are partially overlapping nanorings (see Figure 4.9c and Figure 4.11a). The height of two overlapping single rings (see Figure 4.11b) is 0.40 nm and is consistent with the observation of two stacked rings. Also, the bright overlapping region between the single and the double ring is consistent with the measured ring height of a triple stack.

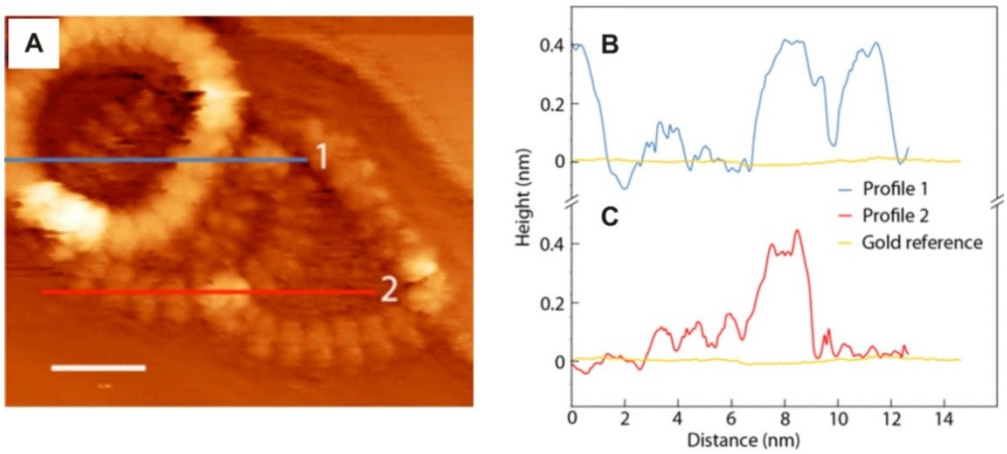

Figure 4.11. (a) Overlapping arrangement of one double ring (left) and two single rings. Scale bar length is 5 nm. (b,c) The height profiles indicate that a double stacked ring is consistent with two overlapping single rings. All images acquired and all figures are made by S. Svatek and Dr. L. Perdigao and reprinted from ref. 24.

The dependence on solvent indicates that the columnar stacks are formed prior to deposition on the surface. The formation of such stacks through alternative mechanisms where rings are adsorbed as monomers and then undergo organizational changes leading to the observed structures are highly unlikely and would not be expected to have a dependence on solvent. Furthermore the stacked nanorings are, like the single layers, found to be preferentially adsorbed at step edges indicating that these complex aggregates can diffuse intact across the surface following adsorption.

For comparison, the Figure 4.8b shows an STM image of ***c*-P$_{C8}$12**. In this case, however, the deposition was performed from the toluene/MeOH (3:1) solvent mixtures with no presence of pyridine which should promote the formation of aggregates. Nonetheless, no signs of aggregated of ***c*-P$_{C8}$12** were found in this case. As in the case of ***c*-P$_{C8}$24, *c*-P$_{C8}$12** preferentially adsorbs at Au terrace steps. However, in the case of ***c*-P$_{C8}$12** deviation from a circular shape is much reduced, as compared with ***c*-P$_{C8}$24**. Similar to ***c*-P$_{C8}$12**, no signs of aggregates were found when electrospraying solutions of ***c*-P$_{C8}$16** and ***c*-P$_{C8}$18** under the same conditions. This may be due to higher energy barrier required to planarize the smaller macrocycles or problems with distribution of solubilizing side groups in them.

The stacked nanorings in Figure 4.9 have a shape which is closer to circular than the single height rings. The deviation from circularity is characterized by the parameter $g = a/b - 1$, where a and b are, respectively, the long and short axes of a nanoring. For an ellipse g is related to the flattening factor, f ($g = fb/a$) and for a circle $g = 0$. For ***c*-P$_{C8}$24** there is a systematic dependence of g on stack height with a mean value, $\bar{g}$ = 0.55 ± 0.05 for a single layer, a lower value for a double layer, 0.31 ± 0.08, while for triple layers $\bar{g}$ = 0.28 ± 0.03. For comparison $\bar{g}$ = 0.27 ± 0.02 for single layers of ***c*-P$_{C8}$12**. The reduction in the value of g in the case of ***c*-P$_{C8}$24** implies an increased mechanical stiffness of the nanoring as the number of stacked rings is increased.

The histogram in Figure 4.10 implies that a stack of three nanorings (height 0.7 nm) is particularly stable. For a simple aggregation of nanorings a monotonic decrease in the frequency of occurrence for stacks with increasing layer numbers would be expected. However in the absence of THF the three-

layer stacks seem to be much more frequently observed than the two layer stacks, while for added THF the frequencies are approximately equal. In addition no four component stacks are observed in the absence of THF and a very small fraction are observed when THF is added. This implies that the three layer stack has enhanced stability. Although the mechanism for this enhancement is unclear at this stage, it may be associated with steric effects arising from the packing of the solubilizing side groups as in the case of ***l*-$\mathbf{P_{C8}4_{THS,THS}}$**.[15] However, it was not possible to image those aggregates on the Au(111) surface.

4.4 Conclusions and Outlook

The 10 nm diameter of ***c*-$\mathbf{P_{C8}}$24**, comparable in size to some enzymes, results in increased flexibility which can adversely affect its properties, for example, through disrupting full conjugation. However, supramolecular chemistry provides effective tools to mechanically stiffen ***c*-$\mathbf{P_{C8}}$24** using the power of collective metal-ligand or π-π interactions.

This chapter illustrates that, similar to 12-porphyrin nanoring ***c*-$\mathbf{P_{C8}}$12**, ***c*-$\mathbf{P_{C8}}$24** can be locked into a planar conjugated tertiary structure by formation of the (***c*-$\mathbf{P_{C8}}$24**)$_2$•(DABCO)$_{24}$ sandwich complex. The formation of this structure has been confirmed by means of ^{1}H NMR and UV-*vis*-NIR. The sandwich complex based on ***c*-$\mathbf{P_{C8}}$24** is less rigid compared to that based on ***c*-$\mathbf{P_{C8}}$12**. The formation of (***c*-$\mathbf{P_{C8}}$24**)$_2$•(DABCO)$_{24}$ possesses the highest cooperativity reported to date, as quantified by the extremely large Hill coefficient (n_H = 11.7). However, the cooperativity is not as high as would be expected for a two-state equilibrium with 2:24 stoichiometry (expected Hill coefficient n_H = 15.9).

Alternatively, this chapter demonstrates that π-π interaction between porphyrin subunits may be used to control the shape of ***c*-$\mathbf{P_{C8}}$24** by forming shape-persistent stacked columns. Although no conclusive information about the structure of such aggregates can be obtained in solution, they can be successfully transferred to the Au (111) surface using electrospray and analysed by STM. The choice of solvent affects the structure and distribution of aggregates and thus confirms that these aggregates form in the solution prior to deposition. The largest aggregate observed has a molecular weight >100 kDa, comparable with large protein molecules. The π-π stacking results in an increase in the bending stiffness of ***c*-$\mathbf{P_{C8}}$24** and a transition to a near circular shape. These results provide an analogue of the conformational control afforded by tertiary structure and self-assembly in biopolymers. In addition, a stack of three ***c*-$\mathbf{P_{C8}}$24** molecules demonstrate a particular stability which may originate from the favourable packing of the solubilizing side groups. Interestingly, it has proved impossible to confirm formation of similar aggregates in the case of ***c*-$\mathbf{P_{C8}}$12**, ***c*-$\mathbf{P_{C8}}$16**, and ***c*-$\mathbf{P_{C8}}$18** which suggests existence of a critical size of these macrocycles necessary to form aggregates on the Au (111) surface.

Previous work on linear porphyrin-based molecular wires suggest that the formation of supramolecular stacks can facilitate charge transport by enhancing electronic coupling, creating a narrower distribution of electronic states along the chain[26,27] and, due to an extended π conjugation, hold promise for the exploration of Aharonov–Bohm effects at the molecular level.[1,28]

4.5 References

[1] M. Mayor, C. Didschies, *Angew. Chem., Int. Ed.* **2003**, *42*, 3176–3179.

[2] J. K. Sprafke, D. V. Kondratuk, M. Wykes, A. L. Thompson, M. Hoffmann, R. Drevinskas, W. H. Chen, C. K. Yong, J. Kärnbratt,J. E. Bullock, M. Malfois, M. R. Wasielewski, B. Albinsson, L. M. Herz, D. Zigmantas, D. Beljonne, H. L. Anderson, *J. Am. Chem. Soc.* **2011**, *133*, 17262–17273.

[3] J. K. Sprafke, *Supramolecular Control of Synthesis and Electronic Structure of Porphyrin Oligomers*, D.Phil. thesis, University of Oxford, Oxford, **2011**.

[4] O. Varnavski, P. Bäuerle, T. Goodson III, *Opt. Lett.* **2007**, *32*, 3083–3085.

[5] F. Zhang, G. Götz, H. D. F. Winkler, C. A. Schalley, P. Bäuerle, *Angew. Chem., Int. Ed.* **2009**, *48*, 6632–6635.

[6] T. Kawase, K. Tanaka, H. R. Darabi, M. Oda, *Angew . Chem., Int . Ed.* **2003**, *42*, 1624–1628.

[7] E. Mena-Osteritz, P. Bäuerle, *Adv. Mater.* **2006**,*18*, 447–451.

[8] T. Iwamoto, Y. Watanabe, T. Sadahiro, T. Haino, S. Yamago, *Angew. Chem., Int. Ed.* **2011**, 123, 8492–8494.

[9] M. C. O'Sullivan, J. K. Sprafke, D. V. Kondratuk, C. Rinfray, T. D. W. Claridge, A. Saywell, M. O. Blunt, J. N. O'Shea, P. H. Beton, M. Malfois, H. L. Anderson, *Nature* **2011**, *469*, 72–75.

[10] T. Iwamoto**,** Y. Watanabe**,** Y. Sakamoto**,** T. Suzuki**,** S. Yamago**,** *J. Am. Chem. Soc.* **2011**, *133*, 8354–8361.

[11] B. M. Wong, *J. Phys. Chem. C.* **2009**, *113*, 21921–21927.

[12] J. K. Sprafke, B. Odell, T. D. W. Claridge, H. L. Anderson, *Angew. Chem., Int. Ed.* **2011**, *50*, 5572–5575.

[13] H. L. Anderson, *Inorg. Chem.* **1994**, *33*, 972–981.

[14] P. N. Taylor, H. L. Anderson, *J. Am. Chem. Soc.* **1999**, *121*, 11538–11545.

[15] M. Hutin, J. K. Sprafke, B. Odell, H. L. Anderson, T. D. W. Claridge, *J. Am. Chem. Soc.* **2013**, /10.1021/ja406015r.

[16] C. A. Hunter, J. K. M. Sanders, *J. Am. Chem. Soc.* **1990**, *112*, 5525–5535.

[17] C. A. Hunter, H. L. Anderson, *Angew. Chem. Int. Ed.* **2009**, *48*, 7488–7499.

[18] L. Bartels, *Nat.Chem.* **2010**, *2*, 87–95.

[19] J. V. Barth, G. Costantini, K. Kern, *Nature* **2005**, *437*, 671–679.

[20] T. Kudernac, S. Lei, J. A.A.W. Elemans, S. De Feyter, *Chem. Soc. Rev.* **2009**, *38*, 402–421.

[21] R. Chakrabarty, P. S. Mukherjee, P. J. Stang, *Chem. Rev.* **2011**, *111*, 6810–6918.

[22] F. J. M. Hoeben, P. Jonkheijm, R. Lazzaroni, F. C. DeSchryver, E. W. Meijer, A. P. H. J. Schenning, *Chem. Rev.* **2005**, *105*, 1491–1546.

[23] T. E. O. Screen, J. R. G. Thorne, R. G. Denning, D. G. Bucknall, H. L. Anderson, *J. Mater. Chem.* **2003**, *13*, 2796–2808.

[24] S. A. Svatek, L. M. A. Perdigão, A. Stannard, M. B. Wieland, D. V. Kondratuk, H. L. Anderson, J. N. O'Shea, P. H. Beton, *Nano Lett.* **2013**, *13*, 3391–3395.

[25] A. Saywell, J. K. Sprafke, L. J. Esdaile, A. J. Britton, A. Rienzo, H. L. Anderson, J. N. O'Shea, P. H. Beton, *Angew. Chem. Int. Ed.* **2010**, *49*, 9136–9.

[26] A. A. Kocherzhenko, S. Patwardhan, F. C. Grozema, H. L. Anderson, L. D. A. Siebbeles, J. Am. Chem. Soc. **2009**, *131*, 5522–5529.

[27] F. C. Grozema, C. Houarner-Rassin, P. Prins, L. D. A. Siebbeles, H. L. Anderson, J. Am. Chem. Soc. **2007**, *129*, 13370–13371.

[28] N. Kleemans, I. Bominaar-Silkens, V. Fomin, V. Gladilin, D. Granados, A. Taboada, J. García, P. Offermans, U. Zeitler, P. Christianen, J. Maan, J. Devreese, P. Koenraad, Phys. Rev. Lett. **2007**, *99*, 146808–146811.

Chapter 5

Using Templates to Select Ring Size in the Synthesis of Cyclic Polymers: Targeting 30- and 40-Porphyrin Nanorings

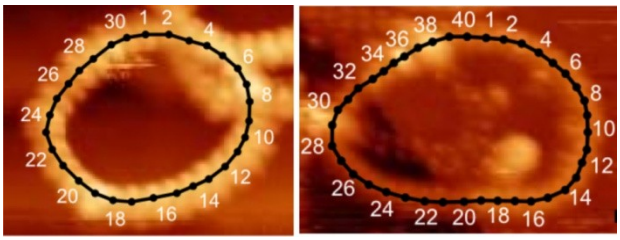

This chapter describes how, by using different templates, it is possible to direct the process of cyclooligomerization of linear porphyrin dimer and decamer towards formation of predominantly one product as opposed to uncontrolled template-free polymerizations. The isolated cyclic porphyrin oligomers (10, 20, 30, 40, 50) are investigated in detail by MALDI-ToF and STM imaging and are the biggest monodisperse macrocyclic systems synthesized to date with diameters of up to 21 nm.

5.1 Background

Chemists have invested considerable efforts into learning how to direct polymerization processes precisely and efficiently, nonetheless, the current state of the art in controlled polymer synthesis is far behind Nature's ability to tackle similar processes. Nature's approach relies on using DNA and RNA molecules as templates which, through weak interaction and molecular recognition of corresponding nucleic residues, translate structural information onto the biological polymer being made.[1,2] Although there have been numerous examples of applying template effects to realize the same principle in the synthesis of polymers in the laboratory (see Chapter 1), the possibility to perform such processes as precisely and efficiently as in Nature remains elusive.

The main distinctive feature of Nature's approach to the synthesis of biopolymers is that termination of polymer chain growth happens once the polymer chain *per se* reaches a certain length, as determined by the required sequence of monomer building blocks, favourable conformation *etc*. This bottom-up approach provides accurate control over polymerization and is exactly how, for example, the biosynthesis of proteins is performed in ribosome which stops elongation of the polypeptide chain once the mRNA stop codon is recognized.[1] The closest artificial analogue of such an approach is sequence-specific solid-phase polymer synthesis, which, despite its high monomer-resolved precision, does not find widespread use.[3] The more conventional approach to polymer chemistry is solution-phase bulk polymerization, where termination of chain growth occurs due to polymer-chain independent factors, such as the loss of reactivity of one of the ends of the growing chain or the full consumption of the starting monomer material.

Classical and Vernier templated synthesis provide a bottom-up digital control over polymer chain growth, similar to that in the ribosomal peptide synthesis, and use the length of the polymer chain as the trigger signal for termination of the chain growth. The templated synthesis of 6-, 8-, 12- and 24-porphyrin nanorings suggest that it is possible to address the size of the macrocycles formed by employing different templates. For example, if ***l*-P$_{t\text{-Bu}}$4** is coupled in the presence of **T8** it forms ***c*-P$_{t\text{-Bu}}$8**, but changing the template to **T6** will direct the cyclooligomerization towards formation of ***c*-P$_{t\text{-Bu}}$12** as the major product. By changing the template, it is possible to switch between classical and Vernier regimes of templating and affect the size of the cyclic oligomers being formed. However, the question remains about the scope of the Vernier approach itself at controlling the size of the rings. Is it possible to switch between different Vernier routes by changing the template, and how different should the templates be to observe this switching? How close to the ring size addressed does the monomer unit need to be (*e.g.* whether to couple ***l*-P$_{C8}$3** or ***l*-P$_{C8}$6** in the presence of **T8** to prepare ***c*-P$_{C8}$24**)? It is in the connection with these questions, that the couplings of ***l*-P$_{C8}$2**, ***l*-P$_{C8}$5** and ***l*-P$_{C8}$10** in the presence of **T5**, **T6** and **T8** templates are considered in this chapter.

5.2 Oligomerization of *l*-P_{C8}10

The coupling of the linear porphyrin decamer ***l*-P$_{C8}$10** in the presence of pentapyridyl template **T5**, hexapyridyl template **T6** and octapyridyl template **T8** should provide an easy access to cyclic porphyrin 10-mer ***c*-P$_{C8}$10**, cyclic porphyrin 30-mer ***c*-P$_{C8}$30** and cyclic porphyrin 40-mer ***c*-P$_{C8}$40**, respectively (Figure 5.1). All of these would be extremely challenging compounds to prepare without Vernier templating. In addition, the latter macrocycle (***c*-P$_{C8}$40**) beats the current size record for the biggest monodisperse macrocyclic structure which is the 32-porphyrin cyclic array described by Osuka.[4]

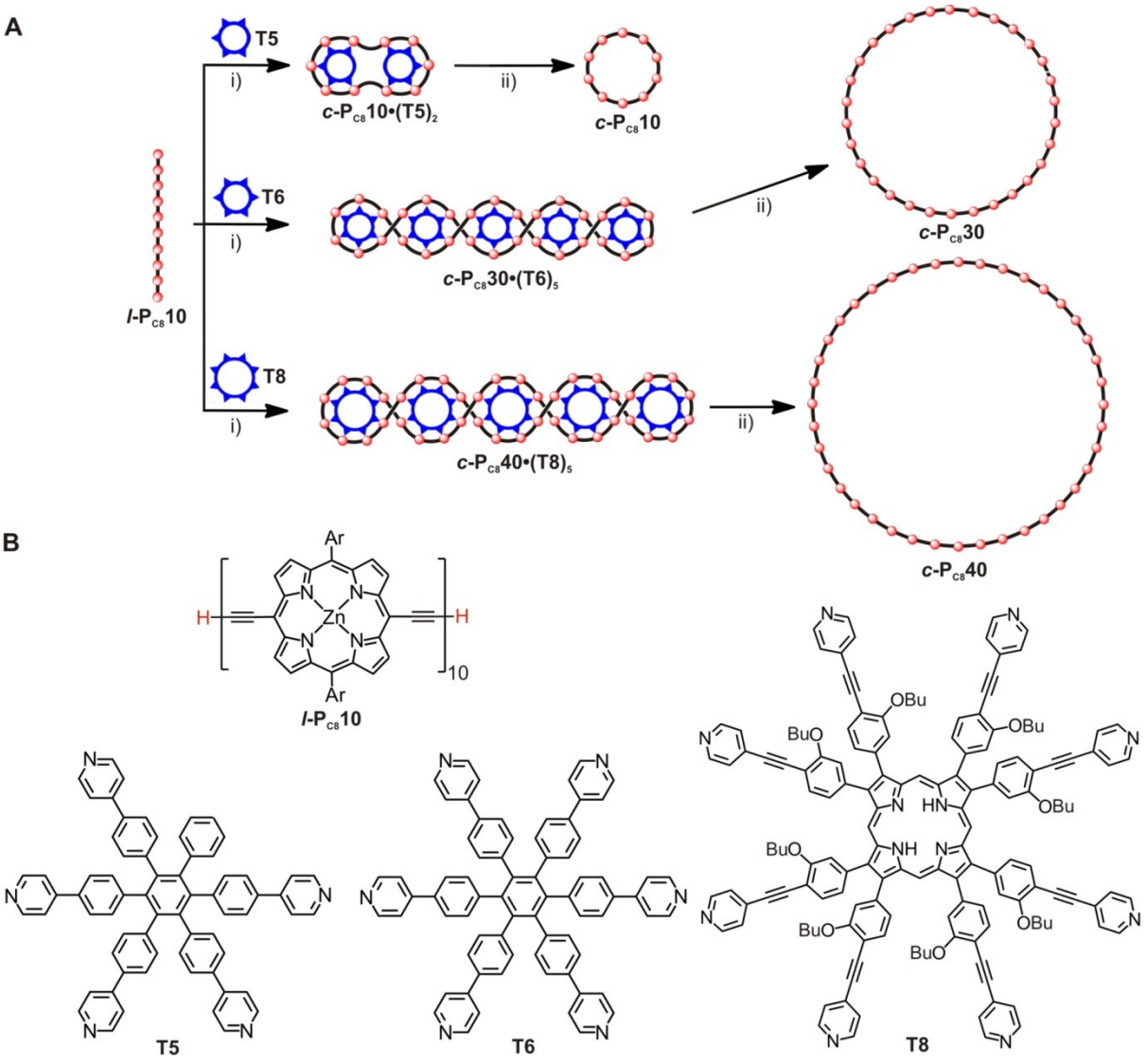

Figure 5.1. (a) Templated synthesis of the nanorings ***c*-P$_{C8}$10**, ***c*-P$_{C8}$30** and ***c*-P$_{C8}$40**. Reagents: i) $PdCl_2(PPh_3)_2$, CuI, 1,4-benzoquinone; ii) pyridine. (b) Structures of ***l*-P$_{C8}$10**, **T5**, **T6** and **T8**; Ar = 3,5-bis(octyloxy)phenyl.

Figure 5.1 shows that the cyclo-oligomerization of ***l*-P$_{C8}$10** in the presence of templates should occur through initial formation of corresponding templated complexes such as ***c*-P$_{C8}$10•(T5)$_2$**, ***c*-P$_{C8}$30•(T6)$_5$**, ***c*-P$_{C8}$40•(T8)$_5$**. As in the case of ***c*-P$_{C8}$24** synthesis (Chapter 3) only one stereoisomer of the template complexes ***c*-P$_{C8}$30•(T6)$_5$** and ***c*-P$_{C8}$40•(T8)$_5$** is shown in Figure 5.1, however

formation of various stereoisomers is expected. Removal of the template from those different stereoisomers will convert them into the same ***c*-P$_{C8}$30** and ***c*-P$_{C8}$40** open rings.

Palladium-catalyzed oxidative coupling of the linear porphyrin octamer ***l*-P$_{C8}$10** in the absence of any template gives only a mixture of linear polymeric materials of high molecular weight, as seen from the analysis of the coupling reaction mixtures using analytical gel permeation chromatography (Figure 5.2a). Using JAIGEL columns (Japan Analytical Industry Co., Ltd.), it has become possible to analyse the mixtures of high molecular weight polymers by gel permeation chromatorgraphy; the Plgel columns (Polymer Laboratories Ltd.) used before only allowed us to analyse cyclic porphyrin oligomers of up to 50-60 porphyrin units, apparently due to higher tendency of linear materials to aggregate. The analysis of the reaction mixtures of the template-free polymerization of ***l*-P$_{C8}$10** performed in the solvents used before for coupling ($CHCl_3$ and toluene) revealed that in $CHCl_3$ the degree of polymerization of ***l*-P$_{C8}$10** is significantly higher as compared to toluene. In addition, under such reaction conditions it was possible to achieve almost full consumption of the starting ***l*-P$_{C8}$10**. As such, in all further cases, $CHCl_3$ was used as a reaction medium to minimize the amount of linear oligomers formed.

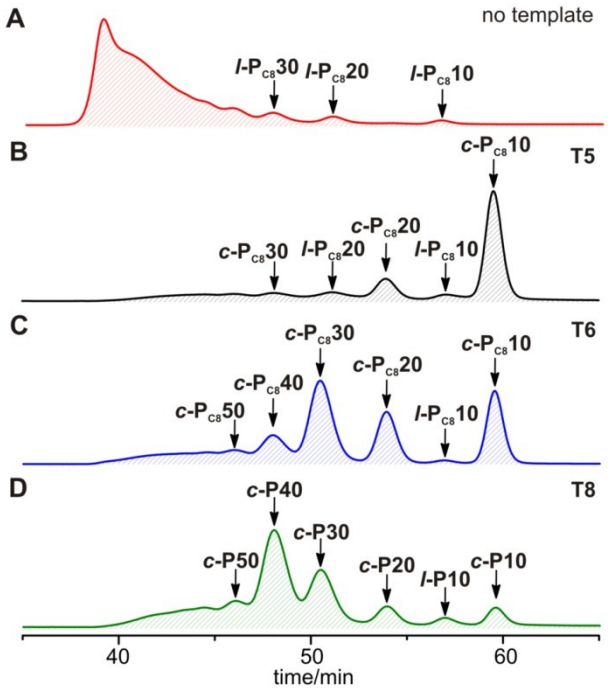

Figure 5.2. Analytical GPC traces (JAIGEL columns, toluene/1% pyridine, detection at 500 nm) of the crude reaction mixtures of coupling (in $CHCl_3$) ***l*-P$_{C8}$10** (a) without or in the presence of (b) **T5**, (c) **T6** or (d) **T8**. The catalysts and 1,4-benzoquinone were removed by passing a sample of the reaction mixture through a short size-exclusion column in $CHCl_3$/10% pyridine as eluent prior to GPC analysis.

Coupling of ***l*-P$_{C8}$10** in the presence of the pentapyridyl template **T5** in mole ratio ***l*-P$_{C8}$10/T5** = 2:1 gives a cyclic porphyrin 10-mer ***c*-P$_{C8}$10** as a major product with formation of trace amounts of cyclic porphyrin 20-mer ***c*-P$_{C8}$20** (Figure 5.2b).

Performing coupling of ***l*-P$_{C8}$10** in the presence of hexapyridyl template **T6**, having one additional pyridyl binding site as compared to **T5**, drastically changes the distribution of species formed in the

course of coupling process and shifts products distribution towards high molecular weight products (Figure 5.2c). The main product formed is the expected cyclic porphyrin 30-mer ***c*-P$_{C8}$30** (34% analytical yield), however other minor products such as cyclic porphyrin 10-mer ***c*-P$_{C8}$10**, 20-mer ***c*-P$_{C8}$20**, 40-mer ***c*-P$_{C8}$40** and 50-mer ***c*-P$_{C8}$50** are formed (Figure 5.2c), which can be easily separated by the recycling GPC (Figure 5.3a). As in the case of ***c*-P$_{C8}$24** ring synthesis, the mole ratio between the rings depends on the amount of **T6** in the reaction mixture. Increasing the amounts of **T6** shifts the reaction towards formation of lower molecular weight products; in contrast use of stoichiometric or slightly sub-stoichiometric amounts of template (mole ratio **T6**/***l*-P$_{C8}$10**<5/3) shifts the reaction towards formation of ***c*-P$_{C8}$30**.

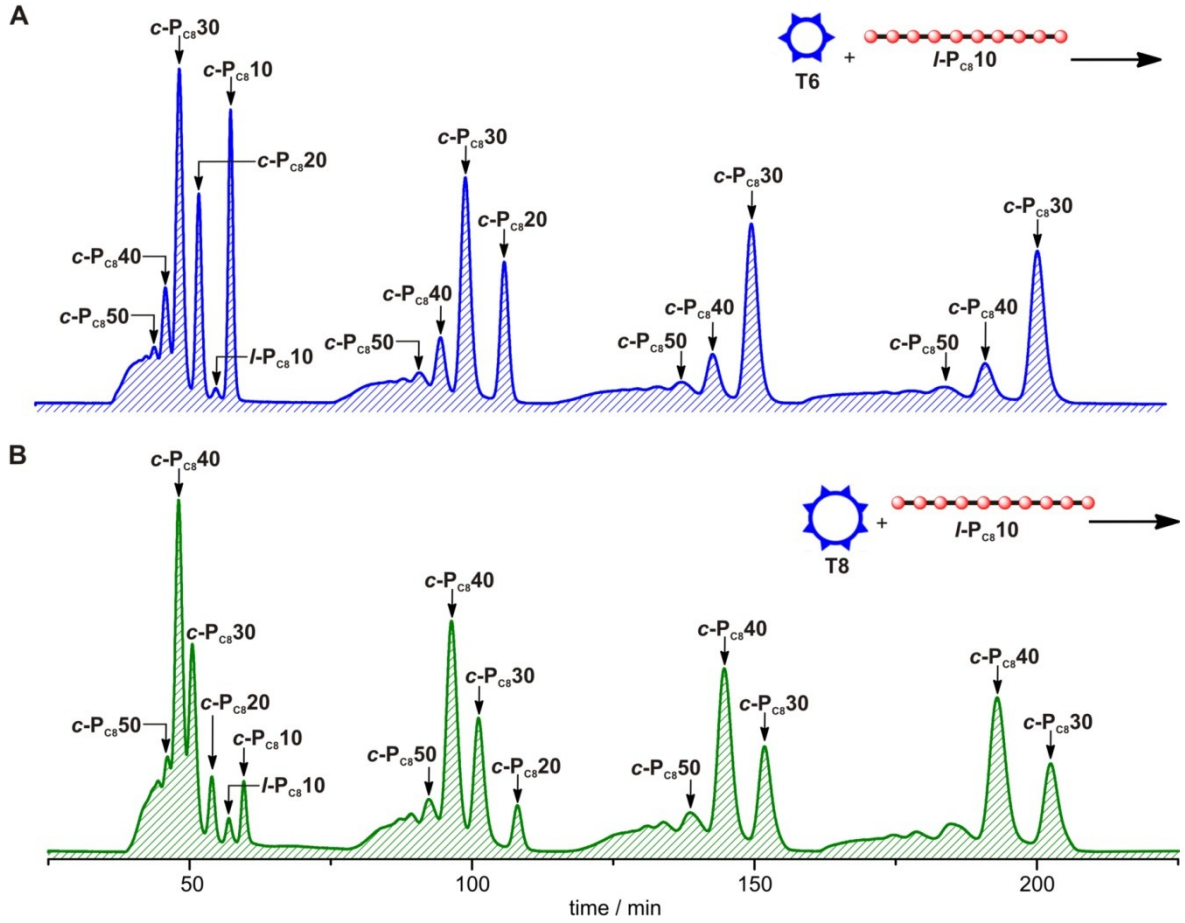

Figure 5.3. Analytical recycling GPC traces (JAIGEL columns, toluene/1% pyridine, detection at 500 nm) of the crude reaction mixtures of coupling ***l*-P$_{C8}$10** (in $CHCl_3$) in the presence of (a) **T6** or (b) **T8**. Each sample was cycled 4 times. Resolved peaks were collected after 1st (***l*-P$_{C8}$10** and ***c*-P$_{C8}$10**) and 2nd (***c*-P$_{C8}$20**) cycles to compensate for the broadening of the chromatogram. The catalysts and 1,4-benzoquinone were removed by passing a sample of the reaction mixture through a short size-exclusion column in $CHCl_3$/10% pyridine as eluent prior to GPC analysis.

Changing template to octapyridyl template **T8** further shifts the average weight of the cyclic species formed in the reaction (Figure 5.2d), in accordance with the increase of the Vernier number that characterizes the reaction mixture in this case. As in the previous case, the reaction produces separable (Figure 5.3b) mixture of cyclic porphyrin oligomers ***c*-P$_{C8}$10**, ***c*-P$_{C8}$20**, ***c*-P$_{C8}$30**, ***c*-P$_{C8}$40** and ***c*-P$_{C8}$50**, with the main product being ***c*-P$_{C8}$40** (36 % analytical yield). Similarly to the case of **T6**, the ratio between the rings depends on the amount of **T8** in the reaction mixture and maximum yields of

***c*-P$_{C8}$40** are achieved when using a slightly sub-stoichiometric amount of template (mole ratio **T8**/ ***l*-P$_{C8}$10**<5/4); increased amounts of **T8** shift the reaction towards formation of lower molecular weight products.

As mentioned above, the composition of the reaction mixtures was analysed using analytical recycling GPC and then separated using the preparative version of the same technique. Sets of sharp and narrow peaks were observed for each case of coupling ***l*-P$_{C8}$10**. Initially, the columns were calibrated using known porphyrin oligomers. Figure 5.4 shows semilogarithmic plot of molecular weight versus retention times for known linear (***l*-P$_{C8}$5$_{THS,THS}$**, ***l*-P$_{C8}$6$_{THS,THS}$**, ***l*-P$_{C8}$8$_{THS,THS}$**, ***l*-P$_{C8}$10$_{THS,THS}$** and ***l*-P$_{C8}$18$_{THS,THS}$**) and cyclic (***c*-P$_{C8}$6**, ***c*-P$_{C8}$8**, ***c*-P$_{C8}$12**, ***c*-P$_{C8}$16**, ***c*-P$_{C8}$18** and ***c*-P$_{C8}$24**) porphyrin oligomers. The data for linear and cyclic species form two separate straight lines. The retention times predicted for ***c*-P$_{C8}$10**, ***c*-P$_{C8}$20**, ***c*-P$_{C8}$30**, ***c*-P$_{C8}$40** and ***c*-P$_{C8}$50** from the correlation line for the cyclic species are highly consistent with the observed retention times of peaks from analytical GPC traces of coupled reaction mixtures, assuming the assignments indicated in Figures 5.2/5.3. In turn, using the linear calibration curve in Figure 5.4, one can predict the retention times for ***l*-P$_{C8}$20**, ***c*-P$_{C8}$30**, ***c*-P$_{C8}$40**, ***c*-P$_{C8}$50**, which are believed to be main impurities in the targeted cyclic species. Assuming the parallel arrangement of calibration curves for cyclic and linear species (Figure 5.4) one can determine a factor k=0.667 in the relationship $M_w(\text{lin}) = k \times M_w(\text{cyc})$ which connects molecular weights of linear and cyclic oligomers with the same retention time. It follows from this relationship that the cyclic species are much more compact, as compared to their linear analogues and thus move noticeably slower on the column. This relationship predicts that for ***c*-P$_{C8}$40** and ***c*-P$_{C8}$50** there are linear species that can form in the course of oligomerization of ***l*-P$_{C8}$10** with very close retention times (such as in the ***c*-P$_{C8}$40**/ ***l*-P$_{C8}$30** pair). Nonetheless, based on almost full consumption of ***l*-P$_{C8}$10** and observing almost no detectable traces of ***l*-P$_{C8}$20** and ***l*-P$_{C8}$30** in the coupled mixtures, the cyclization process appears to be efficient which is consistent with data analysis presented later in this chapter.

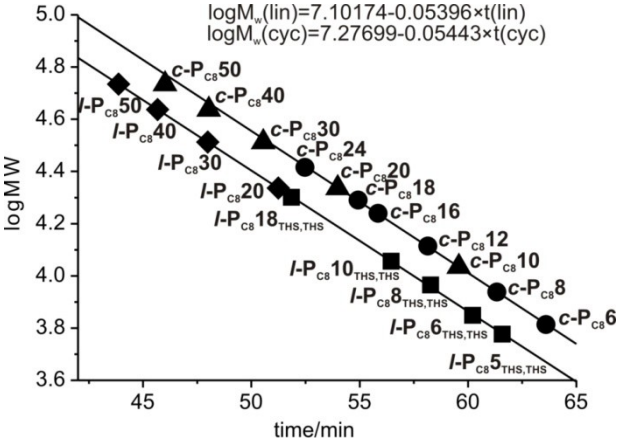

Figure 5.4. Calibration of the used GPC columns with previously reported cyclic (circles) and linear (squares) porphyrin oligomers plotted together with corresponding predicted values for ***c*-P$_{C8}$10**, ***c*-P$_{C8}$20**, ***c*-P$_{C8}$30**, ***c*-P$_{C8}$40** and ***c*-P$_{C8}$50** (triangles) and ***l*-P$_{C8}$20**, ***l*-P$_{C8}$30**, ***l*-P$_{C8}$40** and ***l*-P$_{C8}$50** (diamonds). The points were collected using the line of JAIGEL 3H (20 × 600 mm) and JAIGEL 4H (20 × 600 mm) columns in toluene/1% pyridine at a flow rate of 3.5 mL/min.

From recycling GPC data it is possible to evaluate the analytical yields of the various species formed in the course of cyclooligomerization of ***l*-P$_{C8}$10** in the presence of **T6** and **T8**, assuming no absorption of porphyrin oligomers in the process of separation (Table 5.1). As noted before, changing the template from **T5** and **T6** to **T8** increases the amount of high-molecular weight products formed in the reaction, in accordance with the increase of the Vernier number, as well as dramatically lowers the amount of ***c*-P$_{C8}$10** formed (Figure 5.2). Dr. Guzmán Gil-Ramírez previously established that the cavity of the 12-porphyrin nanoring ***c*-P$_{t\text{-}Bu}$12** can efficiently accommodate two molecules of the template **T8** inside to form highly stable "caterpillar" complexes (Figure 5.5a) (unpublished work). It was assumed that the formation of similar 1:2 complexes is possible based on ***c*-P$_{C8}$10** and **T5** or **T6**. The energy-minimized structures of complexes ***c*-P$_{C8}$10•(T6)$_2$** and ***c*-P$_{C8}$10•T8** (Figure 5.5b,c) show that the cavity of ***c*-P$_{C8}$10** can easily accommodate two molecules of either **T5** or **T6**, however only one molecule of **T8** template can be fitted inside. In the intermediate complexes such as ***l*-P$_{C8}$10•(T5)$_2$** and ***l*-P$_{C8}$10•(T6)$_2$** the ends of the ***l*-P$_{C8}$10** are held closer together as compared to the "loose" complex ***l*-P$_{C8}$10•T8**, which accounts for the higher proportion of the ***c*-P$_{C8}$10** formed in the case of the former complexes.

Table 5.1. Analytical yields of ***c*-P$_{C8}$10**, ***c*-P$_{C8}$20**, ***c*-P$_{C8}$30**, ***c*-P$_{C8}$40** and ***c*-P$_{C8}$40** after coupling ***l*-P$_{C8}$10** in the presence of **T6** or **T8**. The yields were determined by comparison of resolved peaks in the corresponding analytical recycling GPC traces.

cycle	***l*-P$_{C8}$10/T6** (%)	***l*-P$_{C8}$10/T8** (%)
***c*-P$_{C8}$10**	27.8	6
***c*-P$_{C8}$20**	14.5	6.1
***c*-P$_{C8}$30**	33.6	18.7
***c*-P$_{C8}$40**	8.1	36.2
***c*-P$_{C8}$50**	5.1	9.6

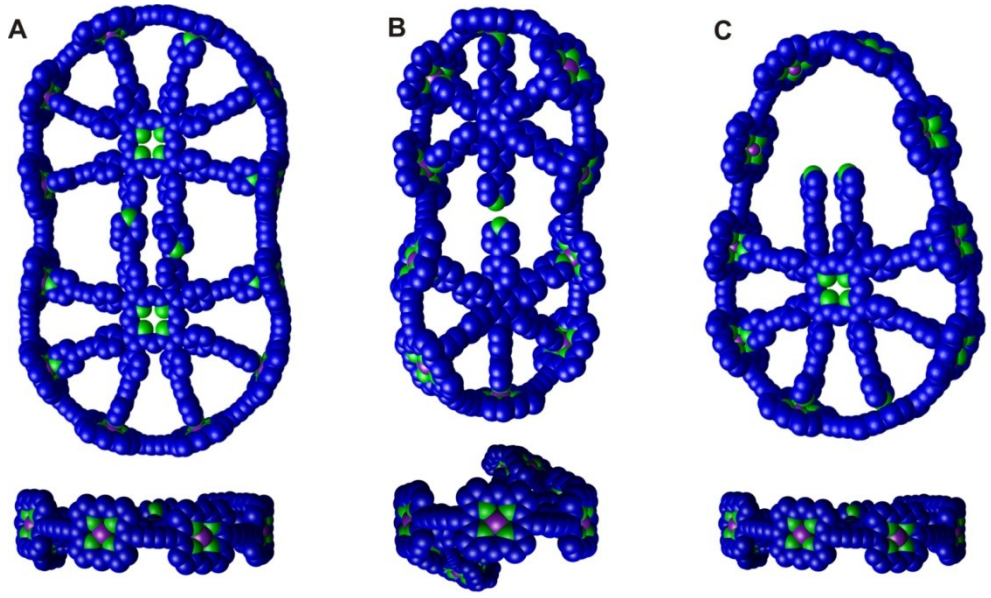

Figure 5.5. The energy-minimized (MM+ force field, HyperChem™) molecular structures of the complexes (a) ***c*-P$_{t\text{-}Bu}$12•(T8)$_2$**, (b) ***c*-P$_{C8}$10•(T6)$_2$** and (c) ***c*-P10•T8**. Side aryl groups and hydrogen atoms were omitted for clarity.

5.3 Oligomerization of *l*-P_{C8}5

Coupling of ***l*-P$_{C8}$5** in the presence of **T5**, **T6** or **T8** should potentially result in formation of the same products as when using ***l*-P$_{C8}$10**. Indeed, when applying the reaction conditions of Section 5.2 to ***l*-P$_{C8}$5** in the presence of **T5** (mole ratio ***l*-P$_{C8}$5/T5** = 1:1), formation of the expected ***c*-P$_{C8}$10** as the major product and traces of ***c*-P$_{C8}$15** (Figure 5.6a) was observed. However, coupling ***l*-P$_{C8}$5** in the presence of either **T6** (mole ratio ***l*-P$_{C8}$5/T6** = 6:5) or **T8** (mole ratio ***l*-P$_{C8}$5/T8** = 8:5) only results in formation of target Vernier products ***c*-P30** and ***c*-P40** as minor products (Figure 5.6b,c) and cannot be shifted towards formation of Vernier products as major species by changing the ratio between reagents. The authenticity of the products was confirmed by comparison of corresponding retention times.

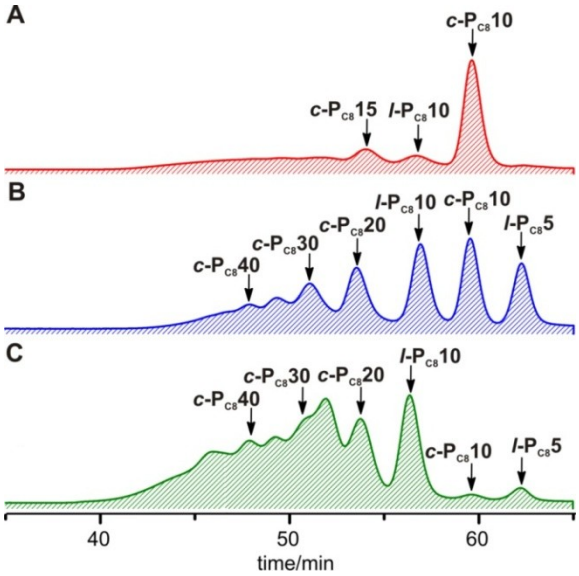

Figure 5.6. Analytical GPC traces (JAIGEL, toluene/1% pyridine, detection at 500 nm) of the crude reaction mixtures of coupling ***l*-P$_{C8}$5** in the presence of (a) **T5**, (b) **T6** or (c) **T8**. The catalysts and 1,4-benzoquinone were removed by passing a sample of the reaction mixture through a short size-exclusion column in $CHCl_3$/10% pyridine as eluent prior to GPC analysis.

5.4 Oligomerization of *l*-P_{C8}2

The results of the Sections 5.2 and 5.3 suggest that it might be possible to synthesize ***c*-P$_{C8}$10** by coupling ***l*-P$_{C8}$2** in the presence of **T5** (Figure 5.7). However, in all previous cases, efficient Vernier templating was only achieved by coupling together no more than 4 linear porphyrin building blocks, as when preparing ***c*-P$_{C8}$12** from ***l*-P$_{C8}$4**, ***c*-P$_{C8}$24** from ***l*-P$_{C8}$6** or ***l*-P$_{C8}$8**, ***c*-P$_{C8}$30** or ***c*-P$_{C8}$40** from ***l*-P$_{C8}$10**. When shorter building blocks were used, formation of only trace amounts of Vernier products was observed as, for example, when coupling ***l*-P$_{C8}$3** in the presence of **T8** or ***l*-P$_{C8}$5** in the presence of **T6** or **T8**. In addition, as follows from Section 5.2, the possibility of forming a favoured smaller cycle, as in the case of coupling ***l*-P$_{C8}$10** in the presence of **T6**, can lower the amounts of the Vernier cyclic species formed in the reaction. In the case of coupling of ***l*-P$_{C8}$2** in the presence of **T5**, such a species might be the complex ***c*-P$_{C8}$6•T5** which has been shown before to be very stable.[5]

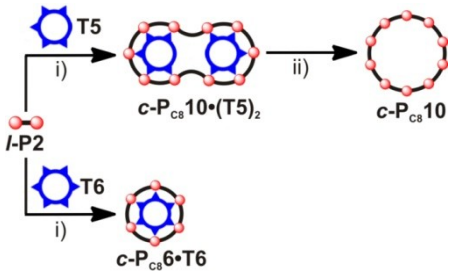

Figure 5.7. Templated synthesis of the nanorings ***c*-P$_{C8}$6** and ***c*-P$_{C8}$10**, from ***l*-P$_{C8}$2**. Reagents: i) $PdCl_2(PPh_3)_2$, CuI, 1,4-benzoquinone, *i*-Pr_2NH; ii) pyridine.

Palladium-catalyzed oxidative coupling of ***l*-P$_{C8}$2** in the presence of the hexa-pyridyl template **T5** in the stoichiometric mole ratio ratio ***l*-P$_{C8}$2/T5** = 5:2 gave the templated complex of the cyclic porphyrin decamer ***c*-P$_{C8}$10**, as well as noticeable amounts of the expected ***c*-P$_{C8}$6•T5** (Figure 5.8a). Adding just one pyridyl binding site to the template, as in the case of using **T6**, changes the distribution of species completely (Figure 5.8b) and makes the cyclic porphyrin 6-mer ***c*-P$_{C8}$6•T6** the major product, with trace amounts of ***c*-P$_{C8}$12** also formed. Control experiments showed that the coupling of ***l*-P$_{C8}$2** in the absence of any template gives only linear polymers.

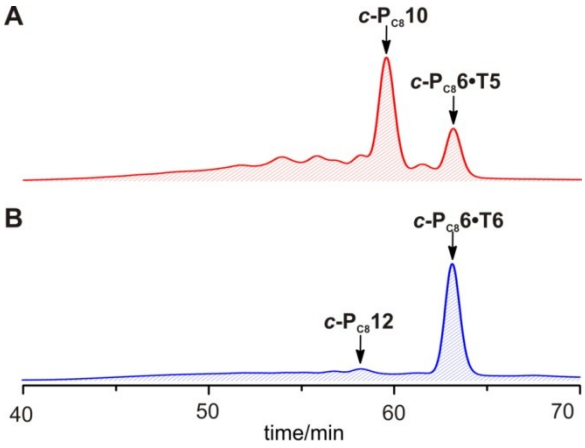

Figure 5.8. Analytical GPC traces (JAIGEL columns, toluene/1% pyridine, detection at 500 nm) of the crude reaction mixtures of coupling ***l*-P$_{C8}$2** in the presence of (a) **T5** or (b) **T6**. The catalysts and 1,4-benzoquinone were removed by passing a sample of the reaction mixture through a short size-exclusion column in $CHCl_3$/10% pyridine as eluent.

5.4 Characterization of Cyclic Species

5.4.1 MALDI-ToF Mass Spectrometry

All the new cyclic porphyrin oligomers were characterized by matrix-assisted laser desorption/ionization mass spectrometry. The experiments were run using 5% pyridine/toluene mixture as a solvent to prevent aggregation in the presence of DCTB as a matrix. All spectra were acquired by the EPSRC National Mass Spectrometry Centre at Swansea University.

The spectra show the presence of the expected molecular ions of ***c*-P$_{C8}$10** (*m/z* 10,852; *calc* 10,848), ***c*-P$_{C8}$20** (*m/z* 21701; *calc* 21,696), ***c*-P$_{C8}$30** (*m/z* 32676; *calc* 32,543) and ***c*-P$_{C8}$40** (*m/z* 43722; *calc* 43,391) as the dominant peaks. Although the sample of ***c*-P$_{C8}$50** showed the presence of the expected molecular ion of ***c*-P$_{C8}$50** (*m/z* 54,406; *calc* 54,239), it showed up together with the

molecular ion peaks corresponding to porphyrin oligomers comprised of 10 (*m/z* 11216) and 40 (*m/z* 44359) porphyrin subunits. The latter impurity is most likely a linear 40-porphyrin oligomer ***c*-P$_{C8}$40** which is very difficult to separate from ***c*-P$_{C8}$50** as follows from Figure 5.4. The origin of the 10 porphyrin oligomer is unknown.

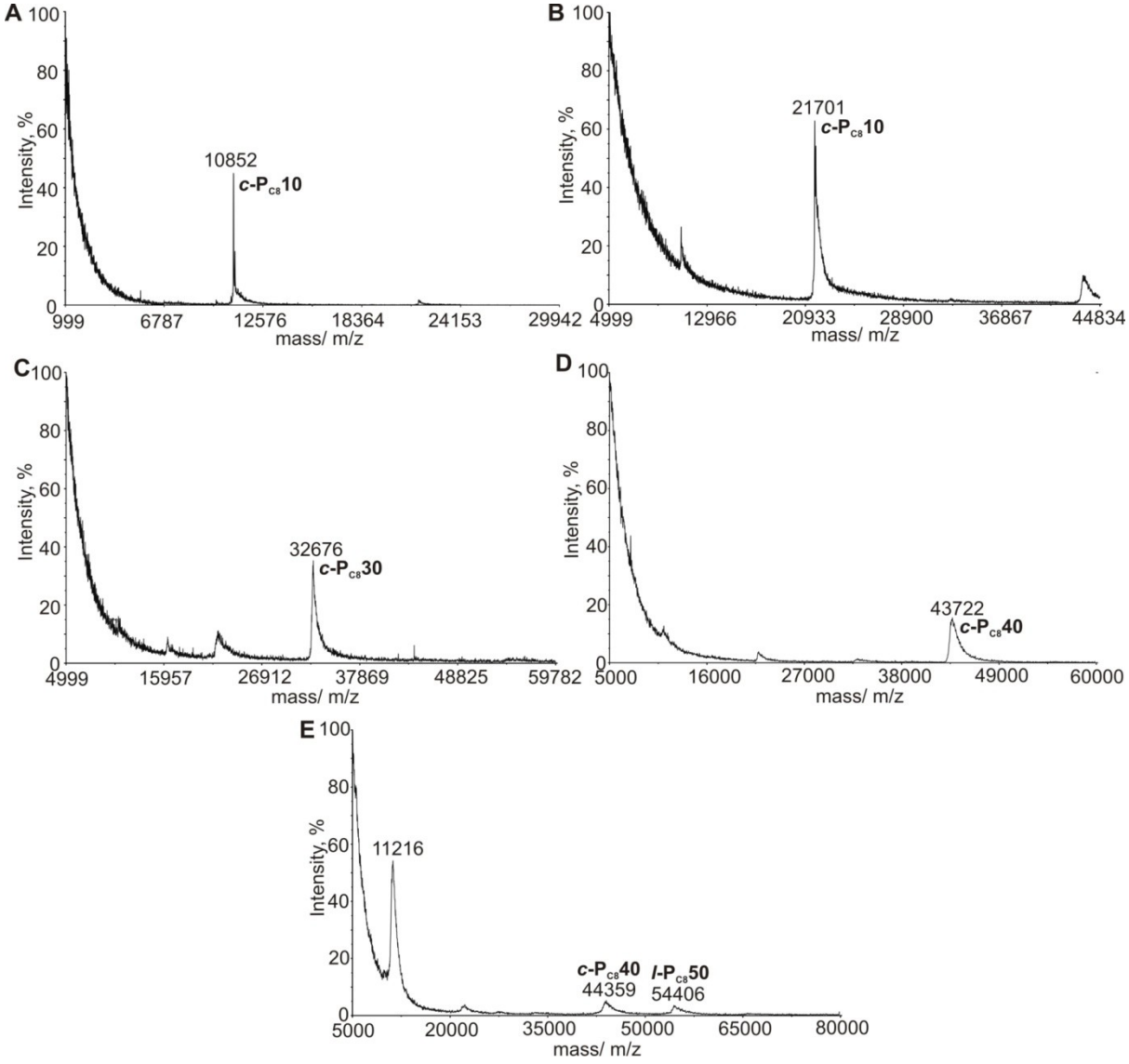

Figure 5.9. MALDI-ToF analysis of (a) ***c*-P$_{C8}$10**, (b) ***c*-P$_{C8}$20** (b), (c) ***c*-P$_{C8}$30**, (d) ***c*-P$_{C8}$40** and (e) ***c*-P$_{C8}$50** samples. DCTB was used as a matrix. All spectra were acquired by the EPSRC National Mass Spectrometry Centre at Swansea University.

5.4.2 STM Imaging

The samples of ***c*-P$_{C8}$10**, ***c*-P$_{C8}$20**, ***c*-P$_{C8}$30**, ***c*-P$_{C8}$40** and ***c*-P$_{C8}$50** were analysed using scanning tunneling microscopy (STM) by Dr. Luis Perdigao, Dr. James O'Shea and Prof. Peter Beton (University of Nottingham, UK). The molecules were deposited using an electrospray source on a Au(111) surface in ultrahigh vacuum,[6] from the solutions in a toluene/MeOH (3:1) solvent mixture, which was expected to favour aggregation of the molecules as in the case of ***c*-P$_{C8}$24** (Chapter 4).

Individual porphyrin subunits are clearly resolved on the STM images of ***c*-P$_{C8}$10**, ***c*-P$_{C8}$20**, ***c*-P$_{C8}$30** and ***c*-P$_{C8}$40** (Figure 5.10). They provide direct evidence about the size of these nanorings

which are consistent with the predicted values. According to the data of the STM, all of the samples are of high purity and do not contain significant amounts of linear porphyrin oligomers, nor of nanorings of other sizes. These images show some common features with the previous surface studies of smaller nanorings and the nanorings are preferentially adsorbed in terrace steps on the Au(111) surface.[6-8]

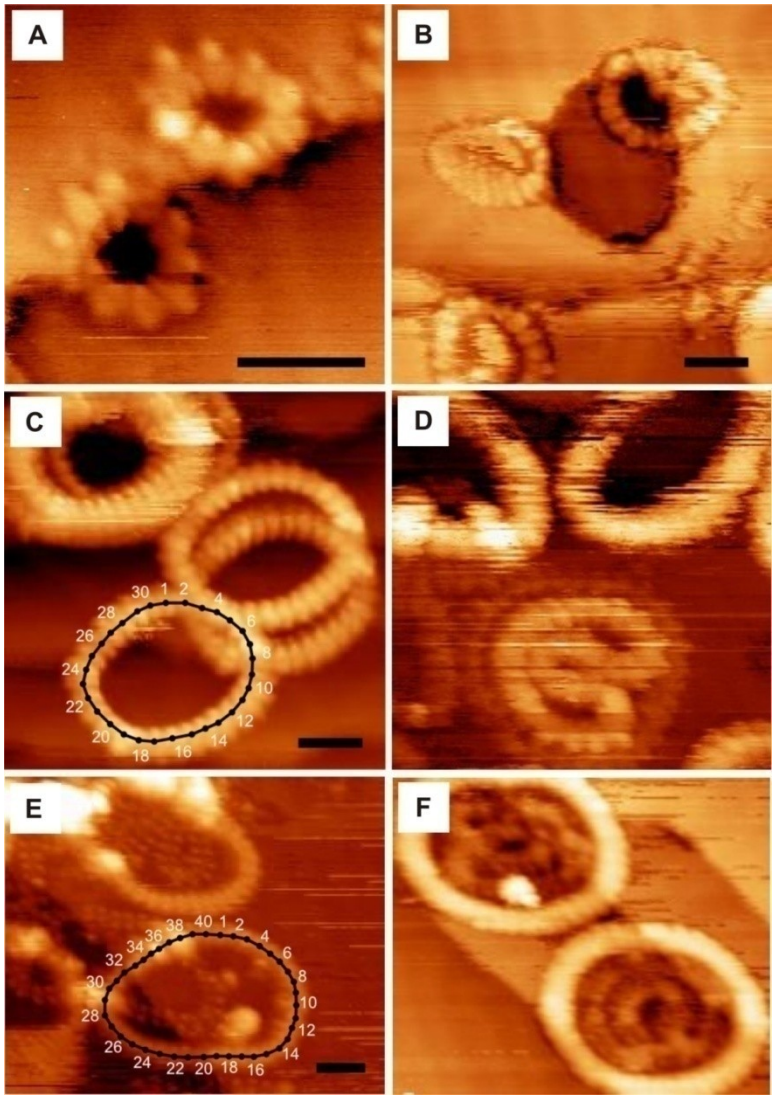

Figure 5.10. STM images of (a) ***c*-P$_{C8}$10**, (b) ***c*-P$_{C8}$20**, (c, d) ***c*-P$_{C8}$30** and (e, f) ***c*-P$_{C8}$40** single molecules on a gold surface (scale bar, 10 nm). The images were deposited from the toluene/MeOH (3:1) solvent mixtures. Images (d) and (e) show the presence of ring-in-ring complexes.

The STM analysis of the sample of ***c*-P$_{C8}$50** also showed the presence of the expected nanorings with a diameter of approximately 21 nm, but in this case it proved impossible to resolve individual porphyrin subunits (Figure 5.11). In addition, the STM images revealed the presence of a significant amount of the linear porphyrin polymer of undetermined size which is consistent with the MALDI-ToF analysis data of this sample in Figure 5.9e.

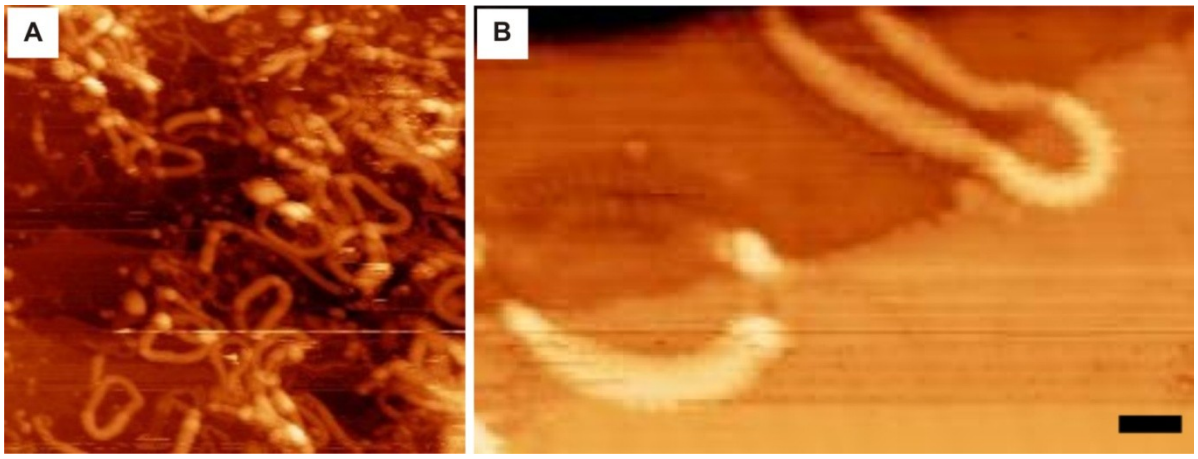

Figure 5.11. (a) Large and (b) small area STM images of ***c*-P$_{C8}$50** single molecules on a Au (111) surface (scale bar, 10 nm). The molecules were deposited from the toluene/MeOH (3:1) solvent mixtures.

In the case of ***c*-P$_{C8}$30, *c*-P$_{C8}$40** and ***c*-P$_{C8}$50**, a stacking effect similar, to that observed for ***c*-P$_{C8}$24** (Chapter 4) was observed on the gold surface. The height of these rings corresponds to columnar stacks of 2 or 3 rings, in contrast to the single height rings observed for ***c*-P$_{C8}$10** and ***c*-P$_{C8}$20**. The stacking occurs through aggregation in solution prior to deposition and can be suppressed by the addition of either pyridine or tetrahydrofuran. Interestingly, formation of some unexpected ring-in-ring inclusion complexes was also observed in the case of ***c*-P$_{C8}$30** (Figure 5.10d) and ***c*-P$_{C8}$40** (Figure 5.10f) rings. These ring-in-ring complexes are probably stabilized by interdigitated alignment of the octyl side chains that are believed to drive the self-assembly of the analogous linear porphyrin oligomers on the gold surface.[6]

5.5 Conclusions and Outlook

The results presented in this chapter clearly outline the scope of the two templating approaches (classical and Vernier) for the controlled cyclooligomerization of linear porphyrin oligomers and demonstrate their potential at accessing extremely challenging targets.

The cyclooligomerization of ***l*-P$_{C8}$10** can be controlled by applying different templates and be directed to ***c*-P$_{C8}$10** when using **T5**, to ***c*-P$_{C8}$30** when using **T6** and to ***c*-P$_{C8}$40** when using **T8**. However, by applying the templates **T6** and **T8**, it was not possible to efficiently bring together 6 and 8 molecules of ***l*-P$_{C8}$5** to form ***c*-P$_{C8}$30** and ***c*-P$_{C8}$40**, respectively via corresponding Vernier routes. The highest degree of the Vernier oligomerization (5) was achieved when coupling ***l*-P$_{C8}$2** in the presence of **T5** to give ***c*-P$_{C8}$10**. Thus, the results so far have shown that when more than 9 components are involved in the Vernier synthesis it is unlikely to achieve efficient Vernier macrocyclization. This is probably due to the instability of the corresponding Vernier complexes as well as increased probability of mismatches in the course of cyclization. The other process that can interfere with the Vernier cyclization is the formation of the stable "caterpillar" mismatch complexes which, however, can be ruled out by tuning the size of a template. For the first time, it has been demonstrated that it is

possible to efficiently switch between two Vernier routes by simple changing of the templates. The very slight changes in the template, such as removal of just one pyridyl site, can drastically change the process of oligomerization. The data of this chapter further confirm that Vernier cyclization tends to give a library of cyclic species, both smaller and bigger than the expected Vernier product. The advantage of this is the possibility to access even larger cyclic species than expected from the Vernier number as was the case with ***c*-P$_{C8}$50** ring. However, the broad distribution of products formed in these high-order Vernier templating reactions is a problem because it prevents the formation of a single product in higher yield. In future it may be possible to increase the selectivity of these reactions by increasing the strength of binding to the template, either by changing the coupling conditions (*eg* reducing the concentration of *i*-Pr_2NH) or by changing the Lewis acidity of the porphyrin units.[9]

The STM experiments have further demonstrated that the aggregation behavior of the isolated rings on a gold surface depends on their size. The larger macrocycles, ***c*-P$_{C8}$30, *c*-P$_{C8}$40** and ***c*-P$_{C8}$50**, showed the same stacking effect as ***c*-P$_{C8}$24**, in contrast to ***c*-P$_{C8}$10** and ***c*-P$_{C8}$20** that did not aggregate on the gold surface.

The isolated and characterized ***c*-P$_{C8}$40** and ***c*-P$_{C8}$50** are the biggest fully artificial monodisperse macrocyclic species ever prepared, with the ***c*-P$_{C8}$50** reaching the 21 nm in diameter! The current size record for the biggest monodisperse macrocyclic structure was set up by Osuka in 2008 with the synthesis of the 32-porphyrin cyclic array.[4] They provide a different size level for the investigation of the optoelectronic properties and fast energy migration in the molecular systems.

Some future work in the area of the Vernier templated synthesis might involve studying the effects of mismatches and selectivity of the Vernier cyclizations by performing Vernier cyclizations in the presence of short porphyrin oligomers or a second template.

5.6 References

[1] *Biochemistry* (Eds L. Stryer, J. M., Berg, J. L. Tymoczko), W. H. Freeman, **2002**.
[2] N. Badi, J.-F. Lutz, *Chem. Soc. Rev*. **2009**, *38*, 3383–3390.
[3] R. B. Merrifield, *Angew. Chem., Int. Ed.* **1985**, *24*, 799–810.
[4] T. Hori, X. Peng, N. Aratani, A. Takagi, T. Matsumoto, T. Kawai, Z. S. Yoon, M.-C. Yoon, J. Yang, D. Kim, A. Osuka, *Chem. Eur. J.* **2008**, *14*, 582–595.
[5] H. J. Hogben, J. K. Sprafke, M. Hoffmann, M. Pawlicki, H. L. Anderson, *J. Am. Chem. Soc.* **2011**, *133*, 20962–20969.
[6] A. Saywell, J. K. Sprafke, L. J. Esdaile, A. J. Britton, A. Rienzo, H. L. Anderson, J. N. O'Shea, P. H. Beton, *Angew. Chem. Int. Ed.* **2010**, *49*, 9136–9139.
[7] M. C. O'Sullivan, J. K. Sprafke, D. V. Kondratuk, C. Rinfray, T. D. W. Claridge, A. Saywell, M. O. Blunt, J. N. O'Shea, P. H. Beton, M. Malfois, H. L. Anderson, *Nature* **2011**, *469*, 72–75.
[8] D. V. Kondratuk, L. M. A. Perdigao, M. C. O'Sullivan, S. Svatek, G. Smith, J. N. O'Shea, P. H. Beton, H. L. Anderson, *Angew. Chem., Int. Ed.* **2012**, *51*, 6696–6699.
[9] D. W. J. McCallien, J. K. M. Sanders, *J. Am. Chem. Soc.* **1995**, *117*, 6611–6612.

Chapter 6

Structure and Optoelectronic Properties of Porphyrin Nanorings

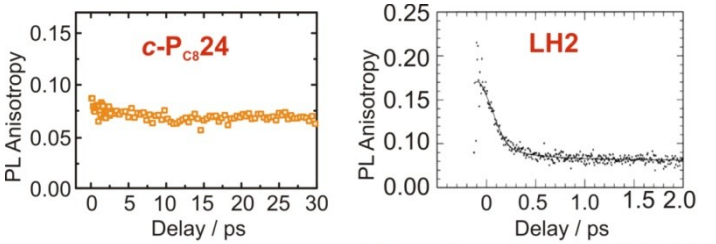

J. Phys. Chem. **1996**, *100*, 6825-6834

This chapter sums up advances in structure elucidation and optoelectronic properties of the fully-conjugated nanorings synthesized in the course of this work. Crystal structures of the templated complexes of 6- and 12-porphyrin nanorings provide ultimate information about their geometries and show that the strain in both cases is localized in the acetylenes and does not affect the geometry of the zinc coordination spheres. In addition, the first STM images of the 12-porphyrin template complex on the gold surface are reported. Electrochemical studies on the 6-porphyrin nanoring show that the corresponding templated complex can undergo six one-electron reductions and six one-electron oxidations, most of which are resolved, and also demonstrate that the HOMO–LUMO gap of the 6-porphyrin nanoring is less than that of the linear porphyrin hexamer or polymer. Finally, polarization-sensitive ultrafast time-resolved photoluminescence (PL) studies show that the rings as large as 24-porphyrin exhibit full delocalization of the absorbing excited state – just as in natural light harvesting systems!

Parts of the results in this chapter have been published in the following articles:

Belt-Shaped π-Systems: Relating Geometry to Electronic Structure in a Six-Porphyrin Nanoring
J. K. Sprafke, D. V. Kondratuk, M. Wykes, A. L. Thompson, M. Hoffmann, R. Drevinskas, W.-H. Chen, C. K. Yong, J. Kärnbratt, J. E. Bullock, M. Malfois, M. R. Wasielewski, B. Albinsson, L. M. Herz, D. Zigmantas, D. Beljonne, H. L. Anderson, *J. Am. Chem. Soc.* **2011**, *133*, 17262–17273.

Linear and Cyclic Porphyrin Hexamers as Near-Infrared Emitters in Organic Light-Emitting Diodes
O. Fenwick, J. K. Sprafke, J. Binas, D. V. Kondratuk, F. Di Stasio, H. L. Anderson, F. Cacialli *Nano Lett.* **2011**, *11*, 2451–2456.

6.1 Background

Cyclic porphyrin hexamer ***c*-P$_{t\text{-Bu}}$6** has been shown to possess intriguing optoelectronic[1] and supramolecular properties,[2] which justifies great interest in understanding its behaviour and that of larger nanorings. The ***c*-P$_{t\text{-Bu}}$6** system (and ***c*-P$_{t\text{-Bu}}$6•T6**) has been most studied because the templated complex is now accessible at >100 mg scale directly from a porphyrin monomer.[1] Work by Dr. Johannes Sprafke has showed that ***c*-P$_{t\text{-Bu}}$6•T6** is shape persistent in solution, even as the template-free nanoring ***c*-P$_{t\text{-Bu}}$6** (as evidenced by analysis of SAXS data), and its HOMO-LUMO gap is less than that of the linear porphyrin hexamer or even linear porphyrin polymer (as evidenced by analysis of the absorption and fluorescence spectra). This chapter supplements these conclusions by presenting a long-sought crystal structure of ***c*-P$_{t\text{-Bu}}$6•T6** and studying ***c*-P$_{t\text{-Bu}}$6•T6/*c*-P$_{t\text{-Bu}}$6** by means of electrochemistry. In addition, the X-ray structure and STM imaging (on a gold surface) of ***c*-P$_{t\text{-Bu}}$12•(T6)$_2$**, are reported. PL anisotropy measurements allow exciton delocalization in porphyrin nanorings to be followed and compared to the results obtained with naturally occuring light harvesting systems. Previously, such measurements have only been performed for ***c*-P$_{t\text{-Bu}}$6•T6** and have showed that the excited state is delocalized over the whole π-system within less than 0.5 ps.[1] Here the PL anisotropy measurement results for a system as large as ***c*-P$_{C8}$24** (exceeding in size both LHs) are presented.

6.2 X-ray Structure of *c*-P$_{t\text{-Bu}}$6•T6

Determination of the crystal structure of ***c*-P$_{t\text{-Bu}}$6•T6** was challenging because it forms small weakly diffracting crystals, with large unit cells and substantial amounts of disordered solvent. It is near the upper limit of the size range of synthetic molecules that have been characterized crystallographically, and the Cambridge Structural Database (CSD, version 5.32) contains only two previous structures of covalent porphyrin oligomers with more than five porphyrin units, namely Osuka's porphyrin boxes comprised of six and seven porphyrin units.[3]

Crystals of ***c*-P$_{t\text{-Bu}}$6•T6** were grown by vapour diffusion of *n*-hexane into a solution in $CHCl_3$/1% pyridine. Diffraction data were collected and the structure solved and refined by Dr. Amber L. Thompson (Chemistry Research Laboratory, University of Oxford). The data were collected at 150 K using synchrotron X-ray radiation at the Diamond Light Source, Beamline I19. The structure was solved using SuperFlip[4] and refined using full-matrix least-squares within the CRYSTALS software suite.[5] The crystals are assigned to *Pccn* space group with a cell of a = 59.310(5) Å, b = 25.141(3) Å, c = 31.080(4) Å, V = 46,299(8) Å^3. The asymmetric unit contains 0.5 molecules of ***c*-P$_{t\text{-Bu}}$6•T6** and there is a crystallographic inversion centre at the centre of the molecule. A second polymorph was also observed, however assignment of the space group was not possible in that case due to the poor quality of the data. Crystals of the second polymorph were

observed as black hexagonal plates with a cell of a = 49.85 Å, b = 49.85 Å, c = 29.46 Å, α = 90º, β = 90º, γ = 120º, V = 63,395 Å^3. This polymorph was persistent and was seen on many occasions. The *c*-axis length was found to vary, perhaps as a function of solvation. Although the structure was never solved, it is postulated to consist of flat layers with pseudo 6-fold symmetry caused by the ***c*-P$_{t\text{-Bu}}$6•T6** forming a hexagonal array. Ordering between the ***c*-P$_{t\text{-Bu}}$6•T6** layers (separated by solvent) is poor, leading to a two dimensional diffraction pattern that could not be solved.

In the orthorhombic polymorph the nanoring molecules are packed in layers, in a side-to-face herringbone arrangement (Figure 6.1).

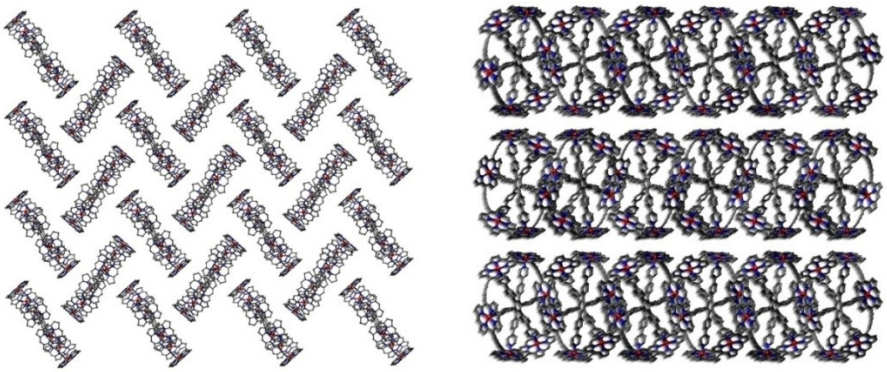

Figure 6.1. The packing diagram for ***c*-P$_{t\text{-Bu}}$6•T6** showing two orthogonal views of the crystal structure. Hydrogen atoms, solvent molecules and aryl side groups have been omitted for clarity.

The experimental mean transannular Zn···Zn distance (24.35 ± 0.08 Å) is in excellent agreement with the previously published calculated value of 24.2 Å in ***c*-P$_{t\text{-Bu}}$6•T6**.[6] Molecules of ***c*-P$_{t\text{-Bu}}$6•T6** are slightly distorted from ideal D_{6h} symmetry, and the nanoring adopts a "chair-like" conformation, with alternate butadiyne links above and below the mean plane of the six zinc atoms (mean deviations of 0.80 Å at C_α and 0.89 Å at C_β, Figure 6.2a,b. Calculated using Crystal Maker™ software, version 7.2.4). This distortion makes the ***c*-P$_{t\text{-Bu}}$6** ring contract slightly round the **T6** template, and it reveals that the template is slightly too small for the cavity of the nanoring.

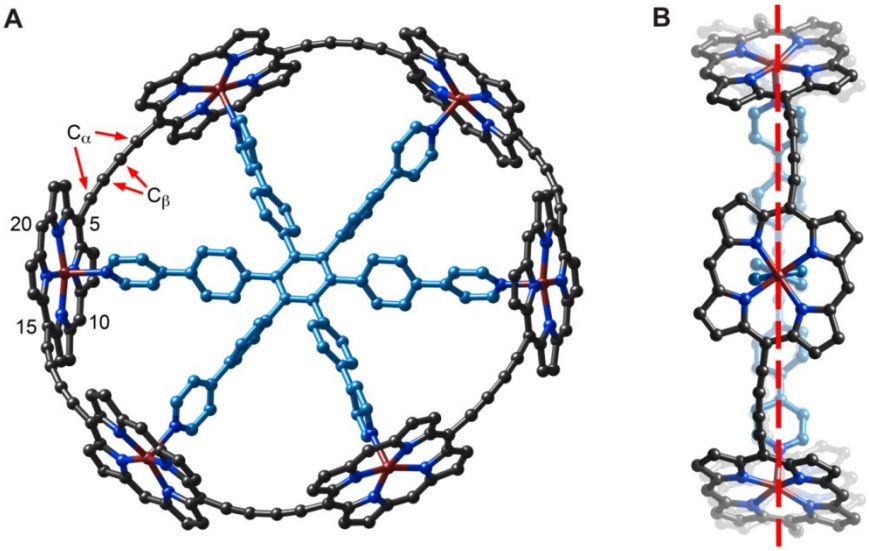

Figure 6.2. (a) Front and (b) side views of individual molecules of ***c*-P$_{t\text{-Bu}}$6•T6** in the crystal with mean plane fitted through six zinc-centres (red dashed line). Hydrogen atoms, aryl groups, and solvent molecules are omitted for clarity.

Despite significant distortion of ***c*-P$_{t\text{-Bu}}$6•T6**, the zinc coordination geometry stays essentially normal. The mean zinc to pyridine nitrogen bond length ($d_{Zn–Py}$ = 2.15 ± 0.02 Å) in ***c*-P$_{t\text{-Bu}}$6•T6** is the same as that reported in the crystal structure of the linear dimer ***l*-P$_{t\text{-Bu}}$2$_{THS,THS}$** (2.164 ± 0.002 Å)[7] and in other five-coordinate Zn-porphyrin pyridine complexes as indicated by the corresponding search of CSD (Figure 6.3a; mean value from the CSD, $d_{Zn–Py}$ = 2.16 ± 0.03 Å). Only porphyrins with no substituents in β- and adjacent *meso*-positions have been included in the search of CSD; porphyrins with bulky substituents in meso-positions were also excluded. The porphyrin units in ***c*-P$_{t\text{-Bu}}$6•T6** are almost planar: the root-mean-squared deviation for the 24 atoms of the porphyrin core, averaged over all three crystallographically inequivalent porphyrin units, is 0.020 Å, which is less than in the linear dimer ***l*-P$_{t\text{-Bu}}$2$_{THS,THS}$** (0.043 Å).

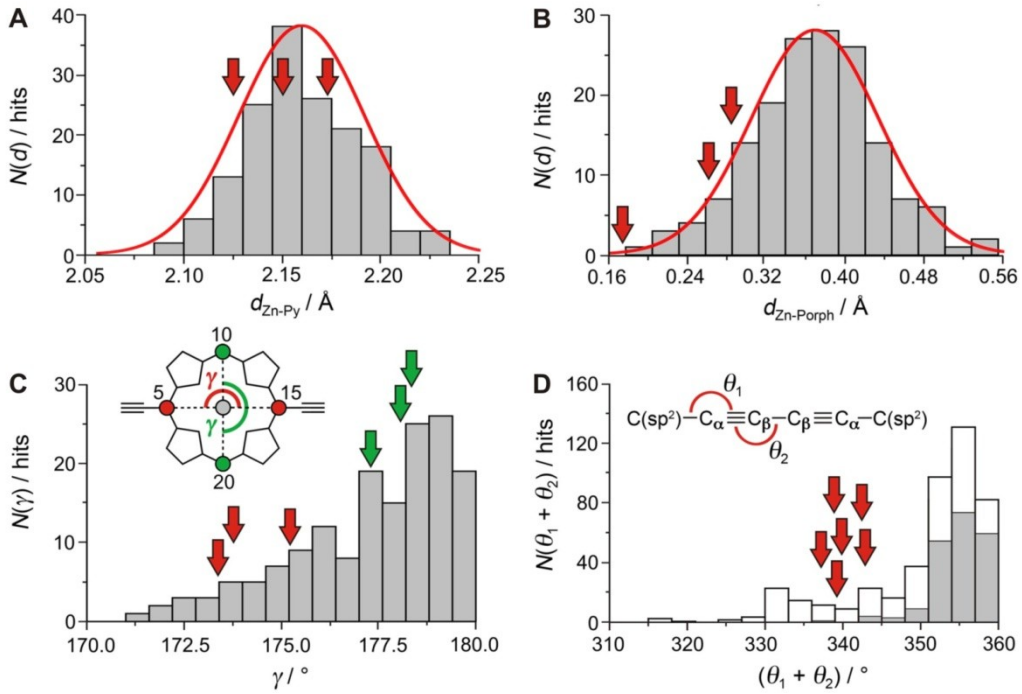

Figure 6.3. Comparison of crystallographic parameters in ***c*-P$_{t\text{-Bu}}$6•T6** with those of structural fragments from the Cambridge Crystallographic Database: (a) Zn–N bond length $d_{Zn–Py}$ of the pyridyl nitrogen; (b) out-of-plane distance $d_{Zn–plane}$ of the Zn atom from the plane of the 24-atom porphyrin core; (c) angle between opposite *meso*-positions and centroid of four pyrrole nitrogens γ ; (d) sum of the angles C(sp^2)–C$_\alpha$≡C$_\beta$ (θ_1) and C$_\alpha$≡C$_\beta$–C$_\beta$ (θ_2), compared with acyclic (gray bars) and cyclic (white bars) 1,3-butadiynes. Red and green arrows indicate the values of $d_{Zn–plane}$, $d_{Zn–Py}$, γ, and (θ_1 + θ_2) over the three inequivalent butadiyne and porphyrin units in ***c*-P$_{t\text{-Bu}}$6•T6**.

The porphyrin units are slightly curved around the nanoring, which reduces the distance from the zinc atom to the mean plane of the 24-atom porphyrin core (Figure 6.3b, $d_{Zn–Porph}$ = 0.24 ± 0.06 Å; mean value from the CSD, $d_{Zn–Porph}$ = 0.37 ± 0.06 Å; in ***l*-P$_{t\text{-Bu}}$2$_{THS,THS}$**, $d_{Zn–Porph}$ = 0.32 Å). The strain in the porphyrin units pulls the 5 and 15 *meso*-carbon atoms away from the plane of the porphyrin, whereas the 10 and 20 carbon atoms lie in the plane of the porphyrin, as in the typical 5-coordinate Zn-porphyrin pyridine complexes. The curvature in the porphyrins is most clearly revealed by the angles between *meso* carbon atoms C(5) and C(15) and the centroid of four pyrrole nitrogens (mean γ = 174.2° ± 0.9°), which is less than the corresponding angle between *meso* carbon atoms C(10) and C(20) (mean γ = 177.9° ± 0.5°; Figure 6.3c). A similar curved distortion is evident in the porphyrin

tetramer nanobarrel reported recently by Osuka and co-workers.[8]

Most of the strain in ***c*-P$_{t\text{-Bu}}$6•T6** is distributed among the acetylenes. The averages of the C(sp^2)-C$_\alpha$≡C$_\beta$ and C$_\alpha$≡C$_\beta$–C$_\beta$ bond angles for the six nonequivalent C≡C units in ***c*-P$_{t\text{-Bu}}$6•T6** deviate significantly from values found for linear butadiynes in the CSD (Figure 6.3d). Only the butadiyne fragments connected to sp2-carbon atoms were included in the CSD analysis; those with triple bonds coordinated to metals were excluded. However the distortion in these acetylenes is less than that found in many other butadiyne-linked macrocycles.[9-14] The average crystallographic C$_\beta$–C$_\beta$ and C$_\alpha$≡C$_\beta$ bond lengths in ***c*-P$_{t\text{-Bu}}$6•T6** are 1.386 ± 0.022 Å and 1.223 ± 0.016 Å, respectively, reflecting a normal level of bond length alternation for a 1,3-butadiyne, in contrast to the behavior observed in longer polyynes.[15]

6.3 X-ray Structure of *c*-P$_{t\text{-Bu}}$12•(T6)$_2$

The three-dimensional structure of ***c*-P$_{t\text{-Bu}}$12•(T6)$_2$** was initially deduced from a detailed analysis of its complex ^{1}H NMR spectrum and SAXS,[16] but numerous attempts were undertaken to characterize it by X-ray crystallography. It has taken hundreds of crystallization and many weeks of refinement of the structure before it was finally obtained. Certainly, the main motivation for such perseverance was the hope to obtain information about the slightest peculiarities of the structure of ***c*-P$_{t\text{-Bu}}$12•(T6)$_2$** similar to the case of ***c*-P$_{t\text{-Bu}}$6•T6** (see Section 6.2). However, one cannot also neglect the call for a challenge from the fact that a search of the Cambridge Structural Database does not produce any other covalently bound molecule quite as large (in particular in terms of the number of atoms per asymmetric unit).

Crystals of ***c*-P$_{t\text{-Bu}}$12•(T6)$_2$** were grown by diffusion of methanol vapor into a solution of ***c*-P$_{t\text{-Bu}}$12•(T6)$_2$** in $CHCl_3$ over a period of 2–3 days. The crystals diffracted best when freshly grown crystals were used. Diffraction data were collected and the structure solved and refined by Dr. Amber L. Thompson (Chemistry Research Laboratory, University of Oxford). The data were collected at 100 K using synchrotron X-ray radiation at the Diamond Light Source, Beamline I19. The structure was solved using SuperFlip[4] and refined using full-matrix least-squares within the CRYSTALS software suite.[5]

The crystals contained >60% of disordered solvent resulting in weak diffraction. The crystals are assigned to *C2/c* space group with a cell of a = 117.44(5) Å, b = 21.009(7) Å, c = 57.23(2) Å, α = 90º, β = 115.385(4)º, γ = 90º, V = 127,561 Å^3. The asymmetric unit contains half a molecule of ***c*-P$_{t\text{-Bu}}$12•(T6)$_2$** with a C_2 axis bisecting the molecule at the cross-point of central butadiyne moieties; thus a molecule of ***c*-P$_{t\text{-Bu}}$12•(T6)$_2$** has D_2 symmetry and is chiral. However, ***c*-P$_{t\text{-Bu}}$12•(T6)$_2$** crystallizes as a racemate, and each enantiomer constitutes a separate flat layer in which molecules are stacked side-to-side (Figure 6.4a). The faces of two six-porphyrin loops are tilted by 27.9º (Figure 6.4d) to each other.

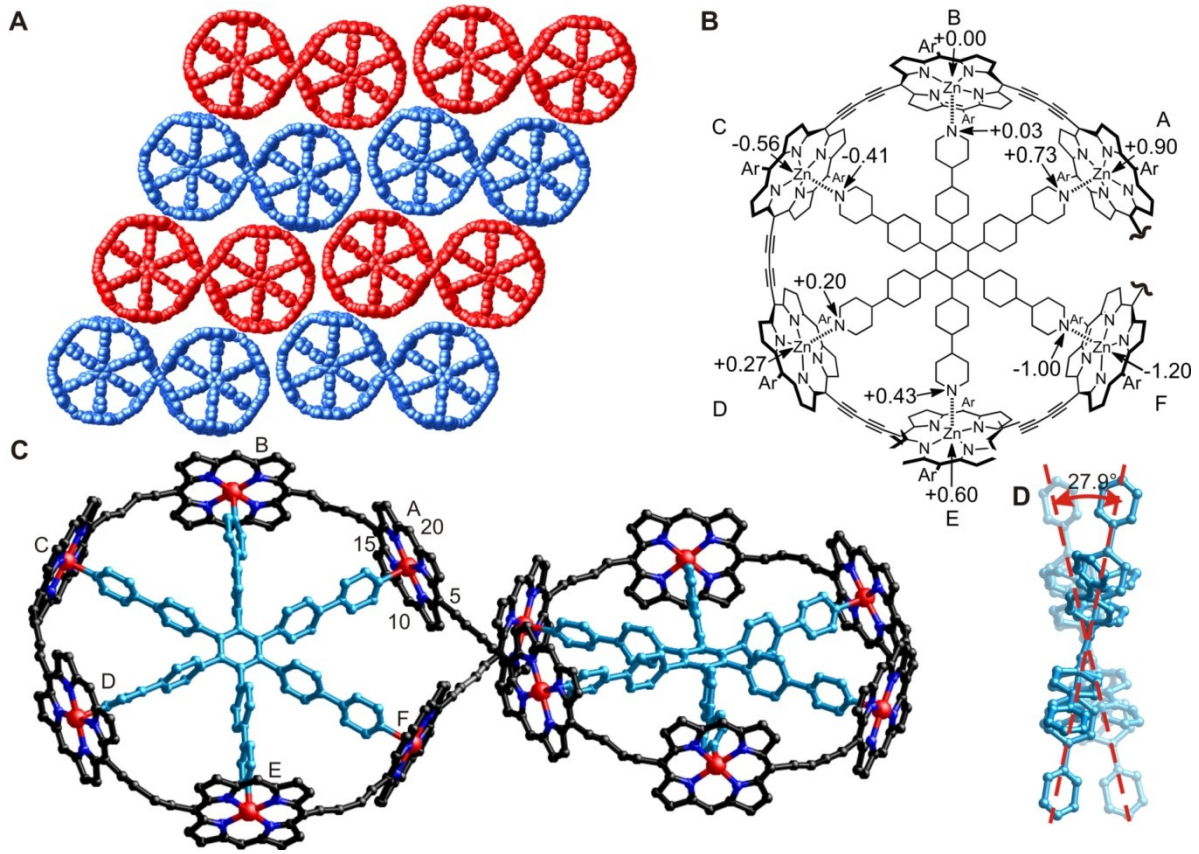

Figure 6.4. (a) Packing diagram for ***c*-P$_{t\text{-Bu}}$12•(T6)$_2$**. Two enantiomers of ***c*-P$_{t\text{-Bu}}$12•(T6)$_2$** are shown in red and blue. (b) Deviations of Zn atoms and pyridyl nitrogen atoms from the mean plane of the six Zn centres in the crystal structure of ***c*-P$_{t\text{-Bu}}$12•(T6)$_2$**. (c) Side and (d) front views of individual molecules of ***c*-P$_{t\text{-Bu}}$12•(T6)$_2$** with two mean planes fitted through six zinc centres of each six porphyrin fragment (red dashed line). In the side view (d) the porphyrin core is removed for clarity. Hydrogen atoms, aryl groups, and solvent molecules are omitted for clarity.

Locking two six-porphyrin loops into a figure-of-eight significantly alters the geometry (Figure 6.4b, c). The two 4-pyridylphenylene fragments pointing towards the centre of the molecule (mean deviations of +0.73 Å at N_A and -1.00 Å at N_F, Figure 6.4b) are significantly more out of mean plane compared to other four legs of a template (mean deviations of +0.03 Å at N_B, -0.41 Å at N_C, +0.20 Å at N_D and +0.43 Å at N_E Figure 6.4b). The out-of-plane distortion of the pyridyl nitrogens is mirrored in the mean deviations of corresponding Zn atoms (mean deviations of +0.90 Å at Zn_A, +0.003 Å at Zn_B, -0.57 Å at Zn_C, +0.27 Å at Zn_D, +0.60 Å at Zn_E and -1.20 Å at Zn_F). In the case of ***c*-P$_{t\text{-Bu}}$6•T6**, the seamless six porphyrin ring surface is already almost ideally preorganized for the binding of a template and the cooperative ligation of a slightly smaller template with six zinc-pyridine interactions leads to a noticeable contraction and a slight "chair-like" character of the cycle. The rupture in the six porphyrin structure implemented by a figure-of-eight topology does not seem to affect the size of the six porphyrin cycles as judged by the mean Zn···Zn distances (mean Zn···Zn distance in ***c*-P$_{t\text{-Bu}}$12•(T6)$_2$** is 24.3635 ± 0.05 Å and that in ***c*-P$_{t\text{-Bu}}$6•T6** is 24.35 ± 0.08 Å). Unfortunately, due to the poor quality of the solved structure it was impossible to judge reliably on the values of the mean zinc to pyridine nitrogen bond length in ***c*-P$_{t\text{-Bu}}$12•(T6)$_2$**. For the same reason, there is little or no evidence that the "chair-like" character of 6-porphyrin loops observed in ***c*-P$_{t\text{-Bu}}$6•T6** preserves in ***c*-P$_{t\text{-Bu}}$12•(T6)$_2$**.

6.4 STM Imaging of *c*-P_{C8}12•$(T6)_2$

The scanning tunneling microscopy (STM) provides an alternative way of direct evaluation of the structure of the molecules of ***c*-P_{C8}12•$(T6)_2$** (Figure 6.5). The deposition and STM experiments were performed by Simon Svatek, Dr. Luis Perdigao and Prof. Peter Beton at the University of Nottingham, UK.

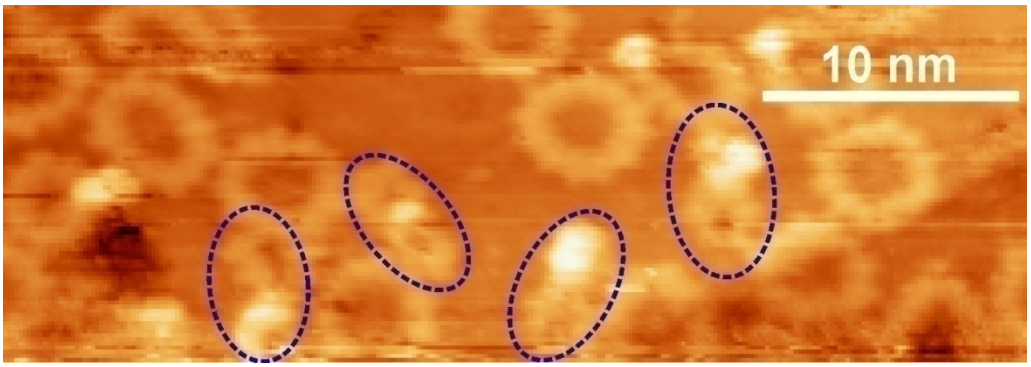

Figure 6.5. Large area image of ***c*-P_{C8}12•$(T6)_2$**. Most of the molecules of the complex unfold into the free ***c*-P_{C8}12**. The intact molecules of ***c*-P_{C8}12•$(T6)_2$** are encircled in blue.

Molecules of ***c*-P_{C8}12•$(T6)_2$** were deposited using electrospraying on a Au(111) surface in ultrahigh vacuum. The experiments were performed at room temperature using solutions of the compounds in 5% MeOH solution in toluene, applying the same conditions as used before in the case of ***c*-P_{C8}12**. Most of the molecules are evident in the form of unfolded ***c*-$P12_{C8}$,** but the images showed the presence of few intact molecules of ***c*-$P12_{C8}$·$(T6)_2$** with clearly defined six porphyrin loops approximately 2 nm in diameter consistent with the calculated value of approximately 2 nm (Figure 6.5).[6] In contrast to the case of ***c*-P_{C8}12**, the molecules of ***c*-P_{C8}12•$(T6)_2$** lie with the planes of their individual porphyrin units set perpendicular to the gold surface.

6.5 Electrochemistry of *c*-$P_{t\text{-}Bu}$6•T6

The electronic properties of ***c*-$P_{t\text{-}Bu}$6•T6** and ***c*-$P_{t\text{-}Bu}$6** were probed by cyclic and square-wave (SW) voltammetry in THF in the presence of NBu_4PF_6 (0.10 M). The SW voltammograms are plotted in Figure 6.6a, for the range −2.2 to +0.8 V (relative to internal ferrocene Fc/Fc^+). The trace for ***c*-$P_{t\text{-}Bu}$6•T6** appears to show six one-electron reductions and six one-electron oxidations, although the first and second reductions potentials are unresolved, as are the $1^{st}/2^{nd}$ and $5^{th}/6^{th}$ oxidations.

In Figure 6.6b, the first and sixth oxidation and reduction potentials of ***c*-$P_{t\text{-}Bu}$6•T6** and ***c*-$P_{t\text{-}Bu}$6** (E_{Ox}^1, E_{Ox}^6, E_{Red}^1, E_{Red}^6) are compared with the first and N^{th} oxidation and reduction potentials of ***l*-P_{C8}N**, which vary linearly with 1/N (where N = 1, 2 and 4; data from ref. 17). The HOMO–LUMO gap of ***c*-P6·T6** ($E_g = E_{ox}^1 - E_{red}^1 = 1.55$ V) is smaller than the gap extrapolated for an infinite polymer (1.71 eV). The splittings between the first and sixth oxidation and reduction potentials of ***c*-$P_{t\text{-}Bu}$6•T6** ($E_{Ox}^1 - E_{Ox}^6 = 0.39$ V; $E_{Red}^1 - E_{Red}^6 = 0.50$) are also wider than the extrapolated splittings for the

infinite polymer (0.31 and 0.29 V, respectively). Both these comparisons indicate that the electronic coupling in the nanoring is stronger than in the linear oligomers. Removal of the template reduces the resolution between the different redox processes and increases the HOMO–LUMO gap to 1.62 V, but this is still less than the gap expected for an infinite polymer. Thus the strong electronic coupling in ***c*-P$_{t\text{-Bu}}$6•T6** seems to be partly a consequence of the rigid geometry enforced by the template and partly a consequence of distortion of the π-system. Electrochemical measurements on cyclo[10]thiophene[18] and [8]cycloparaphenylene[19] revealed similar strain-induced decreases in the first oxidation potentials, although reduction potentials were not reported for either of these systems, so it is not known whether strain also reduces the electrochemical HOMO–LUMO gap in other π-conjugated macrocycles. Unfortunately, the attemps to study electrochemistry on the larger systems such as ***c*-P$_{t\text{-Bu}}$12•(T6)$_2$** failed.

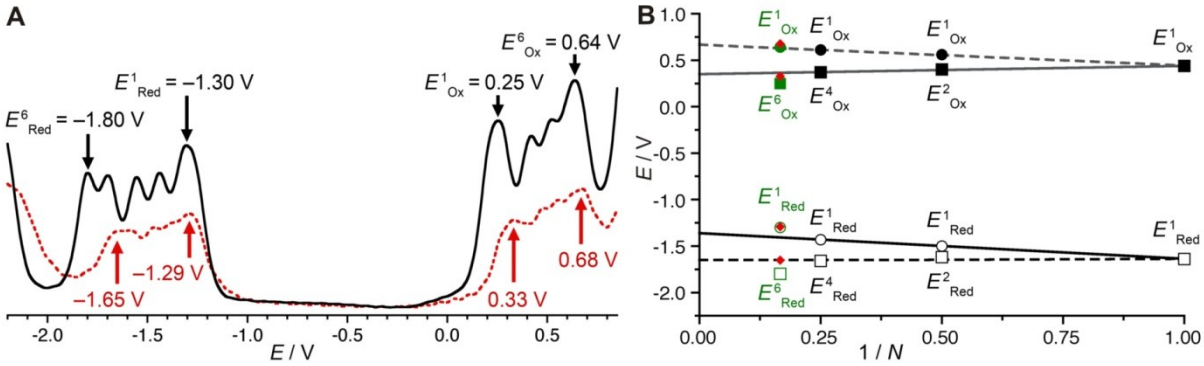

Figure 6.6. (a) Square wave voltammograms of ***c*-P$_{t\text{-Bu}}$6•T6** (black line) and ***c*-P$_{t\text{-Bu}}$6** (red line) in THF in the presence of NBu_4PF_6 (0.10 M) referenced to internal ferrocene (Fc/Fc^+ at 0 V) and (b) comparison of the oxidation and reduction potentials of ***c*-P$_{t\text{-Bu}}$6•T6** with those of ***l*-P$_{C8}$*N***, measured under the same conditions.[19]

6.6 Ultrafast Energy Migration in *c*-P$_{C8}$24.

Organized assemblies of chromophores have attracted great interest of researchers as potential models of light-harvesting complexes for practical solar energy consumption. It was hoped, in particular, that the ultrafast exciton delocalization observed in LH2[20,21] can be reproduced. However, most of the previous attempts to realize this in arrays of chromophores failed (in particular, due to their non-conjugated nature) and only showed slow exciton hopping.[22-25] The only exception to this is the recent observation of the exciton delocalization in a fully-conjugated 6 nm thiophene nanoring.[26] It was hoped, that the strong electronic coupling between individual porphyrin subunits in the full-conjugated porphyrin nanorings would assist efficient energy migration around the nanorings. Of these, studies on the ***c*-P$_{C8}$24** are particularly interesting as it slightly exceeds in size LH1 and significantly exceeds in size LH2 of purple bacteria (Figure 6.7a).

Figure 6.7b shows the steady-state absorption and emission spectra of ***c*-P$_{C8}$24** in solution. As described in Chapter 1, the π-conjugation through the butadiyne link lifts the degeneracy of the lowest-energy Q-band of porphyrin monomer subunits into transitions polarized parallel (Q_x) and perpendicular (Q_y) to the molecular backbone. Upon increasing the number of porphyrin units, such as

in ***c*-P$_{C8}$24**, the Q_y transition remains weakly visible in the absorption spectra at 600 nm, whereas the Q_x transition red-shifts and increases in magnitude with respect to the B-band (400-500 nm) indicating an increase in effective conjugation lenght.

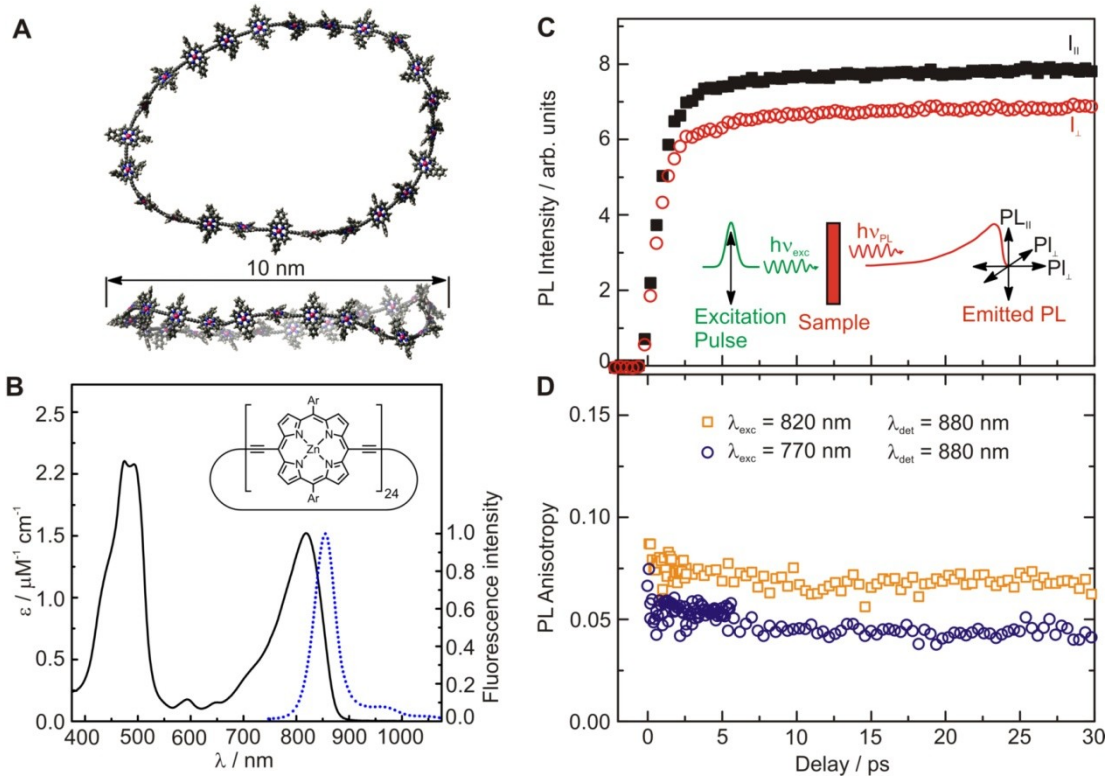

Figure 6.7. (a) Two orthogonal views of a snapshot of ***c*-P$_{C8}$24** from a molecular dynamics simulations at 300 K (MM+ force field, HyperChem™). Side chains were removed for clarity. (b) Normalized steady-states absorption (black lines) and photoluminescence (blue lines) spectra at 295K of ***c*-P$_{C8}$24** in toluene/1% pyridine. The emission was recorded after excitation at 770 nm (1.61 eV). Emission spectrum was recorded by Dr. Johannes Sprafke (c) PL emission transients of ***c*-P$_{C8}$24** in toluene/1% pyridine for excitation at a photon wavelength of 770 nm and detection at 880 nm. Solution samples were excited with pulse polarization either parall ($I_\parallel$, black squares) or perpendicular ($I_\perp$, red circles) to the detection polarization, as illustrated in the inset. (d) The derived PL anisotropy $\gamma = (I_\parallel - I_\perp)/((I_\parallel + 2I\perp)$ as a function of time after excitation at 770 nm and 820 nm, for detection at 880 nm. Measurements with excitation at 770 nm and detection at 870 nm give identical results to those with excitation at 770 nm and detection at 880 nm. Dara of plots (c) and (d) were recorded, analysed and plotted by Dr. Chaw Keong Yong, Wei-Hsin Chen and Dr. Laura Herz (Department of Physics, University of Oxford).

The extent of exciton delocalization following photoexcitation of the porphyrin nanorings was probed by the polarization-sensitive ultrafast time-resolved photoluminescence (PL) measurements performed and analysed by Dr. Chaw Keong Yong, Wei-Hsin Chen and Dr. Laura Herz (Deparment of Physics, University of Oxford). Solutions of ***c*-P$_{C8}$24** were excited by 100-fs laser pulses at 770 nm and the PL dynamics were monitored at the emission peak energy. Figure 6.7c shows the transient PL of ***c*-P$_{C8}$24** probed at the emission wavelength of 880 nm. Two types of excitation pulses were applied: with pulse polarization either parallel ($I_\parallel$) or perpendicular ($I_\perp$) to the detection polarization, as indicated in the inset of Figure 6.7c. From these traces the time-dependent PL emission anisotropy (γ) was extracted from the relationship: $\gamma = (I_\parallel - I_\perp)/((I_\parallel + 2I\perp)$. For a rigid linear butadiyne-linked porphyrin oligomer, selective excitation near the Q_x band will create an excited state with a well-defined transition dipole moment oriented along the long axis of the molecule.[27,28] For random

distribution of such linear molecules in solution, a polarized excitation will hence preferentially excite molecules oriented in the direction of this polarization, resulting in an initial PL anisotropy γ (0) of 0.4, in the absence of any depolarization machanisms. However, γ (0) = 0.1 can be expected when full polarization memory loss occcurs in the 2D plane.[29] For an ideal flat porphyrin nanoring exhibiting fully delolized absorbing states one should therefore expect γ (0) = 0.1 withing the timescale of the excitation pulse. However, due to out-of-plane ring distortions additional depolarization may arise and the value of γ drop below 0.1. Figure 6.7d shows the evolution of γ as a function of time delay after excitation for ***c*-P$_{C8}$24**. Within first 30 ps after excitation γ is constant, which indicates that slower effects such as molecular re-orientation are absent. Interestingly, γ depends on the excitation energy but not the emission energy. Exciting ***c*-P$_{C8}$24** at the high-energy edge of the Qx band results in a relatively low value of γ (0) = 0.056 suggesting that significant out-of-plane distortions are possible and that these distorted conformers have blue-shifted absorption. In contrast, exciting nearter to the red edge of the absorption (820 nm), the γ (0) value rises to 0.08, which is close to the value expected for full excitation delocalization on a planar ring. As a reference, similar measurements were performed for ***l*-P$_{C8}$18$_{THS,THS}$** (not presented here) which showed that this linear system retains significantly more polarization memory as compared to ***c*-P$_{C8}$24**.

These results demonstrate that the absorption state is fully delocalized even in such a giant system as ***c*-P$_{C8}$24**, which represents the longest delocalization length among synthetic molecular rings examined to date. Exciton dynamics described above for the case of ***c*-P$_{C8}$24** reproduces that observed in LH2 of purple bacteria, which similarly exhibited transition anisotropy values of ≤0.1 within a time scale of ~100 fs when BChl *a* B850 is probed by absorption[30] and emission[20] spectroscopy.

6.8 Conclusions and Outlook

Crystal structures of ***c*-P$_{t\text{-Bu}}$6•T6** and ***c*-P$_{t\text{-Bu}}$12•(T6)$_2$** provide valuable information about the geometry and distribution of strain in these unusual species. In both molecules, most of the distortion is located in the acetylenic bridges. The solid-state structure of ***c*-P$_{t\text{-Bu}}$6•T6** reveals a surprising ruffling of the whole nanoring, indicating that the template is slightly too small for the cavity of the macrocycle. STM was used to directly visualize molecules of ***c*-P$_{C8}$12•(T6)$_2$**, although in this case, due to the low resolution of the STM images and the high proportion of template-free molecules formed during deposition, little information about the structure of this molecule could be obtained.

The electrochemical HOMO–LUMO gap (E_g = 1.55 V) of ***c*-P$_{t\text{-Bu}}$6•T6** is lower than that of the analogous linear oligomers (including the infinite linear polymer) and confirms that the bending of the π-conjugated surface leads to enhanced conjugation, as previously concluded based on the data of steady-state optical spectroscopy. However, the most striking results stemmed from the data of PL anisotropy studies, which suggest that even in a giant 10 nm ***c*-P$_{C8}$24** an excited state delocalizes around the whole ring, similarly to natural light harvesting systems. These results suggest that

porphyrin nanorings may offer a wealth of possible technological applications as light-harvesting materials.

6.9 References

[1] J. K. Sprafke, D. V. Kondratuk, M. Wykes, A. L. Thompson,M. Hoffmann, R. Drevinskas, W. H. Chen, C. K. Yong, J. Kärnbratt,J. E. Bullock, M. Malfois, M. R. Wasielewski, B. Albinsson, L. M. Herz, D. Zigmantas, D. Beljonne, H. L. Anderson, *J. Am. Chem. Soc.* **2011**, *133*, 17262–17273.

[2] H. J. Hogben, J. K. Sprafke, M. Hoffmann, M. Pawlicki, H. L. Anderson, *J. Am. Chem. Soc.* **2011**, *133*, 20962**–**20969**.**

[3] J. Song, N. Aratani, P. Kim, D. Kim, H. Shinokubo, A. Osuka, *Angew. Chem., Int. Ed.* **2010**, *49*, 3617–3620.

[4] L. Palatinus, G. J. Chapuis, *Appl. Cryst.* **2007**, *40*, 786–790.

[5] P. W. Betteridge, J. R. Carruthers, R. I. Cooper, K. Prout, D. J. Watkin, *J. Appl. Cryst.* **2003**, *36*, 1487.

[6] M. Hoffmann, J. Kärnbratt, M.-H. Chang, L. M. Herz, B. Albinsson, H. L. Anderson, *Angew. Chem., Int. Ed.* **2008**, *47*, 4993–4996.

[7] P. N. Taylor, J. Huuskonen, G. Rumbles, R. T. Aplin, E. Williams, H. L. Anderson, *Chem. Commun.* **1998**, 909–910.

[8] J. Song, N. Aratani, H. Shinokubo, A. Osuka, *J. Am. Chem. Soc.* **2010**, *132*, 16356–16357.

[9] S. Eisler, R. McDonald, G. R. Loppnow, R. R. Tykwinski, *J. Am. Chem. Soc.* **2000**, *122*, 6917–6928.

[10] S. K. Collins, G. P. A. Yap, A. G. Fallis, *Angew. Chem., Int. Ed.* **2000**, *39*, 385–388.

[11] L. Zhang, H. Gopee, D. L. Hughes, A. N. Cammidge, *Chem. Commun.* **2010**, *46*, 4255–4257.

[12] F. Mitzel, C. Boudon, J.-P. Gisselbrecht, P. Seiler, M. Gross, F. Diederich, *Chem. Commun.* **2003**, 1634– 1635.

[13] J. Ojima, N. Hiraiwa, H. Higuchi, I. Kobayashi, K. Yamamoto, T. Yoshida, T. Adachi, H. Matsubara, G. J. Yamamoto, *Chem. Soc., Perkin Trans. 1* **1996**, 2755–2763.

[14] G. Yamamoto, Y. Mazaki, R. Kobayashi, H. Higuchi, J. Ojima, *Chem. Soc., Perkin Trans. 1* **1997**, 3183–3188.

[15] W. A. Chalifoux, R. McDonald, M. J. Ferguson, R. R. Tykwinski, *Angew. Chem., Int. Ed.* **2009**, *48*, 7915–7919.

[16] M. C. O'Sullivan, J. K. Sprafke, D. V. Kondratuk, C. Rinfray, T. D. W. Claridge, A. Saywell, M. O. Blunt, J. N. O'Shea, P. H. Beton, M. Malfois, H. L. Anderson, *Nature* **2011**, *469*, 72–75.

[17] M. U. Winters**,** E. Dahlstedt**,** H. E. Blades**,** C. J. Wilson**,** M. J. Frampton**,** H. L. Anderson**,** B. Albinsson**,** *J. Am. Chem. Soc.* **2007**, *129*, 4291–4297.

[18] F. Zhang, G. Goetz, H. D. F. Winkler, C. A. Schalley, P. Bauerle, *Angew. Chem., Int. Ed.* **2009**, *48*, 6632–6635.

[19] T. Iwamoto, Y. Watanabe, Y.-I. Sakamoto, T. Suzuki, S. Yamago, *J. Am. Chem. Soc.* **2011**, *133*, 8354–8361.

[20] R. Jimenez, S. N. Dikshit, S. E. Bradforth, G. R. Fleming, *J. Phys. Chem.* **1996**, *100*, 6825–6834.

[21] J. L. Herek, W. Wohlleben, R. J. Cogdell, D. Zeidler, M. Motzkus, *Nature* **2002**, *417*, 533–535.

[22] N. Aratani, D. Kim, A. Osuka, *Acc. Chem. Res.* **2009**, *42*, 1922–1934.

[23] M. S.Choi, T. Yamazaki, I. Yamazaki, T. Aida, *Angew. Chem., Int. Ed.* **2004**, *43*, 150–158.

[24] D. Holten, D. F. Bocian, J. S. Lindsey, Acc. Chem. Res. **2002**, *35*, 57–69.

[25] M. R. Wasielewski, *Acc. Chem. Res.* **2009**, *42*, 1910–1921.

[26] J. E. Donehue, O. P. Varnavski, R. Cemborski, M. Iyoda, T. J. Goodson *J. Am. Chem. Soc.* **2011**, *133*, 4819–4828.

[27] M. H. Chang, M. Hoffmann, H. L. Anderson, L. M. Herz *J. Am. Chem. Soc.* **2008**, *130*, 10171–10178.

[28] V. S.-Y. Lin, S. G. DiMagno, M. J. Therien *Science* **1994**, *264*, 1105–1111.

[29] D. Magde *J. Chem. Phys.* ***1978***, *68*, 3717–3733.
[30] J. T. M. Kennis, A. M. Streltsov, S. I. E. Vulto, T. J. Aartsma, T. Nozawa, J. Amesz, *J. Phys. Chem. B* **1997**, *101*, 7827–7834.

Chapter 7

Experimental Procedures

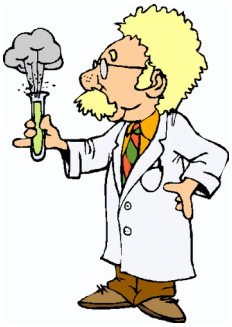

This chapter contains experimental details about the techniques used in this thesis as well as experimental procedures and characterization data for known and new compounds synthesized in the course of this work.

7.1 General Procedures

All manipulations of air- or water- sensitive compounds were performed using standard high-vacuum techniques. When required, solutions were degassed by boiling under reduced pressure followed by saturating with N_2 or freeze-pump-thaw degassing cycle followed by backfilling with N_2. This cycle was then repeated twice further. Dried THF, CH_2Cl_2 and toluene were obtained by passing through alumina under N_2 pressure. *i*-Pr_2NH was distilled over CaH_2 under nitrogen before use. Tert-butyl-3,4-bis(3-butoxy-4-(pyridin-4-ylethynyl)phenyl)-1*H*-pyrrole-2-carboxylate for the synthesis of octa-dentate template **T8** was prepared by Dr. Georg Fischer, Dr. Melanie O'Sullivan and Corentine Rinfray; pentadentate template **T5** was prepared by Dr. Hannah Hogben; zinc 5,15-bis-(3,5-*bis*-octyloxy-phenyl)-10,20-dibromo-porphyrin for the synthesis of fully protected octyloxy porphyrin monomer ***l*-$\mathbf{P_{C8}1_{THS,THS}}$** was made by Dr. Markus Hoffmann and Dr. Craig Wilson. All other reagents were used as commercially supplied. Flash column chromatography was carried out on silica gel 60 under positive pressure. Where mixtures of solvents were used, ratios are reported by volume. Alumina columns were run using activated basic alumina (Brockmann I, standard grage, ~150 mesh, 58 Å, Sigma Aldrich). For known compounds, only ^{1}H NMR spectra are presented, however, in all cases MALDI-ToF spectra were also recorded.

NMR data were collected at 700 MHz using a Bruker AVIII 700, at 500 MHz using a Bruker AVII 500 or a Bruker DRX 500, at 400 MHz using a Bruker DPX 400 or at 250 MHz using a Bruker DPX250. Samples were measured in $CDCl_3$ or $CDCl_3$/1% d_5-pyridine at 298 K and chemical shifts are quoted as parts per million (ppm) relative to residual $CHCl_3$ at δ_H = 7.27 ppm. Coupling constants (*J*) are quoted in Hertz (Hz). When diffusion editing of ^{1}H spectra was used to preferentially suppress solvent resonances the bipolar-pair LED sequence (BPP-LED) was employed. Mass spectra were measured by electrospray ionisation (ESI) using a Bruker micOTOF or by the matrix assisted laser desorption ionisation time of flight (MALDI-TOF) technique on a Micromass MALDI micro MX, by the EPSRC National Mass Spectrometry Service Centre on a Applied Biosystems Voyager-DE-STR and by Dr. Gareth Smith (University of Manchester). The MALDI-TOF mass spectra were recorded using dithranol (1,8,9-trihydroxyanthracene) or DCTB (*trans*-2-[3-(4-*tert*-butylphenyl)-2-methyl-2-propenylidene]malononitrile) as the matrix. Only the peak of the molecular ion (100%, most intense peak) is given.

Size exclusion chromatography (SEC) was carried out using Bio-Beads S-X1, 200-400 mesh (Bio Rad). Analytical and semi-preparative GPC was carried out using the line of PLgel 3 μm Mixed-E columns (2 × 300 mm length, 7.5 mm diameter) and Plgel 5 μm Mixed-D columns (3 × 300 mm length, 7.5 mm diameter) in THF/1% pyridine or toluene as eluent with a flow rate of 1.0 mL/min. Preparative GPC was carried out using the line of PLgel 10μm 500 Å columns (600+300 mm length, 25 mm diameter) and Plgel 10μm 1000 Å column (300 mm length, 25 mm diameter) in toluene with a

flow rate of 8.5 mL/min. Analytical and semi-preparative GPC was also carried out on Shimadzu Recycling GPC system equipped with LC-20 AD pump, SPD-20A UV detector and a set of JAIGEL 3H (20 x 600 mm) and JAIGEL 4H (20 x 600 mm) columns in toluene/1% pyridine as eluent at a flow rate of 3.5 mL/min.

Steady-state UV-*vis*-NIR absorption spectra were measured with Perkin Elmer Lambda 9 and Perkin Elmer Lambda 20 photospectrometers with a scan rate of 960 nm/min. A steady-state fully corrected emission spectrum of ***c*-$\mathbf{P_{C8}}$24** was measured by Dr. Johannes using a custom-build system consisting of a 75 W Xenon Lamp and a nitrogen cooled InGaAs detector. The photoluminescence up-conversion technique was used to detect the PL emitted from solutions held in a quartz cuvette. Samples were excited with the output of a mode-locked Ti:Sapphire laser providing pulses of 100 fs duration at a photon energy of 1.61 eV (770 nm) or 1.51 eV(820 nm) and a repetition rate of 80 MHz. The emerging photoluminescence was collected in a front-excitation, back-emisssion mode and optically gated in a beta-barium-oxide (BBO) crystal by a time-delayed linearly-polarized gate pulse.

The synchrotron radiation small angle X-ray scattering (SAXS) data were collected using standard procedures on the I22 beamline at Diamond Light Source (UK) equipped with a photon counting detector. The beam was focused onto the detector placed at a distance of 1.25 m from the sample cell. The covered range of momentum transfer was $0.03 < q < 1.0$ Å^{-1} ($q = 4\pi \sin(\theta)/\lambda$ where 2θ is the scattering angle and $\lambda = 1.00$ Å is the X-ray wavelength). The data were normalized to the intensity of the incident beam; the scattering of the solvent was subtracted using an in-house program. To check for radiation damage and aggregation during the SAXS experiment, the data were collected in 10 successive 60 s frames. All SAXS measurements were performed in either toluene or toluene/1% pyridine at known concentrations (~10^{-4} M) in a solution cell with mica windows.

Molecular modelling was carried out using the MM+ force field (molecular mechanics) integrated in the HyperChem™ 8.0 (Hypercube Inc.) package.

7.2 Synthetic Procedures for Previously Known Compounds

2,2'-Dipyrromethane

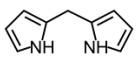

Formaldehyde (33% w/w solution in water, 8.1 mL, 97.0 mmol) was added to pyrrole (150 mL, 2.16 mol) and the solution degassed. Trifluoroacetic acid (0.81 mL, 10.9 mmol) was added with vigorous stirring, and the reaction was allowed to proceed for 5 minutes before CH_2Cl_2 (100 mL) was added, followed immediately by Na_2CO_3 (aq) (sat., 100 mL). The organic layer was washed with Na_2CO_3 (aq) (sat., 2 × 100 mL) and water (100 mL). Distillation of the oily residue in a Kugelrohr apparatus yielded the product as a white crystalline solid (5.70 g, 40%).

^{1}H NMR (250 MHz, $CDCl_3$) δ_H 3.96 (s, 2H, -CH_2), 6.06 (m, 2H, -ArH_β), 6.17 (m, 2H, -ArH_β), 6.66 (m, 2H, -ArH_α), 7.83 (br. s, 2H, -N*H*). As lit.[2]

Ethynyltrihexylsilane[2]

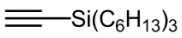

Chlorotrihexylsilane (6.4 mL, 17.5 mmol) was added dropwise under N_2 to a stirred solution of ethynylmagnesium chloride (0.5 M in THF, 42 mL, 21.0 mmol). The reaction mixture was heated at reflux for 1 h. before HCl (aq) (2 M, 125 mL) was added. The organic layer was extracted with Et_2O (2 × 50 mL) and solvents removed. The flash chromatography using a short silica gel column (CH_2Cl_2) yielded a yellow oil (5.34 g, 99%).

^{1}H NMR (400 MHz, $CDCl_3$) δ_H 0.56–0.63 (m, 6H, -CH_2), 0.83–0.89 (m, 9H, -CH_3), 1.26–1.41 (m, 24H, -CH_2), 2.35 (s, 1H, ≡C*H*). as lit.[2]

Free Base 5,15-bis-(3,5-bis-*tert*-butyl-phenyl)-porphyrin *l*-P$_{t\text{-Bu}}$1$_{FB}$ [2]

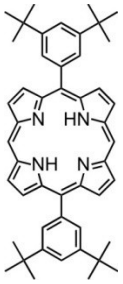

3,5-Bis(*tert*-butyl)benzaldehyde[3] (0.9 g, 4.1 mmol) and dipyrromethane (0.6 g, 4.1 mmol) were placed in a dry flask under N_2 and dissolved in CH_2Cl_2 (800 mL). The solution was degassed three times by repeated evacuation and purging with nitrogen. Trifluoroacetic acid (0.20 mL, 2.6 mmol) was added and the reaction mixture stirred in the dark for 3 h. DDQ (1.19 g, 5.25 mmol) was added and stirring continued for 0.5 h. After quenching of the acid by addition of triethylamine (4.0 mL) the mixture was passed over a short silica column (CH_2Cl_2). Recrystallization from CH_2Cl_2/methanol gave a red powder (0.69 g, 49%).

^{1}H NMR (400 MHz, $CDCl_3$): δ_H -3.10 (br. s, 2H, N*H*), 1.58 (s, 36H, -*t*-Bu*H*), 7.85 (t, 2H, *J* = 2.0 Hz, -ArH_{para}), 8.16 (d, 4H, *J* = 2.0 Hz, -ArH_{ortho}), 9.15 (d, 4H, *J* = 4.5 Hz, -ArH_β), 9.42 (d, 4H, *J* = 4.5 Hz, -ArH_β), 10.33 (s, 2H, -ArH_{meso}). As lit.[2]

Zinc 5,15-bis-(3,5-bis-*tert*-butyl-phenyl)-porphyrin *l*-$\mathbf{P_{t\text{-}Bu}1_{Zn}}$[2]

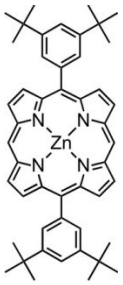

$Zn(OAc)_2 \cdot 2H_2O$ (1.13 g, 5.16 mmol) was dissolved in methanol (10 mL) and added to a solution of free-base porphyrin (0.69 g, 1.0 mmol) in $CHCl_3$ (100 mL). The reaction was stirred at room temperature for 1 h. The mixture was passed through a short silica gel column (CH_2Cl_2). The crude product was recrystallized by layer addition (CH_2Cl_2/methanol) to give a purple powder (0.75 g, 99%).

^{1}H NMR (400 MHz, $CDCl_3$): δ_H 1.59 (s, 36H, -*t*-Bu*H*), 7.86 (t, 2H, *J* = 2.0 Hz, -ArH_{ortho}), 8.17 (d, 4H, *J* = 2.0 Hz, -ArH_{ortho}), 9.23 (d, 4H, *J* = 4.5 Hz, -ArH_{β}), 9.45 (d, 4H, *J* = 4.5 Hz, -ArH_{β}), 10.36 (s, 2H, -ArH_{meso}). As lit.[2]

Zinc 5,15-bis-(3,5-bis-*tert*-butyl-phenyl)-10,20-dibromo-porphyrin *l*-$\mathbf{P_{t\text{-}Bu}1_{Br,Br}}$[2]

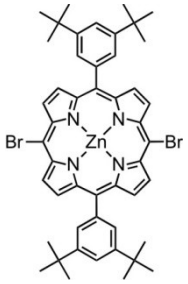

To a solution of zinc porphyrin base ***l*-$\mathbf{P_{t\text{-}Bu}1_{Zn}}$** (0.53 g, 0.7 mmol) in $CHCl_3$ (25 mL) and pyridine (0.33 mL) was added dropwise solution of *N*-bromosuccinimide (0.25 g, 1.4 mmol) in $CHCl_3$ (20 mL). After stirring in the dark for 60 minutes, the reaction was quenched with acetone (100 mkL). The solvent was removed and the crude product recrystallized by layer addition from CH_2Cl_2/methanol to give a purple solid (0.50 g, 79%).

^{1}H NMR (400 MHz, $CDCl_3$): δ_H 1.50 (s, 36H, -*t*-Bu*H*), 7.80 (t, *J* = 2.0 Hz, -ArH_{para}), 7.99 (d, *J* = 2.0 Hz, 4H, -ArH_{ortho}), 8.91 (d, *J* = 4.5 Hz, 4H, -ArH_{β}), 9.66 (d, *J* = 4.5 Hz, 4H, -ArH_{meso}). As lit.[2]

Zinc 5,15-bis-(3,5-bis-*tert*-butyl-phenyl)-10,20-bis-trihexylsilanylethynyl-porphyrin *l*-$\mathbf{P}_{t\text{-Bu}}\mathbf{1}_{\mathbf{THS,THS}}$[2]

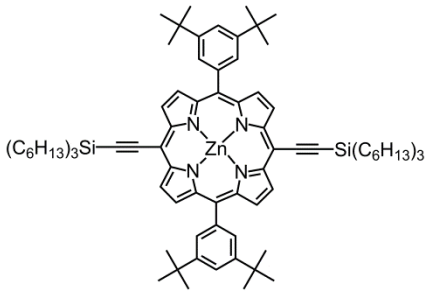

tris-(Dibenzylideneacetone)-di-palladium(0) (64 mg, 70 µmol), copper(I) iodide (28 mg, 0.14 mmol), triphenylphosphine (36 mg, 0.14 mmol) and dibromoporphyrin ***l*-$\mathbf{P}_{t\text{-Bu}}\mathbf{1}_{\mathbf{Br,Br}}$** (0.64 g, 0.7 mmol) were placed in a dried Schlenk tube under argon. Toluene (45 mL), *i*-Pr_2NH (24 mL) and pyridine (1.27 mL) were added and the reaction mixture deoxygenated. Trihexylsilyl acetylene (0.81 mL, 2.1 mmol) was added by syringe. The reaction mixture was stirred at 80 °C for 2 h., solvents removed and the residue passed through a short silica gel column (CH_2Cl_2). Recrystallization by layer addition (CH_2Cl_2/methanol) gave the product ***l*-$\mathbf{P}_{t\text{-Bu}}\mathbf{1}_{\mathbf{THS,THS}}$** as a green solid (0.96 g, 99 %).

^{1}H NMR (400 MHz, $CDCl_3$): δ_H 0.90 (t, 18H, J = 7.0 Hz, -CH_3), 1.02 (m, 12H, -CH_2), 1.39 (m, 24H, -CH_2), 1.58–1.51 (m, 48H, -CH_2, -*t*-BuH), 1.77 (m, 12H, -CH_2), 7.83 (t, 2H, J = 1.5 Hz, -ArH_{para}), 8.06 (d, 4H, J = 1.5 Hz, -ArH_{ortho}), 8.98 (d, 4H, J = 4.5 Hz, -ArH_β), 9.74 (d, 4H, J = 4.5 Hz, -ArH_β). As lit.[2]

Zinc 5,15-bis-(3,5-bis-*tert*-butyl-phenyl)-10-ethynyl-20-trihexylsilanylethynyl-porphyrin *l*-$\mathbf{P}_{t\text{-Bu}}\mathbf{1}_{\mathbf{H,THS}}$[2]

Zinc 5,15-bis-(3,5-bis-*tert*-butyl-phenyl)-10,20-bis-ethynyl-porphyrin *l*-$\mathbf{P}_{t\text{-Bu}}\mathbf{1}$[2]

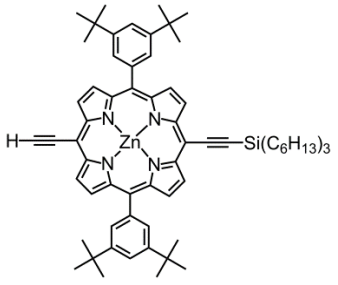

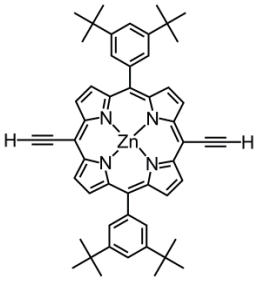

Protected porphyrin monomer ***l*-$\mathbf{P}_{t\text{-Bu}}\mathbf{1}_{\mathbf{THS,THS}}$** (1.91 g, 1.40 mmol) was dissolved in CH_2Cl_2 (325 mL) and $CHCl_3$ (325 mL). Tetra-*n*-butylammonium fluoride (1.6 mL, 1 M in THF, 1.6 mmol) was added to the stirred solution. The progress of the reaction was monitored by TLC until an optimal product mixture was reached and the reaction then quenched with CH_3COOH (1.0 mL, 17.0 mmol). The volume was reduced and the mixture passed through a short silica gel column (CH_2Cl_2). Column chromatography (50:1:1, 40-60 petroleum ether : ethyl acetate : pyridine) gave ***l*-$\mathbf{P}_{t\text{-Bu}}\mathbf{1}_{\mathbf{H,THS}}$** (0.47 g, 37 %) and ***l*-$\mathbf{P}_{t\text{-Bu}}\mathbf{1}$** (0.31 g, 33 %) as green solids.

***l*-P$_{t\text{-Bu}}$1$_{H,THS}$**

^{1}H NMR (400 MHz, $CDCl_3$): δ_H 0.91 (t, 9H, J = 7.0 Hz, -CH_3), 1.01–1.05 (m, 6H, -CH_2), 1.37–1.44 (m, 12H, -CH_2), 1.52–1.57 (m, 42H, -CH_2, -*t*-BuH), 1.76–1.81 (m, 6H, -CH_2), 4.15 (s, 1H, ≡CH), 7.81 (t, 2H, J = 2.0 Hz, -ArH_{para}), 8.03 (d, 4H, J = 2.0 Hz, -ArH_{ortho}), 8.92 (m, 4H, -ArH_β), 9.68 (m, 4H, -ArH_β). As lit.[2]

***l*-P$_{t\text{-Bu}}$1**

^{1}H NMR (400 MHz, $CDCl_3$): δ_H 1.55 (s, 36H, -*t*-BuH), 4.15 (s, 2H, ≡CH), 7.79 (t, 2H, J = 1.5 Hz, -ArH_{para}), 8.01 (d, 4H, J = 1.5 Hz, -ArH_{ortho}), 8.91 (d, 4H, J = 4.5 Hz, -ArH_β), 9.67 (d, 4H, J = 4.5 Hz, -ArH_β). As lit.[2]

Zinc 5,15-bis-(3,5-*tert*-butyl-phenyl)-10,20-trihexylsilanylethynyl-porphyrin dimer *l*-P$_{t\text{-Bu}}$2$_{THS,THS}$[2]

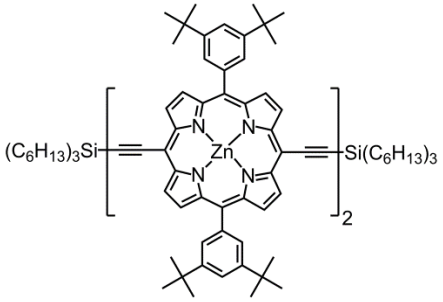

$Pd(PPh_3)_2Cl_2$ (14 mg, 20 µmol), copper(I) iodide (38 mg, 0.20 mmol) and 1,4-benzoquinone (28 mg, 0.26 mmol) were dissolved in toluene (6 mL) and *i*-Pr_2NH (2 mL). The solution of half-protected porphyrin monomer ***l*-P$_{t\text{-Bu}}$1$_{H,THS}$** (212 mg, 0.196 mmol) in toluene (4 mL) was added to the catalysts solution and the reaction mixture stirred for 30 min. The reaction mixture was passed through a short silica gel column (CH_2Cl_2) and purified by size exclusion chromatography on Biobeads SX-1 (toluene). Recrystallization by layer addition (CH_2Cl_2/methanol) gave the product as a dark green solid (190 mg, 90%).

^{1}H NMR (400 MHz, $CDCl_3$/1% d_5-pyridine): δ_H 0.91 (t, 18H, J = 7.0 Hz, -CH_3), 1.00–1.04 (m, 12H, -CH_2), 1.35–1.45 (m, 24H, -CH_2), 1.51–1.61 (m, 72H, -*t*-BuH, -CH_2), 1.73–1.82 (m, 12H, -CH_2), 7.81–7.82 (m, 4H, -ArH_{para}), 8.05 (d, 8H, J = 1.5 Hz, -ArH_{ortho}), 8.89 (d, 4H, J = 4.5 Hz, -ArH_β), 8.99 (d, 4H, J = 4.5 Hz, -ArH_β), 9.66 (d, 4H, J = 4.5 Hz, -ArH_β), 9.89 (d, 4H, J = 4.5 Hz, -ArH_β). As lit.[2]

Zinc 5,15-bis-(3,5-*tert*-butyl-phenyl)-10-ethynyl-20-trihexylsilanylethynyl-porphyrin dimer *l*-$\mathbf{P}_{t\text{-Bu}}\mathbf{2}_{\mathbf{H,THS}}$[2]

Zinc 5,15-bis-(3,5-bis-octyloxy-phenyl)-10,20-bis-ethynyl-porphyrin dimer *l*-$\mathbf{P}_{t\text{-Bu}}\mathbf{2}$[3]

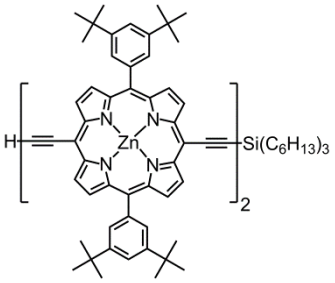

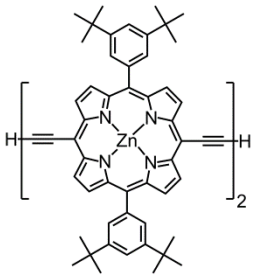

Tetra-*n*-butylammonium fluoride (0.28 mL, 1.00 M in THF, 0.28 mmol) was added to a solution of porphyrin dimer ***l*-$\mathbf{P}_{t\text{-Bu}}\mathbf{2}_{\mathbf{THS,THS}}$** (200 mg, 0.093 mmol) in a mixture of CH_2Cl_2 (20 mL) and $CHCl_3$ (20 mL). The reaction was monitored by TLC and after achieving the maximum formation of the half-protected product stopped by adding CH_3COOH (0.10 mL, 1.79 mmol). The volume was reduced and the reaction mixture passed through a short silica gel column (CH_2Cl_2/1% pyridine). Chromatography on silica gel (10:1:1, 40-60 °C petroleum ether : ethyl acetate : pyridine) and recrystallization by layer addition (CH_2Cl_2/methanol) yielded ***l*-$\mathbf{P}_{t\text{-Bu}}\mathbf{2}_{\mathbf{H,THS}}$** (72 mg, 68%) and ***l*-$\mathbf{P}_{t\text{-Bu}}\mathbf{2}$** (25 mg, 28%) as green solids.

***l*-$\mathbf{P}_{t\text{-Bu}}\mathbf{2}_{\mathbf{H,THS}}$**

^{1}H NMR (500 MHz, $CDCl_3$/1% d_5-pyridine): δ_H 0.91 (t, 9H, J = 6.5 Hz, -CH_3), 1.03 (m, 6H, -CH_2), 1.40 (m, 12H, -CH_2), 1.56 (m, 6H, -CH_2), 1.58 (s, 72H, -*t*-BuH), 1.76 (m, 6H, -CH_2), 4.18 (s, 1H, ≡CH), 7.82 (t, 2H, J =2.0 Hz, -ArH_{para}), 7.83 (t, 2H, J =2.0 Hz, -ArH_{para}), 8.06 (d, 4H, J = 2.0 Hz, -ArH_{ortho}), 8.07 (d, 4H, J = 2.0 Hz, -ArH_{ortho}), 8.90 (d, 2H, J = 5.0 Hz, -ArH_β), 8.94 (d, 2H, J = 5.0 Hz, -ArH_β), 9.00 (d, 2H, J = 5.0 Hz, -ArH_β), 9.01 (d, 2H, J = 5.0 Hz, -ArH_β), 9.68 (d, 2H, J = 5.0 Hz, -ArH_β), 9.69 (d, 2H, J = 5.0 Hz, -ArH_β), 9.90 (d, 2H, J = 5.0 Hz, -ArH_β), 9.92 (d, 2H, J = 5.0 Hz, -ArH_β). As lit.[2]

***l*-$\mathbf{P}_{t\text{-Bu}}\mathbf{2}$**

^{1}H NMR (400 MHz, $CDCl_3$/1% d_5-pyridine): δ_H 1.56 (s, 72H, -*t*-BuH), 4.17 (s, 2H, ≡CH), 7.82 (br. s, 4H, -ArH_{para}), 8.05 (br. s, 8H, -ArH_{ortho}), 8.92 (d, 4H, J = 4.5 Hz, -ArH_β), 9.00 (d, 4H, J = 4.5 Hz, -ArH_β), 9.67 (d, 4H, J = 4.5 Hz, -ArH_β), 9.90 (d, 4H, J = 4.5 Hz, -ArH_β). As lit.[2]

Zinc 5,15-bis-(3,5-*tert*-butyl-phenyl)-10,20-trihexylsilanylethynyl-porphyrin tetramer

***l*-P$_{t\text{-Bu}}$4$_{\text{THS,THS}}$**[2,4]

Zinc 5,15-bis-(3,5-*tert*-butyl-phenyl)-10,20-trihexylsilanylethynyl-porphyrin hexamer

***l*-P$_{t\text{-Bu}}$6$_{\text{THS,THS}}$**[4]

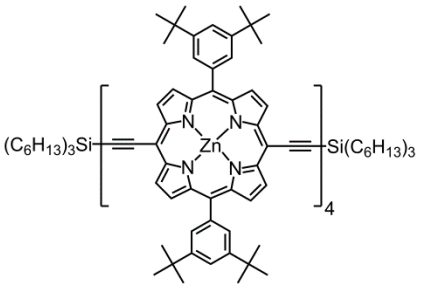

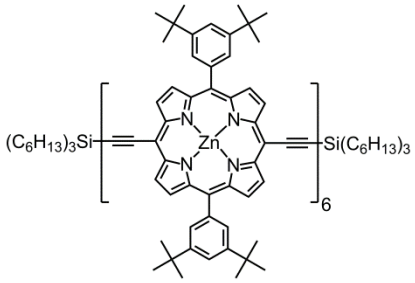

Fully-deprotected linear porphyrin dimer ***l*-P$_{t\text{-Bu}}$2** (33.0 mg, 20.7 μmol) and half-deprotected linear porphyrin dimer ***l*-P$_{t\text{-Bu}}$2$_{\text{H,THS}}$** (350 mg, 0.187 mmol) were dissolved in a mixture of toluene (48 mL). A catalyst solution was prepared by dissolving dichlorobis(triphenylphosphine)-palladium(II) (14.5 mg, 20.7 μmol), copper(I) iodide (39.5 mg, 0.207 mmol) and 1,4-benzoquinone (31.4 mg, 0.29 mmol) in the mixture of toluene (24.0 mL) and freshly distilled *i*-Pr$_2$NH (3.5 mL) and added to the solution of porphyrin dimers. The reaction mixture was stirred at 20 °C for 1 h. The reaction mixture was passed through a short silica column (CH_2Cl_2/1% pyridine) to remove the catalysts and then over a size exclusion column on Biobeads SX-1 (toluene/1% pyridine) to remove the 1,4-benzoquinon. Preparative GPC (toluene/10% pyridine) yielded ***l*-P$_{t\text{-Bu}}$4$_{\text{THS,THS}}$** (271 mg, 99%) and ***l*-P$_{t\text{-Bu}}$6$_{\text{THS,THS}}$** (72 mg, 65%) as brown solids.

***l*-P$_{t\text{-Bu}}$4$_{\text{THS,THS}}$**

^{1}H NMR (500 MHz, $CDCl_3$/1% d_5-pyridine): δ_H 0.92 (t, 18H, J = 7.0 Hz, -CH_3), 1.05 (m, 12H, -CH_2), 1.42 (m, 24H, -CH_2), 1.56 (m, 12H, -CH_2), 1.59 (s, 72H, -*t*-BuH), 1.61 (s, 72H, -*t*-BuH), 1.81 (m, 12H, -CH_2), 7.85 (t, 4H,J = 2.0 Hz, -ArH_{para}), 7.87 (t, 4H,J = 2.0 Hz, -ArH_{para}), 8.07 (d, 8H, J = 2.0 Hz, -ArH_{ortho}), 8.11 (d, 8H, J = 2.0 Hz, -ArH_{ortho}), 8.88 (d, 4H, J = 5.0 Hz, -ArH_β), 8.98 (d, 4H, J = 5.0 Hz, -ArH_β), 8.99 (d, 4H, J = 5.0 Hz, -ArH_β), 9.00 (d, 4H, J = 5.0 Hz, -ArH_β), 9.67 (d, 4H, J = 5.0 Hz, -ArH_β), 9.90 (d, 4H, J = 5.0 Hz, -ArH_β), 9.91 (d, 4H, J = 5.0 Hz, -ArH_β), 9.92 (d, 4H, J = 5.0 Hz, -ArH_β). As lit.[4]

***l*-P$_{t\text{-Bu}}$6$_{\text{THS,THS}}$**

^{1}H NMR (500 MHz, $CDCl_3$/1% d_5-pyridine): δ_H 0.92 (t, 18H, J = 7.0 Hz, -CH_3), 1.05 (m, 12H, -CH_2), 1.41 (m, 24H, -CH_2), 1.58 (m, 12H, -CH_2), 1.61 (s, 144H, -*t*-BuH), 1.62 (s, 72H, -*t*-BuH), 1.81 (m, 12H, -CH_2), 7.85 (t, 4H, J = 2.0 Hz, -ArH_{para}), 7.87 (t, 4H, J = 2.0 Hz, -ArH_{para}), 7.88 (t, 4H, J = 2.0 Hz, -ArH_{para}), 8.06 (d, 8H, J = 2.0 Hz, -ArH_{ortho}), 8.11 (d, 8H, J = 2.0 Hz, -ArH_{ortho}), 8.12 (d, 8H, J = 2.0 Hz, -ArH_{ortho}), 8.87 (d, 4H, J = 5.0 Hz, -ArH_β), 8.99 (m, 20Hz, -ArH_β), 9.67 (d, 4H, J = 5.0 Hz, -ArH_β), 9.90 (m, 20Hz, -ArH_β). As lit.[4]

Zinc 5,15-bis-(3,5-bis-octyloxy-phenyl)-10,20-bis-trihexylsilanylethynyl-porphyrin *l*-$\mathbf{P_{C8}1_{THS,THS}}$[2]

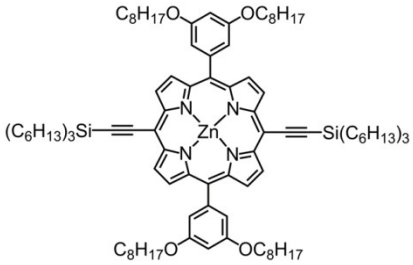

tris-(Dibenzylideneacetone)-di-palladium(0) (153 mg, 0.17 mmol), copper(I) iodide (63.7 mg, 0.33 mmol), triphenylphosphine (87.7 mg, 0.33 mmol) and corresponding dibromoporphyrin (2.0 g, 1.67 mmol) were placed in a dried Schlenk tube under argon. Toluene (110 mL), *i*-Pr_2NH (55 mL) and pyridine (3.0 mL) were added and the reaction mixture deoxygenated. Trihexylsilyl acetylene (1.94 mL, 5.01 mmol) was added. The reaction mixture was stirred at 60 °C for 2 h., solvents removed and the residue passed through a short silica gel column (CH_2Cl_2). Recrystallization by layer addition (CH_2Cl_2/methanol) gave the product ***l*-$\mathbf{P_{C8}1_{THS,THS}}$** as a green solid (2.75 g, 99 %).

^{1}H NMR (400 MHz, $CDCl_3$/1% d_5-pyridine): δ_H 1.15–1.01 (m, 40H, -CH_2,-CH_3), 1.34–1.68 (m, 78H, -CH_2), 1.75–1.94 (m, 20H, -CH_2), 4.15 (t, 8H, J = 6.5 Hz, -OCH_2), 6.89 (t, 2H, J = 2.0 Hz, -ArH_{para}), 7.32 (d, 4H, J = 2.0 Hz, -ArH_{ortho}), 9.08 (d, 4H, J = 4.5 Hz, -ArH_β), 9.76 (d, 4H, J = 4.5 Hz, -ArH_β). As lit.[2]

Zinc 5,15-bis-(3,5-bis-octyloxy-phenyl)-10-ethynyl-20-trihexylsilanylethynyl-porphyrin *l*-$\mathbf{P_{C8}1_{H,THS}}$[2]

Zinc 5,15-bis-(3,5-bis-octyloxy-phenyl)-10,20-bis-ethynyl-porphyrin *l*-$\mathbf{P_{C8}1}$[2]

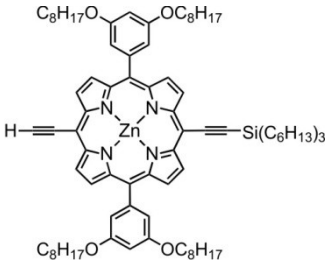

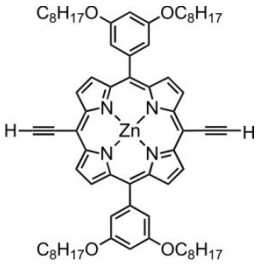

Tetra-*n*-butylammonium fluoride (1.00 M in THF, 2.2 mL, 2.2 mmol) was added to a solution of porphyrin monomer ***l*-$\mathbf{P_{C8}1_{THS,THS}}$** (2.75 g, 1.67 mmol) in CH_2Cl_2 (175 mL) and $CHCl_3$ (175 mL). The reaction was monitored by TLC and after achieving the maximum formation of the half-protected product stopped by adding CH_3COOH (0.45 mL, 4.25 mmol). The volume was reduced by evaporation of most of the solvent and the reaction mixture passed through a short silica gel column (CH_2Cl_2). Chromatography on silica gel (100:1:1, 40-60 °C petroleum ether : ethyl acetate : pyridine) and recrystallization by layer addition (CH_2Cl_2/methanol) yielded ***l*-$\mathbf{P_{C8}1_{H,THS}}$** (0.85 g, 37%) and ***l*-$\mathbf{P_{C8}1}$** (0.21 g, 12%) as green solids.

***l*-$\mathbf{P_{C8}1_{H,THS}}$**

^{1}H NMR (400 MHz, $CDCl_3$/1% d_5-pyridine): δ_H 0.86–0.95 (m, 21H, -CH_3), 0.97–1.10 (m, 6H, -CH_2),1.39–1.62 (m, 58H, -CH_2), 1.75–1.83 (m, 6H, -CH_2), 1.85–1.92 (m, 8H, -CH_2), 4.14 (s, 1H, ≡C*H*), 4.15 (t, 8H, *J* = 6.5 Hz, -OCH_2), 6.90 (t, 2H, *J* = 2.0 Hz, -ArH_{para}), 7.35 (d, 4H, *J* = 2.0 Hz, -ArH_{ortho}), 8.99 (t, 4H, *J* = 4.5 Hz, -ArH_β), 9.65 (m, 4H, -ArH_β). As lit.[2]

***l*-$\mathbf{P_{C8}1}$**

^{1}H NMR (400 MHz, $CDCl_3$/1% d_5-pyridine): δ_H 0.87 (t, 12H, *J* = 6.5 Hz , -CH_3), 1.22–1.55 (m, 40H, -CH_2), 1.83–1.91 (m, 8H, -CH_2), 4.14 (t, 8H, *J* = 5.5 Hz, -OCH_2; s, 2H, ≡C*H*), 6.89 (t, 2H, *J* = 2.0 Hz, -ArH_{para}), 7.33 (d, 4H, *J* = 2.0 Hz, -ArH_{ortho}), 8.99 (m, 4H, -ArH_β), 9.65 (m, 4H, -ArH_β). As lit.[2]

Zinc 5,15-bis-(3,5-bis-octyloxy-phenyl)-10,20-trihexylsilanylethynyl-porphyrin dimer

***l*-$\mathbf{P_{C8}2_{THS,THS}}$**[2]

Zinc 5,15-bis-(3,5-bis-octyloxy-phenyl)-10,20-trihexylsilanylethynyl-porphyrin trimer

***l*-$\mathbf{P_{C8}3_{THS,THS}}$**[2]

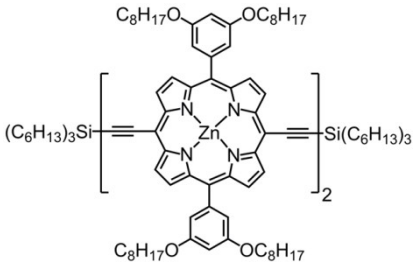

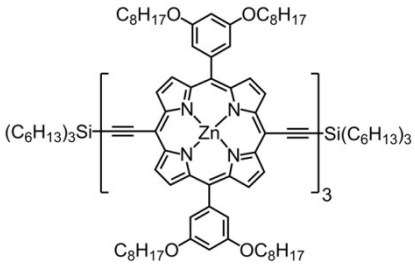

Fully-deprotected porphyrin monomer ***l*-$\mathbf{P_{C8}1}$** (0.3 g, 0.28 mmol) and half-deprotected porphyrin monomer ***l*-$\mathbf{P_{C8}1_{H,THS}}$** (1.5 g, 1.1 mmol) were dissolved in a mixture of $CHCl_3$ (300 mL) and pyridine (6 mL). A catalyst solution was prepared by dissolving dichlorobis(triphenylphosphine)-palladium(II) (0.2 g, 0.21 mmol), copper(I) iodide (0.27 mg, 1.42 mmol) and 1,4-benzoquinone (0.6 g, 5.8 mmol) in the mixture of $CHCl_3$ (150 mL) and freshly distilled *i*-Pr_2NH (6.0 mL) and added to the solution of porphyrin monomers. The reaction mixture was stirred at 20 °C for 1 h. The reaction mixture was passed through a short silica column (CH_2Cl_2/1% pyridine) to remove the catalysts and then over a size exclusion column on Biobeads SX-1 (toluene/1% pyridine) to remove the 1,4-benzoquinon. Preparative GPC (toluene/10% pyridine) yielded ***l*-$\mathbf{P_{C8}2_{THS,THS}}$** (0.98 g, 65%) and ***l*-$\mathbf{P_{C8}3_{THS,THS}}$** (0.29 g, 27%) as green (dimer) and brown (trimer) solids.

***l*-$\mathbf{P_{C8}2_{THS,THS}}$**

^{1}H NMR (400 MHz, $CDCl_3$/1% d_5-pyridine): δ_H 0.93–1.01 (m, 42H, -CH_3), 1.03–1.17 (m, 12H, -CH_2), 1.35–1.67 (m, 116H, -CH_2), 1.82–1.98 (m, 28H, -CH_2), 4.20 (t, 16H, *J* = 6.5 Hz, -OCH_2), 6.93 (s, 4H, -ArH_{para}), 7.43 (d, 8H, *J* = 2.0 Hz, -ArH_{ortho}), 9.06 (d, 4H, *J* = 4.5 Hz, -ArH_β), 9.17 (d, 4H, *J* = 4.5 Hz, -ArH_β), 9.74 (d, 4H, *J* = 4.5 Hz, -ArH_β), 9.98 (d, 4H, *J* = 4.5 Hz, -ArH_β). As lit.[2]

***l*-$\mathbf{P_{C8}3_{THS,THS}}$**

^{1}H NMR (400 MHz, $CDCl_3$/1% d_5-pyridine): δ_H 0.86–0.94 (m, 54H, -CH_3), 1.01–1.06 (m, 12H, -CH_2), 1.29–1.45 (m, 120H, -CH_2), 1.50–1.58 (m, 36H, -CH_2), 1.75–1.81 (m, 12H, -CH_2), 1.87–1.94 (m, 24H, -CH_2), 4.16–4.21 (m, 24H, -OCH_2), 6.91–6.94 (m, 6H, -ArH_{para}), 7.39 (d, J = 2.0 Hz, 8H, -ArH_{ortho}), 7.42 (d, J = 2.0 Hz, 4H, -ArH_{ortho}), 8.97 (d, J = 4.5 Hz, 4H, -ArH_β), 9.07–9.08 (m, 8H, -ArH_β), 9.65 (d, J = 4.5 Hz, 4H, -ArH_β), 9.87–9.89 (m, 8H, -ArH_β). As lit.[2]

Zinc 5,15-bis-(3,5-bis-octyloxy-phenyl)-10-ethynyl-20-trihexylsilanylethynyl-porphyrin dimer *l*-$\mathbf{P_{C8}2_{H,THS}}$[2]

Zinc 5,15-bis-(3,5-bis-octyloxy-phenyl)-10,20-bis-ethynyl-porphyrin dimer *l*-$\mathbf{P_{C8}2}$[2]

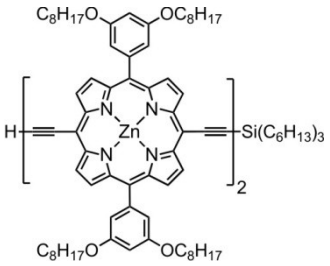

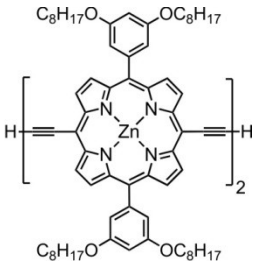

Tetra-*n*-butylammonium fluoride (1.00 M in THF, 0.52 mL, 0.52 mmol) was added to a solution of porphyrin dimer ***l*-$\mathbf{P_{C8}2_{THS,THS}}$** (0.94 g, 0.34 mmol) in a mixture of CH_2Cl_2 (30 mL) and $CHCl_3$ (30 mL) and stirred at 20 °C. The progress of the reaction was monitored by TLC until an optimal product mixture was reached and the reaction then quenched with CH_3COOH (50 µL, 0.47 mmol). The volume was reduced and the reaction mixture passed through a short silica gel column (CH_2Cl_2). Chromatography on silica gel (25:1:1, 40-60 °C petroleum ether : ethyl acetate : pyridine) and recrystallization by layer addition (CH_2Cl_2/methanol) yielded ***l*-$\mathbf{P_{C8}2_{H,THS}}$** (0.39 g, 46%) and ***l*-$\mathbf{P_{C8}2}$** (0.14 g, 19%) as green solids.

***l*-$\mathbf{P_{C8}2_{H,THS}}$**

^{1}H NMR (400 MHz, $CDCl_3$/1% d_5-pyridine): δ_H 0.96–1.04 (m, 33H, -CH_3), 1.12–1.33 (m, 6H, -CH_2), 1.42–1.70 (m, 98H, -CH_2), 1.86–2.03 (m, 22H, -CH_2), 4.25–4.29 (m, 17H, -OCH_2, ≡CH), 7.02 (s, 4H, -ArH_{para}), 7.49 (d, 8H, J = 2.5 Hz, -ArH_{ortho}), 9.08 (d, 4H, J = 4.5 Hz, -ArH_β), 9.19 (d, 4H, J = 4.5 Hz, -ArH_β), 9.74 (m, 4H, -ArH_β), 10.00 (m, 4H, -ArH_β). As lit.[2]

***l*-$\mathbf{P_{C8}2}$**

^{1}H NMR (400 MHz, $CDCl_3$/1% d_5-pyridine): δ_H 0.87 (t, 24H, J = 6.5 Hz, -CH_3), 1.29–1.57 (m, 80H, -CH_2), 1.90 (m, 16H, -CH_2), 4.17 (t, 16H, J = 6.5 Hz, -OCH_2), 4.18 (s, 2H, ≡CH), 6.92 (d, 4H, J = 2.0 Hz, -ArH_{para}), 7.38 (d, 8H, J = 2.0 Hz, -ArH_{ortho}), 9.03 (m, 4H, -ArH_β), 9.10 (m, 4H, -ArH_β), 9.67 (m, 4H, -ArH_β), 9.91 (m, 4H, -ArH_β). As lit.[2]

Zinc 5,15-Bis-(3,5-bis-octyloxy-phenyl)-10-ethynyl-20-trihexylsilanylethynyl-porphyrin trimer *l*-$\mathbf{P_{C8}3_{H,THS}}$[2]

Zinc 5,15-bis-(3,5-bis-octyloxy-phenyl)-10,20-bis-ethynyl-porphyrin trimer *l*-$\mathbf{P_{C8}3}$[2]

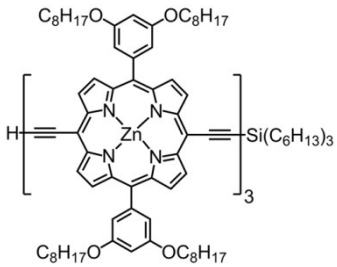

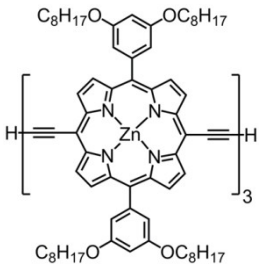

Tetra-*n*-butylammonium fluoride (1.00 M in THF, 0.15 mL, 0.15 mmol) was added to a solution of porphyrin trimer ***l*-$\mathbf{P_{C8}3_{THS,THS}}$** (0.29 g, 75.9 μmol) in a mixture of CH_2Cl_2 (10 mL) and $CHCl_3$ (10 mL) and stirred at 20 °C. The progress of the reaction was monitored by TLC until an optimal product mixture was reached and the reaction then quenched with CH_3COOH (15 μL, 0.14 mmol). The volume was reduced and the reaction mixture passed through a short silica gel column (CH_2Cl_2/1% pyridine). Chromatography on silica gel (17:3, 40-60 °C petroleum ether : pyridine) and recrystallization by layer addition (CH_2Cl_2/methanol) yielded ***l*-$\mathbf{P_{C8}3_{H,THS}}$** (0.14 g, 52%) and ***l*-$\mathbf{P_{C8}3}$** (71 mg, 29%) as brown solids.

***l*-$\mathbf{P_{C8}3_{H,THS}}$**

^{1}H NMR (400 MHz, $CDCl_3$/1% d_5-pyridine): δ_H 0.83–0.93 (m, 45H, -CH_3), 1.00–1.05 (m, 6H, -CH_2), 1.28–1.44 (m, 108H, -CH_2), 1.49–1.59 (m, 30H, -CH_2), 1.74–1.82 (m, 6H, -CH_2), 1.86–1.94 (m, 24H, -CH_2), 4.15–4.20 (m, 24H, -OCH_2), 6.91–6.93 (m, 6H, -ArH_{para}), 7.37–7.41 (m, 12H, -ArH_{ortho}), 8.96–8.99 (m, 4H, -ArH_β), 9.06–9.08 (m, 8H, -ArH_β), 9.63–9.66 (m, 4H, -ArH_β), 9.86–9.90 (m, 8H, -ArH_β). As lit.[2]

***l*-$\mathbf{P_{C8}3}$**

^{1}H NMR (400 MHz, $CDCl_3$/1% d_5-pyridine): δ_H 0.79–0.83 (m, 36H, -CH_3), 1.19–1.37 (m, 96H, -CH_2), 1.43–1.52 (m, 24H, -CH_2), 1.80–1.52 (m, 24H, -CH_2), 4.11 (t, 24H, J = 6.8 Hz, -OCH_2), 4.14 (s, 2H, ≡CH), 6.86–6.89 (m, 6H, -ArH_{para}), 7.32 (d, 6H, J = 2.0 Hz, -ArH_{ortho}), 7.36 (d, 6H, J = 2.0 Hz, -ArH_{ortho}), 8.95 (d, 4H, J = 4.6 Hz, -ArH_β), 9.03 (m, 8H, -ArH_β), 9.61 (d, 4H, J = 4.6 Hz, -ArH_β), 9.84 (m, 8H, -ArH_β). As lit.[5]

Zinc 5,15-bis-(3,5-bis-octyloxy-phenyl)-10,20-trihexylsilanylethynyl-porphyrin tetramer *l*-$\mathbf{P_{C8}4_{THS,THS}}$[2]

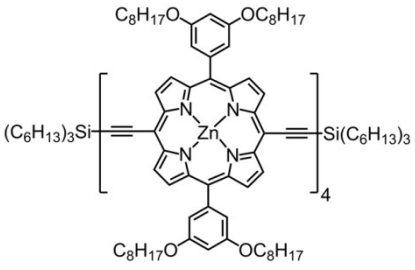

$Pd(PPh_3)_2Cl_2$ (47.5 mg, 68 µmol), copper(I) iodide (0.12 g, 0.62 mmol) and 1,4-benzoquinone (0.11 g, 1.02 mmol) were dissolved in toluene (37 mL) and *i*-Pr_2NH (7.5 mL). The catalysts solution was added to the solution of half-protected porphyrin dimer ***l*-P$_{C8}$2$_{H,THS}$** (0.5 g, 0.21 mmol) in toluene (70 mL) and the reaction mixture stirred for 1h. at 20 °C. The reaction mixture was passed through a short silica gel column (CH_2Cl_2/1% pyridine) and purified by size exclusion chromatography on Biobeads SX-1 (toluene/1% pyridine). Recrystallization by layer addition (CH_2Cl_2/methanol) gave the product as a dark brown solid (0.47 g, 93%).

^{1}H NMR (400 MHz, $CDCl_3$/1% d_5-pyridine): δ_H 0.85–1.08 (m, 78H, -CH_3), 1.30–1.56 (m, 196H, -CH_2), 1.72–1.93 (m, 44H, -CH_2), 4.20 (m, 32H, -OCH_2), 6.93 (m, 8H, -ArH_{para}), 7.39 (d, 8H, J = 2.0 Hz, -ArH_{ortho}), 7.44 (d, 8H, J = 2.0 Hz, -ArH_{ortho}), 8.98 (d, 4H, J = 4.5 Hz, -ArH_β), 9.08 (m, 12H, -ArH_β), 9.65 (d, 4H, J = 4.5 Hz, -ArH_β), 9.90 (m, 12H, -ArH_β). As lit.[2]

Zinc 5,15-bis-(3,5-bis-octyloxy-phenyl)-10,20-trihexylsilanylethynyl-porphyrin hexamer *l*-P$_{C8}$6$_{THS,THS}$[2]

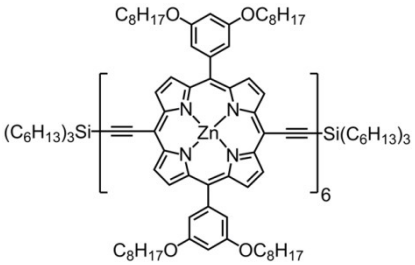

$Pd(PPh_3)_2Cl_2$ (9 mg, 12 µmol), copper(I) iodide (22 mg, 0.12 mmol) and 1,4-benzoquinone (21 mg, 0.19 mmol) were dissolved in toluene (7 mL) and *i*-Pr_2NH (1.4 mL). The catalysts solution was added to the solution of half-protected porphyrin trimer ***l*-P$_{C8}$3$_{H,THS}$** (0.14 g, 38.4 µmol) in toluene (18 mL) and the reaction mixture stirred for 1h. at 20 °C. The reaction mixture was passed through a short silica gel column (CH_2Cl_2/1% pyridine) and purified by size exclusion chromatography on Biobeads SX-1 (toluene/1% pyridine) and preparative GPC (toluene/10% pyridine). Recrystallization by layer addition (CH_2Cl_2/methanol) gave the product as a dark brown solid (108 mg, 79%).

^{1}H NMR (400 MHz, $CDCl_3$ / 1% d_5-pyridine): δ_H 0.86–0.94 (m, 90H, -CH_3), 1.01–1.05 (m, 12H, -CH_2), 1.26–1.42 (m, 192H, -CH_2), 1.50–1.58 (m, 72H, -CH_2), 1.75–1.81 (m, 12H, -CH_2), 1.89–1.94 (m, 60H, -CH_2), 4.16–4.20 (m, 48H, -OCH_2), 6.91–6.92 (m, 4H, -ArH_{para}), 6.94–6.95 (m, 8H, -ArH_{para}), 7.38–7.39 (m, 8H, -ArH_{ortho}), 7.42–7.44 (m, 16H, -ArH_{ortho}), 8.97 (d, J = 4.5 Hz, 4H, -ArH_β), 9.07–9.10 (m, 20H, -ArH_β), 9.65 (d, J = 4.5 Hz, 4H, -ArH_β), 9.87–9.91 (m, 20H, -ArH_β). As lit.[2]

Zinc 5,15-Bis-(3,5-bis-octyloxy-phenyl)-10-ethynyl-20-trihexylsilanylethynyl-porphyrin tetramer *l*-$\mathbf{P_{C8}4_{H,THS}}$[2]

Zinc 5,15-Bis-(3,5-bis-octyloxy-phenyl)-10,20-bis-ethynyl-porphyrin tetramer *l*-$\mathbf{P_{C8}4}$[2]

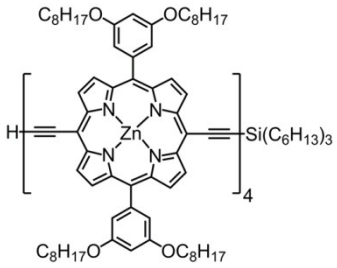

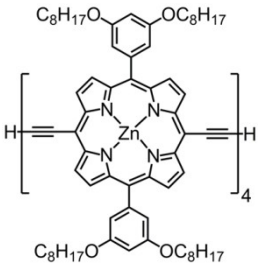

Tetra-*n*-butylammonium fluoride (1.00 M in THF, 185 µL, 0.185 mmol) was added to a solution of porphyrin tetramer ***l*-$\mathbf{P_{C8}4_{THS,THS}}$** (0.28 g, 0.057 mmol) in CH_2Cl_2 (10 mL) and $CHCl_3$ (10 mL) and the reaction mixture stirred at 20 °C. The progress of the reaction was monitored by TLC until an optimal product mixture was reached and the reaction then quenched with CH_3COOH (20 µL, 0.14 mmol). The volume was reduced and the reaction mixture passed through a short silica gel column (CH_2Cl_2/1% pyridine). Chromatography on silica gel (85:15, 40-60 °C petroleum ether : pyridine) and recrystallization by layer addition (CH_2Cl_2/methanol) gave ***l*-$\mathbf{P_{C8}4_{H,THS}}$** (92 mg, 35%) and ***l*-$\mathbf{P_{C8}4}$** (60 mg, 24%) as brown solids.

***l*-$\mathbf{P_{C8}4_{H,THS}}$**

^{1}H NMR (400 MHz, $CDCl_3$/1% d_5-pyridine): δ_H 0.91–1.11 (m, 63H, -CH_3), 1.35–1.67 (m, 178H, -CH_2), 1.81–1.88 (m, 6H, -CH_2), 1.93–2.02 (m, 32H, -CH_2), 4.24 (m, 33H, -OCH_2, ≡CH), 6.98 (s, 4H, -ArH_{para}), 7.00 (s, 4H, -ArH_{para}), 7.45 (s, 8H, -ArH_{ortho}), 7.49 (d, 8H, J = 2.0 Hz, -ArH_{ortho}), 9.04 (m, 4H, -ArH_β), 9.15 (m, 12H, -ArH_β), 9.70 (m, 4H, -ArH_β), 9.95 (m, 12H, -ArH_β). As lit.[2]

***l*-$\mathbf{P_{C8}4}$**

^{1}H NMR (400 MHz, $CDCl_3$/1% d_5-pyridine): δ_H 0.87 (m, 48H, -CH_3), 1.29–1.53 (m, 160H, CH_2), 1.90 (m, 32H, CH_2), 4.18 (m, 32H, OCH_2), 6.92 (m, 8H, ArH^{para}), 7.38 (s, 8H, ArH^{ortho}), 7.42 (s, 8H, ArH^{ortho}), 8.98 (d, 4H, J = 4.5 Hz, -ArH_β), 9.08 (m, 12H, -ArH_β), 9.63 (d, 4H, J = 4.5 Hz, -ArH_β), 9.89 (m, 12H, -ArH_β). As lit.[2]

Zinc 5,15-Bis-(3,5-bis-octyloxy-phenyl)-10,20-trihexylsilanylethynyl-porphyrin octamer *l*-$\mathbf{P_{C8}8_{THS,THS}}$[2]

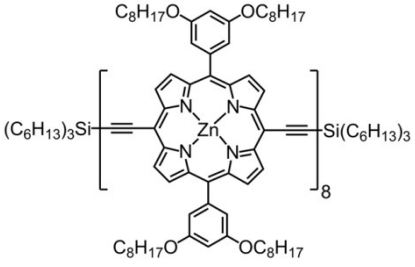

$Pd(PPh_3)_2Cl_2$ (4 mg, 5.7 μmol), copper(I) iodide (10 mg, 52 μmol) and 1,4-benzoquinone (9.4 mg, 87 μmol) were dissolved in toluene (3 mL) and *i*-Pr_2NH (0.7 mL). The catalysts solution was added to the solution of half-protected porphyrin tetramer ***l*-$\mathbf{P_{C8}4_{H,THS}}$** (40 mg, 8.7 μmol) in toluene (4 mL) and the reaction mixture stirred for 12 h. at 20 °C. The reaction mixture was passed through a short silica gel column (CH_2Cl_2/1% pyridine) and purified by size exclusion chromatography on Biobeads SX-1 (toluene/1% pyridine) and preparative GPC (toluene/10% pyridine). Recrystallization by layer addition (CH_2Cl_2/methanol) gave the product as a dark brown solid (38 mg, 95%).

^{1}H NMR (400 MHz, $CDCl_3$/1% d_5-pyridine): δ_H 0.86–0.94 (m, 114H, -CH_3), 1.00–1.07 (m, 6H, -CH_2), 1.25–1.61 (m, 372H, -CH_2), 1.75–1.82 (m, 6H, -CH_2), 1.87–1.96 (m, 60H, -CH_2), 4.21 (m, 64H, -OCH_2), 6.91–6.95 (m, 32H, -ArH_{para}), 7.38–7.44 (m, 32H, -ArH_{ortho}), 8.97 (d, 4H, J = 4.5 Hz, -ArH_β), 9.08 (m, 30H, -ArH_β), 9.64 (d, 4H, J = 4.5 Hz, -ArH_β), 9.89 (m, 30H, -ArH_β). As lit.[2]

Hexakis(4-bromophenyl) benzene[2]

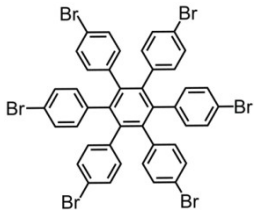

Neat bromine (4.1 g, 1.3 ml, 25.8 mmol) was added dropwise over 30 min to hexaphenylbenzene (1.0 g, 1.87 mmol). Stirring of the dark orange slurry was continued after the addition for 45 min. Ethanol (20 mL) was carefully added, while cooling the reaction flask in a dry-ice/acetone bath. The precipitate was collected by filtration and washed with an aqueous $Na_2S_2O_3$ solution. The crude product was dissolved in $CHCl_3$ and washed with aq. $Na_2S_2O_3$ and water. Solvents were removed under vacuum and the residue was recrystallized from hot CH_2Cl_2/methanol to give the product as a white solid (1.50 g, 80%).

^{1}H NMR (400 MHz, $CDCl_3$): δ_H 6.61 (d, J = 8.5 Hz, 12H, -ArH), 7.07 (d, J = 8.5 Hz, 12H, -ArH). As lit.[2]

Hexadentate template T6[2]

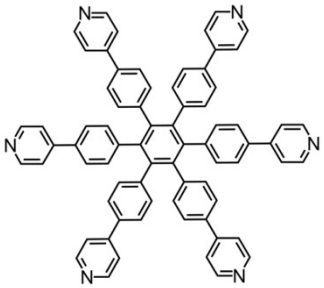

To a solution of hexakis-(4-bromophenyl)benzene (0.6 g, 0.60 mmol) in dimethyleneglycol (18.0 mL) and tetrahydrofuran (34 mL) was added dichlorobis(triphenylphosphine)-palladium(II) (80.0 mg, 0.12 mmol). After addition of water (24 mL), $NaHCO_3$ (0.9 g, 10.7 mmol) and 4-pyridineboronic acid

(1.76 g, 14.3 mmol), the mixture was deoxygenated and stirred at 80 °C for 5 days. Solvents were removed and the crude product was purified by column chromatography (10:1:0.05, CH_2Cl_2 : methanol : triethylamine). Washing the residue with water gave the template as a white solid (209 mg, 35%).

^{1}H–NMR (400 MHz, $CDCl_3$): δ_H ppm 6.96 (d, J = 8.5 Hz, 12H, -pyridylH_α), 7.18 (d, J = 8.5 Hz, 12H, -pyridylH_β), 7.29 (d, J = 5.5 Hz, 12H, -Ar*H*), 8.36 (d, J = 5.5 Hz, 12H, -Ar*H*). As lit.[2]

Octadentate template T8[5]

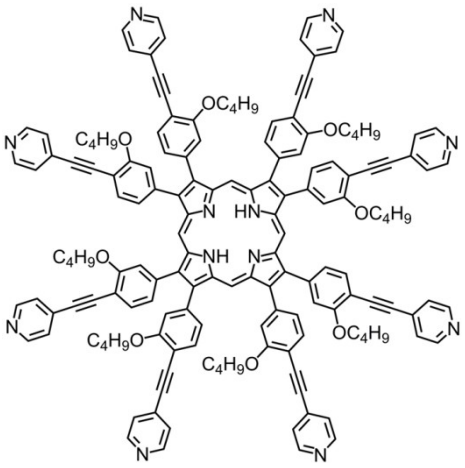

Lithium aluminium hydride (1.0 M in THF, 2.0 eq., 1.51 mL, 1.51 mmol) was added dropwise to a solution of *tert*-butyl 3,4-bis(3-butoxy-4-(pyridin-4-ylethynyl)phenyl)-1*H*-pyrrole-2-carboxylate (500 mg, 0.75 mmol) in dry THF (19 mL) cooled in an ice bath. The reaction mixture was stirred 0.5 hours at 0 °C before NaOH (1.0 M, aq, 25 mL) and CH_2Cl_2 (50 mL) were added. The organic layer was separated and washed with water (2 × 25 mL) and solvents removed. Dry CH_2Cl_2 (50 mL) and $CH_3OCH_2OCH_3$ (194 µL, 2.25 mmol) were added and the solution deoxygenated. *p*-Toluene sulfonic acid (572 mg, 3.00 mmol) was added and the reaction mixture stirred for 16 hours in the dark. DDQ (131 mg, 0.577 mmol) was added and the reaction stirred 10 minutes before washing with Na_2CO_3 (sat., aq., 2 × 50 mL) and water (2 × 25 mL). Column chromatography (100:1:1 to 100:2:2, CH_2Cl_2 : MeOH : triethylamine) followed by recrystallisation by layer addition (CH_2Cl_2 / MeOH) and washing with acetone gave a red powder (39 mg, 9%).

^{1}H–NMR (400 MHz, $CDCl_3$): δ_H -2.88 (s, 2H, -N*H*), 1.00 (t, 24H, J = 7.3 Hz, -CH_3), 1.49–1.67 (m, 16H, -CH_2), 1.77–1.90 (m, 16H, -CH_2), 3.92 (t, 16H, J = 6.3 Hz, -OCH_2), 7.45 (d, 16H, J = 5.0 Hz, -pyridylH_β), 7.54 (m, 8H, -Ar*H*), 7.61 (m, 8H, -Ar*H*), 7.81 (m, 8H, -Ar*H*), 8.66 (d, 16H, J = 5.0 Hz, -pyridylH_α), 10.57 (s, 4H, H_{meso}). As lit.[5]

Zinc (3,5-bis-*tert*-butyl-phenyl)-porphyrin[6] nanoring–template complex *c*-P$_{t\text{-Bu}}$6·T6[2]

Figure-of-eight complex *c*-P$_{t\text{-Bu}}$12·(T6)$_2$[2]

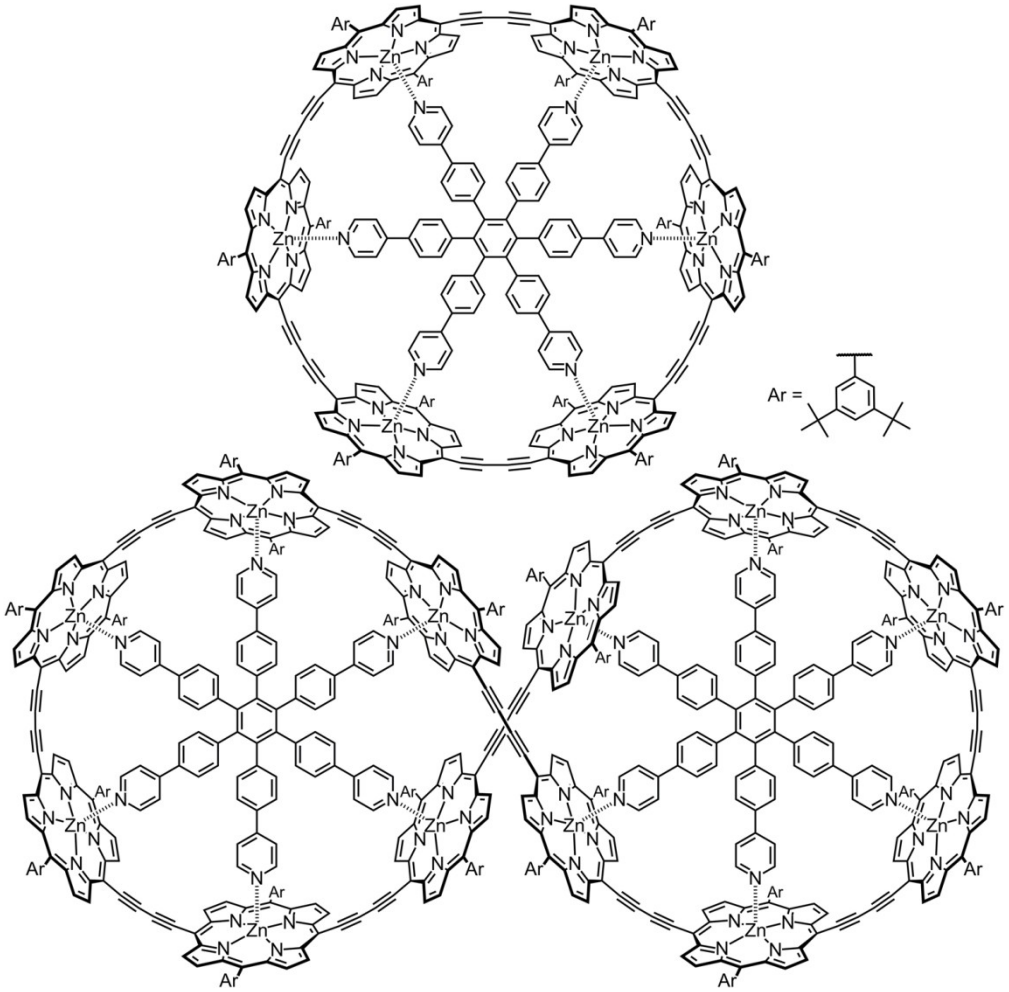

Hexadentate template **T6** (128 mg, 0.134 mmol) and deprotected porphyrin monomer ***l*-P$_{t\text{-Bu}}$1** (0.4 g, 0.50 mmol) were dissolved in $CHCl_3$ (560 mL) and sonicated for 2 h. A catalyst solution was prepared by dissolving dichlorobis(triphenyl-phosphine)-palladium(II) (116 mg, 0.165 mmol), CuI (158.4 mg, 0.831 mmol) and 1,4-benzoquinone (0.37 g, 3.41 mmol) in 80 mL of freshly opened $CHCl_3$ and 1 mL of freshly distilled *i*-Pr_2NH. The catalysts solution was added to the template and porphyrin monomer mixture and stirred at 20 °C overnight. The reaction mixture was passed over a short alumina column ($CHCl_3$) and then purified by size exclusion chromatography on Biobeads SX-1 (toluene) and preparative GPC (toluene) to give ***c*-P$_{t\text{-Bu}}$6·T6** (58.0 mg, 13 %) and ***c*-P$_{t\text{-Bu}}$12·(T6)$_2$** (15.0 mg, 3 %) as brown solids.

***c*-P$_{t\text{-Bu}}$6·T6**

^{1}H NMR (400 MHz, $CDCl_3$): δ_H 1.54 (s, 108H, -*t*Bu*H*), 1.58 (s, 108H, -*t*-Bu*H*), 2.33 (d, *J* = 7.0 Hz, 12H, -pyridylH_α), 5.00 (d, *J* = 7.0 Hz, 12H, -pyridylH_β), 5.48 (d, *J* = 9.0 Hz, 12H, -Ar*H*), 5.52 (d, *J* = 9.0 Hz, 12H, -Ar*H*), 7.81 (s, 12H, -ArH_{para}), 7.86 (s, 12H, -ArH_{ortho}), 8.05 (s, 12H, -ArH_{ortho}), 8.81 (d, *J* = 4.5 Hz, 24H, -ArH_β), 9.59 (d, *J* = 4.5 Hz, 24H, -ArH_β). As lit.[2]

***c*-P$_{t\text{-Bu}}$12·(T6)$_2$**

^{1}H NMR (700 MHz, $CDCl_3$): δ_H -0.64 (s, 36H, -*t*-Bu*H*), 1.14 (s, 36H, -*t*-Bu*H*), 1.46 (s, 36H, -*t*-Bu*H*), 1.51–1.53 (m, 144H, -*t*-Bu*H*), 1.54–1.55 (m, 72H, -*t*-Bu*H*), 1.58 (m, 72H, -*t*-Bu*H*), 1.70 (s, 36H, --*t*-Bu*H*), 2.19–2.22 (m, 24H, -pyridylH_α), 4.81 (d, 8H, *J* = 9.5 Hz, -pyridylH_β), 4.94–4.97 (m, 16H, -pyridylH_β), 5.22 (d, 4H, *J* = 9.5 Hz, -Ar*H*), 5.27 (d, 4H, *J* = 10.0 Hz, -Ar*H*), 5.39 (d, 4H, *J* = 9.0 Hz, -Ar*H*), 5.42–5.49 (m, 32H, -Ar*H*), 5.53 (d, 4H, *J* = 10.0 Hz, -Ar*H*), 6.40 (s, 4H, -Ar*H*), 6.98 (s, 4H, -Ar*H*), 7.37 (s, 4H, -Ar*H*), 7.74–7.83 (m, 36H, -Ar*H*), 7.89 (s, 4H, -Ar*H*), 8.02–8.06 (m, 16H, -Ar*H*), 8.08 (d, 4H, *J* = 4.0 Hz, -ArH_β), 8.11 (s, 4H, -Ar*H*), 8.32 (d, 4H, *J* = 3.5 Hz, -ArH_β), 8.72 (d, 4H, *J* = 4.0 Hz, -ArH_β), 8.75–8.80 (m, 28H, -ArH_β), 8.86 (d, 4H, *J* = 4.5 Hz, -ArH_β), 9.03 (d, 4H, *J* = 3.5 Hz, -ArH_β), 9.30 (d, 4H, *J* = 3.5 Hz, -ArH_β), 9.48 (d, 4H, *J* = 4.0 Hz, -ArH_β), 9.53–9.57 (m, 32H, -ArH_β), 10.16 (d, 4H, *J* = 3.5 Hz, -ArH_β), 10.92 (d, 4H, *J* = 4.5 Hz, -ArH_β). As lit.[2]

Free base (3,5-bis-*tert*-butyl-phenyl)-porphyrin[6] nanoring *c*-P$_{t\text{-Bu}}$6$_{FB}$[7]

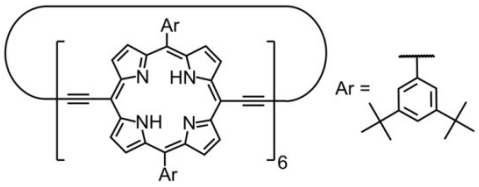

A sample of ***c*-P$_{t\text{-Bu}}$6·T6** (9.2 mg, 1.59 μmol) in $CHCl_3$ (10 mL) was titrated with solution of TFA (10/1 *v/v*, 1.1 mL, 1.43 mmol) in $CHCl_3$ and stirred for 15 min. Once UV-*vis*-IR showed the reaction to be complete, pyridine (0.1 mL, 1.6 mmol) was added and the reaction mixture filtered through a short silica gel column ($CHCl_3$), solvents removed to give ***c*-P$_{t\text{-Bu}}$6$_{FB}$** (6.0 mg, 86 %) as a dark green solid. ^{1}H NMR (400MHz, $CDCl_3$): δ_H -1.33 (s, 8H, -N*H*), 1.51 (s, 216H, -*t*-Bu*H*), 7.83 (t, *J* = 1.3 Hz, 12H, -ArH_{para}), 7.96 (d, *J* = 1.3 Hz, 24H, -ArH_{ortho}), 8.80 (d, *J* = 4.5 Hz, 24H, H_β), 9.62 (d, *J* = 4.5 Hz, 24H, H_β). As lit.[7]

Zinc (3,5-bis-*tert*-butyl-phenyl)-porphyrin[6] nanoring *c*-P$_{t\text{-Bu}}$6[7]

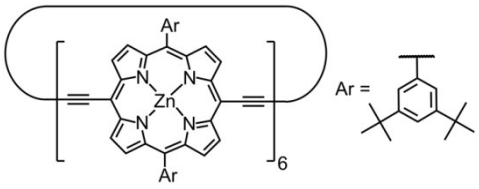

$Zn(OAc)_2$·$2H_2O$ (47 mg, 0.21 mmol) was dissolved in methanol (1 mL) and added to a solution of free-base porphyrin nanoring ***c*-P$_{t\text{-Bu}}$6$_{FB}$** (6.5 mg, 1.47 μmol) in CH_2Cl_2 (10 mL). The reaction mixture was stirred at 35 °C for 2 h, after which the solvents were removed and the residue recrystallized (CH_2Cl_2/methanol) to give a product as a brown powder (7.0 mg, 99 %).

^{1}H NMR (400 MHz, $CDCl_3$/1% d_5-pyridine): δ_H 1.49 (s, 216 H, -*t*-Bu*H*), 7.75 (d, *J* = 1.5 Hz, 12 H, -ArH_{para}), 7.90 (d, *J* = 1.5 Hz, 24 H, -ArH_{ortho}), 8.79 (d, *J* = 4.5 Hz, 24 H, -ArH_β), 9.62 (d, *J* = 4.5 Hz, 24 H, -ArH_β). As lit.[2]

Zinc (3,5-bis-*tert*-butyl-phenyl)-porphyrin[12] nanoring *c*-$P_{t\text{-}Bu}12$

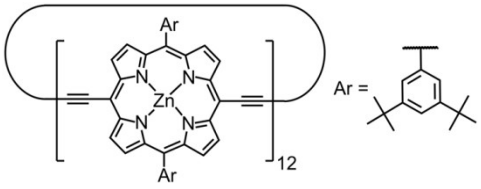

The figure-of-eight complex ***c*-$P_{t\text{-}Bu}12$·(T6)$_2$** (3.0 mg, 0.26 μmol) was dissolved in toluene (2 mL) and pyridine (0.2 mL) and passed over a size exclusion column on Biobeads SX-1 (toluene/1% pyridine). Recrystallization by layer addition ($CHCl_3$/methanol) gave the product as a dark brown solid (2.4 mg, 96%).

^{1}H NMR (500 MHz, $CDCl_3$/1% d_5-pyridine): δ_H 1.56 (s, 432H, -*t*-Bu*H*), 7.81 (t, 24H, *J* = 1.5 Hz, -ArH_{para}), 8.05 (d, 48H, *J* = 1.5 Hz, -ArH_{ortho}), 8.95 (d, 48H, *J* = 4.5 Hz, -ArH_β), 9.84 (d, 48H, *J* = 4.5 Hz, -ArH_β).

Zinc (3,5-bis-octyloxy-phenyl)-porphyrin[12] nanoring *c*-$P_{C8}12$

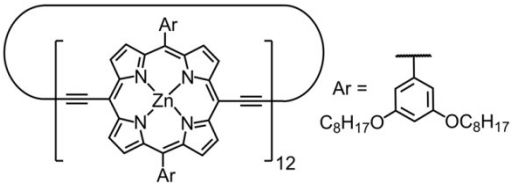

Hexadentate template **T6** (2.5 mg, 2.5 μmol) and deprotected porphyrin tetramer ***l*-P_{C8}4** (10.0 mg, 2.3 μmol) were dissolved in CH_2Cl_2 (5 mL) and sonicated for 15 min. The solvent was removed and the residue redissolved in toluene (11 mL). A catalyst solution was prepared by dissolving $Pd(PPh_3)_2Cl_2$ (2.0 mg, 2.8 μmol), copper(I) iodide (2.0 mg, 11 μmol) and 1,4-benzoquinone (7.0 mg, 65 μmol) in toluene (2 mL) and freshly distilled *i*-Pr_2NH (80 μL). The catalyst solution was added to the reaction mixture. The reaction mixture was stirred at 20 °C for 2 h. and then refluxed for 6 h. under air. The mixture was passed through a short alumina column (toluene) and then over a size exclusion column on Biobeads SX-1 (toluene). The first band was isolated and passed over a short size exclusion column on Biobeads SX-1 (toluene/1% pyridine) to remove the template from figure-of-eight complex. Recrystallization by layer addition (CH_2Cl_2/methanol) gave the product as a dark brown solid (3.0 mg, 30%).

^{1}H NMR (400 MHz, $CDCl_3$/1% d_5-pyridine): δ_H 0.84 (t, 144H, *J* = 6.5 Hz, -CH_3), 1.41–1.25 (m, 384H, -CH_2), 1.56–1.48 (m, 96H, -CH_2), 1.93–1.86 (m, 96H, -CH_2), 4.17 (s br, 96H, -OCH_2), 6.91 (t, 24H, *J* = 2.0 Hz, -ArH_{para}), 7.38 (d, 48H, *J* = 2.0 Hz, -ArH_{ortho}), 9.03 (d, 48H, *J* = 4.5 Hz, -ArH_β), 9.82 (d, 48H, *J* = 4.5 Hz, -ArH_β). As lit.[2]

7.3 Synthetic Procedures for Novel Compounds

Zinc 5,15-Bis-(3,5-bis-octyloxy-phenyl)-10,20-trihexylsilanylethynyl-porphyrin pentamer ***l*-$P_{C8}5_{THS,THS}$

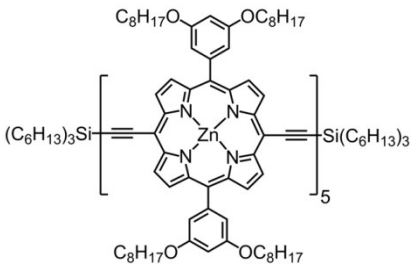

Method 1

Deprotected porphyrin trimer ***l*-P$_{C8}$3** (78.0 mg, 24.0 μmol) and half-deprotected porphyrin monomer ***l*-P$_{C8}$1$_{H,THS}$** (166 mg, 0.12 mmol) were dissolved in the mixture of $CHCl_3$ (50 mL) and pyridine (1.0 mL). A catalyst solution was prepared by dissolving dichlorobis(triphenylphosphine)-palladium(II) (18.0 mg, 19.7 μmol), copper(I) iodide (24.0 mg, 0.13 mmol) and 1,4-benzoquinone (54.4 mg, 0.29 mmol) in mixture of $CHCl_3$ (15.0 mL) and freshly distilled *i*-Pr_2NH (1.0 mL) and added to the solution of porphyrin oligomers. The reaction mixture was stirred at 20 °C for 3 h. Once UV-*vis*-IR spectroscopy showed no changes, the reaction mixture was passed through short silica column ($CHCl_3$/1% pyridine) to remove the catalysts and then over a size exclusion column on Biobeads SX-1 (toluene/1% pyridine) to remove the 1,4-benzoquinone. Preparative GPC (toluene/10% pyridine) yielded ***l*-P$_{C8}$2$_{THS,THS}$** (92 mg, 55 %) and ***l*-P$_{C8}$5$_{THS,THS}$** (41 mg, 29 %) as brown solids.

***l*-P$_{C8}$2$_{THS,THS}$**

^{1}H-NMR: as above.

***l*-P5$_{THS,THS}$**

^{1}H-NMR (400 MHz, $CDCl_3$/1% d_5-pyridine): δ_H 0.86–0.78 (m, 78H, -CH_3), 0.99–0.95 (m, 12H, -CH_2), 1.53–1.18 (m, 224H, -CH_2), 1.76–1.69 (m, 12H, -CH_2), 1.88–1.79 (m, 52H, -CH_2), 4.13–4.08 (m, 40H, -OCH_2), 6.89–6.85 (m, 10H, -ArH_{para}), 7.37–7.31 (m, 20H, -ArH_{ortho}), 8.92 (d, 4H, J = 4.5 Hz, -ArH_β), 9.04–9.02 (m, 16H, -ArH_β), 9.61(d, 4H, J = 4.7 Hz, -ArH_β), 9.85–9.82 (m, 16H, -ArH_β); *m/z* (MALDI-ToF) 5992 ($C_{376}H_{488}N_{20}O_{20}Zn_5$, M^+ requires 5991); λ_{max} (toluene/1% pyridine) / nm (log ε) 464 (5.76), 590 (4.68), 796 (5.45).

Method 2

Half-deprotected porphyrin tetramer ***l*-P$_{C8}$4$_{H,THS}$** (50.0 mg, 10.8 μmol) and half-deprotected porphyrin monomer ***l*-P$_{C8}$1$_{H,THS}$** (245 mg, 0.15 mmol) were dissolved in toluene (30 mL). A catalyst solution was prepared by dissolving dichlorobis(triphenylphosphine)-palladium(II) (76.0 mg, 0.11 mmol), copper(I) iodide (185 mg, 0.97 mmol) and 1,4-benzoquinone (175 mg, 1.62 mmol) in mixture of toluene (57.0 mL) and freshly distilled *i*-Pr_2NH (12.7 mL) and added to the solution of porphyrin oligomers. The reaction mixture was stirred at 20 °C for 11 h. Once UV-*vis*-IR spectroscopy showed no changes, the reaction mixture was passed through short silica column ($CHCl_3$/1% pyridine) to remove the catalysts and then over a size exclusion column on Biobeads SX-1 (toluene/1% pyridine) to remove the 1,4-benzoquinone. Preparative GPC (toluene/10% pyridine) yielded ***l*-P$_{C8}$2$_{THS,THS}$** (164 mg, 81 %) and ***l*-P$_{C8}$5$_{THS,THS}$** (43 mg, 66 %) as brown solids.

***l*-P$_{C8}$2$_{THS,THS}$**

^{1}H-NMR: as above.

***l*-P$_{C8}$5$_{THS,THS}$**

^{1}H-NMR: as above.

Zinc 5,15-Bis-(3,5-bis-octyloxy-phenyl)-10,20-trihexylsilanylethynyl-porphyrin dodecamer

***l*-P$_{C8}$10$_{THS,THS}$**

Zinc 5,15-Bis-(3,5-bis-octyloxy-phenyl)-10,20-trihexylsilanylethynyl-porphyrin 18-mer

***l*-P$_{C8}$18$_{THS,THS}$**

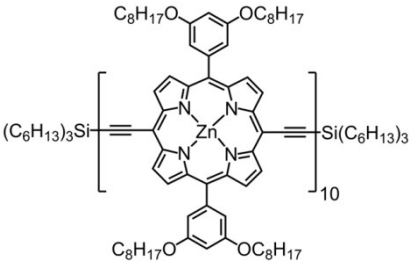

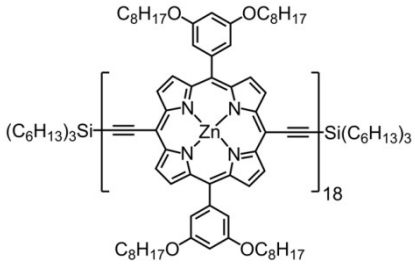

Fully-protected linear porphyrin 8-mer ***l*-P$_{C8}$8$_{THS,THS}$** (54.0 mg, 5.8 μmol) was dissolved in CH_2Cl_2 (30.0 mL) and the solution degassed. Tetra-*n*-butylammonium fluoride (1 M in THF, 160 μL, 0.160 mmol) was added and the reaction mixture stirred at 20 °C for 1 h. under N_2 atmosphere. The reaction was quenched with MeOH (1.0 mL), the volume reduced, the ***l*-P$_{C8}$8** precipitated with MeOH (50 mL), filtered off and dried in high vacuum. All obtained ***l*-P$_{C8}$8** and half-deprotected porphyrin monomer ***l*-P$_{C8}$1$_{H,THS}$** (0.31 g, 0.23 mmol) were dissolved in the mixture of toluene (100 mL) and pyridine (1.0 mL). A catalyst solution was prepared by dissolving dichlorobis(triphenylphosphine)-palladium(II) (107 mg, 0.15 mmol), copper(I) iodide (263 mg, 1.38 mmol) and 1,4-benzoquinone (249 mg, 2.30 mmol) in the mixture of toluene (80.0 mL) and freshly distilled *i*-Pr_2NH (18.0 mL) and added to the solution of ***l*-P$_{C8}$8** and ***l*-P$_{C8}$1$_{H,THS}$**. The reaction mixture was stirred at 20 °C for 3 h, after which half of the initial amount of the catalyst solution was added and the mixture stirred at 60 °C for 2 h. Once UV-*vis*-IR spectroscopy showed no changes, the reaction mixture was passed through short silica column ($CHCl_3$/1% pyridine) to remove the catalysts and then over a size exclusion column on Biobeads SX-1 (toluene/1% pyridine) to remove the 1,4-benzoquinone. Preparative GPC (toluene/10% pyridine) followed by the recycling GPC yielded ***l*-P$_{C8}$2$_{THS,THS}$** (242 mg, 79 %), ***l*-P$_{C8}$10$_{THS,THS}$** (47 mg, 70 %) and ***l*-P$_{C8}$18$_{THS,THS}$** (4 mg, 7 %) as brown solids.

***l*-P$_{C8}$2$_{THS,THS}$**

^{1}H-NMR: as above.

***l*-P$_{C8}$10$_{THS,THS}$**

^{1}H-NMR (400 MHz, $CDCl_3$/1% d_5-pyridine): δ_H 0.74–0.66 (m, 138H, -CH_3), 0.89–0.85 (m, 12H, -CH_2), 1.42–1.07 (m, 424H, -CH_2), 1.65–1.59 (m, 12H, -CH_2), 1.76–1.67 (m, 92H, -CH_2), 3.99 (m, 80H, -OCH_2), 6.80–6.77 (m, 20H, -ArH_{para}), 7.28–7.21 (m, 40H, -ArH_{ortho}), 8.84 (d, 4H, J = 4.4 Hz,

-ArH_{β}), 8.96–8.93 (m, 36H, -ArH_{β}), 9.54 (d, 4H, J = 4.5 Hz, -ArH_{β}), 9.77–9.73 (m, 36H, -ArH_{β}); *m/z* (MALDI-ToF) 11419 ($C_{716}H_{898}N_{40}O_{40}Zn_{10}$, M^+ requires 11415); λ_{max} (toluene/1% pyridine) / nm (log ε) 471 (6.03), 593 (4.96), 815 (5.84).

***l*-P_{C8}18$_{THS,THS}$**

^{1}H-NMR (400 MHz, $CDCl_3$/1% d_5-pyridine): δ_H 0.60–0.70 (m, 234H, -CH_3), 0.8–0.85 (m, 12H, -CH_2), 0.99–1.35 (m, 774H, -CH_2), 1.55–1.61 (m, 12H, -CH_2), 1.64–1.71 (m, 156H, -CH_2), 3.94 (m, 144H, -OCH_2), 6.75–6.77 (m, 36H, -ArH_{para}), 7.17–7.23 (m, 72H, -ArH_{ortho}), 8.81 (d, 4H, J = 4.5 Hz, -ArH_{β}), 8.93–8.89 (m, 68H, -ArH_{β}), 9.51 (d, 4H, J = 4.5 Hz, -ArH_{β}), 9.70–9.74 (m, 68H, -ArH_{β}); *m/z* (MALDI-ToF) 20181 ($C_{1260}H_{1554}N_{72}O_{72}Zn_{18}$, M^+ requires 20093); λ_{max} (toluene/1% pyridine) / nm 473, 594, 820.

Zinc (3,5-bis-octyloxy-phenyl)-porphyrin[24] nanoring *c*-P_{C8}24

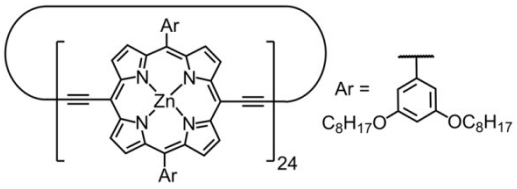

To a suspension of deprotected porphyrin octamer ***l*-P_{C8}8** (106 mg, 12.2 µmol) in CH_2Cl_2 (106 mL) a solution of template **T6** (12.2 mg, 12.2 µmol) in CH_2Cl_2 (6.0 mL) and MeOH (0.60 mL) was added and the mixture sonicated for 2 h. The mixture was then evaporated and dried in high vacuum, redissolved in toluene (180 mL) and sonicated for 1 h. A catalysts solution was prepared by dissolving dichlorobis(triphenylphosphine)-palladium(II) (72.0 mg, 0.10 mmol), copper(I) iodide (96.0 mg, 0.50 mmol) and 1,4-benzoquinone (216 mg, 2.0 mmol) in mixture of toluene (48.0 mL) and freshly distilled *i*-Pr_2NH (2.4 mL) and added to the solution of ***l*-P_{C8}8** and **T8**. The reaction mixture was stirred at 0 °C for 1 hour and then at 20 °C for 10 h., after which the same amount of the catalysts solution was added and the reaction mixture stirred for another 4 h. Once UV-*vis*-IR spectroscopy showed no changes, the same amount of the catalysts solution was added and the reaction mixture additionally stirried at 60 °C for 2 h. The reaction mixture was then cooled down and passed through short alumina column ($CHCl_3$) to remove non-cyclic species. Preparative GPC in toluene yielded the corresponding template complex ***c*-P_{C8}24·(T6)$_4$**. This was passed over a size exclusion column on Biobeads SX-1 ($CHCl_3$/10% pyridine) to remove the template to afford ***c*-P_{C8}24** (14.0 mg, 14 %) as a brown solid.

***c*-P_{C8}24**

^{1}H-NMR (500 MHz, $CDCl_3$/1% d_5-pyridine): δ_H 0.88 (m, 288H, -CH_3), 1.24–1.45 (m, 768H, -CH_2), 1.51–1.59 (m, 192H, -CH_2), 1.88–1.96 (m, 192H, -CH_2), 6.94 (m, 48H, -ArH_{para}), 4.21 (s br, 192H, -OCH_2), 7.43 (m, 96H, -ArH_{ortho}), 9.03 (d, 96H, J = 4.1 Hz, -ArH_{β}), 9.89 (d, 96H, J = 4.1 Hz, -ArH_{β});

m/z (MALDI-ToF) 26124 ($C_{1632}H_{1968}N_{96}O_{96}Zn_{24}$, M^+ requires 26035); λ_{max} (toluene/1% pyridine) / nm (log ε) 474 (6.32), 593 (5.25), 818 (6.18).

Zinc (3,5-bis-octyloxy-phenyl)-porphyrin[16] nanoring *c*-P_{C8}16

Zinc (3,5-bis-octyloxy-phenyl)-porphyrin[24] nanoring *c*-P_{C8}24

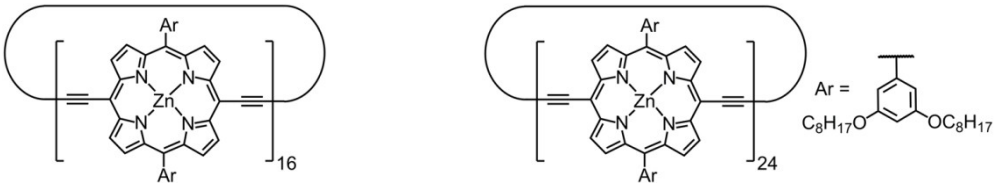

To a suspension of deprotected porphyrin octamer ***l*-P_{C8}8** (15 mg, 1.73 µmol) in CH_2Cl_2 (18 mL) a solution of template **T6** (2.4 mg, 2.4 µmol) in CH_2Cl_2 (1.0 mL) and MeOH (50 µL) was added and the mixture sonicated for 2 h. The mixture was then dried under in high vacuum and redissolved in toluene (45.0 mL) and sonicated for 1 h. A catalysts solution was prepared by dissolving dichlorobis(triphenylphosphine)-palladium(II) (9.0 mg, 9.8 µmol), copper(I) iodide (12.4 mg, 65 µmol) and 1,4-benzoquinone (28.5 mg, 0.26 mmol) in toluene (6.2 mL) and freshly distilled *i*-Pr_2NH (0.3 mL) and added to the solution of ***l*-P_{C8}8** and **T8**. The reaction mixture was stirred at 0 °C for 1 hour and then at 20 °C for 10 h. Once UV-*vis*-IR spectroscopy showed no changes, the same amount of the catalysts solution was added and the reaction mixture additionally stirred at 60 °C for 2 h. The reaction mixture was then cooled down and passed through short alumina column ($CHCl_3$) to remove non-cyclic species. Preparative GPC in toluene yielded corresponding template complexes ***c*-P_{C8}24·(T6)$_4$** and ***c*-P_{C8}16·(T6)$_2$**. Both were passed over a size exclusion column on Biobeads SX-1 ($CHCl_3$/10% pyridine) to remove the template. Semi-preparative GPC (THF/1% pyridine) of the corresponding free rings afforded ***c*-P_{C8}16** (1 mg, 6.7 %) and ***c*-P_{C8}24** (1 mg, 6.7 %) as brown solids.

***c*-P_{C8}16**

^{1}H-NMR (400 MHz, $CDCl_3$/1% d_5-pyridine): δ_H 0.76 (m, 192H, -CH_3), 1.10–1.35 (m, 512H, -CH_2), 1.39–1.55 (m, 128H, -CH_2), 1.76–1.86 (m, 128H, -CH_2), 4.09 (s br, 128H, -OCH_2), 6.85 (m, 32H, -ArH_{para}), 7.33 (m, 64H, -ArH_{ortho}), 9.03 (d, 64H, J = 4.1 Hz, -ArH_β), 9.80 (d, 64H, J = 4.5 Hz, -ArH_β); *m/z* (MALDI-ToF) 17538 ($C_{1088}H_{1312}N_{64}O_{64}Zn_{16}$, M^++dithranol requires 17583); λ_{max} (toluene/1% pyridine) 474, 594, 814.

***c*-P_{C8}24**

^{1}H-NMR: as above.

Zinc (3,5-bis-octyloxy-phenyl)-porphyrin[12] nanoring *c*-P_{C8}12

Zinc (3,5-bis-octyloxy-phenyl)-porphyrin[18] nanoring *c*-P_{C8}18

Zinc (3,5-bis-octyloxy-phenyl)-porphyrin[24] nanoring *c*-P_{C8}24

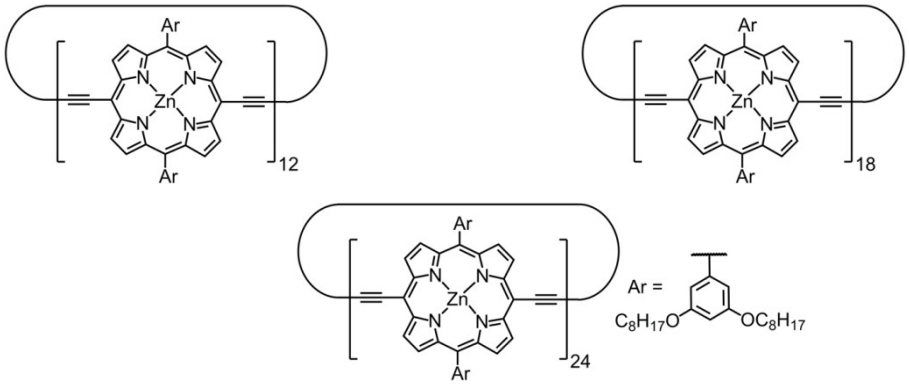

To a suspension of deprotected porphyrin hexamer ***l*-P_{C8}6** (19.8 mg, 3.0 µmol) in 10.0 mL of fresh $CHCl_3$ (10.0 mL) a solution of template **T8** (7.0 mg, 3.0 µmol) in $CHCl_3$ (7.0 mL) was added and the mixture sonicated for 2 h. A catalysts solution was prepared by dissolving dichlorobis(triphenylphosphine)-palladium(II) (66.4 mg, 94.6 µmol), copper(I) iodide (91.4 mg, 0.48 mmol) and 1,4-benzoquinone (210.9 mg, 1.95 mmol) in $CHCl_3$ (12.0 mL) and freshly distilled *i*-Pr_2NH (2.30 mL). The catalysts solution was added to the porphyrin-template mixture and the reaction mixture stirred at 20 °C for 3 h., after which twice the initial amount of the catalysts solution was added twice - after 12 h. of stirring and then after 14 h. of stirring. Once the UV-*vis*-IR spectroscopy showed no changes, the initial amount of the catalysts solution was added and the reaction mixture additionally stirried at 60 °C for 2 h. The solvents were removed, the mixture redissolved in 20 mL of $CHCl_3$, filtered through tight cotton plug and passed over a size-exclusion column on Biobeads SX-1 ($CHCl_3$/10% pyridine) to remove the template, the catalysts and exsess 1,4-benzoquinone. Semi-preparative GPC (THF/1% pyridine) of the mixture of porphyrin oligomers afforded ***c*-P_{C8}12** (4.4 mg, 22 %), ***c*-P_{C8}18** (1.9 mg (9.6 %) and ***c*-P_{C8}24** (4.9 mg, 25 %) as brown solids.

***c*-P_{C8}12** and ***c*-P_{C8}24** ^{1}H-NMR: as above.

***c*-P_{C8}18**

^{1}H-NMR (400 MHz, $CDCl_3$/1% d_5-pyridine): δ_H 0.74 (m, 216H, -CH_3), 1.11–1.33 (m, 576H, -CH_2), 1.48–1.38 (m, 144H, -CH_2), 1.74 – 1.84 (m, 144H, -CH_2), 4.07 (s br, 144H, -OCH_2), 6.84 (m, 36H, -ArH_{para}), 7.32 (m, 72H, -ArH_{ortho}), 9.03 (d, 72H, J = 4.5 Hz, -ArH_β), 9.79 (d, 72H, J = 4.5 Hz, -ArH_β); *m/z* (MALDI-ToF) 19549 ($C_{1224}H_{1476}N_{72}O_{72}Zn_{18}$, M^+ requires 19526); λ_{max} (toluene/1% pyridine) 473, 595, 809.

Zinc (3,5-bis-octyloxy-phenyl)-porphyrin[10] nanoring *c*-P_{C8}10

Zinc (3,5-bis-octyloxy-phenyl)-porphyrin[20] nanoring *c*-P_{C8}20

Zinc (3,5-bis-octyloxy-phenyl)-porphyrin[30] nanoring *c*-P_{C8}30

Zinc (3,5-bis-octyloxy-phenyl)-porphyrin[40] nanoring *c*-P_{C8}40

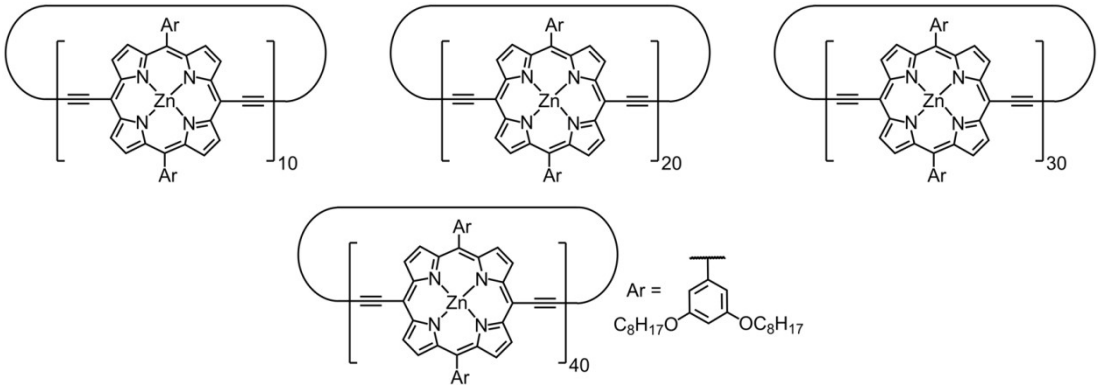

The template **T6** (0.68 mg, 0.68 µmol) and the linear porphyrin 10-mer ***l*-P_{C8}10** (4.7 mg, 0.41 µmol) were dissolved in $CHCl_3$ (5.0 mL) and heated at 50 ºC until clear solution formed. A catalyst solution was prepared by dissolving $Pd(PPh_3)_2Cl_2$ (1.0 mg, 1.41 µmol), copper(I) iodide (1.2 mg, 6.9 µmol) and 1,4-benzuquinone (3.0 mg, 27.9 µmol) in $CHCl_3$ (0.7 mL) and *i*-Pr_2NH (60 µL). 250 µL of the catalysts solution was added to a solution of ***l*-P_{C8}10** and **T6** at 0 ºC and then stirred at 0 ºC for 2 h. and then at 20 ºC for 12 h. Once analytical GPC confirmed full conversion of the ***l*-P_{C8}10**, the porphyrin oligomers mixture was separated from the catalysts by size-exclusion chromatography on Biobeads SX-1 ($CHCl_3$/10% pyridine) and further separated by recycling gel permeation chromatography to yield ***c*-P_{C8}10** (1.2 mg, 26 %), ***c*-P_{C8}20** (0.8 mg, 17 %), ***c*-P_{C8}30** (1.2 mg, 26 %) and ***c*-P_{C8}40** (0.5 mg, 11 %).

***c*-P_{C8}10**

^{1}H-NMR (500 MHz, $CDCl_3$/1% d_5-pyridine): δ_H 0.74–0.82 (m, 120H, -CH_3), 1.16–1.32 (m, 320H, -CH_2), 1.40–1.46 (m, 80H, -CH_2), 1.77–1.83 (m, 80H, -CH_2), 4.07 (s br, 80H, -OCH_2), 6.84 (m, 20H, -ArH_{para}), 7.29 (m, 40H, -ArH_{ortho}), 8.96 (d, 40H, J = 4.5 Hz, -ArH_β), 9.74 (d, 40H, J = 4.5 Hz, -ArH_β); *m/z* (MALDI-ToF) 10852 ($C_{680}H_{820}N_{40}O_{40}Zn_{10}$, M^+ requires 10848); λ_{max} (toluene/1% pyridine) 472, 494, 597, 809.

***c*-P_{C8}20**

^{1}H-NMR (400 MHz, $CDCl_3$/1% d_5-pyridine): δ_H 0.74–0.78 (m, 240H, -CH_3), 1.12–1.31 (m, 640H, -CH_2), 1.40–1.46 (m, 160H, -CH_2), 1.78–1.81 (m, 160H, -CH_2), 4.07 (s br, 160H, -OCH_2), 6.85 (m, 40H, -ArH_{para}), 7.28 (m, 80H, -ArH_{ortho}), 8.96 (d, 80H, J = 4.5 Hz, -ArH_β), 9.80 (d, 80H, J = 4.5 Hz, -ArH_β); *m/z* (MALDI-ToF) 21701 ($C_{1360}H_{1640}N_{80}O_{80}Zn_{20}$, M^+ requires 21696); λ_{max} (toluene/1% pyridine) 473, 594, 817.

***c*-$\mathbf{P_{C8}30}$**

^{1}H-NMR (400 MHz, $CDCl_3$/1% d_5-pyridine): δ_H 0.71 (m, 360H, -CH_3), 1.10–1.25 (m, 960H, -CH_2), 1.40 (m, 240H, -CH_2), 1.76 (m, 240H, -CH_2), 4.03 (s br, 240H, -OCH_2), 6.83 (m, 60H, -ArH_{para}), 7.28 (m, 120H, -ArH_{ortho}), 8.98 (m, 120H, -ArH_β), 9.78 (m, 120H, -ArH_β); *m/z* (MALDI-ToF) 32681 ($C_{2040}H_{2460}N_{120}O_{120}Zn_{30}$, M^+ requires 32543); λ_{max} (toluene/1% pyridine) 475, 494, 594, 822.

***c*-$\mathbf{P_{C8}40}$**

^{1}H-NMR (400 MHz, $CDCl_3$/1% d_5-pyridine): δ_H 0.67–0.70 (m, 480H, -CH_3), 1.07–1.23 (m, 1280H, -CH_2), 1.36 (m, 320H, -CH_2), 1.72 (m, 320H, -CH_2), 3.99 (s br, 320H, -OCH_2), 6.80 (m, 80H, -ArH_{para}), 7.28 (m, 160H, -ArH_{ortho}), 8.98 (d, 160H, -ArH_β), 9.77 (m, 160H, -ArH_β); *m/z* (MALDI-ToF) 43475 ($C_{2720}H_{3280}N_{160}O_{160}Zn_{40}$, M^+ requires 43391); λ_{max} (toluene/1% pyridine) 475, 493, 593, 823.

Zinc (3,5-bis-octyloxy-phenyl)-porphyrin[10] nanoring *c*-$\mathbf{P_{C8}10}$

Zinc (3,5-bis-octyloxy-phenyl)-porphyrin[20] nanoring *c*-$\mathbf{P_{C8}20}$

Zinc (3,5-bis-octyloxy-phenyl)-porphyrin[30] nanoring *c*-$\mathbf{P_{C8}30}$

Zinc (3,5-bis-octyloxy-phenyl)-porphyrin[40] nanoring *c*-$\mathbf{P_{C8}40}$

Zinc (3,5-bis-octyloxy-phenyl)-porphyrin[50] nanoring *c*-$\mathbf{P_{C8}50}$

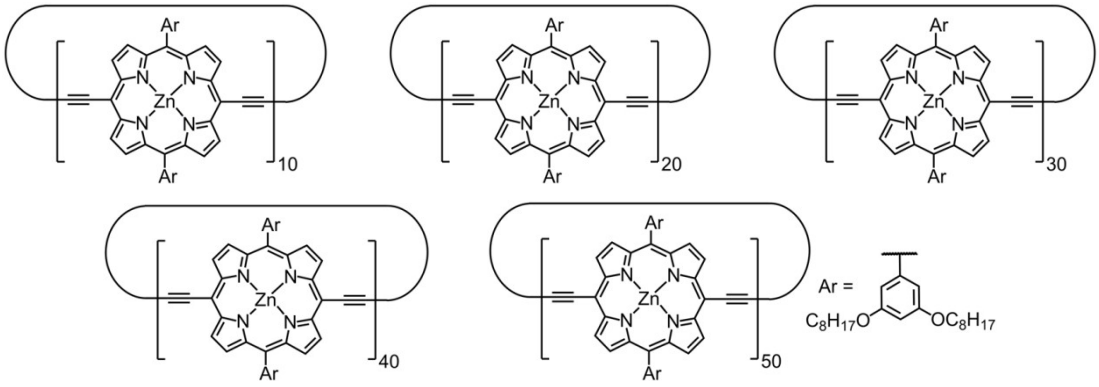

The template **T8** (0.98 mg, 0.42 μmol) and the linear porphyrin 10-mer ***l*-$\mathbf{P_{C8}10}$** (4.5 mg, 0.41 μmol) were dissolved in $CHCl_3$ (5.3 mL) and heated at 50 ºC until clear solution formed. A catalyst solution was prepared by dissolving $Pd(PPh_3)_2Cl_2$ (1.0 mg, 1.41 μmol), CuI (1.2 mg, 6.9 μmol) and 1,4-benzuquinone (3.0 mg, 27.9 μmol) in $CHCl_3$ (700 μL) and *i*-Pr_2NH (60 μL). 260 μL of the catalysts solution was added to a solution of ***l*-$\mathbf{P_{C8}10}$** and **T8** at 0 ºC and then stirred at 0 ºC for 2 h. after which the initial amount of the catalysts solution was added and the mixture stirred at 0 ºC for 2 h. and then at 20 ºC for 10 h. After that 1.56 mL of the catalyst solution was added in three equal portions – after 14 h. of stirring and further stirred at 40 ºC, after 19 h. of stirring and further stirred at 50 ºC and after 17 h. of stirring and further stirred at 50 ºC. Once analytical GPC confirmed full conversion of the ***l*-$\mathbf{P_{C8}10}$**, the porphyrin oligomers mixture was separated from the catalysts by size-exclusion chromatography on Biobeads SX-1 ($CHCl_3$/10% pyridine) and further separated by

recycling gel permeation chromatography to yield ***c*-$\mathbf{P_{C8}}$10** (0.3 mg, 7 %), ***c*-$\mathbf{P_{C8}}$20** (0.3 mg, 7 %), ***c*-$\mathbf{P_{C8}}$30** (0.7 mg, 16 %), ***c*-$\mathbf{P_{C8}}$40** (1.2 mg, 27 %) and ***c*-$\mathbf{P_{C8}}$50** (0.6 mg, 13 %).

***c*-$\mathbf{P_{C8}}$10**

^{1}H-NMR as above.

***c*-$\mathbf{P_{C8}}$20**

^{1}H-NMR as above.

***c*-$\mathbf{P_{C8}}$30**

^{1}H-NMR as above.

***c*-$\mathbf{P_{C8}}$40**

^{1}H-NMR as above.

***c*-$\mathbf{P_{C8}}$50**

^{1}H-NMR (400 MHz, $CDCl_3$/1% d_5-pyridine): δ_H 0.77 (m, 600H, -CH_3), 1.14–1.31 (m, 1600H, -CH_2), 1.44 (m, 400H, -CH_2), 1.81 (m, 400H, -CH_2), 4.06 (s br, 400H, -OCH_2), 6.86 (m, 100H, -ArH_{para}), 7.34 (m, 200H, -ArH_{ortho}), 9.01 (d, 200H, -ArH_β), 9.82 (m, 200H, -ArH_β); *m/z* (MALDI-ToF) 54406 ($C_{3400}H_{4100}N_{200}O_{200}Zn_{50}$, M^+ requires 54239).

7.4 References

[1] B. J. Littler, M. A. Miller, C.-H. Hung, R. W. Wagner, D. F. O'Shea, P. D. Boyle, J. S. Lindsey, *J. Org. Chem.* **1999**, *64*, 1391–1396.

[2] J. K. Sprafke, *Supramolecular Control of Synthesis and Electronic Structure of Porphyrin Oligomers*, D.Phil. thesis, University of Oxford, Oxford, **2011**.

[3] M. S. Newman, L. F. Lee, *J. Org. Chem.* **1972**, *37*, 4468–4469.

[4] P. N. Taylor, H. L. Anderson, *J. Am. Chem. Soc.* **1999**, *121*, 11538–11545.

[5] M. Hoffmann, *Nanosized Porphyrin Molecular Wires and Rings*, D.Phil. Thesis, University of Oxford, Oxford, **2008**.

[6] H. J. Hogben, J. K. Sprafke, M. Hoffmann, M. Pawlicki, H. L. Anderson, *J. Am. Chem. Soc.* **2011**, *133*, 20962–20969**.**

[7] W. J. R. Peveler, *Porphyrin Nanorings*, Part II Thesis, University of Oxford, Oxford, **2011**.

Appendix 1: X-ray Structures Details

***c*-P$_{t\text{-Bu}}$6•T6**	
Empirical formula	$C_{386.19}H_{350.19}Cl_{6.56}N_{30}Zn_6$
Formula weight	6036.69
Temperature	150 K
Wavelength	0.68890 Å
Crystal system	Orthorhombic
Space group	*P c c n*
Unit cell dimensions	a = 59.310(5) Å α = 90º b = 25.141(3) Å β = 90º c = 31.050(4) Å γ = 90º
Volume	46,299 Å^3
Z	4
Density (calculated)	0.866 Mg/m^3
Absorption coefficient	0.388 mm^{-1}
F(000)	12,675.637
Crystal size	0.200×0.150×0.100 mm^3
Theta range for data collection	1.210 to 18.307º
Index ranges	$0 \le h \le 54$, $0 \le k \le 22$, $0 \le l \le 28$
Reflections collected	213,483
Independent reflections	18318 [R(int) = 0.153]
Completeness to theta = 18.307º	99.6%
Absorption correction	Semi-empirical from equivalents
Max. and min. transmission	0.96 and 0.67
Refinement method	Full-matrix least-squares on F^2
Data/restraints/parameters	18128/3401/2291
Goodness of fit on F^2	0.9235
Final R indices [I > 2sigma(I)]	R1 = 0.1047, wR2 = 0.2611
R indices (all data)	R1 = 0.1065, wR2 = 0.2626
Largest diff. peak and hole	0.78 and -0.63 e.Å^{-3}

***c*-$P_{t\text{-Bu}}12$•$(T6)_2$**	
Empirical formula	$C_{768}H_{696}N_{60}Zn_{12}$
Formula weight	11550.89
Temperature	100 K
Wavelength	0.68890 Å
Crystal system	Monoclinic
Space group	*C 1 2/c 1*
Unit cell dimensions	a = 117.44(5) Å α = 90º b = 21.009(7) Å β = 115.385(4)º c = 57.23(2) Å γ = 90º
Volume	127,570(80) $Å^3$
Z	4
Density (calculated)	0.601 Mg/m^3
Absorption coefficient	0.253 mm^{-1}
F(000)	24,336
Crystal size	0.150×0.150×0.05 mm^3
Theta range for data collection	1.116 to 20.225º
Index ranges	$-112 \le h \le 112$, $-11 \le k \le 20$, $-49 \le l \le 52$
Reflections collected	121,443
Independent reflections	49666 [R(int) = 0.180]
Completeness to theta = 15.169º	87.8%
Absorption correction	Semi-empirical from equivalents
Max. and min. transmission	0.99 and 0.14
Refinement method	Full-matrix least-squares on F^2
Data/restraints/parameters	49035/13533/3781
Goodness of fit on F^2	0.9987
Final R indices [I > 2sigma(I)]	R1 = 0.1539, wR2 = 0.1765
R indices (all data)	R1 = 0.2101, wR2 = 0.3049
Largest diff. peak and hole	0.48 and -0.37 e.$Å^{-3}$

Appendix 2: Publications

1. *"Spatially Coherent Excitations in Synthetic Light-Harvesting Nanorings"*
C. K. Yong, W.-H. Chen, **D. V. Kondratuk**, P. Parkinson, A. Stannard, A. Summerfield, J. K. Sprafke, M. C. O'Sullivan, P. H. Beton, H. L. Anderson, L. M. Herz, *submitted.*

2. *"Optimizing the Energy Offset Between Dye and Hole-Transporting Material in Solid-State Dye-Sensitized Solar Cells"*
C. T. Weisspfennig, M. M. Lee, J. Teuscher, P. Docampo, S. D. Stranks, H. J. Joyce, H. Bergmann, I. Bruder, **D. V. Kondratuk**, M. B. Johnston, H. J. Snaith, L. M. Herz, *J. Phys. Chem.* **2013**, *accepted.*

3. "*Mechanical Stiffening of Porphyrin Nanorings through Supramolecular Columnar Stacking"*
S. A. Svatek, L. M. A. Perdigão, A. Stannard, M. B. Wieland, **D. V. Kondratuk**, H. L. Anderson, J. N. O'Shea, P. H. Beton, *Nano Lett*, **2013**, *13*, 3391–3395.

4. "*Amplified Two-Photon Absorption in Trans-A_2B_2-Porphyrins Bearing Nitrophenylethynyl Substituents*"
A. Nowak-Krol, C. J. Wilson, M. Drobizhev, **D.V. Kondratuk**, A. Rebane, H. L. Anderson, D.T. Gryko, *ChemPhysChem.* **2012**, *13*, 3966-3972.

5. "*Synthesis and Structure of Polyyne-Based Rotaxanes*"
L. Movsisyan, **D. V. Kondratuk**, M. Franz, A. L. Thompson, R. R. Tykwinski, H. L. Anderson, *Org. Lett.* **2012**, *14*, 3424-3426.

6. "*Two Vernier-Templated Routes to a 24-Porphyrin Nanoring*"
D. V. Kondratuk, L. M. A. Perdigao, M. C. O'Sullivan, S. Svatek, G. Smith, J. N. O'Shea, P. H. Beton, H. L. Anderson, *Angew. Chem. Int. Ed.* **2012**, *51*, 6696-6699. (**VIP paper**)

7. "*Belt-Shaped π-Systems: Relating Geometry to Electronic Structure in a Six-Porphyrin Nanoring*"
J. K. Sprafke, **D. V. Kondratuk**, M. Wykes, A. L. Thompson, M. Hoffmann, R. Drevinskas, W.-H. Chen, C. K Yong, J. Karnbratt, J. E. Bullock, M. Malfois, M. R. Wasielewski, B. Albinsson, L. M. Herz, D. Zigmantas, D. Beljonne, H. L. Anderson, *J. Am Chem. Soc.* **2011**, *133*, 17262-17273.

8. "*Vernier Templating and Synthesis of a 12-porphyrin Nanoring*"
M. C. O'Sullivan, J. K. Sprafke, **D. V. Kondratuk**, C. Rinfray, T. D. W. Claridge, A. Saywell, M. O. Blunt, J. N. O'Shea, P. H. Beton, M. Malfois, H. L. Anderson, *Nature*, **2011**, *469*, 72-75.